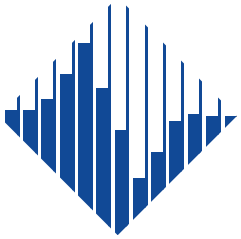

PACIFIC EARTHQUAKE ENGINEERING
RESEARCH CENTER

Direct-Finite-Element Method for Nonlinear Earthquake Analysis of Concrete Dams Including Dam–Water–Foundation Rock Interaction

Arnkjell Løkke

Department of Structural Engineering
Norwegian University of Science and Technology

Anil K. Chopra

Department of Civil and Environmental Engineering
University of California, Berkeley

PEER Report No. 2019/02
Pacific Earthquake Engineering Research Center
Headquarters at the University of California, Berkeley

March 2019

PEER 2019/02
March 2019

Disclaimer

The opinions, findings, and conclusions or recommendations expressed in this publication are those of the author(s) and do not necessarily reflect the views of the study sponsor(s), the Pacific Earthquake Engineering Research Center, or the Regents of the University of California.

Direct-Finite-Element Method for Nonlinear Earthquake Analysis of Concrete Dams Including Dam–Water–Foundation Rock Interaction

Arnkjell Løkke
Department of Structural Engineering
Norwegian University of Science and Technology (NTNU)

Anil K. Chopra
Department of Civil and Environmental Engineering
University of California, Berkeley

PEER Report 2019/02
Pacific Earthquake Engineering Research Center
Headquarters at the University of California, Berkeley
March 2019

ABSTRACT

Evaluating the seismic performance of concrete dams requires nonlinear dynamic analysis of two- or three-dimensional dam–water–foundation rock systems that include all the factors known to be significant in the earthquake response of dams. Such analyses are greatly complicated by interaction between the structure, the impounded reservoir and the deformable foundation rock that supports it, and the fact that the fluid and foundation domains extend to large distances. Presented in this report is the development of a direct finite-element (FE) method for nonlinear earthquake analysis of two- and three-dimensional dam–water–foundation rock systems. The analysis procedure applies standard viscous-damper absorbing boundaries to model the semi-unbounded fluid and foundation domains, and specifies at these boundaries effective earthquake forces determined from a ground motion defined at a control point on the ground surface.

This report is organized in three parts, with a common notation list, references, and appendices at the end of the report. Part I develops the direct FE method for 2D dam–water–foundation rock systems. The underlying analytical framework of treating dam–water–foundation rock interaction as a scattering problem, wherein the dam perturbs an assumed "free-field" state of the system, is presented, and by applying these concepts to a bounded FE model with viscous-damper boundaries to truncate the semi-unbounded domains, the analysis procedure is derived. Step-by-step procedures for computing effective earthquake forces from analysis of two 1D free-field systems are presented, and the procedure is validated by computing frequency response functions and transient response of an idealized dam–water–foundation rock system and comparing against independent benchmark results.

This direct FE method is generalized to 3D systems in Part II of this report. While the fundamental concepts of treating interaction as a scattering problem are similar for 2D and 3D systems, the derivation and implementation of the method for 3D systems is much more involved. Effective earthquake forces must now be computed by analyzing a set of 1D and 2D systems derived from the boundaries of the free-field systems, which requires extensive book-keeping and data transfer for large 3D models. To reduce these requirements and facilitate implementation of the direct FE method for 3D systems, convenient simplifications of the procedure are proposed and their effectiveness demonstrated.

Part III of the report proposes to use the direct FE method for conducting the large number of nonlinear response history analyses (RHAs) required for performance-based earthquake engineering (PBEE) of concrete dams, and discusses practical modeling considerations for two of the most influential aspects of these analyses: nonlinear mechanisms and energy dissipation (damping). The findings have broad implications for modeling of energy dissipation and calibration of damping values for concrete dam analyses. At the end of Part III, the direct FE method is implemented with a commercial FE program and used to compute the nonlinear response of an actual arch dam. These nonlinear results, although limited in their scope, demonstrate the capabilities and effectiveness of the direct FE method to compute the types of nonlinear engineering response quantities required for PBEE of concrete dams.

ACKNOWLEDGMENTS

We are grateful to several individuals who have contributed to this research in different forms:

- Dr. Ushnish Basu at Livermore Software Technology Corporation for his advice on the conceptual framework of treating dam–water–foundation rock interaction as a scattering problem, for his contributions to the development of the direct FE method, and for sharing the source code for two-dimensional acoustic fluid finite elements.
- Dr. Frank McKenna at UC Berkeley for his help with implementing the required element types and tips on how to effectively run 2D and 3D fluid–soil–structure interacting models in the finite-element program OPENSEES.
- Professor Pierre Léger at École Polytechnique de Montréal for his advice on nonlinear modeling of concrete dams, in particular modeling of cracking in concrete.

The first author would also like to thank Professors Svein N. Remseth and Amir M. Kaynia at NTNU for their guidance and support, and for facilitating the collaboration between NTNU and UC Berkeley during the period of which this research was conducted.

This report is the same, except for some editorial changes, as Arnkjell Løkke's doctoral dissertation which has been submitted to the Norwegian University of Science and Technology (NTNU).

Any opinions, findings, and conclusions or recommendations expressed in this material are those of the authors and do not necessarily reflect those of the sponsoring organizations, PEER, or the Regents of the University of California.

CONTENTS

LIST OF TABLES

LIST OF FIGURES

PART I

PART II

PART III

APPENDICES

PART I

Direct-Finite-Element Method for Nonlinear Earthquake Analysis of Two-Dimensional Dam–Water–Foundation Rock Systems

1 Introduction

Evaluating the seismic performance of concrete gravity dams requires dynamic analysis of two- or three-dimensional (2D and 3D, respectively) dam–water–foundation rock systems that include all significant factors in the earthquake response of concrete dams [Chopra 2012a]: dam–foundation rock interaction including inertia effects of the rock [Fenves and Chopra 1985; Tan and Chopra 1996]; dam–water interaction, including water compressibility and energy absorption at the reservoir bottom [Hall and Chopra 1982; Hall and Chopra 1983; and Fenves and Chopra 1983]; radiation damping due to the semi-unbounded sizes of the reservoir and foundation domains[Tan and Chopra 1996; Zhang et al. 2009] and nonlinear behavior of the dam and foundation rock [Mlaker 1987; Dowling and Hall 1989; Vargas-Loli and Fenves 1989; El-Aidi and Hall 1989; Chopra and Zhang 1991; Fenves et al. 1992; Bhattacharjee and Leger 1993; Cervera et al. 1995; and Chávez and Fenves 1995a].

Analysis procedures based on the substructure method have been available since 1984 for 2D frequency-domain analysis of dam–water–foundation rock systems [Fenves and Chopra 1984c]. This method models the semi-unbounded domains rigorously and specifies the ground motion directly at the dam–foundation rock interface; however, it is restricted to homogeneous material properties and simple geometry of the reservoir and foundation domains. More importantly, the substructure method is restricted to linear behavior of the entire system. Thus, nonlinear effects such as cracking of concrete and separation and sliding at joints and interfaces cannot be modeled.

The direct method of analysis, on the other hand, models the entire system directly in the time-domain using finite elements. Such analyses are often conducted using commercial software that ignores one or several of the above factors to facilitate nonlinear dynamic analysis. For many years, the dam engineering profession used a finite-element (FE) model that included a limited extent of foundation rock, assumed to have no mass, and approximated hydrodynamic

effects by an added mass of water moving with the dam. The design ground motion–typically defined at a control point on the free surface–was applied at the bottom fixed boundary of the foundation domain without modification. These approximations are attractive because they simplify the analysis greatly; however, such a model solves a problem that is very different from the real problem on two counts: (1) the assumptions of massless rock and incompressible water–implied by the added mass water model–are unrealistic [Chopra 2012a]; and (2) applying ground motion specified at a control point on the free surface to the bottom boundary of the FE model contradicts recorded evidence that motions at depth generally differ significantly from surface motions. In recent years, some engineers have shifted away from this approach.

To eliminate these unrealistic assumptions, the FE model of the dam must be extended to comprise a foundation domain that includes mass, stiffness, and material damping appropriate for rock, and a fluid domain that includes water compressibility and reservoir bottom absorption. The semi-unbounded foundation and fluid domains must be reduced to bounded sizes with appropriate radiation conditions at the domain boundaries to allow propagation of outgoing waves. Development of such absorbing boundaries is a vast field with rich literature [Lysmer and Kuhlemeyer 1969; Smith 1974; Clayton and Engquist 1977; Engquist and Majda 1977; White et al. 1977; Kausel and Tassoulas 1981; Underwood and Geers 1981; Liao and Wong 1984; Higdon 1986; Higdon 1987; Wolf 1988; Wolf and Song 1995; Wolf and Song 1996; Kellezi 2000; Basu and Chopra 2003; Basu and Chopra 2004; and Basu 2009]. The earthquake motion cannot be specified directly at the model truncations as this would render any absorbing boundary ineffective. Instead, effective earthquake forces are computed from the earthquake motion and applied either directly at the absorbing boundaries [Zienkiewicz et al. 1989; Lemos 1999; and Saouma et al. 2011] or via a layer of elements interior of the boundaries [Bielak and Christiano 1984; Aydinoglu 1993; and Bielak et al. 2003].

Utilizing these concepts, Basu [2004] developed a direct FE procedure for nonlinear analysis of dam–water–foundation rock systems. Here, the high-performing perfectly matched layer (PML) [Basu and Chopra 2004] was used as the absorbing boundary, and the effective seismic input (ESI) method [Bielak and Christiano 1984], also known as the domain reduction method (DRM) [Bielak et al. 2003] was used to apply the effective earthquake forces. Although the procedure rigorously incorporates all the above factors significant in the earthquake response

of dams, the PML boundary and DRM procedure are currently not available in most commercial FE codes; the only exception is LS-DYNA [Hallquist 2016]. Thus, this procedure is not accessible to researchers and practicing engineers who prefer other FE codes. These limitations can be overcome by modeling the absorbing boundaries by viscous dampers [Lysmer and Kuhlemeyer 1969] and specifying the effective earthquake forces directly at these boundaries. Both of these features are available in almost every commercial FE code and are therefore chosen herein. A variation of such a procedure initiated by the U.S. Bureau of Reclamation, wherein effective earthquake forces on the side boundaries are ignored, is often used in the dam engineering profession [Noble and Nuss 2004a; Mills-Bria et al. 2008; and Bureau of Reclamation 2013].

The following chapters develop the formulation for a direct FE method for nonlinear earthquake analysis of semi-unbounded dam–water–foundation rock systems that incorporates all significant factors for the earthquake response of dams, while ensuring broad applicability by using the well-known viscous damper as the absorbing boundaries. Derivation of the analysis method is founded on the idea of treating interaction as a scattering problem [Herrera and Bielak 1977; Bielak and Christiano 1984] and follows a similar outline as the procedure developed by Basu [2004] using PML-boundaries and DRM for seismic input. In Chapter 2, the system and ground motion is defined, and the governing equations for each of three subdomains are presented. In Chapters 3 and 4, the direct FE method is developed for dam–foundation rock and dam–water systems, respectively, by utilizing the concept of treating interaction as a scattering problem and formulating the radiation condition for viscous-damper boundaries in a convenient way. These two procedures are integrated to formulate the analysis procedure for the combined dam–water–foundation rock system in Chapter 5. At the end of Chapters 3–5, the analysis method is validated by computing the response of idealized dam–foundation rock (Chapter 3), dam–water (Chapter 4), and dam–water–foundation rock (Chapter 5) systems and comparing against results obtained using the substructure method. In Chapter 5, the importance of including water–foundation rock interaction is also discussed.

2 System and Ground Motion

2.1 SEMI-UNBOUNDED DAM–WATER–FOUNDATION ROCK SYSTEM

The idealized, 2D dam–water–foundation rock system (Figure 2.1) is composed of three parts: (1) the gravity dam with nonlinear properties; (2) the foundation rock, consisting of a bounded region adjacent to the dam that can be nonlinear and inhomogeneous, and a semi-unbounded region that is restricted to be linear; and (3) the fluid domain, consisting of a bounded region of arbitrary geometry adjacent to the dam that may be nonlinear, and a uniform channel, unbounded in the upstream direction, that is restricted to be linear. Thus, nonlinear effects such as concrete cracking, sliding and separation at construction joints, lift joints, and concrete-rock interfaces, and cavitation in the fluid may be considered in the analysis.

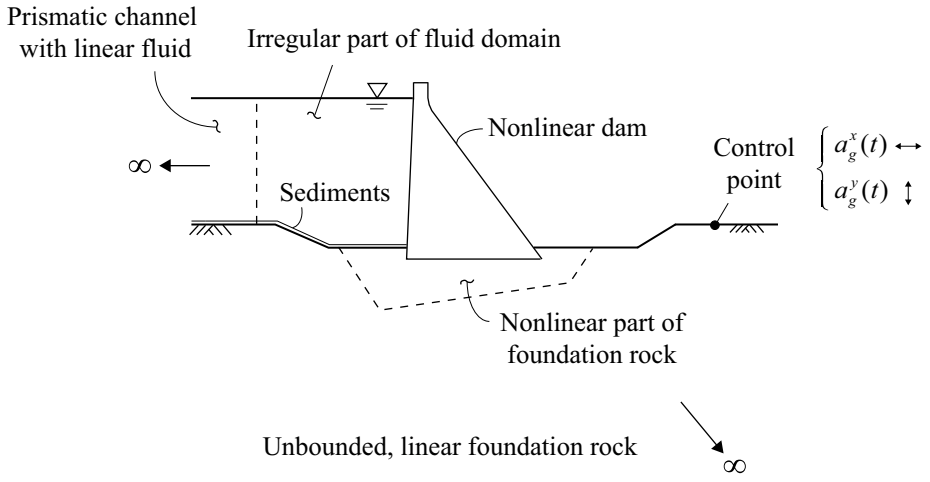

Figure 2.1 **Semi-unbounded dam–water–foundation rock system: (1) the dam itself; (2) the foundation rock, consisting of a bounded, nonlinear region and a semi-unbounded, linear region; and (3) the fluid domain, consisting of an irregular, nonlinear, region, and a semi-unbounded prismatic channel with linear fluid. Figure adapted from Basu [2004].**

The earthquake excitation is defined at a control point at the surface of the foundation rock by two components of free-field ground acceleration (Figure 2.1): the horizontal component $a_g^x(t)$ transverse to the dam axis, and the vertical component $a_g^y(t)$. The surface of the foundation rock is assumed to be at the same elevation in the far upstream and downstream directions; this geometric restriction is introduced to define a convenient free-field state of the foundation rock in Section 3.1.

2.2 MODELING OF SEMI-UNBOUNDED DOMAINS

The dam–water–foundation rock system in Figure 2.1 is modeled by a FE discretization of a bounded system with viscous-damper boundaries to represent the semi-unbounded foundation and fluid domains. The earthquake motion cannot be specified directly at these model truncations as this would render any absorbing boundary ineffective. Instead, effective earthquake forces are computed from the earthquake excitation and applied at the absorbing boundaries.

The size of the foundation and fluid domains included in the FE model is determined by the ability of the absorbing boundaries to absorb outgoing (scattered) waves from the dam. If an advanced boundary such as the PML [Basu and Chopra 2004] is used, a small domain is sufficient to model the fluid and foundation domains [Figure 2.2(a)]. In contrast, the simple viscous-damper boundary applied in this formulation requires much larger domains [Figure 2.2(b)].

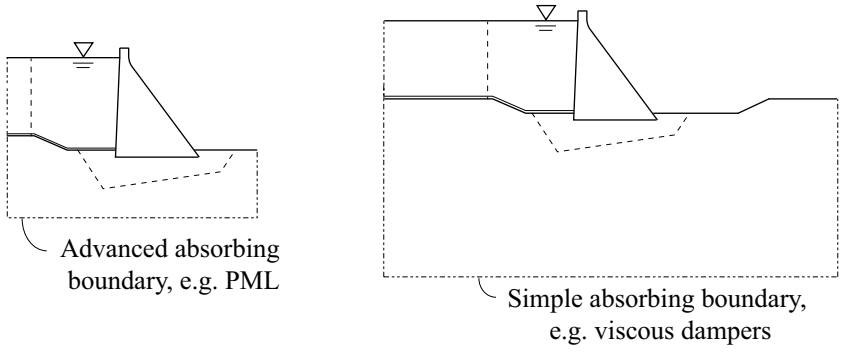

Figure 2.2 **Dam–water–foundation rock system with truncated foundation and fluid domains: (a) small domain sizes with advanced absorbing boundary; and (b) large domain sizes with simple absorbing boundary.**

2.3 GOVERNING EQUATIONS

2.3.1 Dam and Foundation Domain

The equations of motion governing the vector of total displacements $\mathbf{r}^t$ in the FE model of the dam with a truncated foundation domain and absorbing boundary Γ_f (Figure 2.3) are

$$\mathbf{m}\ddot{\mathbf{r}}^t + \mathbf{c}\dot{\mathbf{r}}^t + \mathbf{f}(\mathbf{r}^t) = \mathbf{R}_h^t + \mathbf{R}_b^t + \mathbf{R}_f^t + \mathbf{R}^{\text{st}} \tag{2.1}$$

where **m** and **c** are the mass and damping matrices, respectively; $\mathbf{f}(\mathbf{r}^t)$ is the vector of internal forces, which may be nonlinear in the dam and adjacent part of the foundation rock; $\mathbf{R}_h^t$ and $\mathbf{R}_b^t$ are the vectors of hydrodynamic forces acting at the dam–water interface Γ_h and water–foundation interface Γ_b, respectively; $\mathbf{R}^{\text{st}}$ is the vector of static forces, including self-weight, hydrostatic pressures, and static foundation reactions at Γ_f; and $\mathbf{R}_f^t$ are the forces associated with the absorbing boundary Γ_f, which include the effect of the excitation caused by seismic waves propagating from a distant earthquake source to the dam site, and the radiation condition at the boundary. Expressions for the forces $\mathbf{R}_h^t$, $\mathbf{R}_b^t$, and $\mathbf{R}_f^t$ will be derived later.

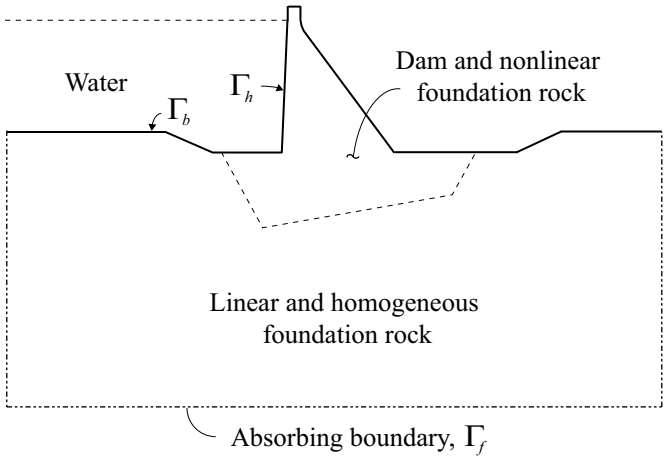

Figure 2.3 **Schematic FE model of the dam and foundation rock, with absorbing boundary Γ_f to truncate the semi-unbounded foundation domain.**

2.3.2 Fluid Domain

The water is modeled as a linear inviscid, irrotational, and compressible fluid with hydrodynamic pressures *p* governed by the acoustic wave equation:

$$\nabla^2 p = \frac{1}{C^2}\ddot{p} \tag{2.2}$$

where C is the speed of pressure waves in water.

Hydrodynamic pressures are caused by acceleration of the boundaries in contact with the reservoir: the upstream dam face Γ_h and the reservoir bottom Γ_b (Figure 2.4). These pressures are related to the total accelerations $\ddot{\mathbf{r}}^t$ at the fluid–solid interface by the boundary conditions:

$$\nabla p \cdot \mathbf{n}_h = -\rho \mathbf{n}_h \cdot \ddot{\mathbf{r}}_h^t, \qquad \text{at } \Gamma_h \tag{2.3a}$$

$$\nabla p \cdot \mathbf{n}_b + q\dot{p} = -\rho \mathbf{n}_b \cdot \ddot{\mathbf{r}}_b^t, \qquad \text{at } \Gamma_b \tag{2.3b}$$

where $\mathbf{n}_h$ and $\mathbf{n}_b$ are the outward normal vectors to the fluid at Γ_h and Γ_b, respectively; and ρ is the density of water. The second term on the left hand side of Equation (2.3b) is associated with the absorption of hydrodynamic pressure waves in sediments deposited at the reservoir bottom. This wave absorption is modeled in an approximate way by a boundary condition that allows partial absorption of incident hydrodynamic waves, where the damping coefficient q is given by

$$qC = \frac{1-\alpha}{1+\alpha} \tag{2.4}$$

where α is the reservoir bottom reflection coefficient [Fenves and Chopra 1983; Fenves and Chopra 1984c]. This simplified model is chosen herein to allow for a meaningful comparison with the substructure method [Fenves and Chopra 1984c] in the numerical validations presented at the end of Chapters 3–5. The effects of reservoir bottom sediments can alternatively be included using more sophisticated methods by directly modeling the thickness and extent of sediments discretized by finite elements with a viscoelastic [Lofti et al. 1981; Medina et al. 1990] or poroelastic [Bougacha and Tassoulas 1991; Dominguez et al. 1997] material model.

At the free-water surface, the boundary condition is simply p = 0; effects of surface waves are not included as these have little influence on the dynamic response of concrete dams [Chopra 1967]. Lastly, an appropriate radiation condition must hold at the absorbing boundary Γ_r.

Discretizing the fluid domain using finite elements and defining $\mathbf{p}^t$ as the vector of total hydrodynamic pressures–where the superscript t has been added for consistency with the notation for the total displacements $\mathbf{r}^t$ –the standard discretization process results in

$$\mathbf{s}\ddot{\mathbf{p}}^t + \mathbf{b}\dot{\mathbf{p}}^t + \mathbf{h}\mathbf{p}^t = -\rho\left[\mathbf{Q}_h^{\mathrm{T}} + \mathbf{Q}_b^{\mathrm{T}}\right]\ddot{\mathbf{r}}^t + \mathbf{H}_r^t \tag{2.5}$$

where **s**, **b**, and **h** are the corresponding "mass," "damping," and "stiffness" matrices of the fluid [Zienkiewicz and Bettess 1978], and $\mathbf{H}_r^t$ is the vector of forces associated with the absorbing boundary Γ_r. In contrast to the "standard" formulation [Zienkiewicz and Bettess 1978], the damping matrix **b** does here not include the effects of the radiation condition because these are represented by the forces $\mathbf{H}_r^t$. Also included in this term are the forces exerted on the absorbing boundary due to excitation of the part of the fluid domain upstream of Γ_r that has been eliminated; an expression for these forces will be derived in Chapter 4.

The matrix $\mathbf{Q}_h$ relates hydrodynamic pressures in the fluid to accelerations in the dam at the dam–water interface Γ_h according to the boundary condition of Equation (2.3a):

$$\mathbf{Q}_h = \int_{\Gamma_h} \bar{\mathbf{N}}_h^{\mathrm{T}} \mathbf{n}_h \mathbf{N}_h d\Gamma \tag{2.6}$$

where $\bar{\mathbf{N}}_h$ and $\mathbf{N}_h$ are the shape functions of the dam and fluid nodes, respectively, on the interface Γ_h. The matrix $\mathbf{Q}_b$ is constructed the same way, but integrated over Γ_b.

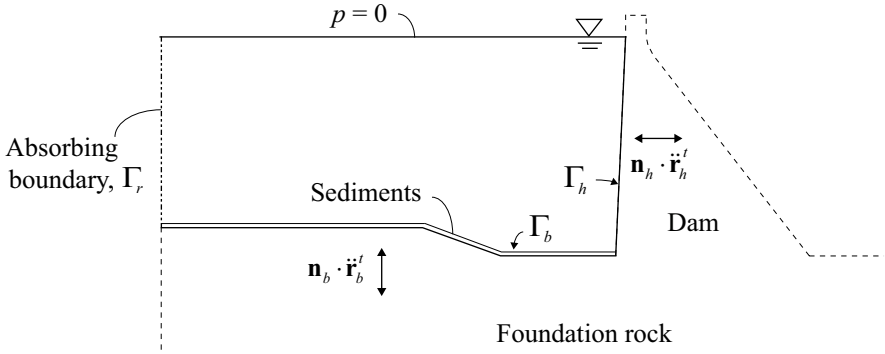

Figure 2.4 **Schematic FE model of the fluid domain highlighting the various boundary conditions at the reservoir boundaries.**

2.3.3 Dam–Water–Foundation Rock System

The hydrodynamic forces $\mathbf{R}_h^t$ and $\mathbf{R}_b^t$ in Equation (2.1) that act on the dam and foundation rock, respectively, can be expressed in terms of the hydrodynamic pressures $\mathbf{p}^t$ as [Zienkiewicz and Bettess 1978]

$$\mathbf{R}_h^t = \mathbf{Q}_h \mathbf{p}_h^t \qquad \mathbf{R}_b^t = \mathbf{Q}_b \mathbf{p}_b^t \tag{2.7}$$

Substituting this equation into Equation (2.1) and combining with Equation (2.5) gives the equations of motion for the dam–water–foundation rock system with truncated foundation and fluid domains:

$$\begin{bmatrix} \mathbf{m} & \mathbf{0} \\ \rho(\mathbf{Q}_h^{\mathrm{T}} + \mathbf{Q}_b^{\mathrm{T}}) & \mathbf{s} \end{bmatrix} \begin{Bmatrix} \ddot{\mathbf{r}}^t \\ \ddot{\mathbf{p}}^t \end{Bmatrix} + \begin{bmatrix} \mathbf{c} & \mathbf{0} \\ \mathbf{0} & \mathbf{b} \end{bmatrix} \begin{Bmatrix} \dot{\mathbf{r}}^t \\ \dot{\mathbf{p}}^t \end{Bmatrix} + \begin{Bmatrix} \mathbf{f}(\mathbf{r}^t) \\ \mathbf{0} \end{Bmatrix} + \begin{bmatrix} \mathbf{0} & -(\mathbf{Q}_h + \mathbf{Q}_b) \\ \mathbf{0} & \mathbf{h} \end{bmatrix} \begin{Bmatrix} \mathbf{r}^t \\ \mathbf{p}^t \end{Bmatrix} = \begin{Bmatrix} \mathbf{R}_f^t + \mathbf{R}^{\mathrm{st}} \\ \mathbf{H}_r^t \end{Bmatrix} \tag{2.8}$$

where the coupling matrices $\mathbf{Q}_h$ and $\mathbf{Q}_b$ have non-zero entries only on the interfaces Γ_h and Γ_b, respectively. Expressions for the unknown forces $\mathbf{R}_f^t$ and $\mathbf{H}_r^t$ associated with the absorbing boundaries Γ_f and Γ_r will be derived in the subsequent chapters.

3 Dam–Foundation Rock System

3.1 DAM–FOUNDATION ROCK INTERACTION AS A SCATTERING PROBLEM

Dam–foundation rock interaction may be treated as a scattering problem in which the dam perturbs the free-field motion in the foundation rock. Procedures based on this idea have been developed for analysis of soil–structure interaction systems [Bielak and Christiano 1984; Aydinoglu 1993; and Bielak et al. 2003], and of dam–water–foundation rock systems using PML absorbing boundaries and the DRM for seismic input [Basu 2004]. In this chapter, these ideas will be utilized to formulate an analysis procedure for the dam–foundation rock subsystem with absorbing boundaries modeled by viscous dampers.

Consider the linear foundation rock in its free-field state, i.e., before the dam was constructed or excavation had started [Figure 3.1(a)]. This domain is separated into two subdomains: Ω^0 denotes the region interior of the future absorbing boundary Γ_f, and Ω^+ is the semi-unbounded exterior region. The vector of free-field displacements at nodes in both subdomains is denoted by $\mathbf{r}^0$ [Figure 3.1(a)]; a procedure to determine this motion will be presented in Section 3.4.

The dam–foundation rock system is also separated into two subdomains [Figure 3.1(b)]: Ω denotes the dam and foundation region interior of the absorbing boundary Γ_f, and Ω^+ is the semi-unbounded exterior region, with the latter identical to the exterior region in the free-field system. Following the approach first proposed by Herrera and Bielak [1977], the displacement field in the dam–foundation rock system is defined by the variables:

$$\mathbf{r}^t, \quad \text{in the interior region } \Omega \tag{3.1a}$$

$$\mathbf{r}^t - \mathbf{r}^0, \text{ in the exterior region } \Omega^+ \tag{3.1b}$$

where $\mathbf{r}^t$ is the vector of total displacements governed by Equation (2.1), and $\mathbf{r}^t - \mathbf{r}^0$ represents the *scattered motion* in the exterior region Ω^+, i.e., the perturbation of the free-field motion

caused by the presence of the dam. This substitution of variables in Ω^+ will subsequently allow formulation of the governing equations for the absorbing boundary in a way that the forces $\mathbf{R}^t_f$ in Equation (2.1) can be determined from the free-field motion $\mathbf{r}^0$.

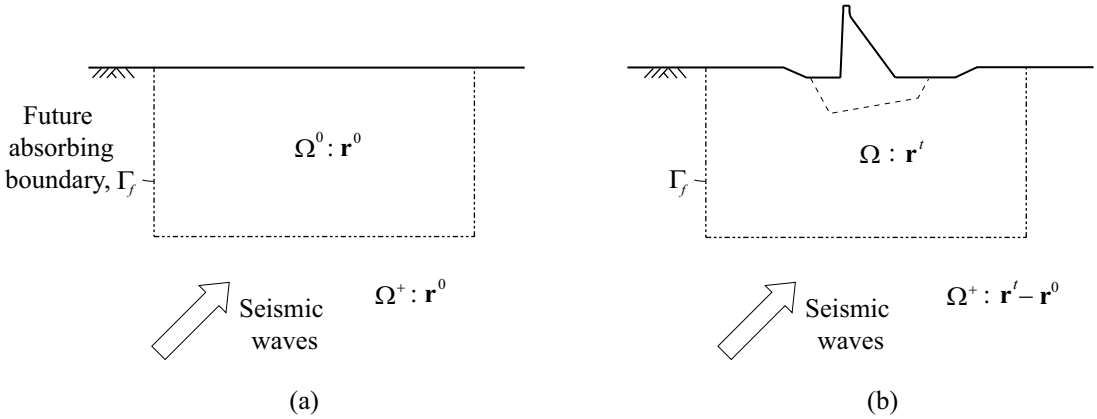

Figure 3.1 **Illustration of dam–foundation rock interaction as a scattering problem: (a) foundation rock in its free-field state with displacement field defined by $\mathbf{r}^0$ in $\Omega^0 \cup \Omega^+$; and (b) dam–foundation rock system with displacement field defined by the total motion $\mathbf{r}^t$ in Ω and the scattered motion $\mathbf{r}^t - \mathbf{r}^0$ in Ω^+.**

3.2 VISCOUS-DAMPER ABSORBING BOUNDARIES

A set of continuously distributed viscous dampers enforces the one-dimensional (1D) radiation condition [Lysmer and Kuhlemeyer 1969]. Assuming that incident waves impinge perpendicular to the boundary, this radiation condition is

$$\sigma + \rho_f V_p \dot{u} = 0 \tag{3.2a}$$

$$\tau + \rho_f V_s \dot{w} = 0 \tag{3.2b}$$

where $\sigma(t)$ and $\tau(t)$ are the normal and tangential tractions; $u(t)$ and $w(t)$ are the normal and tangential displacements[†] (Figure 3.2); ρ_f is the density of the foundation medium; and V_p and V_s its pressure-wave velocity and shear-wave velocity. The viscous damper is a perfect absorber of body waves that arrive normal to the boundary, but only a partial absorber for body wave impinging at an arbitrary angle and for surface waves; however, the accuracy is generally

[†] Temporarily (for convenience of notation), u and w is used instead of r^t for displacements.

acceptable provided the boundary is placed at sufficient distance from the wave source [Wolf 1988].

The viscous-damper boundary simulates the semi-unbounded foundation region Ω^+ where the displacements were defined by the scattered motion [Equation (3.1b)], i.e., $u = u^t - u^0$ and $w = w^t - w^0$. Because the foundation rock in Ω^+ is assumed to be linear, it follows that the boundary tractions associated with the scattered motion are $\sigma = \sigma^t - \sigma^0$ and $\tau = \tau^t - \tau^0$. Substituting for the scattered motion and the corresponding tractions in Equation (3.2) and rearranging terms, one obtains:

$$\sigma^t = \sigma^0 - \rho_f v_p \left[\dot{u}^t - \dot{u}^0 \right] \tag{3.3a}$$

$$\tau^t = \tau^0 - \rho_f v_s \left[\dot{w}^t - \dot{w}^0 \right] \tag{3.3b}$$

Thus, the total tractions on the absorbing boundary consist of two parts: (1) the free-field tractions and (2) the product of a damper coefficient and the scattered motion.

In a discretized model, the distributed dampers can be lumped at the boundary nodes, resulting in discrete viscous dampers with coefficients (Figure 3.2):

$$c_p = A \rho_f V_p \text{, normal to the boundary} \tag{3.4a}$$

$$c_s = A \rho_f V_s \text{, tangential to the boundary} \tag{3.4b}$$

where A is the tributary area (tributary length in a 2D model) for the boundary node. In FE notation, Equation (3.3) can be written for the boundary Γ_f as

$$\mathbf{R}_f^t = \mathbf{R}_f^0 - \mathbf{c}_f \left[\dot{\mathbf{r}}_f^t - \dot{\mathbf{r}}_f^0 \right] \tag{3.5}$$

where $\mathbf{R}_f^0$ is the vector of nodal forces consistent with the free-field tractions, and $\mathbf{c}_f$ is the matrix of damper coefficients c_p and c_s. The vectors $\mathbf{R}_f^t$, $\mathbf{R}_f^0$, and matrix $\mathbf{c}_f$ contain non-zero entries only for nodes on Γ_f.

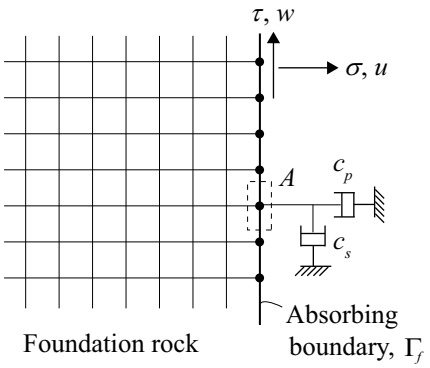

Figure 3.2 **Definition of damper coefficients c_p and c_s for lumped viscous damper on Γ_f.**

3.3 EQUATIONS OF MOTION

Substituting Equation (3.5) in Equation (2.1) and rearranging the terms—note that $\mathbf{R}_h^t \equiv \mathbf{R}_b^t \equiv \mathbf{0}$ in the absence of water in the reservoir—the final equations of motion for the dam–foundation rock subsystem with truncated foundation domain are obtained:

$$\mathbf{m}\ddot{\mathbf{r}}^t + \left[\mathbf{c} + \mathbf{c}_f\right]\dot{\mathbf{r}}^t + \mathbf{f}(\mathbf{r}^t) = \mathbf{R}^{\text{st}} + \mathbf{P}_f^0 \tag{3.6}$$

where the effective earthquake forces acting on the boundary Γ_f are

$$\mathbf{P}_f^0 = \mathbf{R}_f^0 + \mathbf{c}_f\dot{\mathbf{r}}_f^0 \tag{3.7}$$

Observe: by comparing Equations (3.6) and (2.1), the unknown forces $\mathbf{R}_f^t$ associated with the absorbing boundary Γ_f have now been expressed in terms of the viscous-damper forces $\mathbf{c}_f\dot{\mathbf{r}}^t$ and the effective earthquake forces $\mathbf{P}_f^0$. The latter consists of two parts: (1) $\mathbf{R}_f^0$, the forces consistent with the free-field tractions at Γ_f, and (2) the damper forces $\mathbf{c}_f\dot{\mathbf{r}}_f^0$ determined from the spatially varying free-field motion at Γ_f. Working with the scattered displacements in Ω^+ has thus enabled derivation of Equation (3.7) for the effective earthquake forces in terms of the free-field displacements and tractions.

3.4 FREE-FIELD EARTHQUAKE MOTION

The free-field motion $\mathbf{r}_f^0$ required to compute the effective earthquake forces $\mathbf{P}_f^0$ can be determined by various methods. The standard procedure is to define the ground motion at the control point (Figure 2.1) to be consistent with a design spectrum. This target spectrum may be

the uniform hazard spectrum (UHS) determined by probabilistic seismic hazard analysis (PSHA) [McGuire 2004], or a conditional mean spectrum (CMS) [Baker 2011]. Recorded ground motions are selected, scaled, and modified to "match" in some sense the target spectrum; alternatively, synthetic motions may be developed for an earthquake scenario. These methods are well developed for a single component of ground motion; work on extending these methods to two or three components acting simultaneously is in progress.

To determine the required free-field motion at the boundary Γ_f from the ground motion at the control point, it is necessary to introduce assumptions on the type of seismic waves and their incidence angle. The simplest assumption, often used for site response analyses and soil–structure interaction analyses, is vertically propagating *SH*-waves and *P*-waves [Schnabel et al 1972; Wolf 1985]. This is clearly a major simplification of the actual seismic wave field, that generally consists of a superposition of vertically and horizontally propagating *SH*-, *SV*- and *P*-waves, and horizontally propagating surface waves. This assumption is often justified on the basis that most sites are located relatively far away from the earthquake source, and that the gradual softening of rock and soil towards the Earth's surface leads to diffraction of seismic waves towards vertical incidence [Kramer 1996]. It is not obvious that this assumption is appropriate for concrete dams sited on competent bedrock, but at the present time it seems to be the only pragmatic choice.

Under the assumption of vertically propagating waves and homogeneous or layered rock, the free-field motion $\mathbf{r}_f^0$ at Γ_f can be obtained by deconvolution of the ground motion $a_g^k(t)$ at the control point using standard frequency-domain procedures [Schnabel et al. 1972]; software such as SHAKE [Ordóñez 2000] or DEEPSOIL [Hashash et al. 2011] can be utilized for this purpose. In principle, the deconvolution analysis can provide directly the motion at every nodal point on Γ_f; however, such an implementation may become cumbersome if output from the deconvolution analysis is required at a large number of elevations. An alternative method that overcomes this problem is presented in the next section.

3.5 COMPUTING EFFECTIVE EARTHQUAKE FORCES

3.5.1 Bottom Boundary

It was assumed in Section 3.4 that the earthquake motion is caused by vertically incident seismic waves propagating up from an underlying elastic medium. Because the free-field foundation–rock system [Figure 3.1(a)] is assumed to be linear and homogenous or horizontally layered, the boundary tractions at the bottom of the truncated foundation domain can be expressed as the sum of tractions due to the incident and reflected seismic waves:

$$\sigma^0 = \sigma_I^0 + \sigma_R^0 \tag{3.8}$$

where σ_I^0 and σ_R^0 are the normal tractions due to the incident (upward propagating) and reflected (downward propagating) seismic waves, respectively. At the boundary, the radiation condition must be satisfied for both the incident and reflected waves:

$$\sigma_I^0 - \rho_f V_p \dot{u}_I^0 = 0 \qquad \sigma_R^0 + \rho_f V_p \dot{u}_R^0 = 0 \tag{3.9}$$

where u_I^0 and u_R^0 are the displacements at the boundary in the normal direction corresponding to the incident and reflected seismic waves. The free-field velocity $\dot{u}^0$ at the boundary is the sum of the incident and reflected waves, i.e., $\dot{u}^0 = \dot{u}_I^0 + \dot{u}_R^0$. Substituting for $\dot{u}_R^0$ in Equation (3.9), and inserting the result in Equation (3.8), a new expression for the free-field boundary tractions σ^0 is obtained:

$$\sigma^0 = \rho_f V_p \left[2\dot{u}_I^0 - \dot{u}^0 \right] \tag{3.10a}$$

It follows that a similar expression can be derived for the tangential tractions τ^0:

$$\tau^0 = \rho_f V_s \left[2\dot{w}_I^0 - \dot{w}^0 \right] \tag{3.10b}$$

Such expressions were first derived by Joyner and Chen [1975].

Expressing Equation (3.10) in FE notation to obtain $\mathbf{R}_f^0 = \mathbf{c}_f \left[2\dot{\mathbf{r}}_I^0 - \dot{\mathbf{r}}_f^0 \right]$, and substituting the results into Equation (3.7) and cancelling terms, the final expression for the effective earthquake forces at the bottom of the foundation domain is obtained:

$$\mathbf{P}_f^0 = 2\mathbf{c}_f \, \dot{\mathbf{r}}_I^0 \tag{3.11}$$

where $\mathbf{r}_I^0$ is the motion at Γ_f due to the incident (upward propagating) seismic waves.

This equation has the advantage that it requires only the motion $\mathbf{r}_I^0$ of the incident wave, thus avoiding computation of the free-field tractions required if directly using Equation (3.7).

Furthermore, the incident motion $\mathbf{r}_I^0$ is easily computed as one-half the *outcrop motion*[†] at the bottom boundary, which is extracted directly from the deconvolution analysis. The procedure to compute $\mathbf{P}_f^0$ from Equation (3.11) is summarized in Box 3.1.

Box 3.1 Computing $\mathbf{P}_f^0$ at bottom boundary of foundation rock.

1. Determine the outcrop motion at the bottom foundation-rock boundary by 1D deconvolution of each component of the surface control motion $a_g^k(t)$, $k = x, y$.
2. Compute the incident motion $\mathbf{r}_I^0$ as 1/2 the outcrop motion at the bottom boundary determined in Step 1 and obtain $\dot{\mathbf{r}}_I^0$ by taking the time derivative of $\mathbf{r}_I^0$.
3. Calculate the effective earthquake forces $\mathbf{P}_f^0$ at the bottom boundary from Equation (3.11) using $\dot{\mathbf{r}}_I^0$ from Step 2.

3.5.2 Side Boundaries

The free-field motion $\mathbf{r}_f^0$ (and its time derivatives) required to compute the effective earthquake forces $\mathbf{P}_f^0$ at the side boundaries can be obtained directly from the deconvolution analysis; free-field tractions can then be computed from 1D stress–strain relations and these stresses converted to forces. Alternatively, both quantities can be computed by an auxiliary analysis of the foundation rock in its free-field state; see Figure 3.1(a). Analysis of this system reduces to a single column of foundation–rock elements with a viscous damper at its base that is subjected to the forces of Equation (3.11) and analyzed to determine $\dot{\mathbf{r}}_f^0$ and $\mathbf{R}_f^0$ at each nodal point along the height. The procedure is summarized in Box 3.2 and illustrated in Figure 3.3(a).

Although straightforward, both of these approaches requires the force histories $\mathbf{P}_f^0$ at all nodal points on the side boundaries to be stored for later use in setting up Equation (3.7). Clearly, such "book-keeping" may become cumbersome to implement for large models, especially for a 3D system [Saouma et al. 2011]. These difficulties can be avoided by introducing free-field boundary elements in the form of 1D foundation–rock columns at the side boundaries that are solved in parallel with the main FE model [Figure 3.3(b)] [Nielsen 2006]; however, such elements are currently not available in most commercial FE or finite difference codes, and the

[†] The reflected motion must equal the incident motion at every rock outcrop (stress-free boundary), hence the incident motion is exactly equal to 1/2 the outcrop motion.

only exceptions are FLAC [Itasca Consulting Group 2012] and PLAXIS [Brinkgreve et al. 2016].

Box 3.2 Computing $\mathbf{P}_f^0$ at side boundaries of foundation rock.

1. Determine the outcrop motion at the bottom foundation-rock boundary by 1D deconvolution of each component of the surface control motion $a_g^k(t)$, $k = x, y$.
2. Calculate the effective earthquake forces $\mathbf{P}_f^0$ at the bottom boundary from Equation (3.11), with the motion $\mathbf{r}_I^0$ due to the incident (upward propagating) seismic wave computed as one-half the outcrop motion extracted from the deconvolution analysis.
3. Develop a FE model for the free-field foundation-rock system: a single column of elements that has the same mesh density as the main FE model at the side boundaries, with viscous dampers applied at the base in the *x*- and *y*-directions [Figure 3.3(a)].
4. Compute the free-field velocities $\dot{\mathbf{r}}_f^0$ and forces $\mathbf{R}_f^0$ at each node over the height by analyzing the foundation–rock column subjected to forces given by Equation (3.11) at its base.
5. Calculate the effective earthquake forces $\mathbf{P}_f^0$ at the side boundaries from Equation (3.7) using $\dot{\mathbf{r}}_f^0$ and $\mathbf{R}_f^0$ from Step 4.

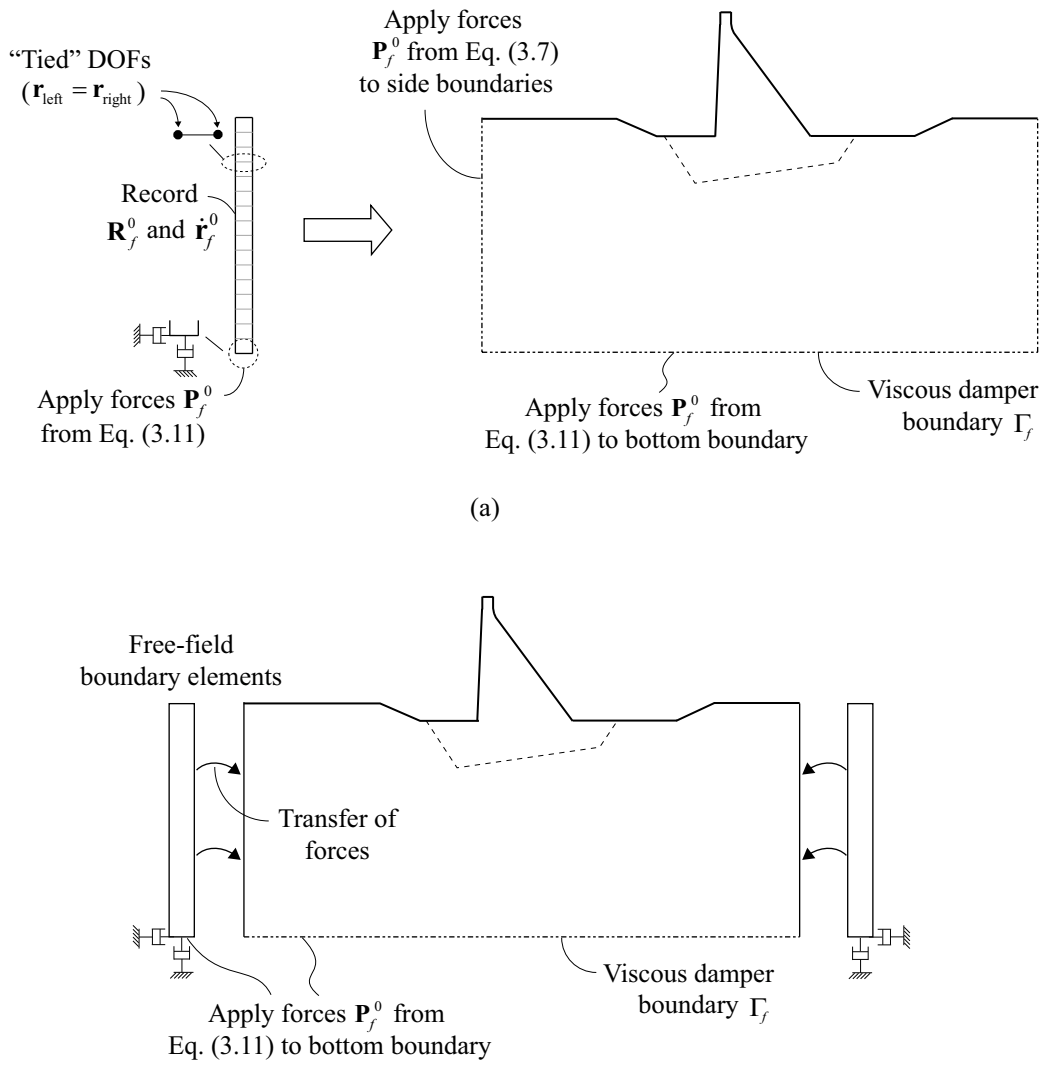

Figure 3.3 **Two methods for application of effective earthquake forces to side boundaries of foundation domain: (a) auxiliary analysis of 1D column to compute $\dot{\mathbf{r}}_f^0$ and $\mathbf{R}_f^0$ followed by direct application of $\mathbf{P}_f^0$; and (b) use of free-field boundary elements.**

3.5.3 Relation to the Domain Reduction Method

The domain reduction method (DRM) [Bielak et al. 2003] is a two-step methodology for modeling earthquake response where large contrasts exist between the physical scales of a "background model" (e.g., a regional fault simulation model) and a smaller structure or topographic feature that is the primary interest of the analysis. The method overcomes the issues

of scale difference by subdividing the original problem into two simpler ones where a local feature (e.g., a structure) perturbs the free-field motion in a larger regional domain. This same idea was utilized in deriving the equations of motion for the dam–foundation rock system, Equations (3.6) and (3.7), earlier in this chapter.

Although initially developed for large-scale regional simulations of earthquake motion, the DRM has also been successfully applied to specify the seismic input in soil–structure interaction problems in a layer of FEs interior of the absorbing boundary [Basu 2004; Kontoe et al. 2009]. This has the advantage that the seismic input can be specified independently of the boundary condition used in the numerical model, unlike the direct FE method developed above where the effective earthquake forces were derived assuming viscous-damper boundaries. Thus, the DRM can be used with any advanced boundary condition and the domain sizes reduced accordingly; see Figure 2.2.

When developing a general procedure for earthquake analysis of concrete dams, this benefit is outweighed by two disadvantages of using DRM: (1) the only commercial FE code where DRM has been implemented is LS-DYNA [Hallquist 2016]; and (2) specifying seismic input for a dam–water–foundation rock system with small domain sizes (which is the main attractiveness of using DRM) is impractical because it requires auxiliary analysis of a complex water–foundation rock system and extensive data management and transfer to set up and store the seismic input forces [Basu 2004].

To ensure implementation of the direct FE method in all commercial FE codes, it was therefore decided to use simple viscous dampers as the absorbing boundaries and specify effective earthquake forces directly at these boundaries. Appendix B provides a more comprehensive discussion on this topic, as well as a general introduction to DRM and a comparison between the DRM and direct FE method.

3.6 NUMERICAL VALIDATION

The analysis method developed in the preceding sections is validated by computing the dynamic response of the idealized dam–foundation rock system shown in Figure 3.4. All the direct FE method analyses are implemented in the open source FE program OpenSees [McKenna 2011]

using implicit time integration by the HHT-α method [Hilber et al. 1977] to solve the dynamic equilibrium equations [Equation (3.6)].

The idealized, triangular, dam has a vertical upstream face, a downstream slope of 0.8 to 1, and height H = 120 m. The dam concrete and foundation rock is assumed to be isotropic, homogeneous, linearly elastic, and in generalized plane stress. This assumption, while strictly speaking not appropriate for the foundation, is dictated by the expected individual vibration of monoliths during intense ground motions. Material properties for the concrete are: modulus of elasticity E_s = 22.4 GPa, density ρ_s = 2483 kg/m^3, and Poisson's ratio ν_s = 0.20; for the foundation rock: E_f = 22.4 GPa (i.e., E_f / E_s = 1), ρ_f = 2643 kg/m^3, and ν_f = 0.33. Material damping is modeled by Rayleigh damping with $\zeta_s = 2\%$ and $\zeta_f = 2\%$ viscous damping specified for the dam and foundation rock separately, with the damping matrix for the complete system constructed by assembling the individual Rayleigh damping matrices for the two subdomains [Chopra 2012b].

The FE models for the dam and foundation rock both consist of quadrilateral four-node elements [Cook et al. 2007]. The FE mesh for the dam has 15 elements across the width and 29 elements over the height; see Figure 3.4(a). The maximum element size in the foundation rock is limited to less than one-tenth of the shortest wavelength considered in the analysis to ensure satisfactory wave propagation in the mesh [Lysmer and Waas 1972]. The width (on either side of the dam) and depth of the foundation domain is selected as 4H and 2.5H, respectively. These dimensions are sufficiently large to minimize wave reflections from the viscous dampers for the selected system parameters, and were selected based on a parametric study for determining the required size of the foundation domain when using viscous-damper boundaries; see Appendix A.

The ground motion is specified by the ground acceleration $a_g^k(t)$ at the foundation surface; the free-field motion at depth in the model is obtained by deconvolution of this motion. Then, effective earthquake forces at the bottom and sides of the foundation domain are computed from Equations (3.11) and (3.7), respectively, using the procedures outlined in Boxes 3.1 and 3.2.

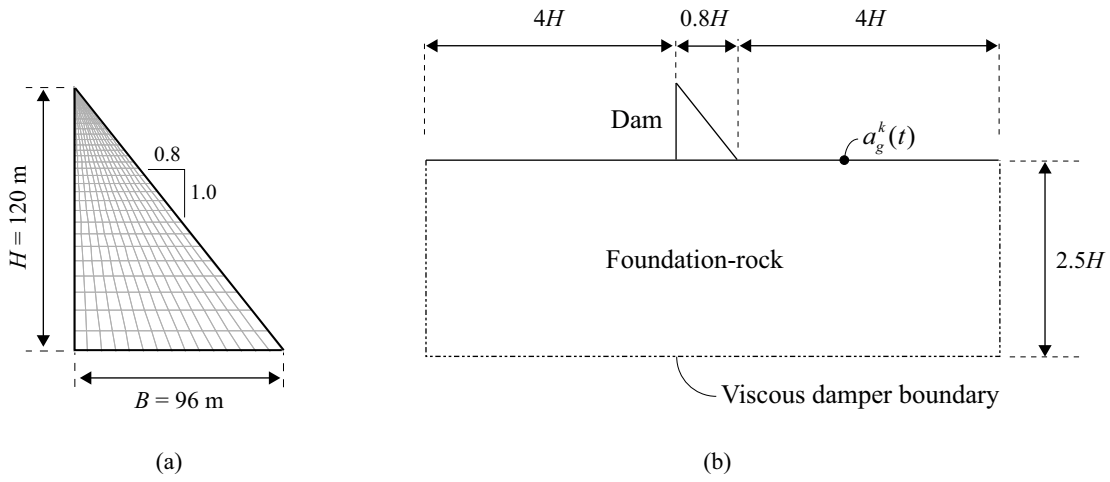

Figure 3.4 **(a) Geometry and FE mesh for triangular dam cross section; and (b) dimensions of FE model for dam–foundation rock system with viscous-damper boundaries to truncate the semi-unbounded foundation domain.**

Frequency response functions are computed by time-domain analysis of the FE system with free-field surface motions $a_g^x(t)$ and $a_g^y(t)$ defined by a harmonic function of unit amplitude. The response of the dam for a single excitation frequency is computed by solving the equations of motion for long enough time to reach steady state; this is then repeated at a sufficient number of frequencies to produce a smooth plot; see Appendix C for additional details on this procedure. The semi-analytical benchmark solution, to which the results of the direct FE method is compared, is obtained directly in the frequency domain by the substructure method [Fenves and Chopra 1984c] using the computer program EAGD84 [Fenves and Chopra 1984b] with a set of pre- and post-processing modules in MATLAB [The Math Works Inc. 2012] that the author has previously developed [Løkke 2013]. In the substructure method, the foundation rock is modeled as a viscoelastic half-space, the fluid domain is treated as an infinitely long continuum, and the earthquake excitation is specified directly at the dam–foundation interface, thus avoiding the need for artificial model truncations, absorbing boundaries, and deconvolution of the ground motion.

Material damping in EAGD84 is modeled by constant hysteretic damping specified by the hysteretic damping factors η_s = 0.04 and η_f = 0.04 for the dam and foundation rock; this corresponds to viscous damping ratios of ζ_s = 2% and ζ_f = 2%. For time-domain analysis in the direct FE method, the Rayleigh coefficients are determined by specifying ζ_s and ζ_f at the excitation frequency $f = \omega / 2\pi$, where ω is the angular frequency of the harmonic excitation

and at f = 1 Hz. This unconventional choice defines frequency-dependent Rayleigh damping to be as consistent as possible with frequency-independent hysteretic damping, thus ensuring a meaningful comparison of the frequency response functions from the direct FE and substructure methods. For the response history analyses to earthquake excitation presented later in Section 5.4.2, ζ_s and ζ_f are specified at the first two natural frequencies of the dam–water–foundation rock system.

3.6.1 Dam on Rigid Foundation Rock

The frequency response function for the amplitude of the relative horizontal acceleration at the crest of the dam on rigid foundation is computed by OpenSees and EAGD84 and compared in Figure 3.5. The near identical results for both horizontal and vertical excitation confirm the equivalency of the two FE models, and validate that the procedure for selecting Rayleigh coefficients provides material damping that is consistent with the constant hysteretic damping model at a given excitation frequency.

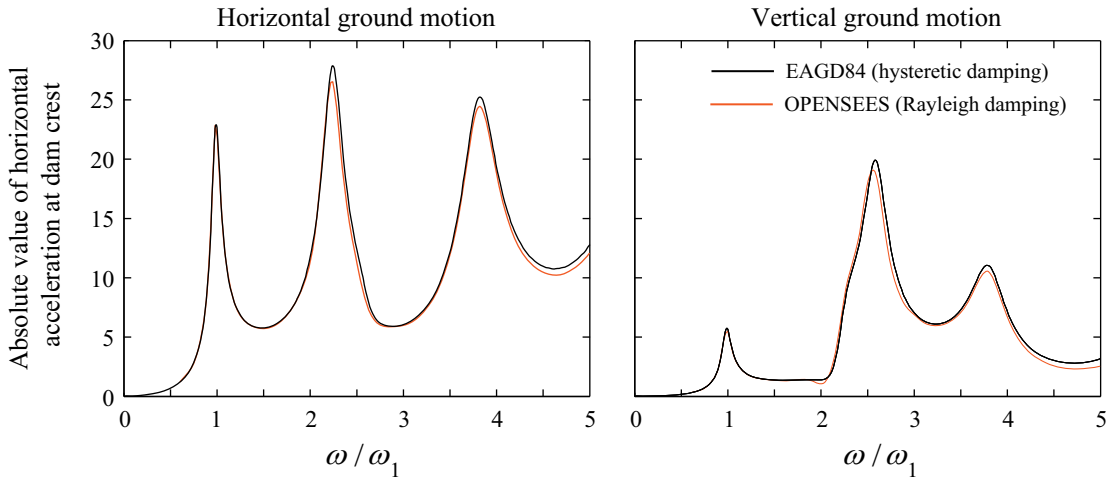

Figure 3.5 **Comparison of frequency response functions from OpenSees and EAGD84 for the amplitude of relative horizontal acceleration at the crest of dam on rigid foundation due to horizontal and vertical ground motion. Results are plotted against normalized frequency ω / ω_1 where ω_1 is the fundamental frequency of the dam on rigid foundation; Ω = 5%.**

3.6.2 Dam–Foundation Rock System

The dynamic response of the dam on flexible foundation rock is presented in Figure 3.6 for several values of E_f / E_s, the ratio of modulus of elasticity for the foundation rock to the dam. The results obtained by the direct FE method with viscous-damper boundaries and truncated foundation domain are generally close to the results from the substructure analysis, thus validating the ability of the direct FE method to model the semi-unbounded dam–foundation rock system.

The small discrepancies observable at some frequencies are due to the inability of the viscous-damper boundary to perfectly absorb outgoing (scattered) waves from the dam. Such discrepancies will generally decrease as the size of the foundation domain included in the FE model increases; see Appendix A.

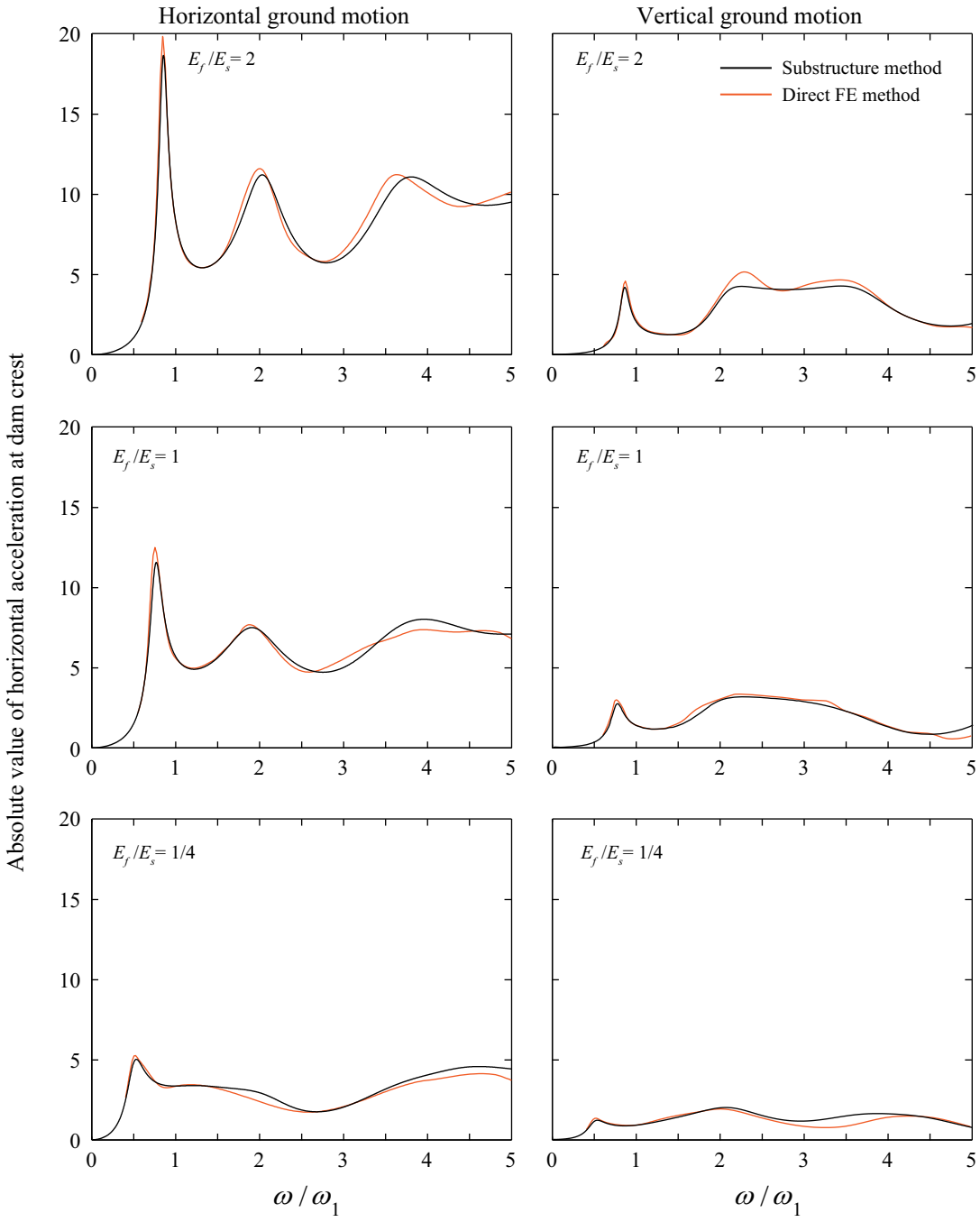

Figure 3.6 **Comparison of frequency response functions from direct FE and substructure methods for the amplitude of relative horizontal acceleration at the crest of dam on flexible foundation rock due to horizontal and vertical ground motion.** $\zeta_s = \zeta_f = 2\%$; $E_f / E_s = 1$.

3.6.3 Ignoring Effective Earthquake Forces at Side Boundaries

The dam engineering profession has been using a variation of the rigorous procedure summarized in Boxes 3.1 and 3.2, wherein the effective earthquake forces $\mathbf{P}_f^0$ are applied only at the bottom boundary but ignored at the side boundaries. Initiated by the U.S. Bureau of Reclamation and applied to actual projects [Noble and Nuss 2004a; Mills-Bria et al. 2008], variations of the method have also been used by other dam engineering professionals [Curtis et al. 2014].

Figure 3.7 presents frequency response functions for the dam on flexible foundation rock obtained using such an analysis procedure where forces are only applied at the bottom foundation boundary. The significant discrepancies observable in the results for both horizontal and vertical ground motion arise from the inability of this model to reproduce free-field conditions. Attempts have been made to correct for this shortcoming by modifying the amplitude and/or frequency content of the input ground motion [Bureau of Reclamation 2013]; however, it is not clear whether such modifications will lead to acceptable results, and neither version of these approximate methods has been validated against the substructure method.

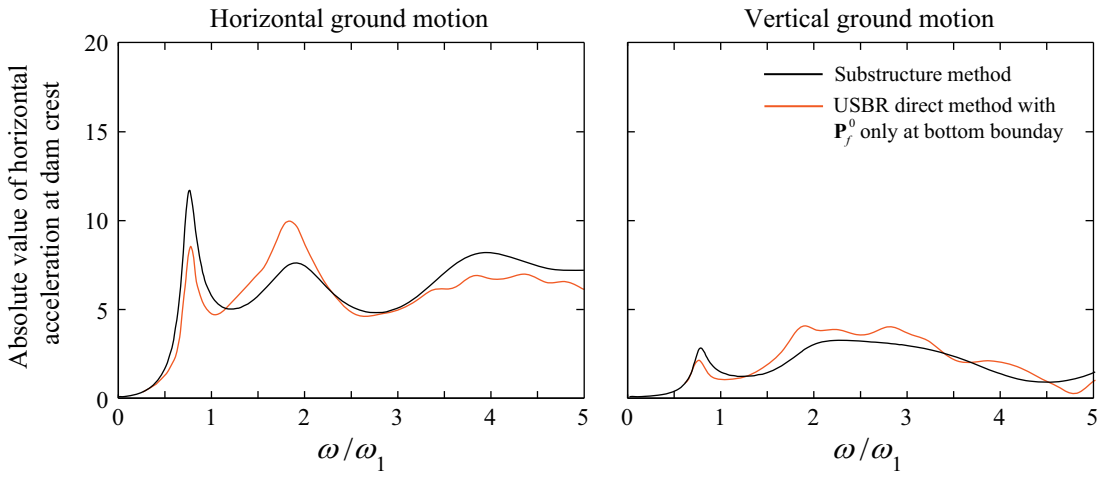

Figure 3.7 **Comparison of frequency response functions from the USBR direct method and substructure method for the amplitude of relative horizontal acceleration at the crest of dam on flexible foundation rock due to horizontal and vertical ground motion.** $\zeta_s = \zeta_f = 2\%$; $E_f / E_s = 1.$

3.6.4 Can Foundation Mass Be Ignored?

The massless foundation model [Clough 1980] is attractive in its simplicity as it only considers the flexibility of the foundation rock, but neglects the inertia and damping effects. The foundation rock can then be modeled by a small bounded-sized foundation model without absorbing boundaries as part of a standard FE analysis. Despite its well documented deficiencies [Chopra 2012a], the massless foundation model is still being used in dam engineering practice.

Presented in Figure 3.8 are frequency response functions for the dam–foundation rock system computed massless foundation approach and compared to the substructure method including foundation mass. Neglecting the foundation mass—and thereby also radiation damping—greatly overestimates the response of the dam; the results are in significant error. Clearly, such a model is unable to capture the dynamic properties associated with dam–foundation interaction and should not be used in earthquake analysis of concrete dams.

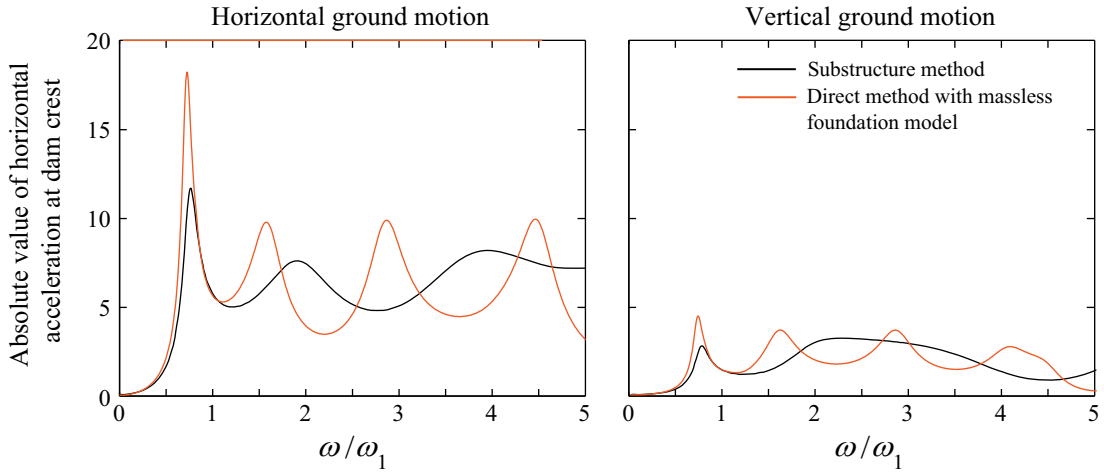

Figure 3.8 **Comparison of frequency response functions from the massless foundation model and substructure method for the amplitude of relative horizontal acceleration at the crest of dam on flexible foundation rock due to horizontal and vertical ground motion.** $\zeta_s = \zeta_f = 2\%$; $E_f / E_s = 1$.

4 Dam–Water System

4.1 DAM–WATER INTERACTION AS A SCATTERING PROBLEM

In this chapter, dam–water interaction is again treated as a scattering problem—in which the dam perturbs a "free-field" state of the system—to derive the effective earthquake forces for the fluid domain at the absorbing boundary Γ_r.

Consider the fluid in its "free-field" state, consisting only of the semi-unbounded prismatic channel Ω^+ upstream of the future absorbing boundary Γ_r [Figure 4.1(a)]. This system is not representative of any physical state of the fluid, but it facilitates formulation of the analysis procedure. Because the bottom boundary of the prismatic channel is horizontal, the free-field hydrodynamic pressures $\mathbf{p}^0$ in Ω^+ will be zero if the ground motion is purely horizontal, but they will be nonzero for vertical ground motion. A procedure for determining these pressures will be presented in Section 4.4.

The dam–water system is separated into two subdomains: Ω denotes the dam and irregular fluid region between the dam and the absorbing boundary Γ_r and Ω^+ is the semi-unbounded prismatic channel [Figure 4.1(b)]; the latter is identical to the free-field system. Following the same approach as for the dam–foundation rock system (Chapter 3), the hydrodynamic pressure field in the dam–water system is defined by the variables

$$\mathbf{p}^t, \qquad \text{in the interior region } \Omega \tag{4.1a}$$

$$\mathbf{p}^t - \mathbf{p}^0, \qquad \text{in the exterior region } \Omega^+ \tag{4.1b}$$

where $\mathbf{p}^t$ is the vector of total hydrodynamic pressures governed by Equation (2.5), and $\mathbf{p}^t - \mathbf{p}^0$ represents the *scattered hydrodynamic pressures* in the exterior region Ω^+, i.e., the perturbation of the free-field pressures caused by the existence of the dam and the irregular fluid region. This choice of variables in Ω^+ will subsequently allow formulation of the governing equations for the viscous-damper boundary in a way that the unknown forces $\mathbf{H}_r^t$ associated with the absorbing

boundary Γ_r, which first appeared in Equation (2.5), can be determined from the free-field pressures.

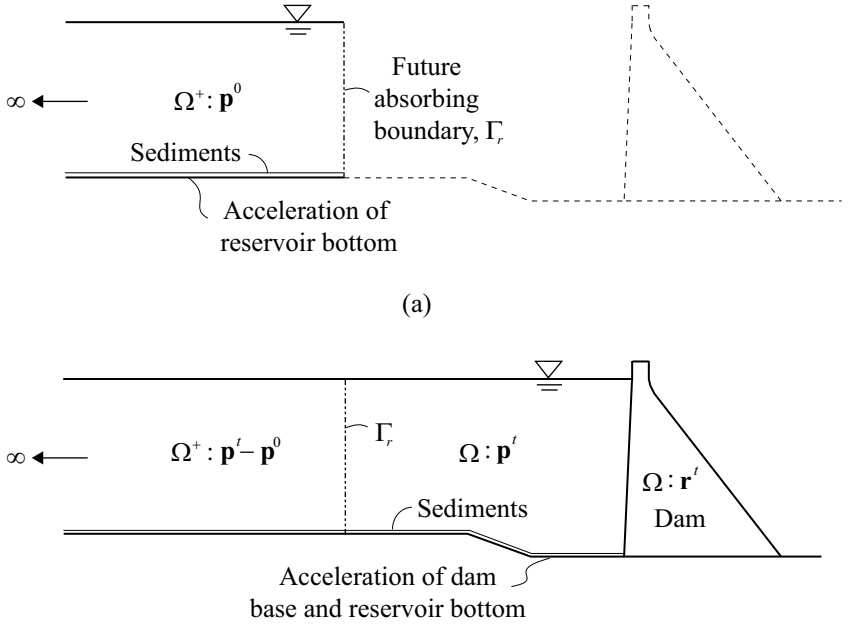

Figure 4.1 **Illustration of dam–water interaction as a scattering problem: (a) fluid domain in its "free-field" state with hydrodynamic pressures defined by $\mathbf{p}^0$ in Ω^+; (b) dam–water system with hydrodynamic pressures defined by $\mathbf{p}^t$ in Ω and the scattered pressures $\mathbf{p}^t - \mathbf{p}^0$ in Ω^+.**

4.2 VISCOUS-DAMPER ABSORBING BOUNDARY

A set of continuously distributed viscous dampers enforces the 1D radiation condition for a fluid [Zienkiewicz and Bettess 1978]. For incident waves perpendicular to the boundary, this condition is

$$\frac{\partial p}{\partial n} + \frac{1}{C}\dot{p} = 0 \tag{4.2}$$

where n denotes the outward normal to the fluid boundary. This boundary condition is also known as the *plane wave approximation*.

The viscous-damper boundary models the unbounded prismatic fluid channel Ω^+ where the scattered pressure $p^t - p^0$ was chosen as the variable to define hydrodynamic pressures [Equation (4.1b)]. Because the fluid in Ω^+ is assumed linear, Equation (4.2) becomes

$$\frac{\partial(p^t - p^0)}{\partial n} + \frac{1}{C}\left(\dot{p}^t - \dot{p}^0\right) = 0 \tag{4.3a}$$

which can be rewritten as

$$\frac{\partial p^t}{\partial n} = \frac{\partial p^0}{\partial n} - \frac{1}{C}\left(\dot{p}^t - \dot{p}^0\right) \tag{4.3b}$$

The distributed dampers are lumped to the boundary nodes in the discretized model, resulting in discrete viscous dampers with coefficient:

$$c_r = A / C \tag{4.4}$$

where A is the tributary area (tributary length in a 2D model) for the node. Equation (4.3) written in FE notation for nodes on the boundary Γ_r is

$$\mathbf{H}_r^t = \mathbf{H}_r^0 - \mathbf{c}_r\left[\dot{\mathbf{p}}_r^t - \dot{\mathbf{p}}_r^0\right] \tag{4.5}$$

where $\mathbf{H}_r^0$ is the vector of nodal forces consistent with the free-field pressure gradient $\partial p^0 / \partial n$, and $\mathbf{c}_r$ is the matrix of damping coefficients c_r. The vectors $\mathbf{H}_r^t$, $\mathbf{H}_r^0$ and matrix $\mathbf{c}_r$ have non-zero entries only for nodes on Γ_r.

Working with the scattered pressures in Ω^+ has enabled the derivation of Equation (4.5) for the unknown forces $\mathbf{H}_r^t$ in Equation (2.1) associated with the absorbing boundary Γ_r in terms of the free-field pressures.

4.3 EQUATIONS OF MOTION

Equation (2.1) that governs the dam–foundation rock subsystem is specialized for the dam alone:

$$\mathbf{m}\ddot{\mathbf{r}}^t + \mathbf{c}\dot{\mathbf{r}}^t + \mathbf{f}(\mathbf{r}^t) = \mathbf{R}_h^t + \mathbf{R}^{\mathrm{st}} \tag{4.6}$$

where $\mathbf{R}^{\mathrm{st}}$ now includes only gravity loads and hydrostatic forces on the dam, and the hydrodynamic forces are $\mathbf{R}_h^t = \mathbf{Q}_h \mathbf{p}^t$, where $\mathbf{Q}_h$ was defined in Equation (2.6). Combining Equation (4.6) with Equation (2.5) for the truncated fluid domain and rearranging terms:

$$\begin{bmatrix} \mathbf{m} & \mathbf{0} \\ \rho\mathbf{Q}_h^{\mathrm{T}} & \mathbf{s} \end{bmatrix} \begin{Bmatrix} \ddot{\mathbf{r}}^t \\ \ddot{\mathbf{p}}^t \end{Bmatrix} + \begin{bmatrix} \mathbf{c} & \mathbf{0} \\ \mathbf{0} & \mathbf{b} \end{bmatrix} \begin{Bmatrix} \dot{\mathbf{r}}^t \\ \dot{\mathbf{p}}^t \end{Bmatrix} + \begin{Bmatrix} \mathbf{f}(\mathbf{r}^t) \\ \mathbf{0} \end{Bmatrix} + \begin{bmatrix} \mathbf{0} & -\mathbf{Q}_h \\ \mathbf{0} & \mathbf{h} \end{bmatrix} \begin{Bmatrix} \mathbf{r}^t \\ \mathbf{p}^t \end{Bmatrix} = \begin{Bmatrix} \mathbf{R}^{\mathrm{st}} \\ \mathbf{H}_r^t - \rho\mathbf{Q}_b^{\mathrm{T}}\ddot{\mathbf{r}}_b^t \end{Bmatrix} \tag{4.7}$$

where $\ddot{\mathbf{r}}_b^t$ denotes the prescribed accelerations of the rigid foundation rock at the water–foundation rock interface Γ_b, and the matrix $\mathbf{Q}_b$ is computed similarly to Equation (2.6) but integrated over Γ_b.

Substituting Equation (4.5) for the unknown forces $\mathbf{H}_r^t$ leads to the final equations of motion for the dam–water system with truncated fluid domain:

$$\begin{bmatrix} \mathbf{m} & \mathbf{0} \\ \rho\mathbf{Q}_h^{\mathrm{T}} & \mathbf{s} \end{bmatrix} \begin{Bmatrix} \ddot{\mathbf{r}}^t \\ \ddot{\mathbf{p}} \end{Bmatrix} + \begin{bmatrix} \mathbf{c} & \mathbf{0} \\ \mathbf{0} & \mathbf{b}+\mathbf{c}_r \end{bmatrix} \begin{Bmatrix} \dot{\mathbf{r}}^t \\ \dot{\mathbf{p}} \end{Bmatrix} + \begin{Bmatrix} \mathbf{f}(\mathbf{r}^t) \\ \mathbf{0} \end{Bmatrix} + \begin{bmatrix} \mathbf{0} & -\mathbf{Q}_h \\ \mathbf{0} & \mathbf{h} \end{bmatrix} \begin{Bmatrix} \mathbf{r}^t \\ \mathbf{p} \end{Bmatrix} = \begin{Bmatrix} \mathbf{R}^{\mathrm{st}} \\ \mathbf{P}_r^0 - \rho\mathbf{Q}_b^{\mathrm{T}}\ddot{\mathbf{r}}_b^t \end{Bmatrix} \tag{4.8}$$

where the effective earthquake forces at Γ_r are

$$\text{DOFS: } \begin{Bmatrix} \mathbf{r}_h^{t(e)} \\ \mathbf{p}_h^{t(e)} \end{Bmatrix} \qquad \text{Mass: } \begin{bmatrix} \mathbf{0} & \mathbf{0} \\ \rho\mathbf{Q}_h^{(e)\mathrm{T}} & \mathbf{0} \end{bmatrix} \qquad \text{Stiffness: } \begin{bmatrix} \mathbf{0} & -\mathbf{Q}_h^{(e)} \\ \mathbf{0} & \mathbf{0} \end{bmatrix} \tag{4.9}$$

The forces $\mathbf{H}_r^0$ are zero for both horizontal and vertical ground motion because the pressure gradient $\partial p^0 / \partial n$ at Γ_r is zero when the foundation rock is rigid and the reservoir bottom is horizontal. The second term $\mathbf{c}_r \dot{\mathbf{p}}_r^0$ represents the contribution from earthquake-induced pressures in the fluid upstream of Γ_r that has been eliminated.

The earthquake excitation enters in Equation (4.8) through two quantities: (1) the forces $-\rho\mathbf{Q}_b^{\mathrm{T}}\ddot{\mathbf{r}}_b^t$ acting on Γ_b due to the prescribed accelerations $\ddot{\mathbf{r}}_b^t$, and (2) the effective earthquake forces $\mathbf{P}_r^0$ acting on Γ_r. Because the foundation rock is rigid, $\ddot{\mathbf{r}}_b^t$ is defined directly by the free-field ground accelerations $a_g^k(t)$ (Figure 2.1); these accelerations are also applied to the base of the dam. Thus, the only information required to specify the earthquake excitation is the free-field ground accelerations $a_g^k(t)$ and the free-field pressures $\mathbf{p}_r^0$.

Accelerations $\ddot{\mathbf{r}}_h^t$ are coupled with the hydrodynamic pressures $\mathbf{p}_h^t$ at the upstream face of the dam (Γ_h) through the matrix $\mathbf{Q}_h$ defined in Equation (2.6). In some FE programs, these conditions can be enforced by specification of tie constraints at the interfaces [Dassault System 2013]. Alternatively, interface elements can be introduced to perform this coupling, These

interface element will have three DOFs, two displacements and one pressure, and are defined by the mass and stiffness matrices [Basu 2004]:

$$\text{DOFs: } \begin{Bmatrix} \mathbf{r}_h^{t(e)} \\ \mathbf{p}_h^{t(e)} \end{Bmatrix} \qquad \text{Mass: } \begin{bmatrix} \mathbf{0} & \mathbf{0} \\ \rho \mathbf{Q}_h^{(e)\mathrm{T}} & \mathbf{0} \end{bmatrix} \qquad \text{Stiffness: } \begin{bmatrix} \mathbf{0} & -\mathbf{Q}_h^{(e)} \\ \mathbf{0} & \mathbf{0} \end{bmatrix} \tag{4.10}$$

Because these matrices are unsymmetric, they lead to an unsymmetric system of global equations in the numerical model. Note: this rarely causes problems in modern FE programs because these normally have efficient and robust solvers for sparse, unsymmetric systems of equations.

4.4 COMPUTING EFFECTIVE EARTHQUAKE FORCES AT Γ_r

The effective earthquake forces $\mathbf{P}_r^0$ at Γ_r are to be computed by analysis of the free-field fluid system, which is a prismatic channel of uniform depth [Figure 4.1(a)]. Because the reservoir bottom is horizontal, horizontal ground motion will not generate any hydrodynamic pressures and $\mathbf{P}_r^0 = \mathbf{0}$. Analysis of the prismatic channel for vertical ground motion reduces to a single column of fluid elements of unit width subjected to forces ρa_g^y at its base [Figure 4.2(a)]. This analysis provides the pressures $\mathbf{p}_r^0$ (and its time derivatives) that are required in Equation (4.9). The procedure is summarized in Box 4.1 and illustrated in Figure 4.2.

Box 4.1 Computing $\mathbf{P}_r^0$ at upstream fluid boundary.

1 Develop a FE model for the free-field fluid [Figure 4.2(a)]: a single column of elements of unit width with the same mesh density as the fluid adjacent to the boundary Γ_r. Apply a single line element to model reservoir bottom sediments.

2. Calculate $\dot{\mathbf{p}}_r^0$ at every nodal point along the height by analyzing the fluid column subjected to forces ρa_g^y at its base for vertical ground motion; $\dot{\mathbf{p}}_r^0 = 0$ for horizontal ground motion.

3 Compute the effective earthquake forces $\mathbf{P}_r^0$ at the fluid boundary Γ_r from Equation (4.9) using $\dot{\mathbf{p}}_r^0$ from Step 2.

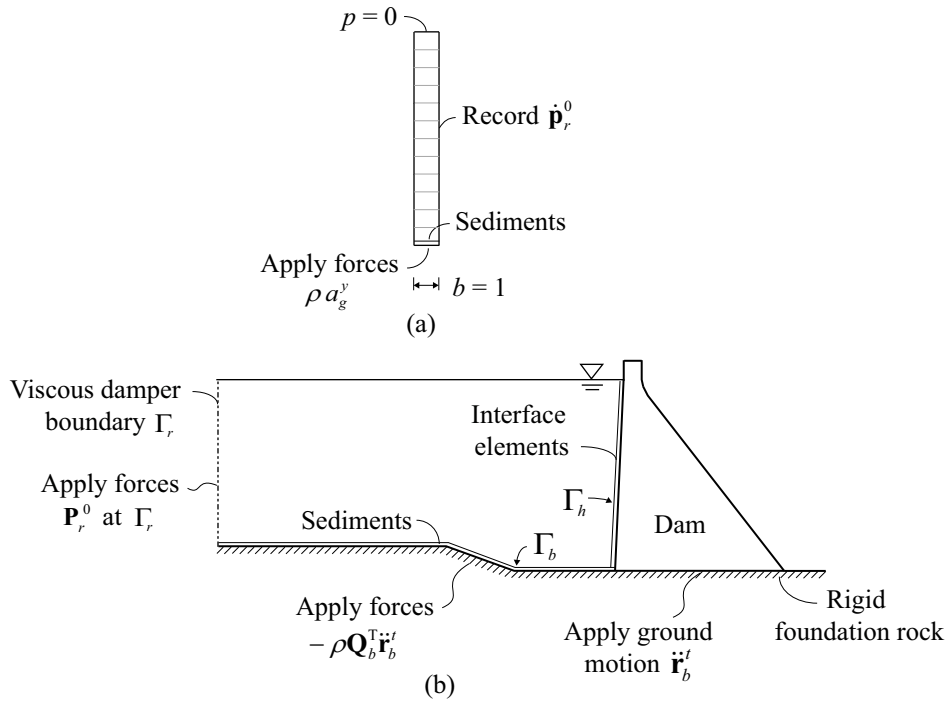

Figure 4.2 **Summary of analysis procedure for dam–water subsystem: (a) auxiliary analysis of single column of fluid elements to determine $\dot{\mathbf{p}}_r^0$ for vertical ground motion; (b) application of earthquake excitation and effective earthquake forces to truncated FE model.**

4.5 NUMERICAL VALIDATION

The analysis procedure developed in the proceeding sections is validated by computing the dynamic response of the idealized dam–water system shown in Figure 4.3 subjected to horizontal and vertical ground motion. The idealized dam has the same cross section, FE discretization, and material properties as the ones used in Section 3.6. Standard solid and acoustic elements [Cook et al. 2007] are used in the dam and fluid, respectively; interface elements are applied at the dam–water interface; and line elements are applied to model sediments at the reservoir bottom using the approximate 1D sediment model [Equation (2.4)]. Material damping in the dam is modeled by Rayleigh damping implemented using the procedure described in Section 3.6 specialized for the dam alone, but with ζ_s = 5% viscous damping selected for the dam concrete to provide reasonable overall energy dissipation in the system with rigid foundation rock. The impounded water has the same depth as the height of the dam, density ρ = 1000 kg/m^3, and pressure-wave velocity C = 1440 m/sec. The ground motion is specified by the ground

acceleration $a_g^k(t)$ of the rigid foundation at the dam base. Effective earthquake forces at the boundary of the fluid domain are computed from Equation (4.9) using the procedure outlined in Box 4.1.

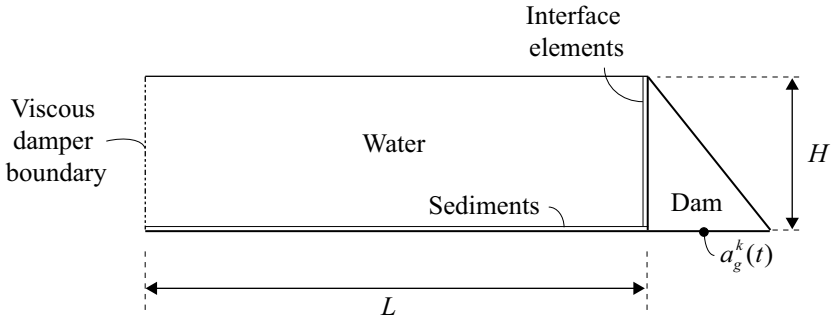

Figure 4.3 **Dimensions of FE model for dam–water system with viscous damper boundary to truncate the semi-unbounded fluid domain.**

4.5.1 Hydrodynamic Forces on Rigid Dam

To determine the influence of the length of the bounded fluid domain on the accuracy of the results, the hydrodynamic forces on a rigid dam are computed first. The frequency response functions for the hydrodynamic forces $|F_0^x(\omega)|$ and $|F_0^y(\omega)|$ on the upstream face of a rigid dam due to horizontal and vertical ground motion, respectively, are determined by computing the steady-state response of the system at many excitation frequencies. These forces are compared with analytical results for an unbounded fluid domain [Fenves and Chopra 1984c] in Figure 4.4, where the results are normalized with respect to the hydrostatic force $F_{st} = 1/2\rho g H^2$.

For horizontal excitation, the viscous-damper boundary is inadequate when using very small domain lengths ($L = H$), and results are unacceptable for all values of α. Increasing the length to $L = 4H$ significantly improves the accuracy, and results are generally acceptable; however, some scatter is still observable for $\alpha = 0.90$. This occurs for high values of α because radiation damping is then effectively the only source of energy dissipation in the system, and the response becomes sensitive for even small wave reflections at the viscous-damper boundary. This effect is much less prominent for low α-values because wave absorption at the reservoir bottom then contributes more to the overall energy dissipation.

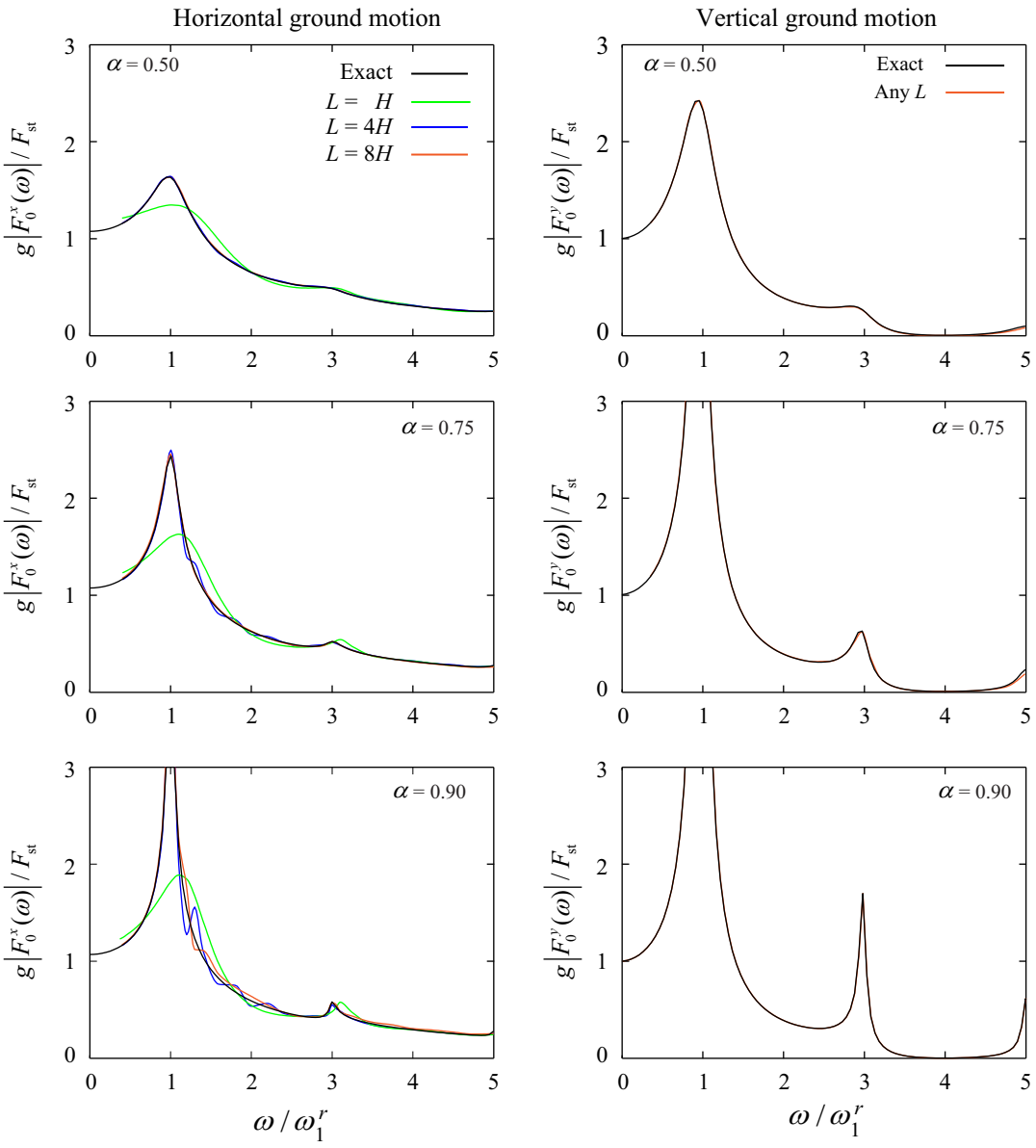

Figure 4.4 **Influence of length of bounded fluid domain on hydrodynamic forces on a rigid dam. Results are plotted against the normalized frequency ω / ω_1^r, where $\omega_1^r = \pi C / 2H$ is the fundamental vibration frequency of the fluid domain. "Exact" results are from Fenves and Chopra [1984c].**

For vertical excitation, the numerical results match the analytical solution for all lengths of the bounded domain, because the simple fluid geometry and uniform excitation at the reservoir bottom leads to a 1D pressure distribution in the fluid. Thus, when the effective earthquake forces $\mathbf{P}_r^0$—representing the contribution from earthquake-induced pressures in the part of the fluid that has been eliminated—are applied at Γ_r, these 1D conditions are exactly

reproduced in the model; however, for a flexible dam, this simple 1D behavior is no longer maintained, and larger domain lengths are required to obtain acceptable results.

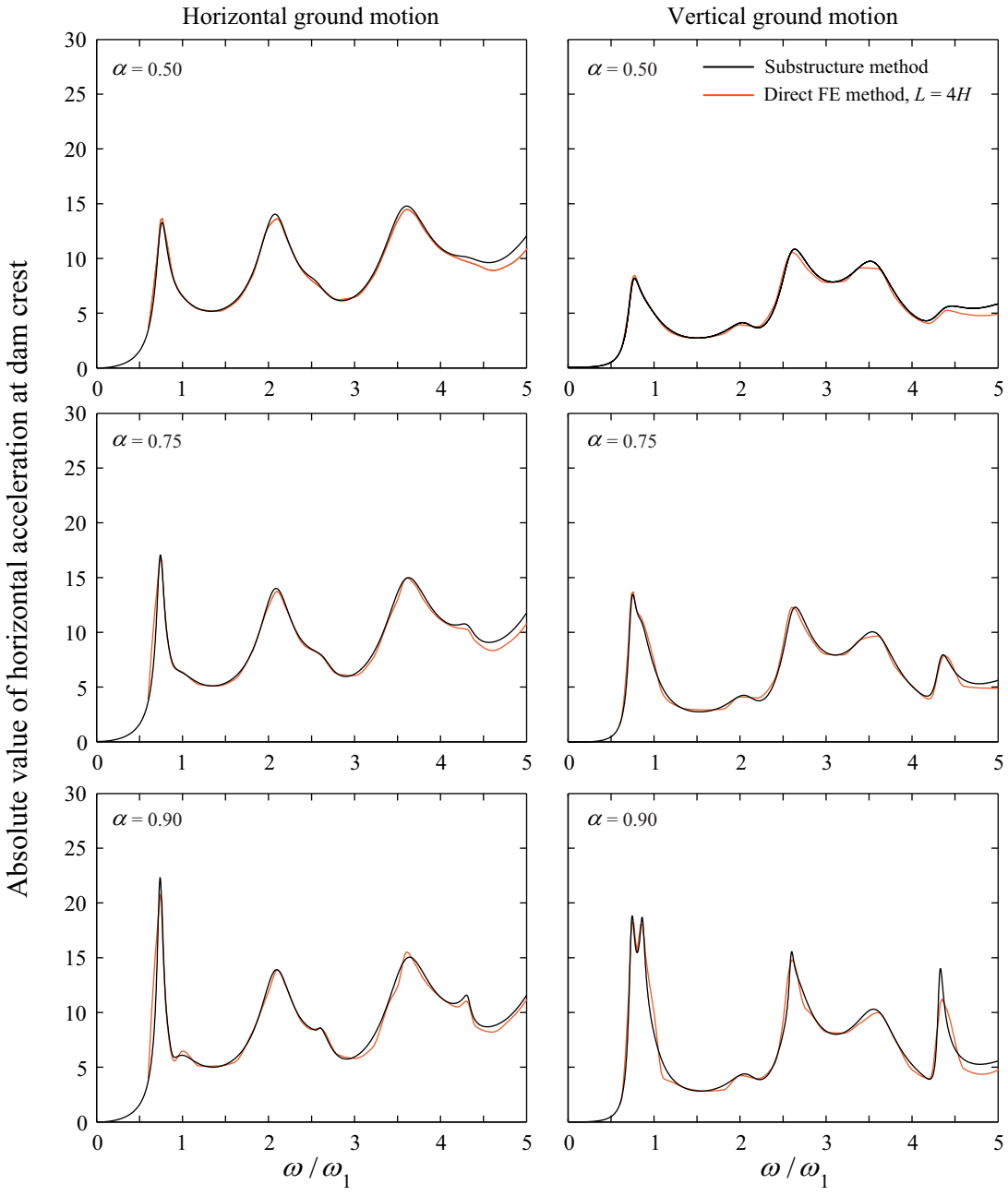

Figure 4.5 **Comparison of frequency response functions from direct FE and substructure methods for the amplitude of relative horizontal acceleration at the crest of dam on rigid foundation with full reservoir due to horizontal and vertical ground motion. ζ_s = 5%.**

4.5.2 Dam–Water System

Frequency response functions for the amplitude of the relative horizontal acceleration at the crest of the dam–water system (Figure 4.3) subjected to $a_g^x(t)$ and $a_g^y(t)$ defined by a harmonic function of unit amplitude are computed. These are compared in Figure 4.5 to results obtained directly in the frequency domain by the substructure method [Fenves and Chopra 1984a] that models the reservoir rigorously using semi-analytical solutions. Results are computed for different values of α and length $L = 4H$ for the truncated fluid domain.

The results computed by the direct FE method are generally close to the results from the substructure method for both vertical and horizontal ground motion, thus validating its ability to model the semi-unbounded dam–water system even with the moderately sized fluid domain of length $L = 4H$.

4.5.3 Ignoring Effective Earthquake Forces on Fluid Boundary Γ_r

Implementation of Equation (4.8) may be simplified by ignoring the effective earthquake forces $\mathbf{P}_r^0$ at Γ_r, which eliminates the need for auxiliary analysis of the 1D fluid column (Section 4.4) for vertical ground motion. This approximation implies that the vertical excitation extends only over the dam and truncated part of the fluid domain, thus neglecting the effect of hydrodynamic pressures caused by excitation of the fluid that has been eliminated upstream of Γ_r.

Presented in Figure 4.6 are frequency response functions for the amplitude of the relative horizontal acceleration at the dam crest due to vertical ground motion for $\alpha = 0.50$ and $\alpha = 0.75$, and different lengths of the bounded fluid domain. Results are computed by the direct FE method for two cases: including and excluding effective earthquake forces $\mathbf{P}_r^0$. Ignoring $\mathbf{P}_r^0$ leads to considerable differences in the response for higher α-values unless the bounded fluid domain is very long ($L = 8H$) because the excitation is now applied only to the base of the dam and truncated part of the fluid domain, and not to the complete semi-unbounded system. For analysis of an actual dam with a reasonable length for the fluid domain (e.g., $L = 4H$), this discrepancy should be of little concern because uniform ground motion obviously cannot extend to infinity in the upstream direction in a real system.

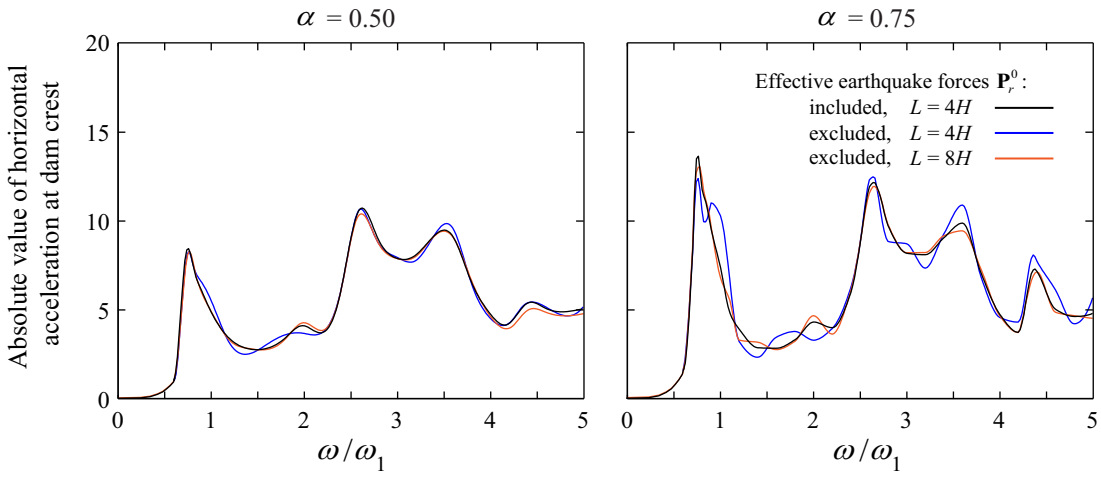

Figure 4.6 **Influence of ignoring effective earthquake forces $\mathbf{P}_r^0$ on the frequency response function for the amplitude of relative horizontal acceleration at the crest of flexible dam with full reservoir due to vertical ground motion. ζ_s = 5%.**

5 Dam–Water–Foundation Rock System

5.1 DAM–WATER–FOUNDATION ROCK INTERACTION AS A SCATTERING PROBLEM

Procedures for computing the earthquake response of a dam–foundation rock system (with empty reservoir) or dam–water system (supported on rigid rock) were developed in the previous chapters. Utilizing the same principle of viewing interaction as a scattering problem, wherein the dam perturbs a free-field state, these procedures are combined and extended to the entire dam–water–foundation rock interacting system.

The auxiliary system is now defined as shown in Figure 5.1(a) as the combination of the two free-field systems introduced in Figures 3.1(a) and 4.1(a). It consists of three subdomains: Ω^a denotes the foundation region interior of the future absorbing boundary Γ_f; Ω_f^+ is the semi-unbounded foundation region exterior to Γ_f; and Ω_f^+ is the prismatic fluid channel upstream of the future absorbing boundary Γ_r. This auxiliary system does not correspond to any physical state, but facilitates formulation of the analysis procedure. The displacements and hydrodynamic pressures in the auxiliary system are defined as $\mathbf{r}^a$ and $\mathbf{p}^a$, respectively.

The dam–water–foundation rock system is also separated into three subdomains [Figure 5.1(b)]: Ω denotes the dam and adjacent foundation and fluid regions interior of Γ_f and Γ_r, and Ω_f^+ and Ω_r^+ are the semi-unbounded foundation and fluid domains exterior to Γ_f and Γ_r; these are identical to the exterior regions of the auxiliary system. In order to subsequently formulate the governing equations for the absorbing boundaries in terms of free-field quantities—following Chapters 3 and 4—the displacements and hydrodynamic pressures are defined by the variables:

$$\mathbf{r}^t \text{ and } \mathbf{p}^t \text{ in the interior region } \Omega \tag{5.1a}$$

$$\mathbf{r}^t - \mathbf{r}^a \text{ and } \mathbf{p}^t - \mathbf{p}^a \text{ in the exterior regions } \Omega_f^+ \text{ and } \Omega_r^+ \tag{5.1b}$$

The variables chosen in Ω_f^+ and Ω_r^+ represent the scattered motion and scattered hydrodynamic pressures, i.e., the perturbation of the free-field motion (Chapter 2) and pressures (Chapter 3) due

to the presence of the dam and the bounded, irregular fluid region. This choice of variables in the exterior domains will subsequently allow reformulation of the governing equations for the absorbing boundaries in a way that the unknown forces $\mathbf{R}_f^t$ and $\mathbf{H}_r^t$ associated with Γ_f and Γ_r [Equation (2.8)] can be determined from $\mathbf{r}^a$ and $\mathbf{p}^a$.

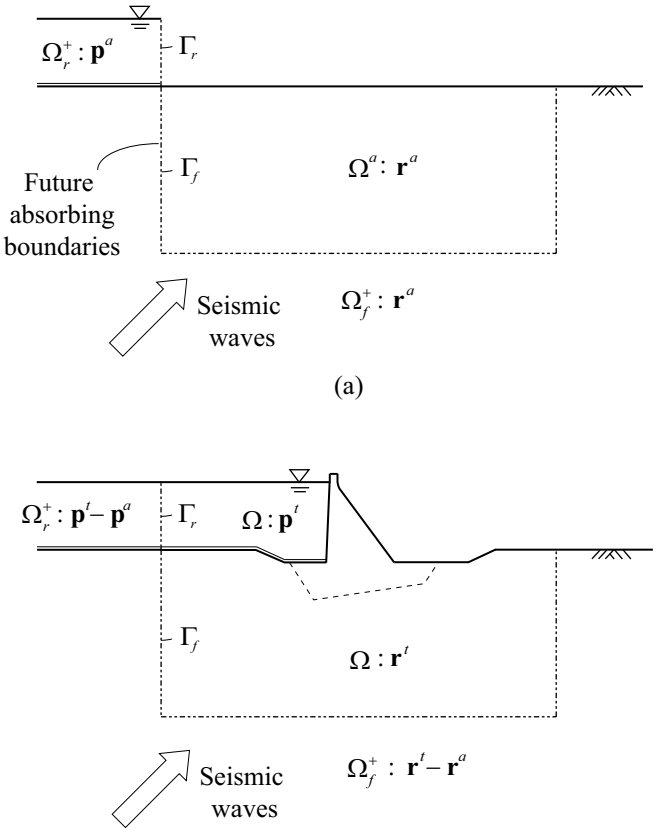

Figure 5.1 **Illustration of dam–water–foundation rock interaction as a scattering problem: (a) auxiliary water–foundation rock system in its "free-field" state with variables defined by $\mathbf{p}^a$ in Ω_r^+ and $\mathbf{r}^a$ in $\Omega^a \cup \Omega_f^+$; and (b) dam–water–foundation rock system with variables defined by $\mathbf{p}^t$ and $\mathbf{r}^t$ in Ω and the scattered variables $\mathbf{p}^t - \mathbf{p}^a$ in Ω_r^+ and $\mathbf{r}^t - \mathbf{r}^a$ in Ω_f^+.**

5.2 EQUATIONS OF MOTION

The equations of motion for the dam–water–foundation rock system contained within the domain Ω are given by Equation (2.8). The unknown forces $\mathbf{R}_f^t$ and $\mathbf{H}_r^t$ associated with the absorbing

boundaries Γ_f and Γ_r are given by Equations (3.5) and (4.5), respectively, with an obvious change of notation:

$$\mathbf{R}_f^t = \mathbf{R}_f^a - \mathbf{c}_f \left[\dot{\mathbf{r}}_f^t - \dot{\mathbf{r}}_f^a \right] \tag{5.2a}$$

$$\mathbf{H}_r^t = \mathbf{H}_r^a - \mathbf{c}_r \left[\dot{\mathbf{p}}_r^t - \dot{\mathbf{p}}_r^a \right] \tag{5.2b}$$

where variables with superscript a are for the auxiliary water–foundation rock system; $\mathbf{R}_f^a$ are the forces consistent with the boundary tractions at Γ_f; and $\mathbf{H}_r^a$ are the forces consistent with the hydrodynamic pressure gradient at Γ_r.

Included in Equation (2.8) are various interaction effects: dam–foundation rock interaction is included directly in the system matrices, dam–water and water–foundation rock interaction is represented by the coupling matrices $\mathbf{Q}_h$ and $\mathbf{Q}_b$, respectively, and reservoir bottom absorption is represented through the damping matrix $\mathbf{b}$. Water–foundation rock interaction is also considered in the exterior domain $\Omega_f^+ \cup \Omega_r^+$ through the variables entering Equation (5.2): (1) the displacements $\mathbf{r}_f^a$ and forces $\mathbf{R}_f^a$ at Γ_f include the effects of hydrodynamic pressures; and (2) the hydrodynamic pressures $\mathbf{p}_r^a$ and forces $\mathbf{H}_r^a$ at Γ_r include the effects of foundation-rock flexibility.

5.2.1 Approximating Water–Foundation Rock Interaction

These quantities are to be determined by analysis of the auxiliary water–foundation rock system [Figure 5.1(a)]. This complicated analysis can be avoided by ignoring the effects of water–foundation rock interaction in $\Omega_f^+ \cup \Omega_r^+$:

$$\mathbf{r}_f^a \approx \mathbf{r}_f^0 \text{ and } \mathbf{R}_f^a \approx \mathbf{R}_f^0 \text{ in the foundation domain } \Omega^a \cup \Omega_f^+ \tag{5.3a}$$

$$\mathbf{p}_r^a \approx \mathbf{p}_r^0 \text{ and } \mathbf{H}_r^a \approx \mathbf{H}_r^0 \equiv \mathbf{0}^{\dagger} \text{ in the fluid domain } \Omega_r^+ \tag{5.3b}$$

where the free-field motion $\mathbf{r}_f^0$ and forces $\mathbf{R}_f^0$ at the boundary Γ_f are computed from analysis of the free-field foundation-rock system [Figure 3.1(a)], thus ignoring the effects of hydrodynamic pressures in Ω_r^+ on the foundation-rock motions; and the free-field hydrodynamic pressures $\mathbf{p}_r^0$ are computed from analysis of the fluid in its "free-field" state [Figure 4.1(a)] with rigid

† Recall from Section 4.3 that the forces $\mathbf{H}_r^0$ associated with the free-field pressure gradient $\partial p^0 / \partial n$ at Γ_r are zero for both horizontal and vertical ground motion.

foundation rock, thus ignoring the effects of foundation-rock flexibility on the hydrodynamic pressures in Ω_r^+.

Numerical results have demonstrated that the response of gravity dams to horizontal ground motion is essentially unaffected by the above approximation of water–foundation rock interaction, and that the response to vertical ground motion is only noticeably affected for large values of the wave-reflection coefficient α, where the approximate results tends to overestimate the response [Basu 2004]. These conclusions were based on analyses using very small domain sizes; the errors will be much smaller when using larger domain sizes that are required by the viscous-damper boundaries; see Figure 2.2.

Although the secondary effects of water–foundation rock interaction in $\Omega_f^+ \cup \Omega_r^+$ are ignored, the dominant effects within the truncated FE domain Ω are still rigorously represented by the coupling matrix $\mathbf{Q}_b$. Alternatively, water–foundation rock interaction can be neglected altogether by setting $\mathbf{Q}_b \equiv \mathbf{0}$; however, because this approximation can lead to significant error, it is not introduced here; see Appendix F.

5.2.2 Dam–Water–Foundation Rock System

With the preceding approximations in modeling water–foundation rock interaction, the forces $\mathbf{R}_f^t$ and $\mathbf{H}_r^t$ can be determined independently of each other by considering the free-field systems of Figure 3.1(a) and Figure 4.1(a), respectively. Substituting Equations (3.5) and (4.5) into Equation (2.8), the final equations of motion for the dam–water–foundation rock system are obtained:

$$\begin{bmatrix} \mathbf{m} & \mathbf{0} \\ \rho(\mathbf{Q}_h^{\mathrm{T}} + \mathbf{Q}_b^{\mathrm{T}}) & \mathbf{s} \end{bmatrix} \begin{Bmatrix} \ddot{\mathbf{r}}^t \\ \ddot{\mathbf{p}}^t \end{Bmatrix} + \begin{bmatrix} \mathbf{c} + \mathbf{c}_f & \mathbf{0} \\ \mathbf{0} & \mathbf{b} + \mathbf{c}_r \end{bmatrix} \begin{Bmatrix} \dot{\mathbf{r}}^t \\ \dot{\mathbf{p}}^t \end{Bmatrix} + \begin{Bmatrix} \mathbf{f}(\mathbf{r}^t) \\ \mathbf{0} \end{Bmatrix} + \begin{bmatrix} \mathbf{0} & -(\mathbf{Q}_h + \mathbf{Q}_b) \\ \mathbf{0} & \mathbf{h} \end{bmatrix} \begin{Bmatrix} \mathbf{r}^t \\ \mathbf{p}^t \end{Bmatrix} = \begin{Bmatrix} \mathbf{R}^{\mathrm{st}} \\ \mathbf{0} \end{Bmatrix} + \begin{Bmatrix} \mathbf{P}_f^0 \\ \mathbf{P}_r^0 \end{Bmatrix} \tag{5.4}$$

The earthquake excitation is specified in Equation (5.4) by the effective earthquake forces $\mathbf{P}_f^0$ at Γ_f defined by Equations (3.11) and (3.7) for the bottom and side boundaries of the foundation domain, respectively; and the effective earthquake forces $\mathbf{P}_r^0$ at Γ_r defined by Equation (4.9). These forces are easily obtained using the procedures developed in Sections 3.5 and 4.4.

5.3 SUMMARY OF PROCEDURE

Analysis of the dam–water–foundation rock system subjected to the free-field ground acceleration $a_g^k(t)$, $k = x, y$, defined at a control point at the surface of the foundation rock (Figure 2.1), is organized in three parts: static analysis, linear analyses of the free-field foundation-rock and fluid systems, and nonlinear dynamic analysis of the dam–water–foundation rock system.

Static analysis:

1. Develop a FE model for static analysis of the dam–foundation rock system with a suitable material model for the dam concrete and a suitable (static) model for the foundation rock.
2. Determine the static response of this system to gravity loads on the dam and hydrostatic forces on the dam and foundation rock.
3. Record the static state of the dam–foundation rock system, including reactions from the foundation rock at the boundary Γ_f.

Linear analysis of free-field foundation-rock system [Figure 5.2(a)]:

4. Obtain the free-field motion at the base of the foundation model by deconvolution of the surface ground motion $a_g^k(t)$.
5. Calculate the effective earthquake forces $\mathbf{P}_f^0$ at the bottom boundary from Equation (3.11), with the motion $\mathbf{r}_I^0$ due to the incident (upward propagating) seismic wave taken as one-half the outcrop motion extracted from the deconvolution analysis.
6. Develop a FE model for the free-field foundation-rock system: a single column of elements that has the same mesh density as the main FE model adjacent to the side boundaries, with viscous dampers applied at the base in the *x*- and *y*-directions.
7. Compute $\dot{\mathbf{r}}_f^0$ and $\mathbf{R}_f^0$ at each node along the height by analyzing the foundation-rock column subjected to forces given by Equation (3.11) at its base.
8. Calculate the effective earthquake forces $\mathbf{P}_f^0$ at the side boundaries of the foundation domain from Equation (3.7) using $\dot{\mathbf{r}}_f^0$ and $\mathbf{R}_f^0$ from Step 7.

Steps 6–8 may be avoided if free-field boundary elements are applied along the side boundaries; see Figure 3.3(b).

Linear analysis of free-field fluid system [Figure 5.2(b)]:

9. Develop a FE model for the free-field fluid: a single column of elements of unit width with the same mesh density as the fluid adjacent to the boundary Γ_r, add a single line element to model reservoir bottom sediments.

10. Calculate $\dot{\mathbf{p}}_r^0$ at every node along the height by analyzing the fluid column subjected to forces ρa_g^y at its base for vertical ground motion; $\dot{\mathbf{p}}_r^0 = \mathbf{0}$ for horizontal motion.

11. Compute the effective earthquake forces $\mathbf{P}_r^0$ at the fluid boundary Γ_r from Equation (4.9) using $\dot{\mathbf{p}}_r^0$ from Step 10.

Nonlinear dynamic analysis of dam–water–foundation rock system [Figure 5.2(c)]:

12. Develop a FE model of the dam–water–foundation rock system with viscous-damper boundaries to truncate the semi-unbounded foundation and fluid domains at Γ_f and Γ_r, respectively. Use standard solid and fluid elements for the dam, foundation rock, and fluid, and apply interface elements (or tie constraints) at the upstream dam face and at the water–foundation rock interface. Reservoir bottom sediments can be approximately modeled using line elements based on the 1D absorption model, or by using one of several more sophisticated methods; see Section 2.3.2.

13. Calculate the response of the FE model of the dam–water–foundation rock system subjected to effective earthquake forces $\mathbf{P}_f^0$ at the boundary Γ_f calculated in Steps 5 and 8, $\mathbf{P}_r^0$ at the boundary Γ_r calculated in Step 11, plus static loads and foundation reactions at Γ_f. The static state of the dam (Step 3) is taken as the initial state in the nonlinear dynamic analysis.

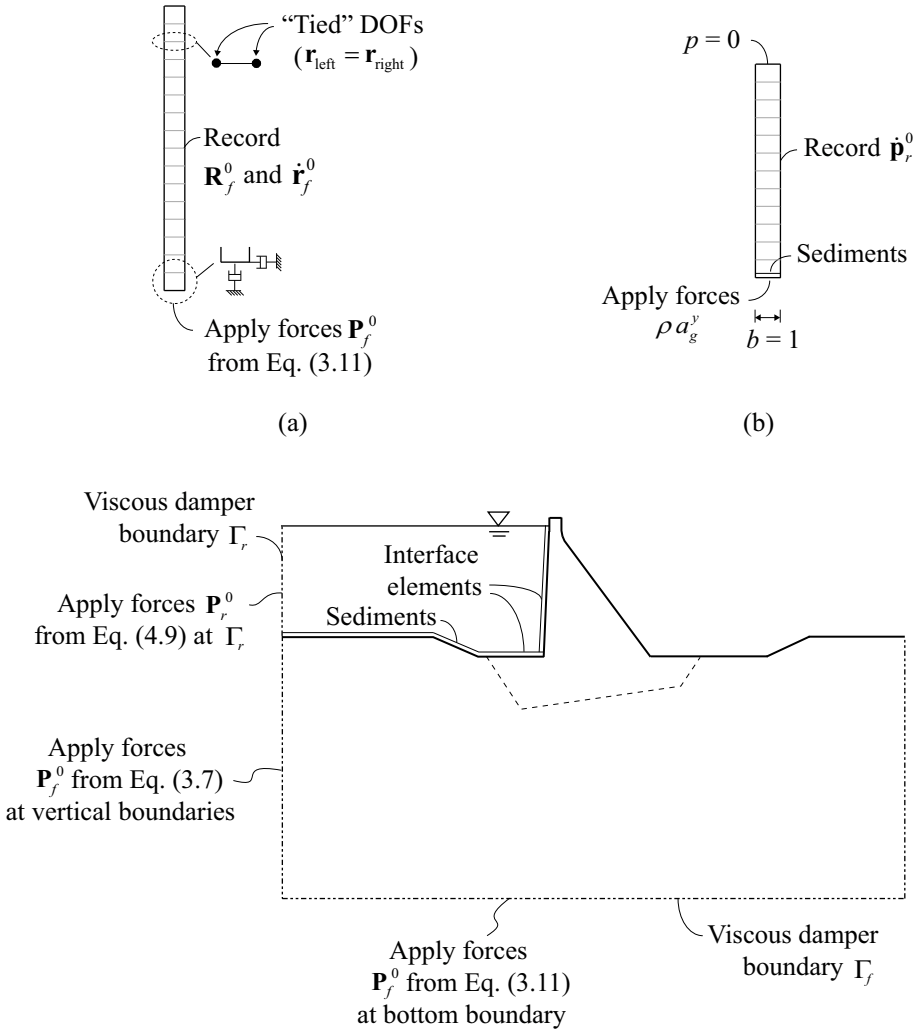

Figure 5.2 **Summary of analysis procedure for dam–water–foundation rock system: (a) auxiliary analysis of single column of foundation-rock elements to compute $\dot{\mathbf{r}}_f^0$ and $\mathbf{R}_f^0$; (b) analysis of 1D column of fluid elements to calculate $\dot{\mathbf{p}}_r^0$ for vertical ground motion; and (c) application of effective earthquake forces to truncated FE model.**

5.4 NUMERICAL VALIDATION

The direct FE method developed in the preceding sections is validated by computing the dynamic response of the dam–water–foundation rock system shown in Figure 5.3 to horizontal and vertical ground motion. The idealized dam–water–foundation rock system has the same geometry, FE mesh, and material parameters as the systems used in Sections 3.6 and 4.5, but is

combined to form the complete dam–water–foundation rock system. Material damping in the dam and foundation rock is modeled by Rayleigh damping with $\zeta_s = 2\%$ and $\zeta_f = 2\%$ viscous damping specified for the dam and foundation rock separately, implemented using the procedure described in Section 3.6.

The ground motion is specified by the ground acceleration $a_g^k(t)$ at the foundation surface. The free-field motion at depth in the model is obtained by deconvolution of this motion; then effective earthquake forces at the bottom and side boundaries of the foundation rock are then computed from Equations (3.11) and (3.7), respectively. For vertical ground motion, the effective earthquake forces at the fluid boundary Γ_r are computed from Equation (4.9).

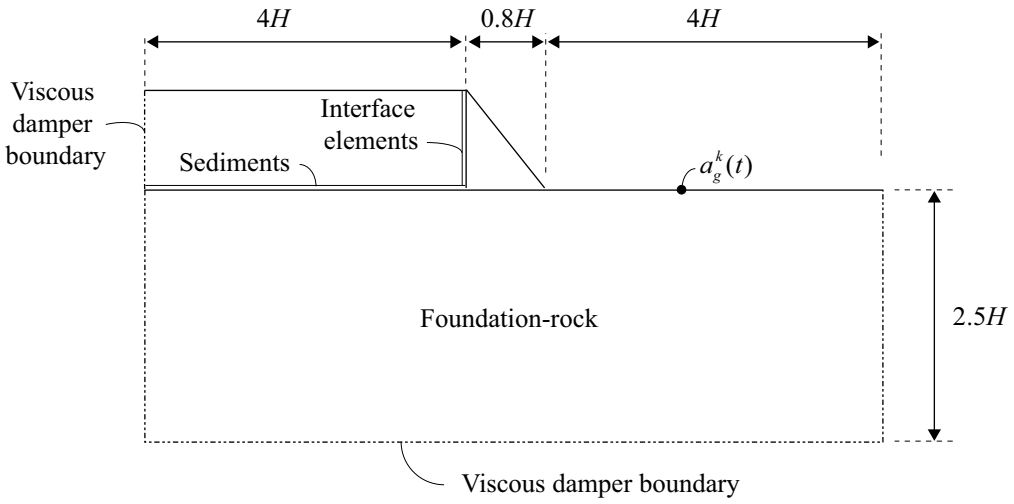

Figure 5.3 **Dimensions of FE model for idealized dam–water–foundation rock system with viscous-damper boundaries to truncate semi-unbounded foundation and fluid domains.**

5.4.1 Frequency Response Functions for Dam Response

Frequency response functions for the amplitude of the relative horizontal acceleration at the crest of the dam are computed and shown in Figure 5.4 for three values of α. The results are compared to results obtained by the substructure method [Fenves and Chopra 1984a] where the foundation rock is modeled as a viscoelastic half-space, hydrodynamic pressures are modeled by analytical solutions, and the earthquake excitation is specified directly at the dam–foundation interface. Because the computer program EAGD84 used to compute the substructure results

ignores water–foundation rock interaction, this interaction is also ignored in the direct FE method for these validation analyses.

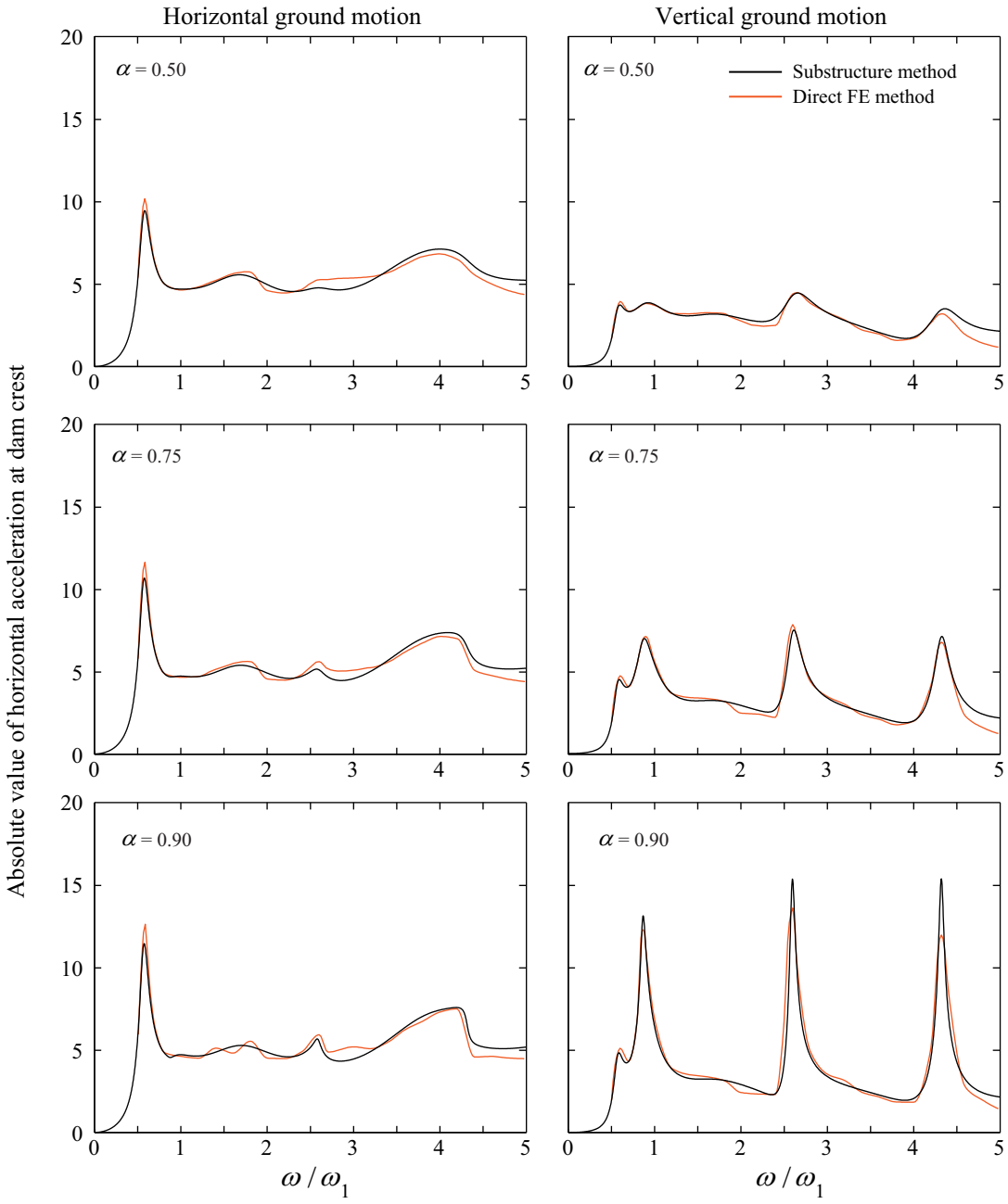

Figure 5.4 **Comparison of frequency response functions from direct and substructure methods for the amplitude of relative horizontal acceleration at the crest of dam on flexible foundation rock with full reservoir due to horizontal and vertical ground motion.** $\zeta_s = \zeta_f = 2\%$; E_f / E_s **= 1.0.**

The results computed by the direct FE method are very close to the results from the substructure analysis for both vertical and horizontal ground motion, thus validating its ability to model the semi-unbounded dam–water–foundation rock system. The slight differences at some frequencies are attributable to the approximate nature of the viscous-damper boundary, which is unable to perfectly absorb all outgoing waves. As previously mentioned, these discrepancies will generally decrease as the sizes of the foundation and fluid domains included in the FE model increases.

5.4.2 Response to Transient Motion

To demonstrate the ability of the direct FE method to accurately compute the response of the dam–water–foundation rock system to earthquake excitation, the system is analyzed for $a_g^x(t)$ and $a_g^y(t)$ specified as the S69E and vertical components, respectively, of the motion recorded at Taft Lincoln School Tunnel during the 1952 Kern County earthquake. The response was also computed by the substructure method. The relative horizontal displacements and accelerations at the dam crest are presented in Figure 5.5, and the envelope values of the maximum principal stresses in Figure 5.6. Note: the results from the direct FE method closely match the substructure method results, as expected to by the close agreement observed earlier for the frequency response functions.

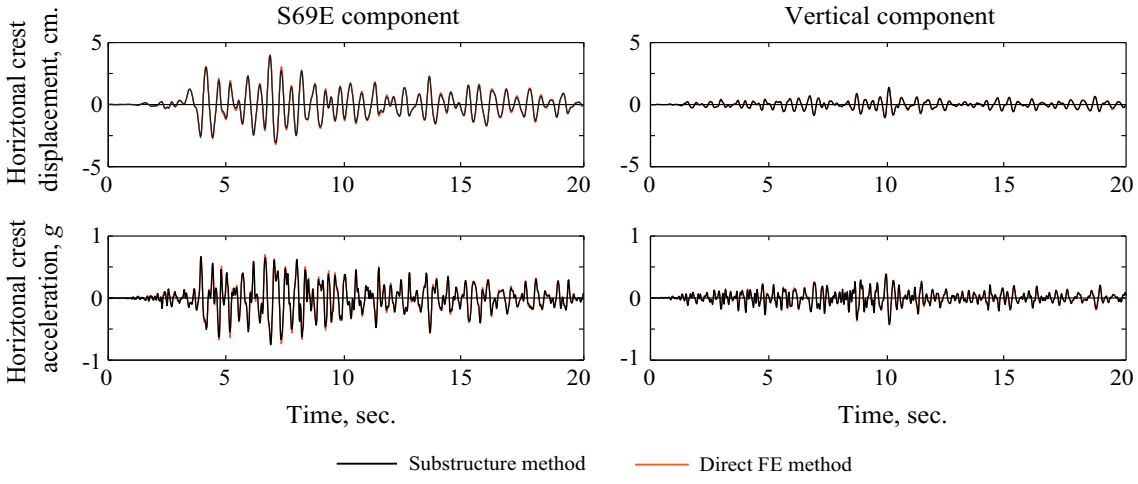

Figure 5.5 **Horizontal displacements and accelerations at the crest of the dam on flexible foundation rock with full reservoir due to the S69E and vertical components, separately, of Taft ground motion.** $\zeta_s = \zeta_f$ **= 2%;** E_f / E_s **= 1.0;** α **= 0.75.**

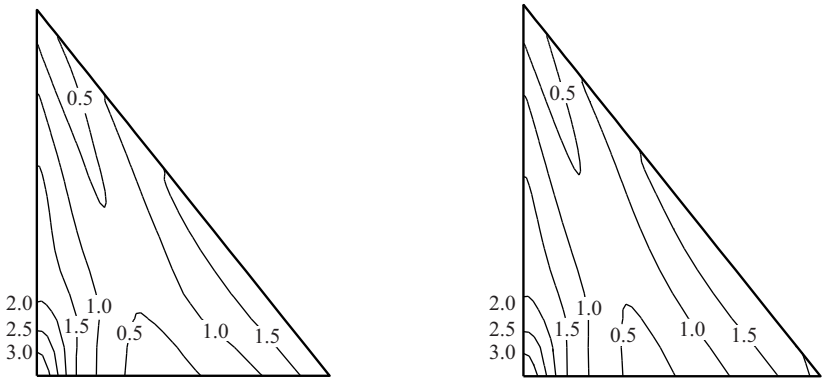

Substructure method Direct FE method

Figure 5.6 **Envelope values of maximum principal stresses (in MPa) in dam on flexible foundation rock with full reservoir due to S69E component of Taft ground motion; initial static stresses are excluded.** $\zeta_s = \zeta_f$ **= 2%;** E_f / E_s **= 1.0;** α **= 0.75.**

6 Conclusions

A direct FE method for earthquake analysis of concrete dams interacting with fluid and foundation rock, which may comprise semi-unbounded domains, has been developed. The analysis procedure uses viscous-damper boundaries to truncate these semi-unbounded domains and specifies the seismic input as effective earthquake forces directly at the model truncations. The analysis procedure is formulated by treating dam–water–foundation rock interaction as a scattering problem [Basu 2004] where the dam perturbs an assumed "free-field" state of the system. The FE model of the fluid includes water compressibility and reservoir bottom absorption, and the FE model of the foundation rock includes mass, stiffness, and material damping appropriate for rock. Thus, the unrealistic assumptions of massless rock and incompressible water, sometimes used in engineering practice, are eliminated.

The seismic input to the procedure is defined by a ground motion specified at a control point on the foundation surface. The free-field motion at the bottom of the foundation rock is determined by deconvolution of this motion. Effective earthquake forces at the boundaries of the foundation and fluid domains are then computed from analysis of two individual 1D free-field systems. Implementation of these analyses is straightforward, and does not require modification of the source code of a commercial FE program.

The analysis procedure is validated numerically by computing the dynamic response of an idealized dam–water–foundation rock system and comparing against results obtained using the substructure method [Fenves and Chopra 1984a]. The excellent agreement demonstrates that: (1) the truncated foundation and fluid models with viscous-damper boundaries are able to model the semi-unbounded domains; and (2) the earthquake excitation is properly defined by the effective earthquake forces determined from the free-field variables.

Because the direct FE method is applicable to nonlinear systems, it allows for modeling of concrete cracking, as well as sliding and separation at construction joints, lift joints, and at

concrete–rock interfaces. Implementation of the procedure is facilitated by commercial FE software, with their nonlinear material models, that permit modeling of viscous-damper boundaries and specification of effective earthquake forces at these boundaries.

PART II

Direct Finite-Element Method for Nonlinear Earthquake Analysis of Three-Dimensional Dam–Water–Foundation Rock System

1 Introduction

Earthquake analysis of arch dams requires three-dimensional (3D) dam–water–foundation rock systems that recognize all factors known to significantly influence their earthquake response [Chopra 2012a]: dam–water interaction including water compressibility and wave absorption at the reservoir bottom [Hall and Chopra 1982; Fok and Chopra 1986]; dam–foundation rock interaction including inertia effects of the rock [Tan and Chopra 1996]; radiation damping due to the semi-unbounded sizes of the reservoir and foundation domains [Tan and Chopra 1996; Zhang et al. 2009]; spatial variation of ground motion at the dam–canyon interface [Alves and Hall 2006; Chopra and Wang 2009]; and nonlinear behavior of the dam and foundation rock [El-Aidi and Hall 1989; Bhattacharjee and Léger 1993; and Zhang et al. 2009].

Most dam engineers prefer to work with the direct method of analysis—implemented in commercial finite-element (FE) software with their user-friendly interfaces—that models the entire system using FEs and analyzes it directly in the time-domain. While these programs are able to model nonlinear mechanisms, they often neglect or use simplistic models for dam–water–foundation rock interaction and the semi-unbounded domains. Furthermore, spatial variation of earthquake motions at the dam–canyon interface is typically ignored in dam engineering practice, even though there is substantial evidence that such variations can significantly influence the response of arch dams [Maeso et al. 2002; Proulx et al. 2004; Alves and Hall 2006; and Chopra and Wang 2009].

Accurate modeling of dam–water–foundation rock systems requires a FE model that includes mass, stiffness, and material damping properties of the foundation rock, the compressibility of water, and the effects of energy dissipation at the reservoir bottom. The semi-unbounded foundation and fluid domains must be reduced to bounded sizes using absorbing boundaries [Wolf 1988; Kellezi 2000], and the seismic input specified by effective earthquake forces applied either directly to these boundaries [Wolf 1988; Zienkiewicz et al. 1989], or via a

single layer of elements interior of the boundaries [Bielak and Christiano 1984; Bielak et al. 2003].

Utilizing the former of these approaches, a direct FE method for nonlinear earthquake analysis of two-dimensional (2D) dam–water–foundation rock systems was developed in Part I of this report. Standard viscous-damper boundaries [Lysmer and Kuhlemeyer 1969] were selected to model the semi-unbounded domains and the seismic input was specified as tractions directly at these boundaries. These are standard features in FE analyses, thus ensuring that this direct FE method can be implemented with any commercial FE software without modification of the source code.

The objective of the work presented here is to generalize the direct FE method to 3D dam–water–foundation rock systems. After defining the components of the 3D dam–water–foundation rock system in Chapter 2, the analysis procedure is developed in Chapter 3, and step-by-step procedures for computing effective earthquake forces at the foundation and fluid boundaries are outlined in Chapter 4. Several examples are presented in Chapter 5 to validate the accuracy of the direct FE method. First, the method is used to compute the free-field motion at the surface of a flat foundation box and at a semi-cylindrical canyon and compared to classical solutions. The dynamic response of an arch dam system is computed next and compared against results from the substructure method. To facilitate implementation of the direct FE method for 3D systems, several simplifications of the procedure are proposed in Chapter 6, and their efficacy is evaluated. Finally, in Chapter 7, the analysis procedure is summarized in step-by-step form.

2 System and Ground Motion

2.1 SEMI-UNBOUNDED DAM–WATER–FOUNDATION ROCK SYSTEM

The idealized, 3D dam–water–foundation rock system considered consists of three subsystems (Figure 2.1): (1) the concrete dam with nonlinear properties; (2) the foundation rock, consisting of a bounded region adjacent to the dam that may be nonlinear, inhomogeneous, and irregular in geometry; and the exterior, semi-unbounded, region with "regular" geometry that has linear constitutive properties and is homogeneous or horizontally layered; and (3) the fluid domain, consisting of a bounded region of arbitrary geometry adjacent to the dam that may be nonlinear; and a uniform channel, unbounded in the upstream direction, that is restricted to be linear.

"Regular" geometry of the semi-unbounded foundation region is defined as the canyon upstream of the bounded region has a uniform cross section, and, similarly, the canyon downstream of the bounded region has a uniform cross section; that said, the two cross sections may be different. The assumption of homogeneous or horizontally layered properties in the exterior foundation region is introduced to permit use of a 1D deconvolution method—based on the assumption of vertically propagating waves—to define the seismic input for the system starting from ground motion specified at the surface of the foundation rock; see Section 2.2.

The semi-unbounded system in Figure 2.1 is modeled by a 3D FE discretization of a bounded system with viscous-damper boundaries at the bottom and side boundaries of the foundation domain to model its semi-unbounded geometry, and at the upstream end of the fluid domain to model its essentially "unbounded length; see Figure 2.2. Many absorbing boundaries have been proposed in the literature, e.g., Lysmer and Kuhlemeyer [1969]; Smith [1974]; White and Lee [1977]; Clayton and Engquist [1977]; Engquist and Majda [1977]; Underwood and Geers [1981]; Kausel and Tassoulas [1981]; Liao and Wong [1984]; Higdon [1986; 1987]; Wolf [1988], Wolf and Song [1995; 1996], Kellezi [2000], Basu and Chopra [2003; 2004]; and Basu [2009]. The well-known viscous damper model of Lysmer and Kuhlemeyer [1969] has been

chosen herein because of its availability in every commercial FE code, acceptable accuracy, and ease of implementation.

The linear, regular parts of the foundation and fluid domains included in the FE model provide a transition from the irregular geometry and nonlinear behavior adjacent to the dam to the regular geometry and linear behavior required at the absorbing boundaries. The minimum sizes for these domains are determined by the ability of the viscous-damper boundaries to absorb outgoing scattered waves from the system. Because the viscous damper is a "simple" absorbing boundary, larger domain sizes are required than if an "advanced" boundary such as PML was used; however, as will be seen in Section 6, the use of larger domains has the advantage that it enables introduction of two simplifications that significantly reduce the complexity of implementing the analysis method.

The use of FEs for the entire system permits modeling of arbitrary geometry and inhomogeneous material properties of the dam, canyon, foundation, and fluid domains adjacent to the dam. Furthermore, it allows for modeling of nonlinear mechanisms (Figure 2.3) such as cracking of the dam concrete [Lee and Fenves 1982; Vargas-Loli and Fenves 1989; Bhattacharjee and Léger 1993; and Zhang et al. 2009], sliding and separation at construction joints, lift joints, and at concrete-rock interfaces [Niwa and Clough 1982; Léger and Katsouli 1989; Fenves et al. 1992; Lau et al. 1998]; and Zhang et al. 2009], discontinuities in the rock due to local cracks and fissures [Lemos 1999; Lemos 2008], and cavitation in the fluid [Zienkiewicz et al. 1983].

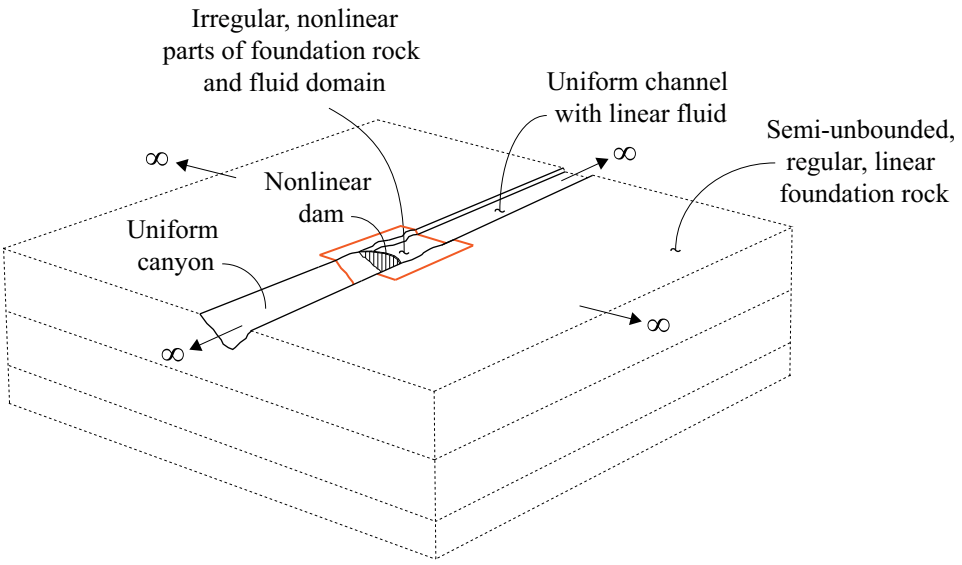

Figure 2.1 **Semi-unbounded dam–water–foundation rock system showing main parts: (1) the nonlinear dam; (2) the foundation rock, consisting of an irregular, nonlinear region and a semi-unbounded region that is linear and has regular geometry and homogeneous properties; and (3) the fluid domain, consisting of an irregular nonlinear region, and a semi-unbounded uniform channel with linear fluid.**

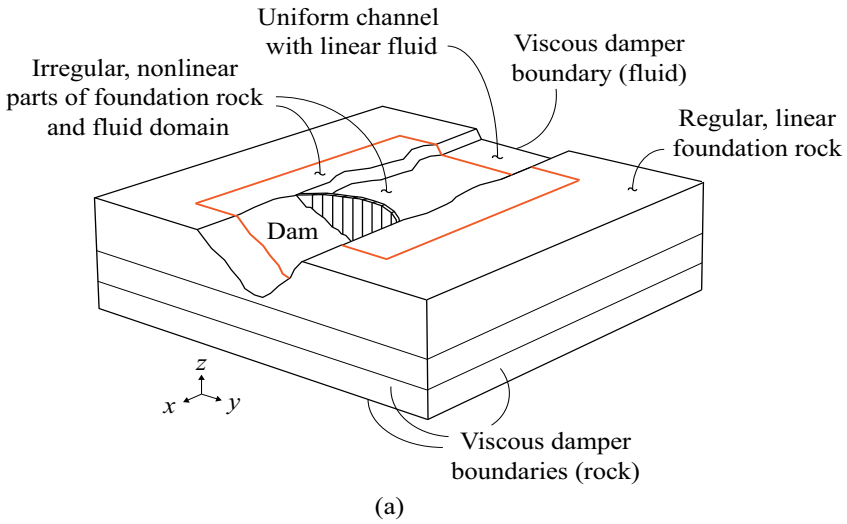

(a)

Figure 2.2 **Dam–water–foundation rock system with truncated foundation and fluid domains; (a) 3D perspective view.**

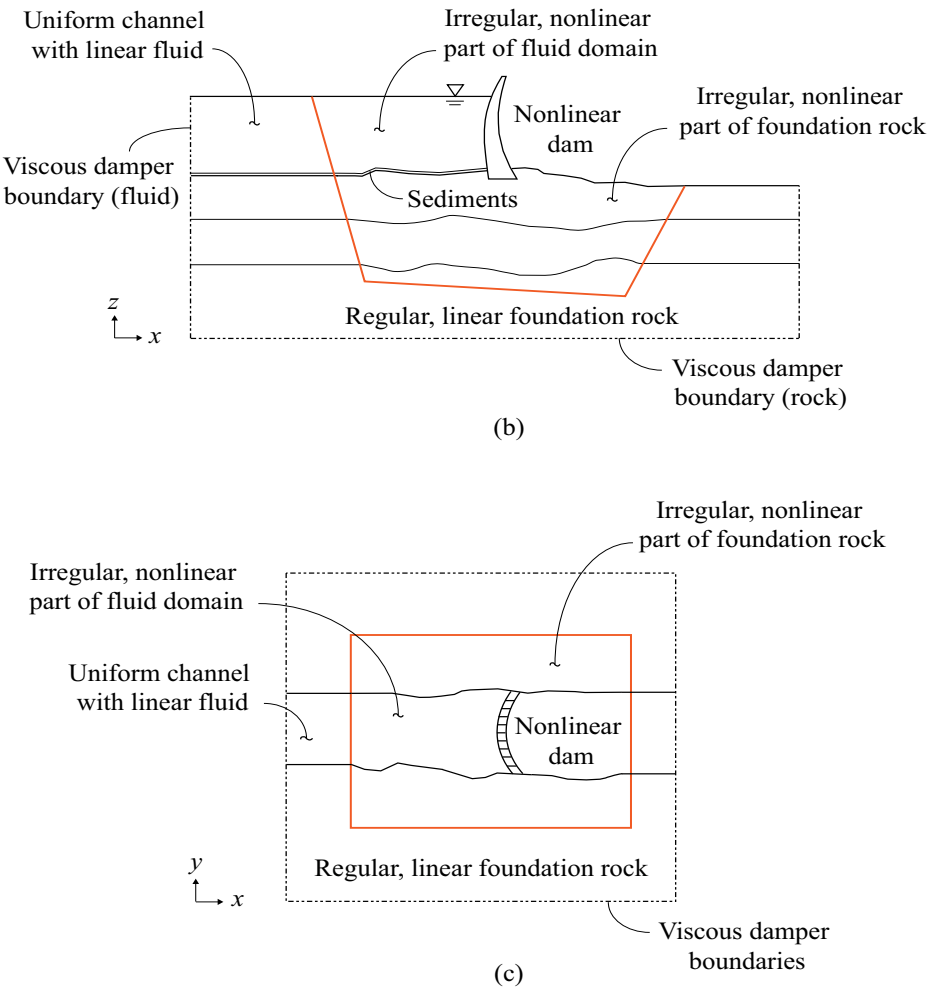

Figure 2.3 **Dam–water–foundation rock system with truncated foundation and fluid domains: (b) section view through center of canyon; and (c) plan view.**

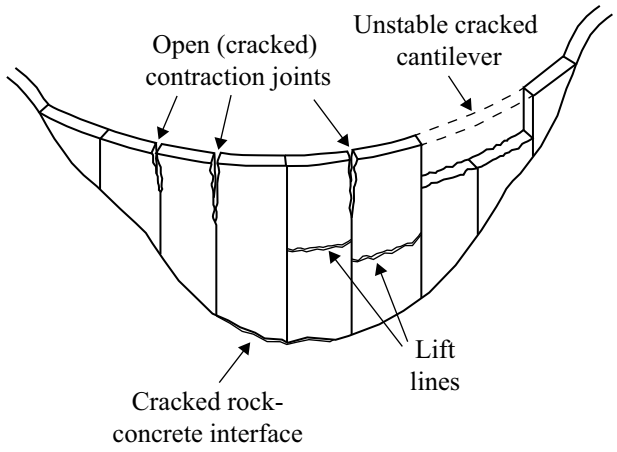

Figure 2.3 **Nonlinear mechanisms for concrete arch dams. Figure adapted from Priscu et al. [1985].**

2.2 EARTHQUAKE EXCITATION

Equations governing the motion of the system shown in Figure 2.2 subjected to earthquake excitation defined by the free-field ground motion—the motion that would occur in the foundation rock without the dam and water present—will be formulated in Chapter 3. These equations require that the spatially varying free-field motions at all future boundaries of the FE model are known. Specifying such motions remains a challenging problem.

The most general approach is to perform large-scale simulation of seismic wave propagation from an earthquake source to the dam site [Bao et al. 1998; Graves 1996; and Moczo et al. 2007], shown schematically in Figure 2.4(a). Here, physics-based FE or finite difference models of large regions subjected to a fault slip are analyzed. Although such regional simulations have been reported in the research literature, they seem impractical for concrete-dam analysis for two reasons: (1) information regarding the details of the earthquake fault rupture and the properties of the geological materials is lacking; and (2) simulation models are currently limited to lower frequencies compared to the vibration properties of concrete dams.

Another approach would be to use boundary element methods (BEM) to compute the free-field motions resulting from incident plane waves propagating from infinity to the dam site at predefined angles, shown schematically in Figure 2.4(b). Such methods have been used to compute the free-field motions at the surface of canyons [Maeso et al. 1982; Zhang and Chopra

1991], and to investigate the influence of assumed incident angles on the dam response [Garcia et al. 2016]; however, due to the obvious difficulty in selecting a combination of wave types and their incidence angles for an actual situation, these methods are rarely applied to solve practical problems.

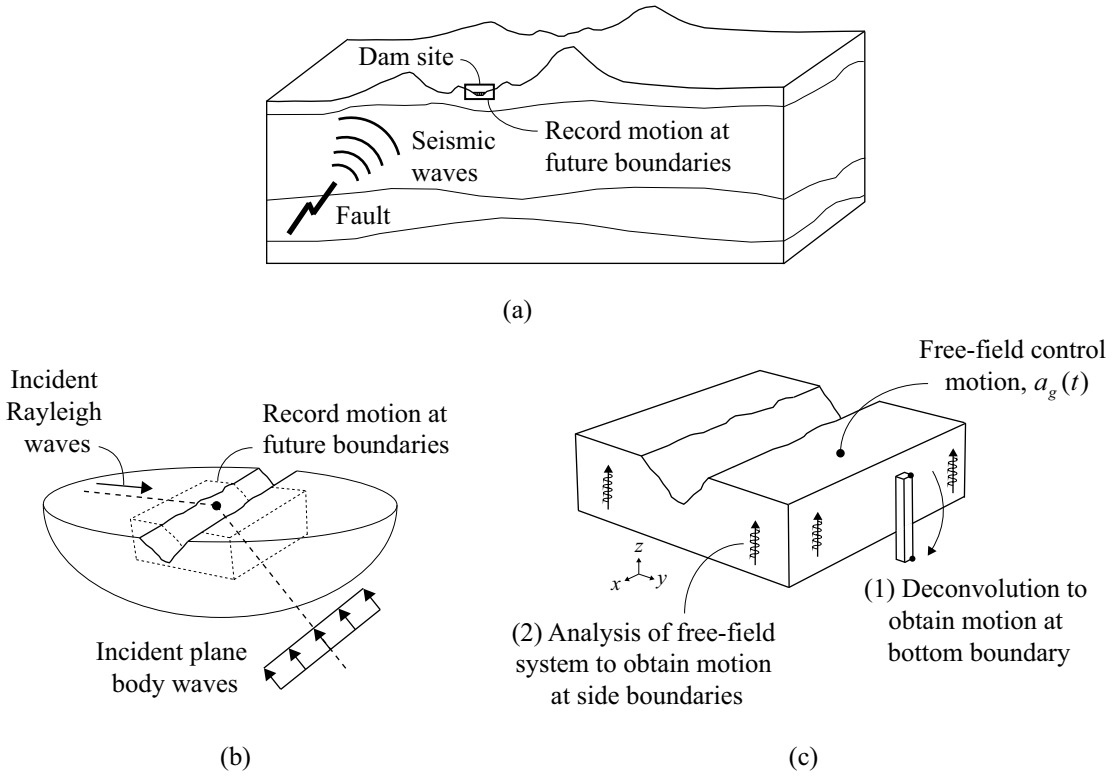

Figure 2.4 **Illustration of methods to obtain free-field earthquake motion: (a) large scale fault-rupture simulation; (b) boundary element method with incident plane waves propagating from infinity at predefined angles; and (c) deconvolution analysis starting with a free-field surface control motion $a_g^k(t)$.**

Presently, the standard approach is to define the earthquake excitation by three components of free-field acceleration specified at a control point on the foundation surface [Figure 2.4(c)]: the stream component, $a_g^x(t)$, the cross-stream component $a_g^y(t)$, and the vertical component $a_g^z(t)$. Because the ground motion cannot be defined uniquely, an ensemble of motions is required. These motions should, in some sense, be consistent with a target design spectrum that represents the seismic hazard at the site, e.g., the uniform hazard spectrum (UHS) or some variation of the conditional mean spectrum (CMS). Several methods have been

developed to select and scale ground motion records to "match" a target spectrum [Kwong et al. 2015; Haselton 2009; and Katsanos et al. 2010]. The UHS (and CMS) applies to an outcrop location on level ground; this control point is chosen at the elevation of the dam abutments in the linear, regular part of the foundation rock; see Figure 2.4(c). It could also be at other locations; for example, if the purpose is to perform analysis using earthquake input motions recorded at specific locations near the dam.

The free-field motion at the bottom and side boundaries of the foundation domain can be determined from the surface control motion $a_g^k(t)$ using a deconvolution-type analysis; see Figure 2.4(c). For this analysis, it will be assumed that the incident wave field consists solely of plane *SH*-, *SV*- and *P*-waves propagating vertically upwards from the underlying semi-unbounded foundation rock. Although clearly a major simplification, at the present time it seems to be a reasonably pragmatic choice.

When specifying the earthquake excitation this way, spatial variation of the ground motion—both amplitude and phase—is automatically considered in the analysis, albeit predominantly in the vertical direction. To demonstrate this, such free-field motions are computed by the direct FE method to be developed in Chapters 3 and 4 applied to analyze the FE model in Figure 2.5 consisting of a canyon without a dam or reservoir. In these analyses, the control motion at the surface of the foundation rock was defined in the stream direction by the S69E component of the motion recorded at Taft Lincoln School Tunnel during the 1952 Kern County earthquake.

Observe from the results in Figure 2.6 that the amplitude and phase of the motion varies greatly with height, and by comparing the motions at two locations at the same elevation (e.g., at z = 0 m), it is evident that scattering and diffraction of waves from the canyon cause variation of the motion also in the horizontal direction. Because of the assumption of vertically incident waves however, this spatial variation is significant in the vertical direction but less so in the horizontal direction. Thus, this method of applying the seismic input is only able to represent parts of the very complex spatially varying wave fields that have been observed at actual dams subjected to earthquakes [Chopra and Wang 2009].

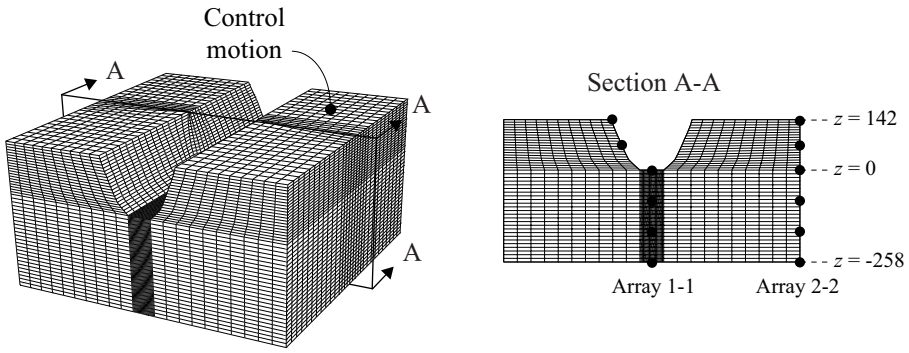

Figure 2.5 **Finite-element model of canyon showing location of two vertical node arrays: array 1-1 at the center of the model, and array 2-2 at the side boundary of the model.**

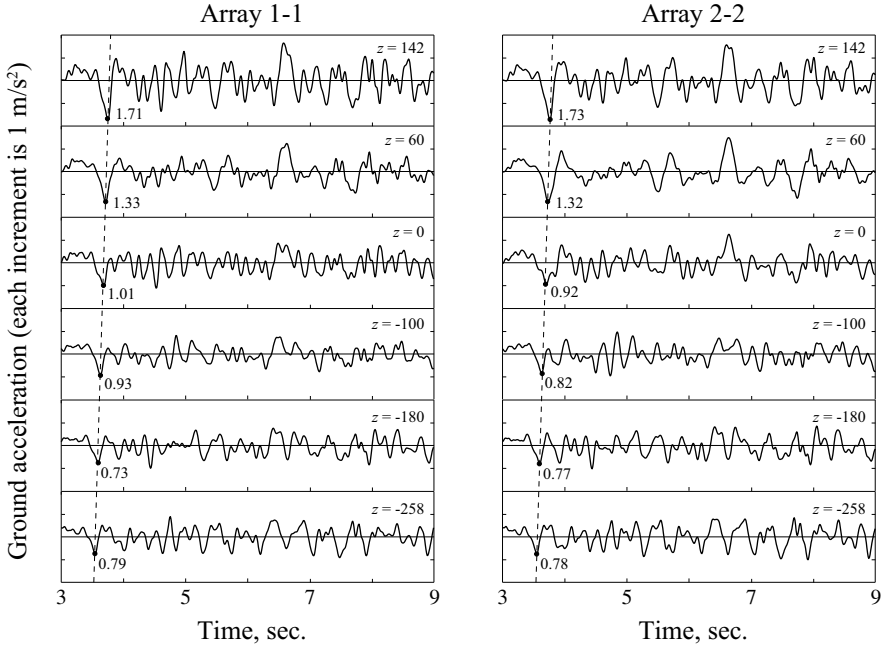

Figure 2.6 **Stream component of free-field earthquake motion computed by the direct FE method at six different elevations at the two arrays. A specific peak in the acceleration history is identified and connected by a dashed line to demonstrate the amplitude change and time shift in the motions at higher elevations.**

3 Equations of Motion

3.1 GOVERNING EQUATIONS

The governing equations for a 2D gravity dam–water–foundation rock system idealized as an ensemble of FEs with viscous-damper boundaries were derived in Part I. These equations are repeated here and generalized for 3D dam–water–foundation rock systems; see Figure 3.1:

$$\begin{bmatrix} \mathbf{m} & \mathbf{0} \\ \rho(\mathbf{Q}_h^{\mathrm{T}} + \mathbf{Q}_b^{\mathrm{T}}) & \mathbf{s} \end{bmatrix} \begin{Bmatrix} \ddot{\mathbf{r}}^t \\ \ddot{\mathbf{p}}^t \end{Bmatrix} + \begin{bmatrix} \mathbf{c} & \mathbf{0} \\ \mathbf{0} & \mathbf{b} \end{bmatrix} \begin{Bmatrix} \dot{\mathbf{r}}^t \\ \dot{\mathbf{p}}^t \end{Bmatrix} + \begin{Bmatrix} \mathbf{f}(\mathbf{r}^t) \\ \mathbf{0} \end{Bmatrix} + \begin{bmatrix} \mathbf{0} & -(\mathbf{Q}_h + \mathbf{Q}_b) \\ \mathbf{0} & \mathbf{h} \end{bmatrix} \begin{Bmatrix} \mathbf{r}^t \\ \mathbf{p}^t \end{Bmatrix} = \begin{Bmatrix} \mathbf{R}_f^t + \mathbf{R}^{\mathrm{st}} \\ \mathbf{H}_r^t \end{Bmatrix} \tag{3.1}$$

where $\mathbf{r}^t$ is the vector of total displacements in the dam and foundation rock; $\mathbf{p}^t$ is the vector of total hydrodynamic pressures in the fluid, idealized as a linear (for convenience of notation), inviscid, irrotational, and compressible Eulerian fluid† [52]; $\mathbf{m}$ and $\mathbf{c}$ are the standard mass and damping matrices, respectively, for the dam–foundation rock system; $\mathbf{f}(\mathbf{r}^t)$ is the vector of internal forces due to (nonlinear) material response; $\mathbf{s}$, $\mathbf{b}$, and $\mathbf{h}$ are the "mass," "damping," and "stiffness" matrices, respectively, for the fluid [Zienkiewicz and Bettess 1978]; ρ is the density of water; $\mathbf{Q}_h$ and $\mathbf{Q}_b$ are matrices that couple accelerations to hydrodynamic pressures at the dam–water interface Γ_h and water–foundation rock interface Γ_b, respectively; $\mathbf{R}^{\mathrm{st}}$ is the vector of static forces, including self-weight, hydrostatic pressures, and static foundation reactions at Γ_f (see Chapter 7 for details); $\mathbf{R}_f^t$ is the vector of dynamic forces associated with the absorbing foundation boundary Γ_f; and $\mathbf{H}_r^t$ is the vector of dynamic forces associated with the absorbing fluid boundary Γ_r. Expressions for the unknown forces $\mathbf{R}_f^t$ and $\mathbf{H}_r^t$ will be derived later in this chapter.

† The analysis procedure is also applicable to a Lagrangian fluid formulation with appropriate modifications of Equation (3.1)

Hydrodynamic wave energy is lost at Γ_b—the bottom and side boundaries of the reservoir—by means of two mechanisms. The first is wave absorption in sediments invariably deposited at the reservoir bottom. To allow for comparison against results from the substructure method in Chapter 5, this mechanism is approximately modeled by the reservoir bottom reflection coefficient α [Fenves and Chopra 1983], and its effects are included in Equation (3.1) through the damping matrix **b**. The second mechanism, associated with water–foundation rock interaction, is explicitly considered in the FE model through the coupling matrix $\mathbf{Q}_b$. Because this mechanism automatically accounts for some radiation of hydrodynamic waves, care should be taken not to overestimate the total amount of energy lost at these boundaries when also including sediment absorption in the FE model. For example, if the foundation consists of sandstone or granite, including water–foundation rock interaction has approximately the same amount of energy dissipation as a 1D absorption model with $\alpha = 0.50$ or $\alpha = 0.75$, respectively.

The wave-absorbing boundaries that enforce the radiation condition at the foundation and fluid boundaries are modeled by viscous dampers (dashpots) lumped at the boundary nodes of the FE model; see Figure 3.2. Their governing equations can be written in FE notation as

$$\mathbf{R}_f + \mathbf{c}_f \dot{\mathbf{r}}_f = \mathbf{0}, \quad \text{at the foundation boundaries } \Gamma_f \tag{3.2a}$$

$$\mathbf{H}_r + \mathbf{c}_r \dot{\mathbf{p}}_r = \mathbf{0}, \quad \text{at the upstream fluid boundary } \Gamma_r \tag{3.2b}$$

In Equation (3.2a), $\mathbf{c}_f$ is the matrix of normal and tangential damper coefficients $c_p = A\rho_f V_p$ and $c_s = A\rho_f V_s$, respectively, where A is the tributary area of the node, and ρ_f, V_s, and V_p are the density, shear-wave velocity, and pressure-wave velocity, respectively, of the rock. In Equation (3.2b), $\mathbf{c}_r$ is the matrix of damper coefficients $c_r = A/C$, where C is the speed of pressure waves in water. In the next section, these equations will be reformulated in terms of the total variables that enter into Equation (3.1).

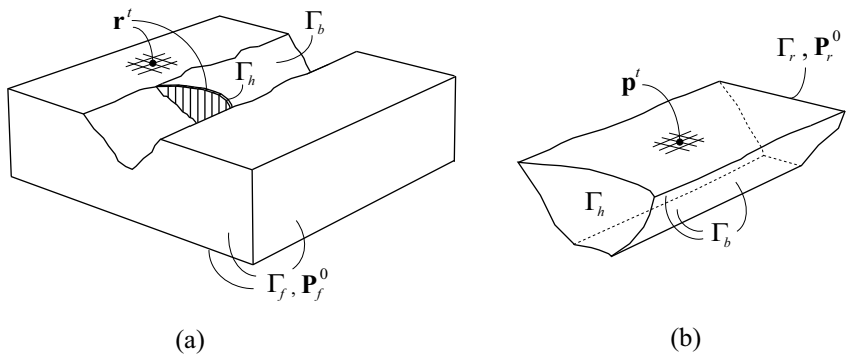

Figure 3.1 **Schematic FE model of (a) dam and foundation domain, and (b) fluid domain. Absorbing boundaries Γ_f and Γ_r at the truncation of the foundation and fluid domains, and interfaces Γ_h at the upstream dam face and Γ_b at the reservoir bottom and sides are highlighted.**

3.2 INTERACTION AS A SCATTERING PROBLEM

Dam–water–foundation interaction may be interpreted as a scattering problem, in which the dam perturbs a "free-field" state of the system. Utilizing this idea, the procedure developed for 2D gravity dam systems in Part I is extended next for 3D dam–water–foundation rock systems.

Consider the auxiliary water–foundation rock system defined in Figure 3.3(a), which consists of three subdomains: Ω^a denotes the foundation region with an irregular canyon interior to the future absorbing boundary Γ_f; Ω_f^+ is the semi-unbounded, regular foundation region exterior to Γ_f; and Ω_f^+ is the semi-unbounded, uniform fluid channel upstream of the future absorbing boundary Γ_r. The displacements and hydrodynamic pressures in this auxiliary water–foundation rock system are defined as $\mathbf{r}^a$ and $\mathbf{p}^a$, respectively. This auxiliary system does not correspond to any physical state, but it is introduced to facilitate formulation of the analysis procedure.

The dam–water–foundation rock system is also separated into three subdomains; Figure 3.3(b): Ω denotes the dam and adjacent parts of the foundation and fluid domains interior to Γ_f and Γ_r; and Ω_f^+ and Ω_r^+ are the semi-unbounded foundation and fluid domains exterior to Γ_f and Γ_r; these are identical to the exterior regions of the auxiliary system. In order to formulate the governing equations for the absorbing boundaries in terms of free-field quantities, the displacements and hydrodynamic pressures are defined by the variables

$\mathbf{r}^t$ and $\mathbf{p}^t$, in the interior region Ω (3.3a)

$\mathbf{r}^t - \mathbf{r}^a$ and $\mathbf{p}^t - \mathbf{p}^a$, in the exterior regions Ω_f^+ and Ω_r^+ (3.3b)

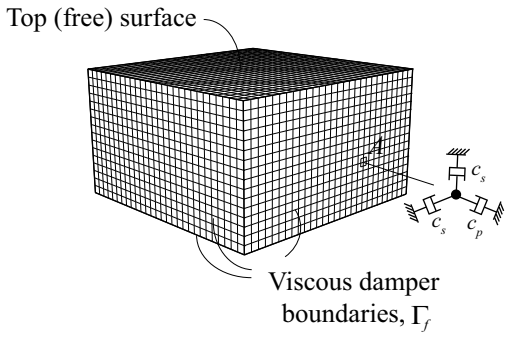

Figure 3.2 Viscous-damper boundary Γ_f for foundation rock.

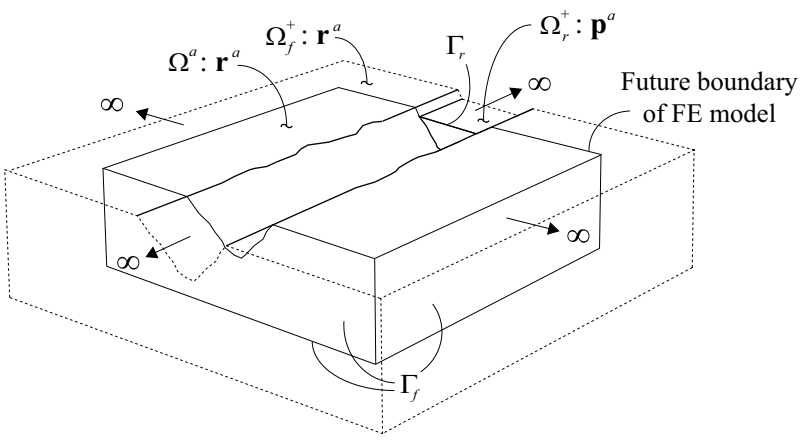

(a)

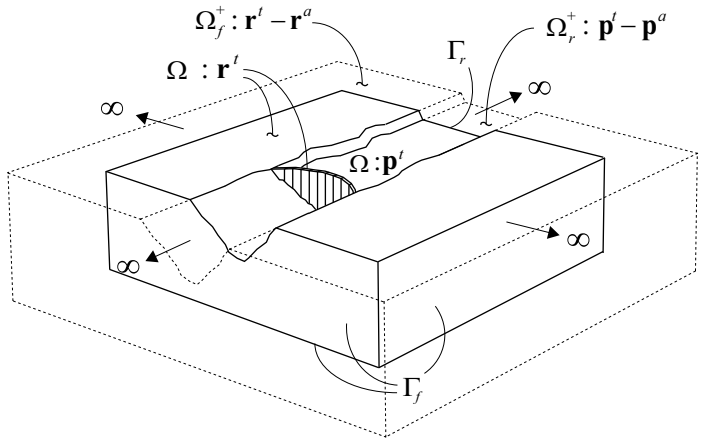

(b)

Figure 3.3 **Illustration of dam–water–foundation rock interaction as a scattering problem: (a) semi-unbounded auxiliary water–foundation rock system in its "free-field" state with variables defined by $\mathbf{p}^a$ in Ω_r^+ and $\mathbf{r}^a$ in $\Omega^a \cup \Omega_f^+$; and (b) dam–water–foundation rock system with variables defined by $\mathbf{p}^t$ and $\mathbf{r}^t$ in Ω and the scattered variables $\mathbf{p}^t - \mathbf{p}^a$ in Ω_r^+ and $\mathbf{r}^t - \mathbf{r}^a$ in Ω_f^+.**

The variables chosen in the exterior regions Ω_f^+ and Ω_r^+ represent the scattered motion and scattered hydrodynamic pressures, i.e., the perturbation of the motion and pressures in the auxiliary water–foundation rock system due to the presence of the dam and irregular fluid region. The viscous-damper boundaries Γ_f and Γ_r are intended to simulate these semi-unbounded regions. Because linear material behavior was assumed in these exterior domains, the boundary forces (tractions) corresponding to the scattered variables are $\mathbf{R}_f = \mathbf{R}_f^t - \mathbf{R}_f^a$ at Γ_f and

$\mathbf{H}_r = \mathbf{H}_r^t - \mathbf{H}_r^a$ at Γ_r. Substituting these expressions into the radiation conditions for the viscous-damper boundaries [Equation (3.2)], one obtains:

$$\mathbf{R}_f^t = \mathbf{R}_f^a - \mathbf{c}_f\left[\dot{\mathbf{r}}_f^t - \dot{\mathbf{r}}_f^a\right] \qquad \mathbf{H}_r^t = \mathbf{H}_r^a - \mathbf{c}_r\left[\dot{\mathbf{p}}_r^t - \dot{\mathbf{p}}_r^a\right] \tag{3.4}$$

The total forces on the viscous-damper boundaries can be seen to consist of two parts: the forces $\mathbf{R}_f^a$ and $\mathbf{H}_r^a$ consistent with the boundary tractions in the auxiliary system at Γ_f and Γ_r, respectively, and the product of damper coefficients and the scattered motion and scattered hydrodynamic pressure.

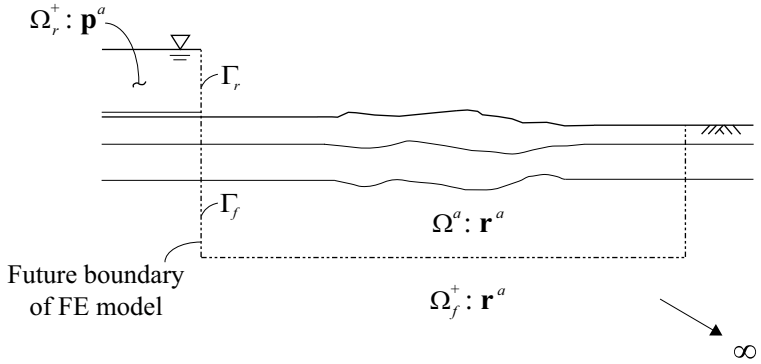

(a)

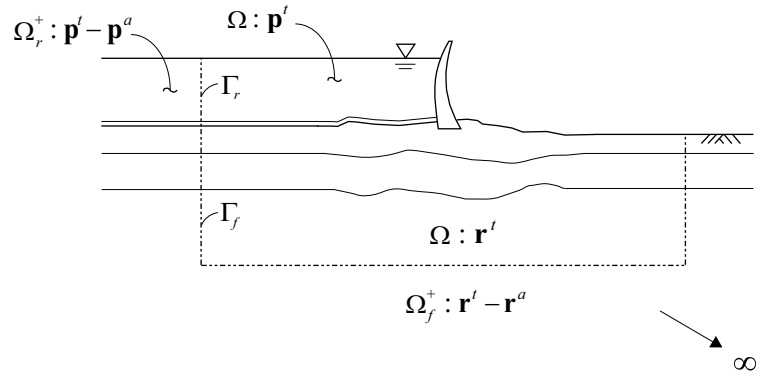

(b)

Figure 3.4 **Illustration of dam–water–foundation rock interaction as a scattering problem, section through center of canyon: (a) semi-unbounded auxiliary water–foundation rock system in its "free-field" state; and (b) dam–water–foundation rock system.**

3.3 APPROXIMATING WATER–FOUNDATION ROCK INTERACTION

The quantities $\mathbf{R}_f^a$, $\dot{\mathbf{r}}_f^a$, $\mathbf{H}_r^a$ and $\dot{\mathbf{p}}_r^a$ that enter into Equation (3.4) are to be determined by dynamic analysis of the auxiliary water–foundation rock system; Figure 3.3(a). This very complex analysis may be simplified by ignoring the effects of water–foundation rock interaction in $\Omega_r^+ \cup \Omega_f^+$, as was done in Part I for the 2D system. This simplification implies the following approximations:

$$\mathbf{r}_f^a \approx \mathbf{r}_f^0 \text{ and } \mathbf{R}_f^a \approx \mathbf{R}_f^0 \text{ in the foundation domain } \Omega^a \cup \Omega_f^+ \tag{3.5a}$$

$$\mathbf{p}_r^a \approx \mathbf{p}_r^0 \text{ and } \mathbf{H}_r^a \approx \mathbf{H}_r^0 \equiv \mathbf{0}^{\dagger} \text{ in the fluid domain } \Omega_r^+ \tag{3.5b}$$

where the free-field motion $\mathbf{r}_f^0$ and forces $\mathbf{R}_f^0$ at the boundary Γ_f are computed from analysis of the foundation domain alone [Figure 3.5(a)], thus ignoring the effects of hydrodynamic pressures in Ω_r^+ on the foundation-rock motions; and the free-field hydrodynamic pressures $\mathbf{p}_r^0$ are computed from analysis of the fluid part alone [Figure 3.5(b] with rigid foundation rock, thus ignoring the effects of foundation-rock flexibility on the hydrodynamic pressures in Ω_r^+.

Although the secondary effects of water–foundation rock interaction in the exterior domain $\Omega_f^+ \cup \Omega_r^+$ distant from the dam are ignored, the dominant effects within the FE domain Ω that contains the dam are still rigorously represented by the coupling matrix $\mathbf{Q}_b$

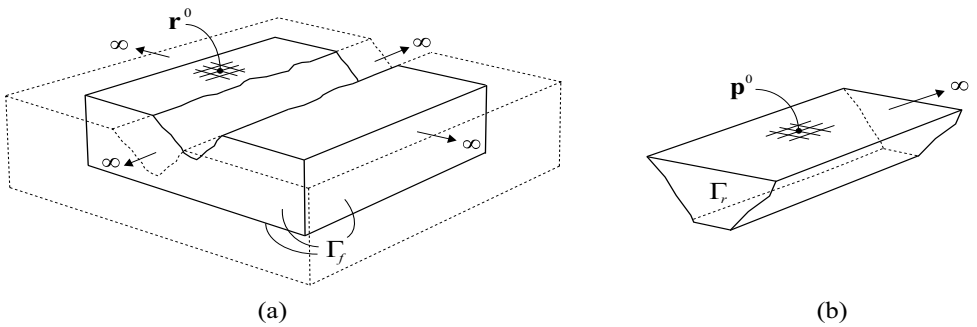

Figure 3.5 **(a) Free-field foundation-rock system with displacements defined by $\mathbf{r}^0$; and (b) "free-field" fluid channel upstream of Γ_r with pressures defined by $\mathbf{p}^0$.**

3.4 FINAL EQUATIONS OF MOTION

† The forces $\mathbf{H}_r^0$ are zero for all components of ground motion because the pressure gradient at Γ_r is zero when the foundation rock is rigid and the semi-unbounded channel has a uniform cross section.

Substituting the above expressions for the viscous-damper boundaries [Equation (3.4)] with the approximations in Equation (3.5) into Equation (3.1), the final equations of motion for the 3D dam–water–foundation rock system are obtained:

$$\begin{bmatrix} \mathbf{m} & \mathbf{0} \\ \rho(\mathbf{Q}_h^{\mathrm{T}} + \mathbf{Q}_b^{\mathrm{T}}) & \mathbf{s} \end{bmatrix} \begin{Bmatrix} \ddot{\mathbf{r}}^t \\ \ddot{\mathbf{p}}^t \end{Bmatrix} + \begin{bmatrix} \mathbf{c} + \mathbf{c}_f & \mathbf{0} \\ \mathbf{0} & \mathbf{b} + \mathbf{c}_r \end{bmatrix} \begin{Bmatrix} \dot{\mathbf{r}}^t \\ \dot{\mathbf{p}}^t \end{Bmatrix} + \begin{Bmatrix} \mathbf{f}(\mathbf{r}^t) \\ \mathbf{0} \end{Bmatrix} + \begin{bmatrix} \mathbf{0} & -(\mathbf{Q}_h + \mathbf{Q}_b) \\ \mathbf{0} & \mathbf{h} \end{bmatrix} \begin{Bmatrix} \mathbf{r}^t \\ \mathbf{p}^t \end{Bmatrix} = \begin{Bmatrix} \mathbf{R}^{\mathrm{st}} \\ \mathbf{0} \end{Bmatrix} + \begin{Bmatrix} \mathbf{P}_f^0 \\ \mathbf{P}_r^0 \end{Bmatrix} \tag{3.6}$$

where the last term on the right hand side represents the effective earthquake forces:

$$\mathbf{P}_f^0 = \mathbf{R}_f^0 + \mathbf{c}_f \dot{\mathbf{r}}_f^0 \text{ at the foundation boundaries } \Gamma_f \tag{3.7a}$$

$$\mathbf{P}_r^0 = \mathbf{c}_r \dot{\mathbf{p}}_r^0 \text{ at the upstream fluid boundary } \Gamma_r \tag{3.7b}$$

Working with the scattered variables in Ω_f^+ and Ω_r^+, and approximating water–foundation rock interaction, has enabled Equation (3.7) to be derived for the effective earthquake forces in terms of free-field variables only. These free-field variables represent the minimal set of seismic input data required for determining the response of the dam–water–foundation rock system to earthquake excitation.

4 Computing Effective Earthquake Forces

4.1 FORCES AT BOTTOM BOUNDARY

Similarly as for the 2D system in Part I, the equation for the effective earthquake forces at the bottom boundary [Equation (3.7a)] is reformulated as:

$$\mathbf{P}_f^0 = 2\mathbf{c}_f\,\dot{\mathbf{r}}_I^0 \tag{4.1}$$

where $\mathbf{r}_I^0$ is the motion at the bottom boundary due to the incident (upward propagating) seismic waves. The incident motion $\mathbf{r}_I^0$ is obtained by 1D deconvolution of the surface motion $a_g(t)$ assuming vertically propagating seismic waves and homogeneous (or horizontally layered) rock. Deconvolution is an inverse procedure to determine the amplitude and frequency content of an input signal to be consistent with the observed output signal. It is most conveniently implemented in the frequency domain, either directly by computing the inverse of the transfer function for a 1D half-space [Kramer 1996], or by utilizing available 1D site response analysis software such as SHAKE [Schnabel et al. 1972] of DEEPSOIL [Hashash et al. 2011].

Although rather straightforward, deconvolution is often subject to considerable confusion because 1D wave-propagation software typically operates with two possible motions at every depth [Mejia and Dawson 2006]: an *outcrop motion* and a *within motion*. By definition, the within motion is the superposition of the incident and reflected waves, i.e., it is the total (or "actual") motion at any given depth in the half-space. In contrast, the outcrop motion is the motion that would occur at a theoretical outcrop location at the same depth; this is equal to twice the amplitude of the incident motion. Thus, the incident motion $\mathbf{r}_I^0$ needed in Equation (4.1) is one-half the outcrop motion at the bottom boundary determined in the deconvolution analysis. The procedure to compute effective earthquake forces $\mathbf{P}_f^0$ from Equation (4.1) is summarized in Box 4.1.

Some researchers have avoided deconvolution of the surface motion by idealizing the foundation rock as a homogeneous, undamped half-space [Zhang et al. 2009; Robbe et al. 2017].

While this simplification may be appropriate for the simple case of a homogeneous, undamped half-space, it can cause significant error in dam response for foundations with damping and for layered foundations, as will be demonstrated later in Section 6.3.

Box 4.1 Computing $\mathbf{P}_f^0$ at bottom boundary of foundation rock.

1. Determine the outcrop motion at the bottom foundation-rock boundary by 1D deconvolution of each component of the surface control motion $a_g^k(t)$, $k = x, y, z$.
2. Compute the incident motion $\mathbf{r}_I^0$ as one-half the outcrop motion at the bottom boundary determined in Step 1 and obtain $\dot{\mathbf{r}}_I^0$ as the time derivative of $\mathbf{r}_I^0$.
3. Calculate the effective earthquake forces $\mathbf{P}_f^0$ at the bottom boundary from Equation (4.1) using $\dot{\mathbf{r}}_I^0$ from Step 2.

4.2 FORCES AT SIDE BOUNDARIES

The computation and application of effective earthquake forces at the four side boundaries of the foundation domain [Equation (3.7a)] can be done automatically within the FE code using a special class of so-called free-field boundary elements [Zienkiewicz et al. 1989; Nielsen 2014]. Such elements solve the radiation condition for 1D wave propagation and apply a form of effective earthquake forces at the boundaries at every time step as the analysis progresses in time. Because very few commercial FE programs have such elements available, an alternative procedure will be presented wherein the effective earthquake forces are computed in a separate auxiliary analysis of the free-field system before the actual dam–water–foundation rock system is analyzed. This approach has the advantage that it does not require modification of the FE source code, but it has the disadvantage that it requires major data transfer.

4.2.1 Computing Forces at Side Boundaries: Uniform Canyon

The free-field motion $\mathbf{r}_f^0$ and boundary forces $\mathbf{R}_f^0$ required to compute the effective earthquake forces $\mathbf{P}_f^0$ at the four side boundaries [Equation (3.7a)] are determined from dynamic analysis of the foundation rock in its free-field state; see Figure 3.4(a). Before presenting the general procedure, a special case is considered where two additional geometric restrictions are imposed: (1) the canyon cross section is assumed to be uniform in the stream direction, and (2) the surface

of the foundation rock is horizontal. Under these assumptions, the free-field foundation-rock system is an infinitely-long canyon of arbitrary, but uniform cross section cut in a homogeneous or horizontally layered half-space; see Figure 4.1(a). Analysis of this 3D system subjected to vertically propagating seismic waves reduces to a 2D analysis [Figure 4.1(b]) where incident *SH*-waves cause the stream (out-of-plane) component of ground motion, and incident *SV*- and *P*-waves cause the cross-stream and vertical components.

For this special system, the quantities $\dot{\mathbf{r}}_f^0$ and $\mathbf{R}_f^0$ that enter into Equation (3.7a) can be determined by two simpler analyses: (1) analysis of a single column of foundation-rock elements subjected to forces of Equation (4.1) at the base [Figure 4.1(c)], which suffices for the two boundaries oriented in the stream direction; and (2) analysis of the 2D system of Figure 4.1(d) subjected to forces of Equation (4.1) at the base, where forces $\mathbf{P}_f^0$ on the sides determined from the first analysis (these latter forces are required because the domain has been truncated) provides the desired results for the boundaries oriented in the cross-canyon direction at the upstream and downstream ends of the foundation domain. The procedure is summarized in Box 4.2.

Box 4.2 Computing $\mathbf{P}_f^0$ at side boundaries of foundation domain: uniform canyon.

Analysis of 1D column

1. Develop a FE model for the 1D foundation-rock column that has the same mesh density as the boundary of the 2D system.
2. For each component of ground motion, $k = x, y, z$, add a viscous damper at the base in the *k*-direction and constrain DOFs in other directions to permit only shear ($k = x, y$) or axial ($k = z$) deformation of the 1D column.
3. Apply effective earthquake forces [Equation (4.1)] to the base in *k*-direction and compute $\dot{\mathbf{r}}_f^0$ and $\mathbf{R}_f^0$ at every node along the height.

Analysis of 2D system

4. Develop a FE model for the 2D foundation-rock system, with the same mesh density as the main FE model at the upstream/downstream boundary.
5. For each component of ground motion, $k = x, y, z$, add viscous dampers at the bottom and side boundaries, and constrain the DOFs at the faces to model the "infinite length" in the direction normal to the model boundary (e.g., if the *x*-axis is parallel to the upstream direction, two nodes with the same *y*-, and *z*-coordinates should be constrained to move identically).
6. Apply effective earthquake forces from Equation (4.1) to the bottom boundary and from Equation (3.7a) to the side boundaries using $\dot{\mathbf{r}}_f^0$ and $\mathbf{R}_f^0$ from the 1D analysis, and compute $\dot{\mathbf{r}}_f^0$ and $\mathbf{R}_f^0$ at every node in the 2D system.

Computing effective earthquake forces for main model

7. Compute the effective earthquake forces $\mathbf{P}_f^0$ at every node along the side boundaries of the foundation domain from Equation (3.7a) using $\dot{\mathbf{r}}_f^0$ and $\mathbf{R}_f^0$ from Step 3 at the along-canyon boundaries and from Step 6 at the cross-canyon boundaries at the upstream and downstream ends of the domain.

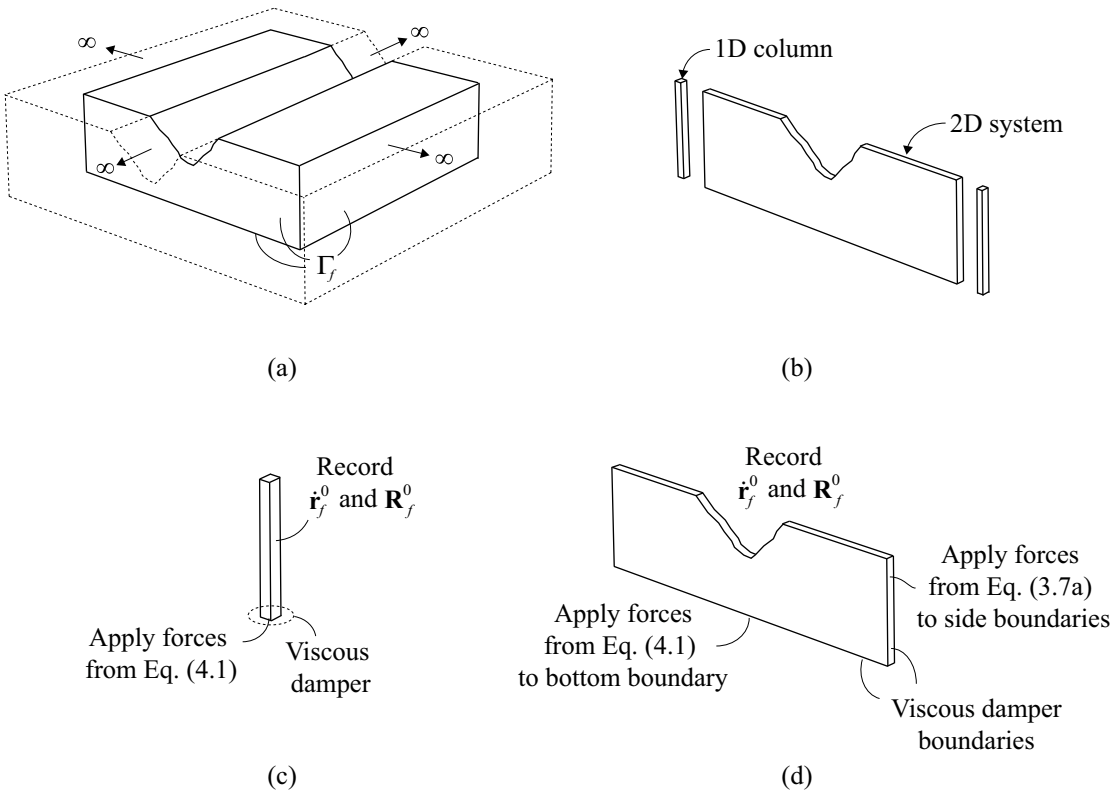

Figure 4.1 **Computing $\mathbf{P}_f^0$ for uniform canyon: (a) 3D free-field system with uniform canyon cut in foundation-rock half space; (b) "two-dimensional" free-field system with corresponding 1D corner columns; (c) analysis of 1D foundation-rock column to compute $\dot{\mathbf{r}}_f^0$ and $\mathbf{R}_f^0$ at side boundaries, and (c) analysis of 2D system to compute $\dot{\mathbf{r}}_f^0$ and $\mathbf{R}_f^0$ at upstream and downstream boundaries.**

4.2.2 Computing Forces at Side Boundaries: Arbitrary Canyon Geometry

Next, the geometric restrictions of a uniform canyon and horizontal foundation surface that were introduced in the preceding section are removed, implying that the free-field system becomes much more complicated. Although a system with arbitrary canyon geometry [Figure 4.2(a)] is not amenable to 2D analyses, the same type of analysis methodology can be extended to the system provided that it satisfies the general constraints described in Section 2.1.

For such a system, the quantities $\dot{\mathbf{r}}_f^0$ and $\mathbf{R}_f^0$ that enter in Equation (3.7a) can be determined by two sets of four simpler analyses: (1) analysis of four 1D corner columns of foundation-rock elements subjected to forces of Equation (4.1) at the base; and (2) analyses of the four 2D systems in Figure 4.2(b) subjected to forces of Equation (4.1) at the base and forces

$\mathbf{P}_f^0$ on the sides determined from the first set of 1D analyses. The latter set of analyses provide $\dot{\mathbf{r}}_f^0$ and $\mathbf{R}_f^0$ for nodes on all four side boundaries. The procedure is illustrated in Figure 4.2 and summarized in Box 4.3.

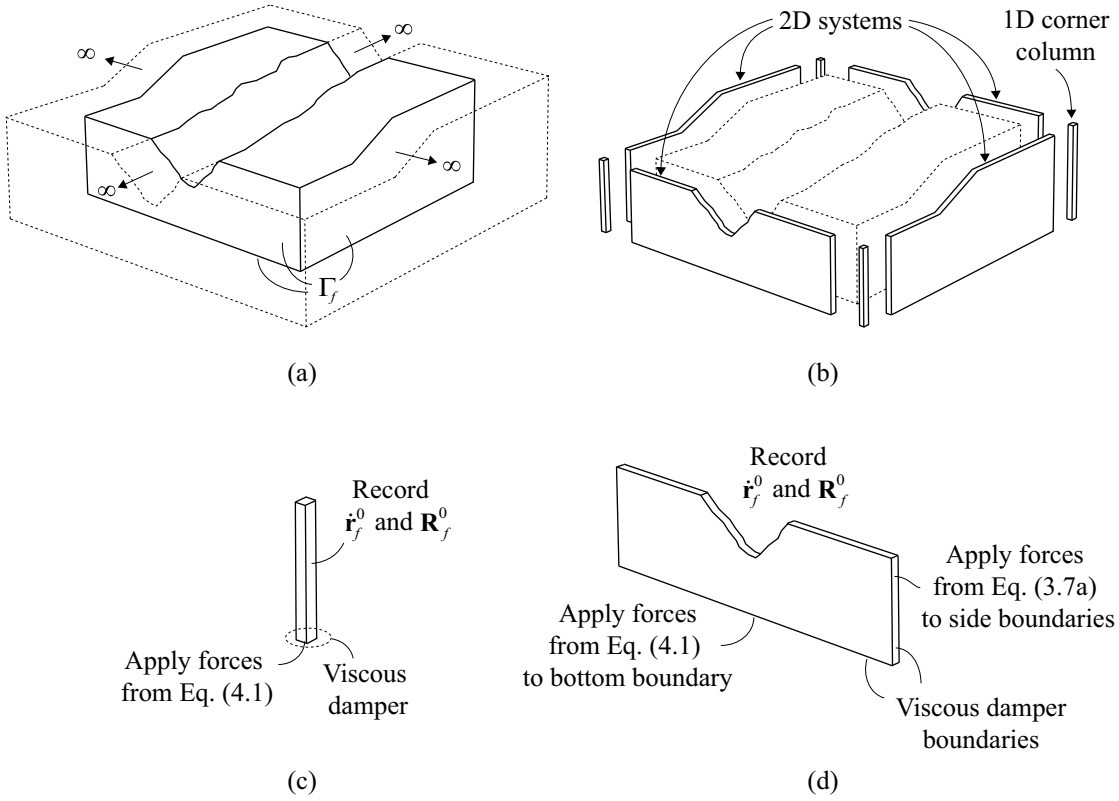

Figure 4.2 **Computing $\mathbf{P}_f^0$ for arbitrary canyon geometry: (a) 3D free-field system with canyon of arbitrary geometry cut in foundation-rock half-space; (b) free-field system with corresponding 1D corner columns and 2D systems; and (c) analysis of 1D corner columns to compute $\dot{\mathbf{r}}_f^0$ and $\mathbf{R}_f^0$ at corners, (d) analysis of 2D systems to compute $\dot{\mathbf{r}}_f^0$ and $\mathbf{R}_f^0$ at the four side boundaries.**

This procedure for computing $\mathbf{P}_f^0$ at the boundaries of a system with arbitrary geometry is based on the assumption that the motion in each of the four 2D systems [Figure 4.2(b)] can be determined independently of the other 2D systems. This assumption seems reasonable as long as the foundation domain is large enough, which is normally the case in the direct FE method

because viscous-damper boundaries generally require large domains to ensure acceptable modeling of the semi-unbounded domains.

Implementation of the procedure in Box 4.3 means that eight auxiliary analyses are required for each of the three components of ground motion. The computational effort required for each of these linear dynamic analyses is minimal, and the procedure can be automated in a pre-processing script that is set up and executed before the nonlinear dynamic analysis of the dam–water–foundation rock system takes place. For example, in this work MATLAB [The Math Works Inc. 2012] is used to compute and store effective earthquake forces used with the FE code OpenSees [McKenna 2011] to analyze the complete system; a similar method has been implemented by Saouma et al. [2011] in the FE code MERLIN [Saouma et al. 2013].

The disadvantage of this approach is that substantial amounts of data management and transfers are required for analyzing 3D models, which may easily have tens of thousands of boundary nodes. In Section 6.1, it will be demonstrated that that under certain conditions it is possible to drastically reduce these requirements by replace the actual 3D free-field system by a much simpler system.

Box 4.3 Computing $\mathbf{P}_f^0$ at side boundaries of foundation domain: arbitrary canyon geometry.

Analysis of four 1D corner columns

1. Develop FE models for each of the four 1D corner columns of the foundation rock that have the same mesh density as the corners of the main FE model.
2. For each component of ground motion, $k = x, y, z$, add a viscous damper at the base in the *k*-direction and constrain DOFs in other directions to permit only shear $(k = x, y)$ or axial $(k = z)$ deformation of the 1D column.
3. Apply effective earthquake forces [Equation (4.1)] to the base in the *k*-direction and compute $\dot{\mathbf{r}}_f^0$ and $\mathbf{R}_f^0$ at every node along the height.

Analysis of four 2D systems

4. Develop FE models for each of the four 2D systems of the foundation rock, with the same mesh density as the main FE model at the boundaries.
5. For each component of ground motion, $k = x, y, z$, add viscous dampers at the bottom and side boundaries and constrain DOFs at the faces to model the "infinite-length" conditions in the direction normal to the boundary.
6. Apply effective earthquake forces from Equation (4.1) to the bottom boundary and from Equation (3.7a) to the side boundaries using $\dot{\mathbf{r}}_f^0$ and $\mathbf{R}_f^0$ from the 1D analyses, and compute $\dot{\mathbf{r}}_f^0$ and $\mathbf{R}_f^0$ at every node in the 2D system.

Computing effective earthquake forces for main model

7. Compute effective earthquake forces $\mathbf{P}_f^0$ at every node at the four sides of the foundation domain from Equation (3.7a) using $\dot{\mathbf{r}}_f^0$ and $\mathbf{R}_f^0$ from Step 6.

4.3 FORCES AT UPSTREAM FLUID BOUNDARY

The free-field pressures $\mathbf{p}_r^0$ required to compute α at Γ_r are to be determined by dynamic analysis of the fluid in its free-field state [Figure 4.3(a)]: a fluid channel of uniform cross section unbounded in the upstream direction. Because this system is uniform in the upstream direction, the analysis reduces to two dimensions. For cross-stream and vertical components of ground

motion, the free-field pressures $\mathbf{p}_r^0$ on the boundary Γ_r can be computed from an analysis of the 2D fluid domain cross section with rigid foundation rock; see Figure 4.3(b). The stream component of ground motion will not generate any hydrodynamic pressures, thus implying $\mathbf{P}_r^0 = \mathbf{0}$. The procedure is summarized in Box 4.4.

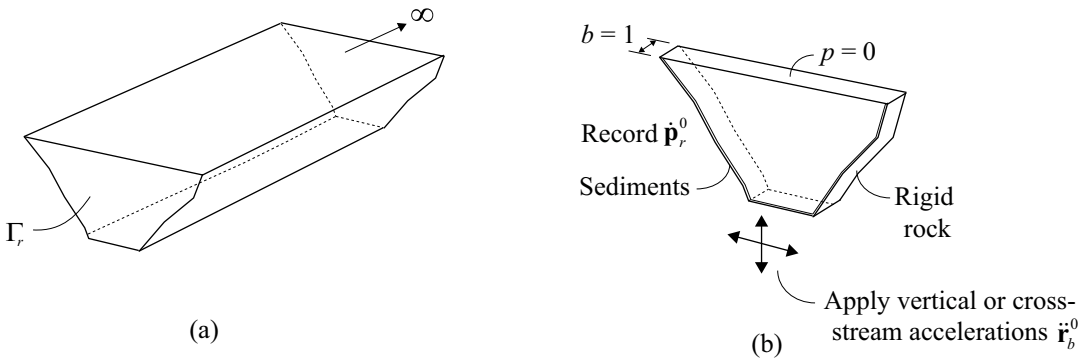

Figure 4.3 **Computing $\mathbf{P}_r^0$ at upstream fluid boundary: (a) 3D "free-field" fluid channel upstream of Γ_r; and (b) analysis of 2D fluid cross section subjected to vertical and cross-stream excitation to compute $\dot{\mathbf{p}}_r^0$.**

Box 4.4 **Computing $\mathbf{P}_r^0$ at upstream fluid boundary.**

Analysis of 2D fluid section

1. Develop a FE model of the 2D fluid cross section with the same mesh density as the main model at the upstream fluid boundary Γ_r, add surface elements at the reservoir bottom and sides to model sediments.

2. For cross-stream and vertical components of ground motion, $k = y, z$, calculate $\dot{\mathbf{p}}_r^0$ at every node by analyzing the 2D model subjected to accelerations $\ddot{\mathbf{r}}_b^0$ at the base, where $\ddot{\mathbf{r}}_b^0$ is the foundation-rock accelerations at the interface $\Gamma_b \cap \Gamma_r$ [Figure 3.1(b)]; these can be extracted from the relevant 2D analysis described in Section 4.2.

Computing effective earthquake forces

3. Compute the effective earthquake forces $\mathbf{P}_r^0$ for every node at the fluid boundary from Equation (3.7b) using $\dot{\mathbf{p}}_r^0$ from Step 2.

The forces $\mathbf{P}_r^0$ are associated with earthquake-induced pressures due to vertical and cross-stream excitation of the part of the fluid domain that has been eliminated upstream of Γ_r. These forces are required because of the system idealization (Figure 2.1), where the excitation is implicitly assumed to extend along the entire length of the unbounded fluid channel. Later in Section 6.4, it will be demonstrated that these forces are inconsequential to the dam response and may be dropped from the analysis.

5 Numerical Validation of the Direct Finite-Element Method

In this chapter several examples are documented to validate the accuracy of the direct FE method that was developed in Chapters 3 and 4 and implemented with the FE program OpenSees [McKenna 2011]. First, the ability of the method to reproduce free-field motions at the surface of a flat foundation box is documented. The free-field response of a uniform, semi-cylindrical canyon cut in a foundation half-space is determined next and compared with classical solutions. Lastly, the dynamic response of Morrow Point Dam is computed for a wide range of conditions and compared with results obtained from the substructure method.

5.1 REPRODUCING FREE-FIELD MOTION IN FOUNDATION ROCK

5.1.1 Free-Field Motion at Flat Box Surface (the Flat Box Test)

The flat box model shown in Figure 5.1 has a domain size and mesh density that is representative of an actual dam–water–foundation rock system with viscous dampers employed at the bottom and side boundaries. The free-field control motion $a_g^k(t)$ is defined at the surface in the two horizontal and vertical directions by the S69E, S21W and vertical components of the Taft ground motion, respectively. Each component of ground motion is deconvolved, effective earthquake forces $\mathbf{P}_f^0$ are computed from the procedures summarized in Box 4.1 and Box 4.3 and applied to the bottom and side boundaries of the foundation box, respectively, and the response of the system is computed.

The results presented in Figure 5.2 show a near perfect match between the specified free-field control motion and the computed surface motions at every node on the surface of the flat box, thus demonstrating that the direct FE method is able to exactly reproduce free-field conditions for this simple system to within FE discretization error. This is achieved without

iterative procedures to adjust the amplitude and/or frequency content of the input motion, which is sometimes used to overcome deficiencies in FE models [Bureau of Reclamation 2013; Cvijanovic et al. 2014].

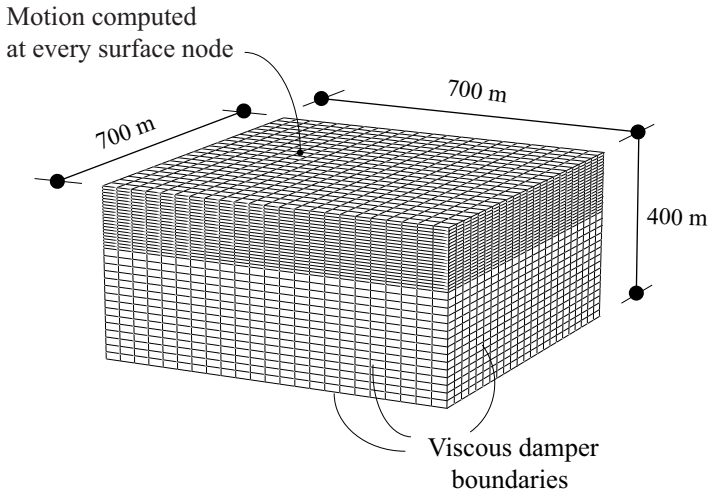

Figure 5.1 Finite-element model of flat foundation box.

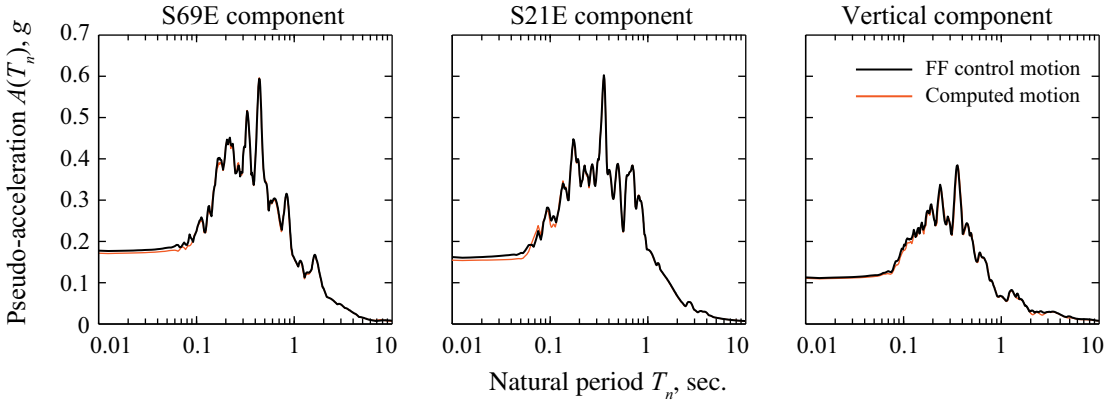

Figure 5.2 Comparison of 5% damped pseudo-acceleration response spectra for control motion and computed motion at nodes on flax box surface.

5.1.2 Free-Field Motion at Canyon Surface

Next, the ability of the direct FE method to accurately compute the free-field earthquake motion at the surface of a semi-cylindrical canyon is evaluated; this is the motion that in turn will excite a dam supported in the canyon. Available analytical and numerical solutions for this classical problem [Trifunac 1972; Wong 1982] serve as the benchmark for the evaluation.

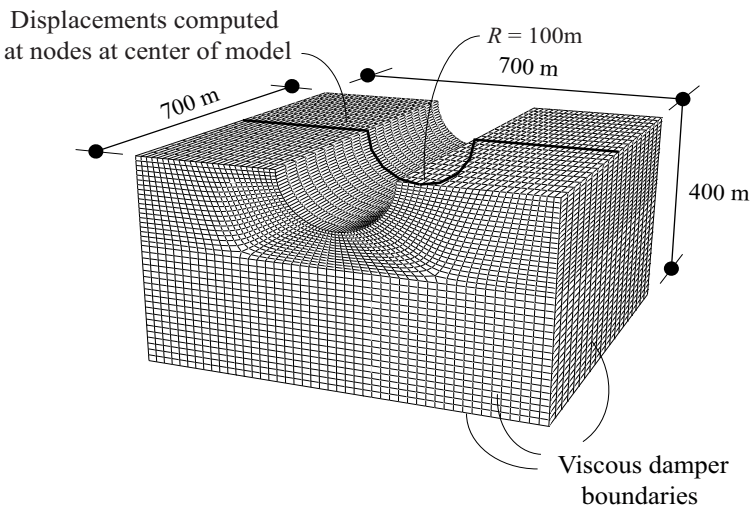

Figure 5.3 Finite-element model of semi-cylindrical canyon cut in half-space.

The semi-cylindrical canyon with radius R discretized as a FE system with viscous-damper boundaries (Figure 5.3) is subjected to effective earthquake forces $\mathbf{P}_f^0$ computed from the procedures summarized in Boxes 4.1 and 4.3 with the vertically incident seismic motion $\mathbf{r}_I^0$ specified as a plane wave of unit amplitude and frequency f. The forces $\mathbf{P}_f^0$ are applied to the bottom and side boundaries of the FE model, and the displacement response along the canyon and top surface of the foundation is computed. Results are presented for Poisson's ratio ν_s = 1/3 and different values of $\eta = 2fR/V_s$, where V_s is the shear-wave velocity of the foundation medium. The dimensionless frequency η may be interpreted as the ratio of the canyon width to the wavelength of the incident waves. When plotted in this form, results are independent of the actual material properties as long as the ratio R/V_s is maintained.

The displacement amplitude, defined as the ratio of the Fourier transform of the computed displacements to the unit amplitude input motion, are presented in Figure 5.4 for incident *SH*-, *SV*- and *P*-waves; these correspond to excitation in the canyon, cross-canyon and vertical directions, respectively. The results obtained by the direct FE method closely match the analytical results by Trifunac [1972] for incident *SH*-waves, and the numerical results by Wong [1982] using boundary integral methods for incident *SV*-waves and *P*-waves. The small discrepancies are due to the inability of viscous-damper boundaries to perfectly absorb all scattered and diffracted waves from the canyon. This is most prominent in the response to incident *SV*-waves and *P*-waves because these excitations generate surface waves that are not

effectively absorbed by the viscous dampers; but even for these excitations, the discrepancies are small. The excellent agreement demonstrates the ability of the direct FE method to accurately predict free-field motions at the surface of a canyon.

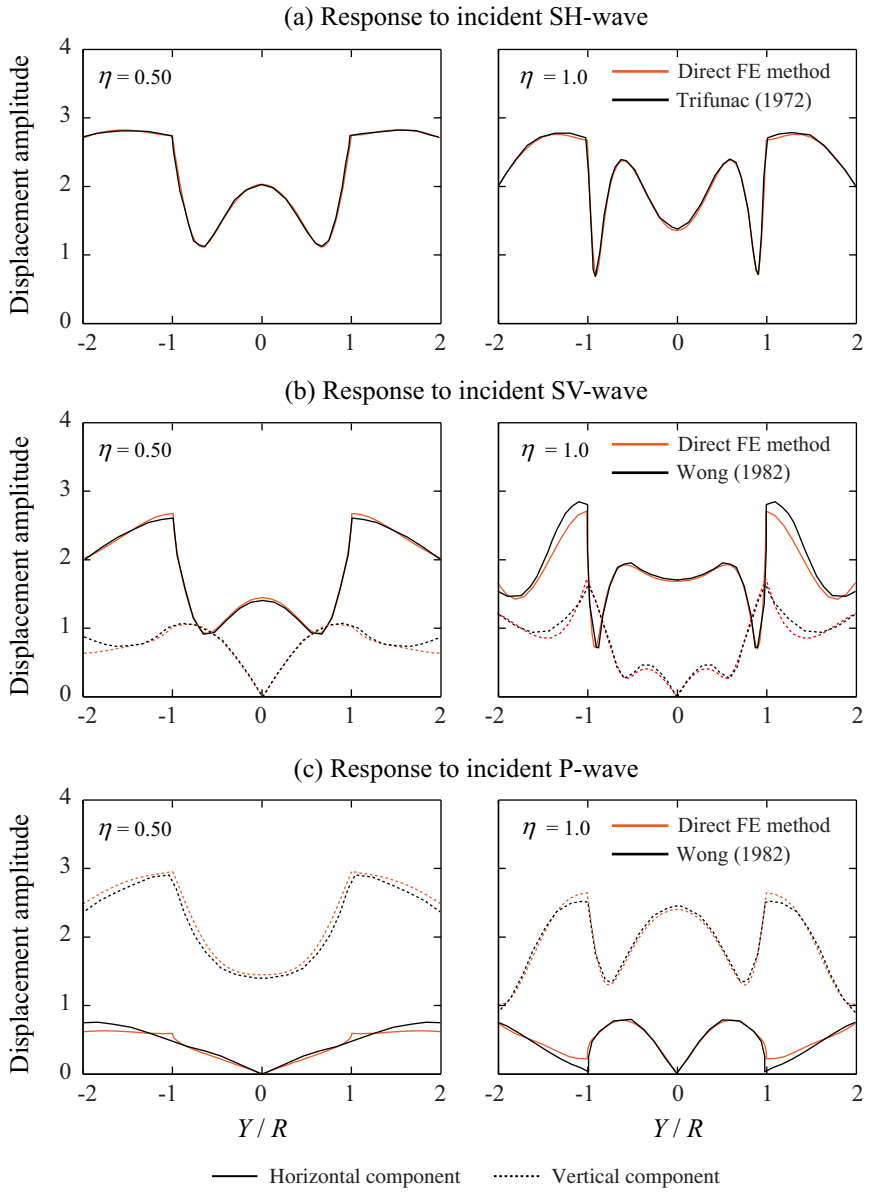

Figure 5.4 **Displacement amplitudes at canyon surface computed by the direct FE method and compared with results by Trifunac [1972] and Wong [1982]. Responses to incident *SH*-, *SV*-, and *P*-waves are plotted against dimensionless distance Y / R, where *Y* is the transverse distance from the center and *R* the radius.**

5.2 DYNAMIC RESPONSE OF MORROW POINT DAM

5.2.1 System Analyzed

The ability of the direct FE method to accurately compute the dynamic response of concrete dams is validated numerically by analyzing Morrow Point Dam, a 142-m-high, approximately symmetric, single-centered arch dam located on the Gunnison River in Colorado. The linear material properties and damping values selected for the dam concrete and foundation rock are based on the results from forced vibration tests of the dam and subsequent numerical studies performed to match the experimental results [Duron and Hall 1988; Nuss 2001]. The concrete and foundation rock is assumed to be homogeneous, isotropic, and linearly elastic. The concrete has a modulus of elasticity E_s = 34.5 GPa, density ρ_s = 2403 kg/m^3, and Poisson's ratio ν_s = 0.20. The foundation rock has a modulus of elasticity E_f = 24.1 GPa (i.e., E_f / E_s = 0.70), density ρ_f = 2723 kg/m^3 and Poisson's ratio ν_f = 0.20. The impounded water has the same depth as the height of the dam, density ρ = 1000 kg/m^3, and pressure-wave velocity C = 1440 m/sec. The reservoir-bottom reflection coefficient is selected as α = 0.80.

Material damping in the dam and foundation rock is modeled in the direct FE method by Rayleigh damping with $\zeta_s = 1\%$ and $\zeta_f = 2\%$ viscous damping specified for the dam concrete and foundation rock, respectively, at two frequencies: f_1 = 5 Hz, the fundamental resonance frequency of the dam alone on rigid rock, and at three times this frequency. The damping matrix for the complete system is then constructed using standard procedures for assembling damping matrices for two subdomains [Chopra 2012b]. Determined by the half-power bandwidth method applied to the resonance curve, the overall damping in the dam–water–foundation rock system is 3–5% for the first few modes of vibration, which is consistent with the range of measured damping values at the dam [Duron and Hall 1988].

The FE mesh shown in Figure 5.5 is assembled using standard 8-node brick elements, with 800 solid elements for the dam, 42,000 solid elements for the foundation rock, and 9200 acoustic fluid elements for the water in the reservoir. Interface elements couple accelerations with hydrodynamic pressures at the fluid–solid interfaces, surface elements at the bottom and sides of the reservoir model the 1D wave absorption due to sediments, and viscous dampers (dashpots) at the foundation domain boundaries and at the upstream end of the fluid domain model the semi-unbounded domains. The combined FE model consists of approx. 63,000

elements and 150,000 DOFs, and the overall dimensions are 700 m × 700 m × 400 m, corresponding to approx. $5H \times 5H \times 3H$, where H is the height of the dam. These dimensions are sufficiently large to minimize reflections from the viscous-damper boundaries and were selected based on an initial study of the influence of domain size on the arch dam response (not included here). Interestingly, the response of the 3D arch dam system was found to be less sensitive to the size of the foundation domain than was the case for 2D gravity dam systems, which may be explained by the observation that dam–foundation interaction generally has less influence on arch dam response than on gravity dam response [Tan and Chopra 1995a].

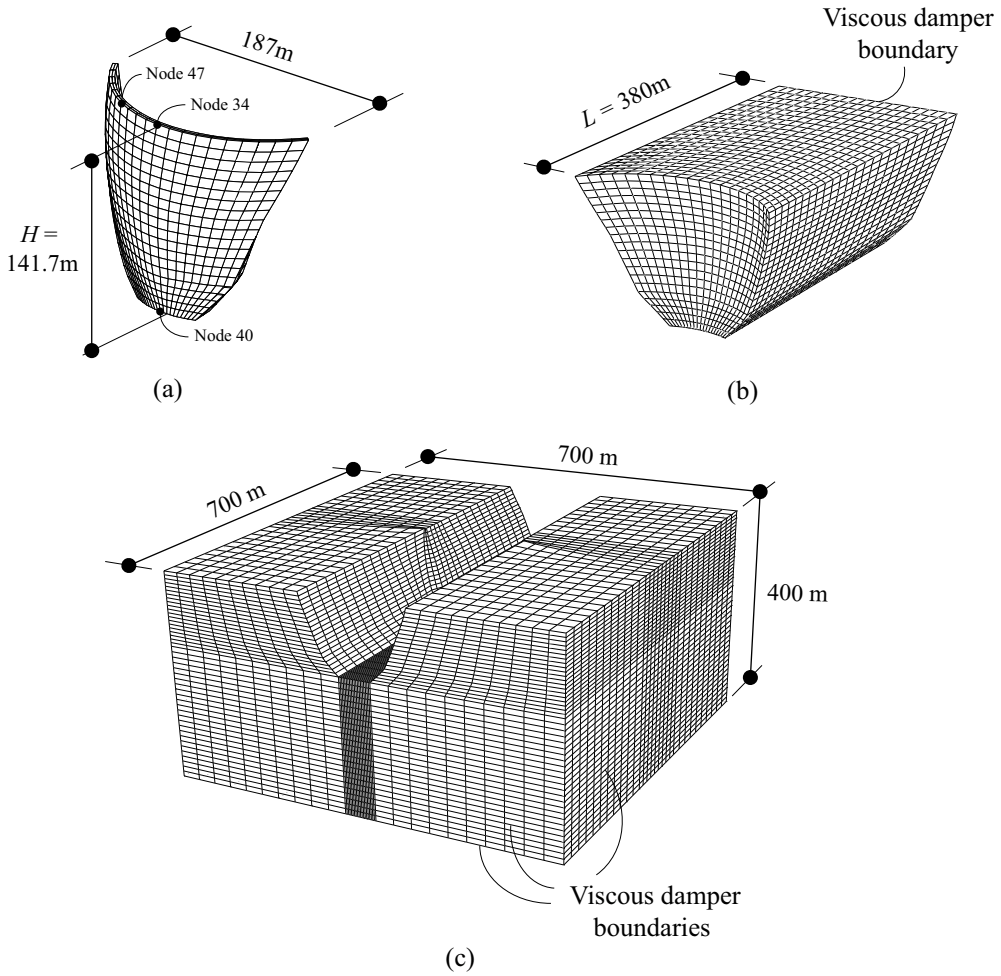

Figure 5.5 **Finite-element model of Morrow Point Dam: (a) dam; (b) fluid domain; and (c) foundation domain.**

5.2.2 EACD3D-08 Model for Substructure Method

The dynamic response of this FE model—computed by the direct FE method—will be compared against independent results obtained using the substructure method Wang and Chopra [2010]. Analyzed using the computer program EACD3D-08 [Wang and Chopra 2008], wherein the foundation rock is treated as a semi-unbounded half-space, the fluid domain as unbounded in the upstream direction, and the earthquake excitation is specified directly at the dam–canyon interface, this method avoids artificial model truncations and absorbing boundaries.

In order to effectively work with this computer program—which does not have a user interface or any pre- or post-processing capabilities—a set of MATLAB modules were developed to perform pre-processing of the input and post-processing the analysis output. These modules significantly increase the accessibility of EACD3D-08 by providing the user with a rational way to set up the analysis model, run the analysis, and gain easy access to the output data in the user-friendly MATLAB interface. The resulting EACD3D-08 model, shown in Figure 5.6, includes 800 solid elements for the dam, the FE mesh for the irregular part of the fluid domain, and the boundary element mesh at the dam–foundation rock interface.

Material damping in the substructure method is modeled by rate-independent, constant hysteretic damping [Chopra 2012b] defined by the damping factors $\eta_s = 0.02$ and $\eta_f = 0.04$ specified for the dam and foundation rock separately; these correspond to viscous damping ratios of ζ_s = 1% and ζ_f = 2% at all frequencies. A numerical investigation confirmed that the damping in the direct FE method, as defined earlier, is adequately consistent with this rate-independent damping over the frequency range of interest. Because EACD3D-08 does not consider water–foundation rock interaction, this is also excluded in the direct FE method for these validation analyses to allow for a meaningful comparison.

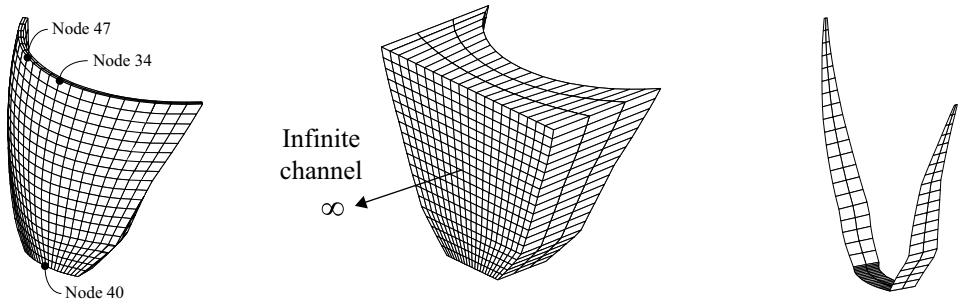

Figure 5.6 **EACD3D-08 model for Morrow Point Dam: (a) FE model for dam; (b) FE model for semi-unbounded fluid domain; and (c) boundary element mesh for foundation rock at dam–canyon interface.**

5.2.3 Frequency Response Functions for Dam Response

Results for the dam response are presented in the form of dimensionless frequency response functions that represent the amplitude of radial acceleration at the crest of the dam due to unit harmonic, free-field motion; the actual location at the dam crest is selected at node 34 (which is the center node) for upstream and vertical ground motions, and at node 47 for cross-stream motion. These frequency response functions are determined in the direct FE method from time-domain analysis of the FE model (Figure 5.5) subjected to effective earthquake forces $\mathbf{P}_f^0$ and $\mathbf{P}_r^0$ computed from the procedures summarized in Boxes 4.1 and 4.3 at the bottom and side boundaries of the foundation rock and Box 4.4 at the upstream fluid boundary, respectively. The free-field control motion, $a_g^k(t)$, is specified at the control point at the foundation surface as a long sequence of unit harmonics with gradually increasing frequency. Details of this procedure are provided in Appendix C.

Implemented in the frequency domain, the substructure method directly provides frequency response functions. The earthquake excitation is here defined by the free-field motion at the dam–canyon interface. To determine this motion consistent with the specified control motion $a_g^k(t)$, a direct FE analysis is implemented of the foundation domain without the dam or impounded water (Figure 5.7) subjected to the same boundary forces $\mathbf{P}_f^0$ as described in the preceding paragraph. The motion recorded at the dam–canyon interface is then used as the spatially varying input excitation to the EACD3D-08 analysis.

Frequency response functions obtained by the direct FE and substructure methods for the dam on flexible foundation rock are compared for two cases: empty reservoir and full reservoir in Figures 5.8 and 5.9, respectively. Results for a full reservoir (Figure 5.9) are presented here only for the upstream component of ground motion because limitations in the EACD3D-08 computer program do not allow for a meaningful comparison with the direct FE method for cross-stream and vertical ground motions[†]

The response results obtained by the direct FE method are very close to those from the substructure method. The small discrepancies near some of the resonant peaks (Figure 5.8), and at frequencies higher than approx. 15 Hz (Figure 5.9), are primarily caused by reflections from the viscous-damper boundaries, which are incapable of perfectly absorbing all scattered waves. Such errors will generally decrease with larger domain sizes. The good agreement demonstrates the ability of the direct FE method to model the factors important for earthquake analysis of arch dams: dam–water–foundation rock interaction including water compressibility and wave absorption at the reservoir boundaries, radiation damping in the semi-unbounded foundation and fluid domains, and the earthquake excitation defined by the control motion at the surface of the foundation rock.

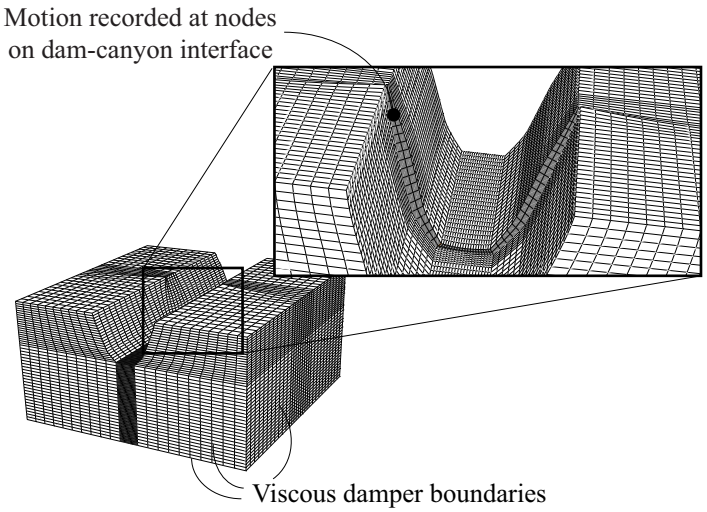

Figure 5.7 **Finite-element model of foundation domain to compute free-field motion at dam–canyon interface used as input to EACD3D-08 analysis.**

[†] EACD3D-08 requires the user to specify the earthquake excitation to the fluid domain directly at the reservoir boundaries, but restricts this motion to be uniform in the upstream direction [Wang and Chopra 2008]. These assumptions cannot be reproduced exactly in the direct FE method. For stream ground motion, however, the issue is avoided when the reservoir boundaries are uniform in the upstream direction [Figure 5.5(b)], thus implying that no hydrodynamic pressures are generated at these boundaries by the stream component of ground motion.

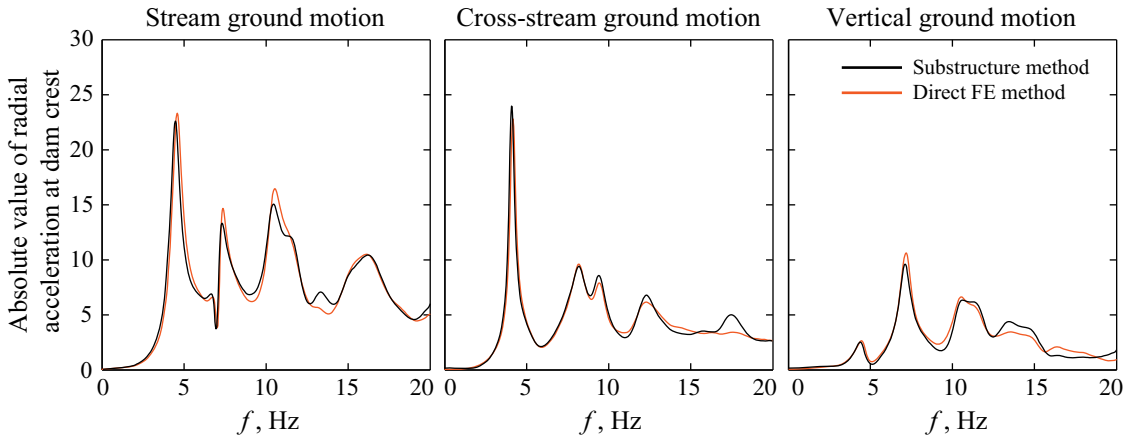

Figure 5.8 **Frequency response functions for the amplitude of radial acceleration at the crest of Morrow Point dam including dam–foundation rock interaction (empty reservoir) due to stream, cross-stream and vertical ground motions. Results are computed by direct FE method and substructure method.**

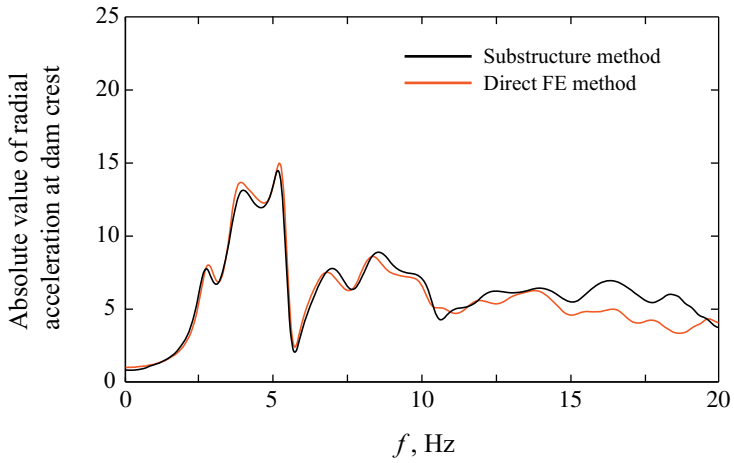

Figure 5.9 **Frequency response functions for the amplitude of radial acceleration at the crest of Morrow Point dam including dam–water–foundation rock interaction (full reservoir) due to stream ground motion. Results are computed by direct FE method and substructure method.**

5.2.4 Response to Transient Motion

To demonstrate the ability of the direct FE method to accurately compute the response of the arch dam–water–foundation rock system to earthquake excitation, the system is analyzed with the free-field control motion in the stream direction, $a_g^x(t)$, defined by the S69E component of the Taft ground motion. The radial displacements and accelerations at the crest of the dam

relative to the base of the dam (node 40) are presented in Figure 5.10 and envelope values of maximum tensile arch and cantilever stresses on the upstream face of the dam in Figure 5.11. The results from the direct FE method closely match those from the substructure method: the displacements and accelerations at the crest show a near perfect match, and the envelope stress values are also close. The small discrepancies in the stress contour plots were found to be caused by differences in the FE stress recovery algorithms in the two computer programs. The effectiveness of the direct FE method is apparent from the fact that these excellent results (Figures 5.8–5.11) are achieved even with relatively moderate domain sizes: the overall dimensions of the FE model are approx. $5H \times 5H \times 3H$, where H is the height of the dam. It is noted that larger domains were required to ensure similar levels of accuracy for 2D analysis of gravity dams; see Appendix A.

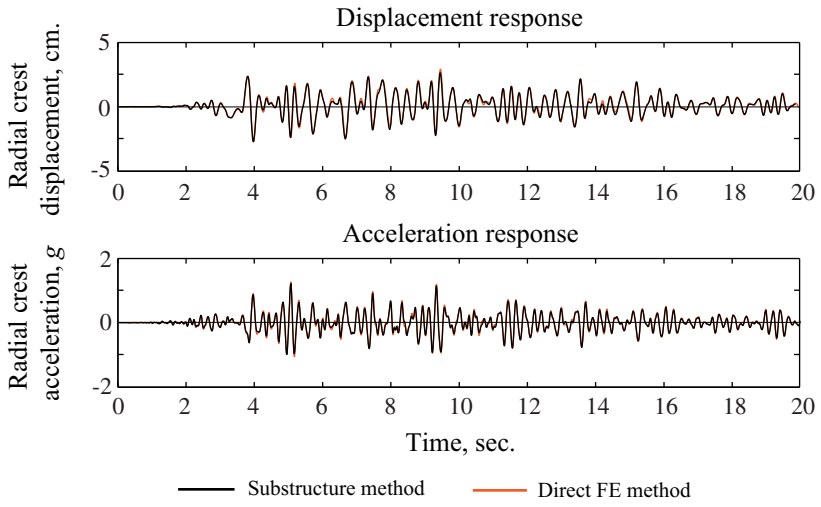

Figure 5.10 **Relative radial displacement and acceleration histories at crest of Morrow Point Dam including dam–water–foundation rock interaction due to S69E component of Taft ground motion applied in the stream direction; static displacements are excluded. Results are computed by direct FE and substructure methods.**

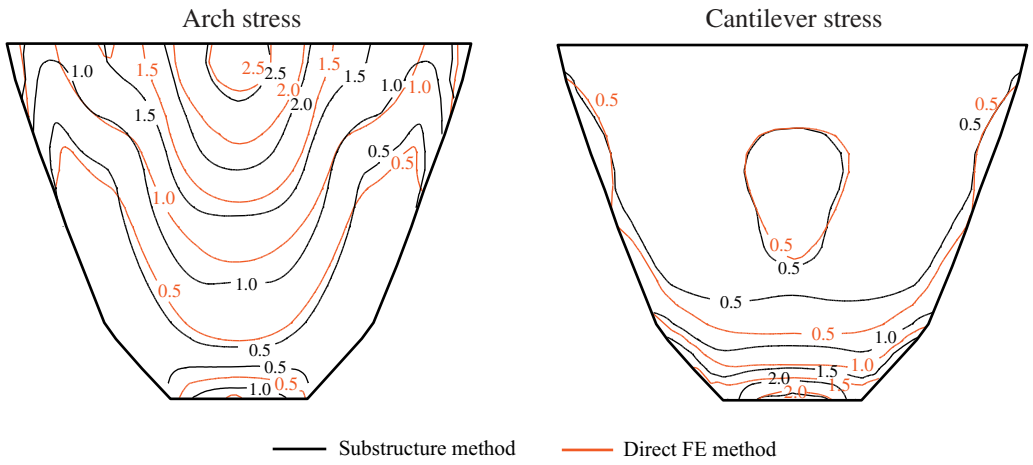

Figure 5.11 **Envelope values of maximum tensile stresses, in MPa, on upstream face of Morrow Point Dam including dam–water–foundation rock interaction due to S69E component of Taft ground motion applied in the stream direction; static stresses are excluded. Results are computed by direct FE and substructure methods.**

The direct FE analyses were implemented in OpenSees on a local workstation (without parallel processing capabilities) using a set of MATLAB scripts to perform the data management for computing and applying effective earthquake forces. The CPU time required to determine the dynamic response of the FE model in Figure 5.5 with roughly 150 000 DOFs was 68 minutes; approximately 13 minutes were required for the auxiliary analyses to set up the effective earthquake forces and 55 minutes for the (linear) dynamic analysis of the dam–water–foundation rock system. The computational effort required to determine the effective earthquake forces for the system is small compared to the time required for dynamic analysis of the overall system. Clearly, it is negligible compared to the time required to perform a more sophisticated nonlinear dynamic analysis of such systems.

5.3 FREQUENCY RESPONSE FUNCTIONS FOR SPATIALLY UNIFORM MOTION

Now that the direct FE method has been validated for the "actual" Morrow Point dam model, it is tested over a wide range of parameters that characterize the properties of the dam, foundation rock, and reservoir bottom materials: E_s, E_f / E_s, and α. For each of the analysis cases in Table 5.1, frequency response functions for the radial acceleration at the crest of the dam (relative to the base of the dam) were computed under the assumption that the free-field

earthquake motion is spatially uniform at the dam–foundation and water–foundation interfaces. This assumption is introduced for two reasons: (1) it facilitates a focused evaluation of the ability of the viscous-damper boundaries to model the semi-unbounded domains; and (2) it circumvents the aforementioned limitation in EACD3D-08 when specifying spatially varying motion in the substructure method (see footnote in Section 5.2.3).

The spatially uniform ground motion at the dam–foundation and water–foundation interfaces is directly input in the substructure method. In the direct FE method, an alternative procedure for seismic input is implemented to achieve such uniform ground motion wherein a different set of effective earthquake forces are computed directly from the uniform ground motion and applied to the dam nodes and to the dam–water and water–foundation interfaces; see Appendix D for details.

Table 5.1 Cases of dam–water–foundation rock system analyzed.

Case	Dam concrete		Foundation rock			Impounded water	
	E_s (GPa)	ζ_s	Condition	E_f / E_s	ζ_f	Condition	α
1	any†	3%	rigid	∞	-	empty	-
2	34.5	1%	flexible	1/2	2%	empty	-
3	34.5	1%	flexible	1	2%	empty	-
4	34.5	1%	flexible	2	2%	empty	-
5	any†	3%	rigid	∞	-	full	0.50
6	any†	3%	rigid	∞	-	full	0.80
7	34.5	1%	flexible	1	2%	full	0.50
8	34.5	1%	flexible	1	2%	full	0.80

5.3.1 Dam on Rigid Foundation

Computed by the two methods, frequency response functions for the dam supported on rigid foundation with empty reservoir (Case 1 in Table 5.1) are presented in Figure 5.12. Results are plotted against the dimensionless frequency ω / ω_1, where ω_1 is the fundamental frequency of the dam alone on rigid foundation. The close agreement between the two set of results demonstrates the equivalency of the computational models employed in the direct FE (OPENSEES) and substructure (EACD3D-08) methods are equivalent, and validates the time-domain procedure for computing frequency response functions in the direct FE method.

† When plotted against the normalized frequency ω / ω_1, these results are valid for all values of E_s.

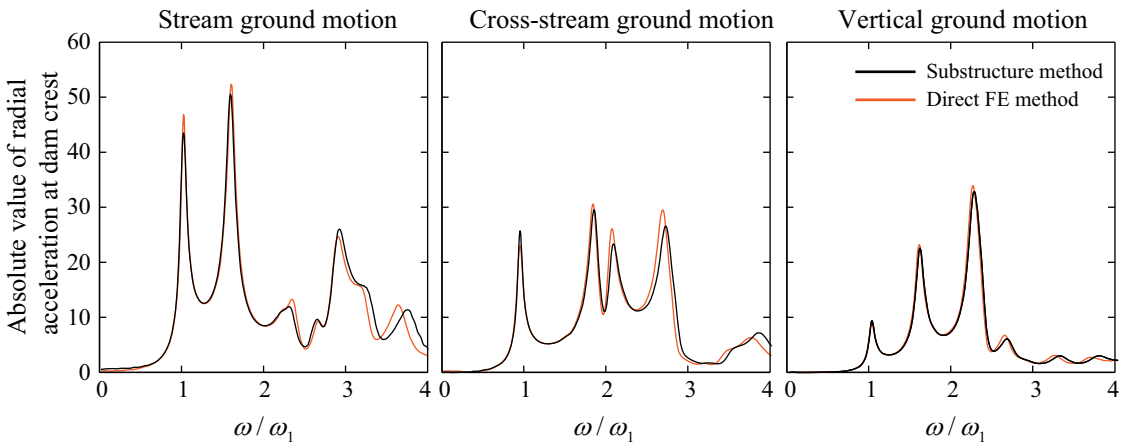

Figure 5.12 **Frequency response functions for the amplitude of relative radial acceleration at the crest of Morrow Point Dam supported on rigid foundation with empty reservoir due to uniform stream, cross-stream and vertical ground motions (Case 1 in Table 5.1). Results are computed by direct FE and substructure methods.**

5.3.2 Dam–Foundation Rock System

The frequency response functions for the dam on flexible foundation rock with empty reservoir obtained by the direct FE and substructure methods are compared in Figure 5.13 for several values of E_f / E_s (Cases 2 to 4 in Table 5.1). The close agreement between the two set of results demonstrates the ability of the direct FE method to model the semi-unbounded foundation domain including radiation damping. The discrepancies observed near some of the resonance peaks are caused by reflections from the viscous-damper boundaries, which are unable to perfectly absorb all scattered waves. Because the accuracy of these boundaries generally improves for higher values of the ratio r / λ, where r is the distance from the dam to the boundary and λ the wavelength of the scattered waves [Wolf 1988], such errors are more prominent for stiff foundations (longer wavelengths) than soft foundations.

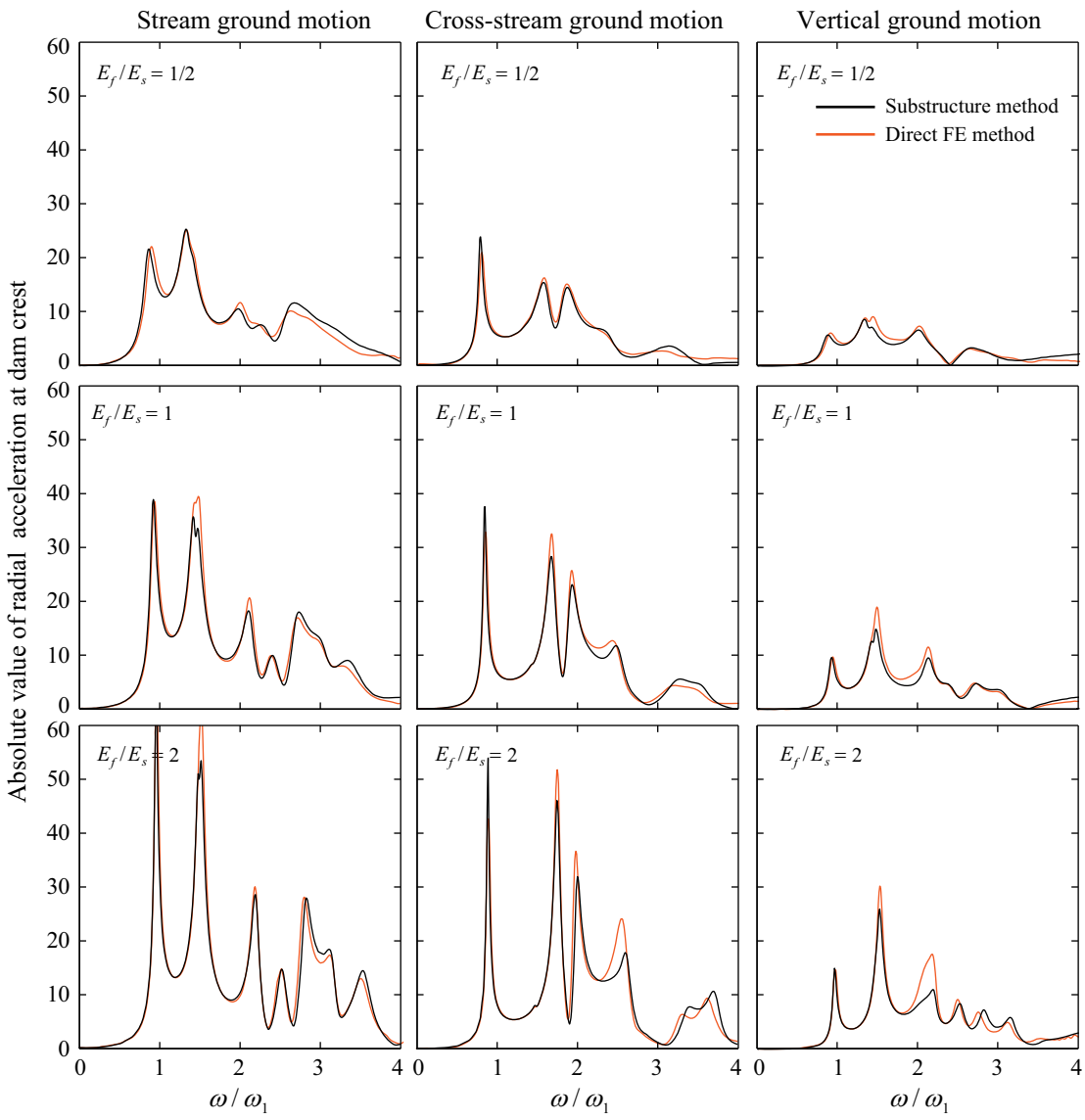

Figure 5.13 **Frequency response functions for the amplitude of relative radial acceleration at the crest of Morrow Point Dam supported on flexible foundation rock with empty reservoir due to uniform stream, cross-stream and vertical ground motions. Results computed by direct FE and substructure methods are presented for three values of the moduli ratio E_f / E_s (Cases 2 to 4 in Table 5.1).**

5.3.3 Dam–Water System

The frequency response functions for the dam on rigid foundation with full reservoir obtained by the two methods are presented in Figure 5.14 for two values of the wave-reflection coefficient α (Cases 5 and 6 in Table 5.1). In the direct FE method, effective earthquake forces $\mathbf{P}_r^0$ are computed by the procedure summarized in Box 4.4 and applied to the fluid boundary Γ_r. The results from the direct FE method closely match those from the substructure method for both values of α, thus validating the ability of the direct FE method to model the semi-unbounded fluid domain and water compressibility, reservoir bottom absorption, and radiation damping in the fluid.

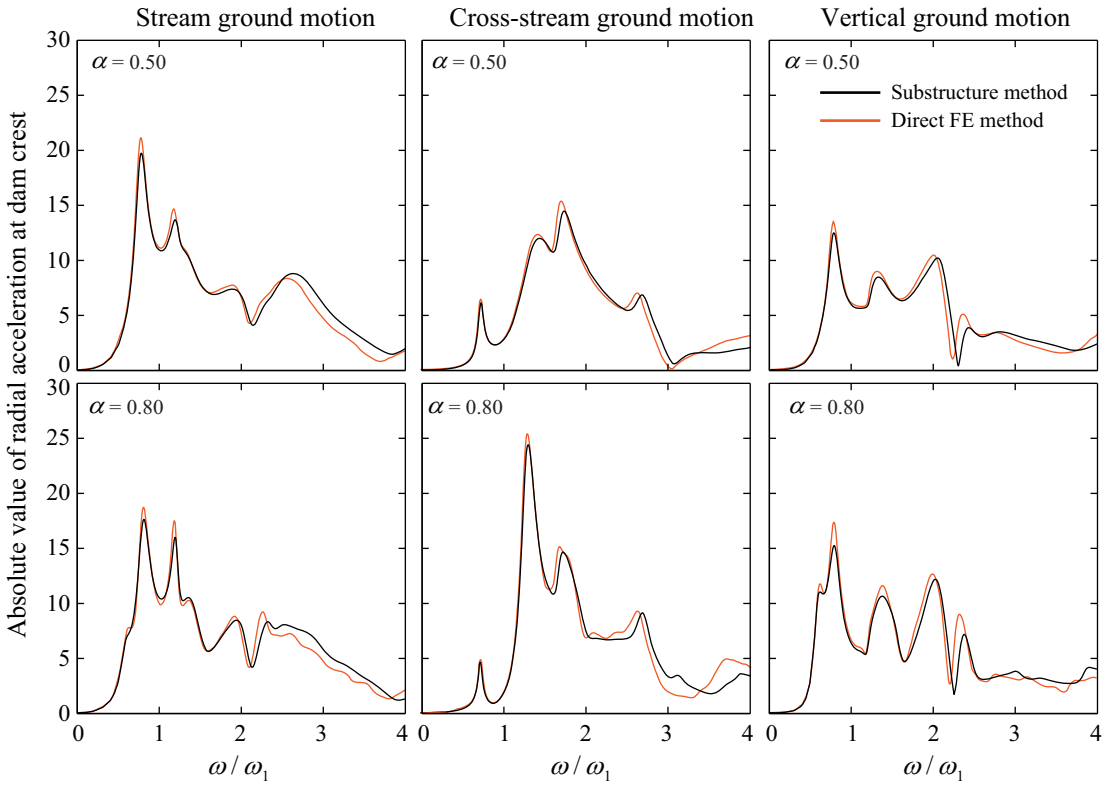

Figure 5.14 **Frequency response functions for the amplitude of relative radial acceleration at the crest of Morrow Point Dam supported on rigid foundation with full reservoir due to uniform stream, cross-stream, and vertical ground motions. Results computed by direct FE and substructure methods are presented for two values of the wave-reflection coefficient α (Cases 5 and 6 in Table 5.1).**

5.3.4 Dam–Water–Foundation Rock System

The frequency response functions for the dam on flexible foundation rock with full reservoir obtained by the two methods are compared in Figure 5.15 for two values of the wave-reflection coefficient α (Cases 7 and 8 in Table 5.1). The close agreement demonstrates that the direct FE method with viscous-damper boundaries is able to accurately model the dam–water–foundation rock system with semi-unbounded subdomains and all its interaction effects. As mentioned previously, the small discrepancies are due to the approximate nature of the viscous dampers, and will generally decrease with larger domain sizes.

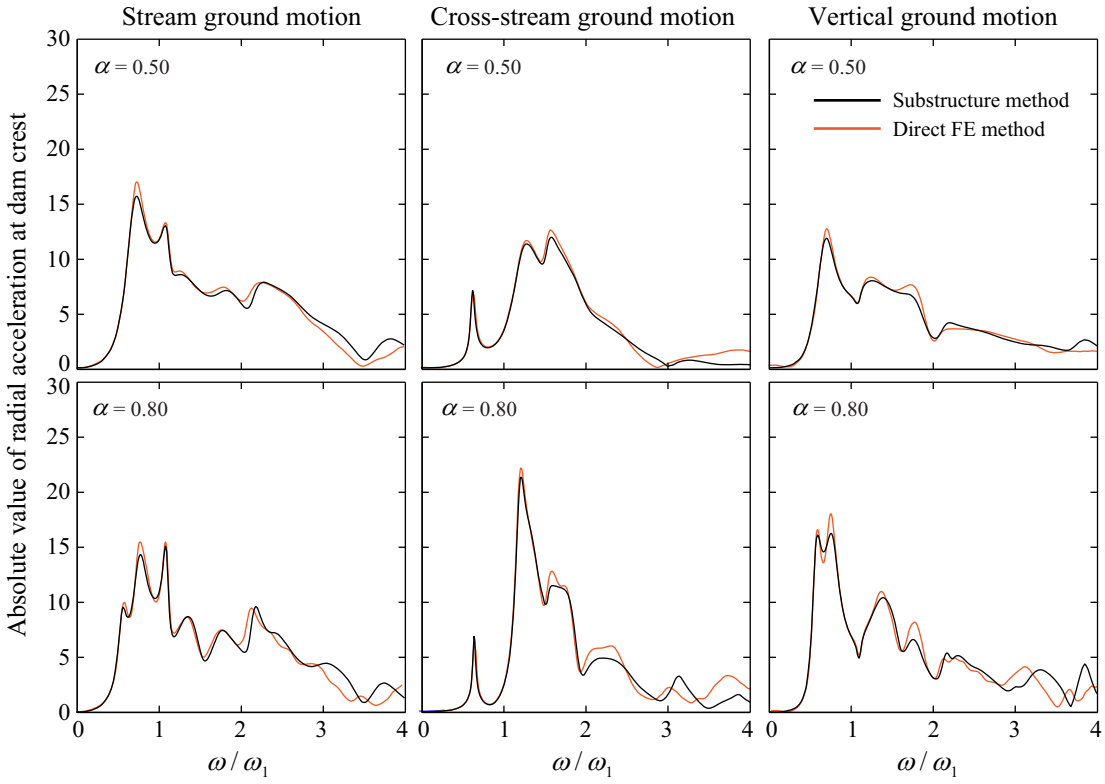

Figure 5.15 **Frequency response functions for the amplitude of relative radial acceleration at the crest of Morrow Point Dam supported on flexible foundation rock with full reservoir due to uniform stream, cross-stream, and vertical ground motions. Results computed by direct FE and substructure methods are presented for two values of the wave-reflection coefficient α (Cases 7 and 8 in Table 5.1).**

6 Simplifications of the Direct-Finite Method

The procedures summarized in Boxes 4.1–4.4 for computing effective earthquake forces are conceptually straightforward; however, they require up to 24 auxiliary analyses for the foundation rock (eight analyses for each component of ground motion), and two auxiliary analyses for the fluid domain (one analysis each for vertical and cross-stream components). Substantial amounts of data management and "book-keeping" is required when using these procedures to analyze 3D models, which may have tens of thousands of boundary nodes. The next section presents simplifications to the direct FE method that drastically reduces these requirements, with the goal of simplifying the practical implementation of the analysis procedure.

6.1 USING ONE-DIMENSIONAL ANALYSIS TO COMPUTE EFFECTIVE EARTHQUAKE FORCES AT SIDE FOUNDATION BOUNDARIES

The use of a combination of 1D and 2D analyses to compute effective earthquake forces $\mathbf{P}_f^0$ at the side boundaries of the foundation domain is necessary to satisfy the general requirement in soil–structure interaction analyses that any admissible free-field system must be identical to the actual system in the region exterior to the absorbing boundaries [Wolf 1988; Bielak et al. 2003] Given this requirement, it is reasonable to expect that even a much simpler system that technically violates this requirement could give accurate results provided the foundation domain is sufficiently large. This is normally the situation in the direct FE method with viscous-damper boundaries, because these always require large domain sizes to ensure acceptable modeling of the semi-unbounded foundation rock.

To test this hypothesis, the actual free-field foundation-rock system shown in Figure 4.2(a) is replaced by a much simpler system shown in Figure 6.1(a): a flat foundation box with homogeneous (or horizontally layered) material properties, implying that the effects of the

canyon are ignored in the free-field analysis. This simplification is especially attractive because analysis of this 3D flat box to vertically propagating seismic waves reduces to analysis of the simple 1D column of foundation-rock elements shown in Figure 6.1(b).

Analysis of the 1D system of Figure 6.1(b), discretized to match the elevations of the boundary nodes in the main model, subjected to the forces of Equation (4.1) at the base provides the motion $\mathbf{r}_f^0$ at every node along the height. Alternatively, $\mathbf{r}_f^0$ may be extracted at every elevation directly from the deconvolution analysis. Boundary tractions are computed from $\mathbf{r}_f^0$ using stress-strain relationships for a 1D system (see Appendix E) and converted to nodal forces for the FE model by multiplying by the tributary area of each node. The analysis is repeated for each component of ground motion (x, y, z) considered in the analysis. Step-by-step instructions for implementation of the procedure are presented in Box 6.1.

Such a 1D free-field analysis is drastically simpler compared to the rigorous procedure developed in Section 4.2.2 that required 24 auxiliary analyses and extensive data transfer; however, because the assumed system in Figure 6.1(a) is not identical to the actual system in the region exterior to the absorbing boundary, it will introduce errors in the solution. The resulting errors in the free-field response at the center of the semi-cylindrical canyon (Figure 5.3) are shown in Figure 6.2, where results obtained by the direct FE method using 1D and 3D free-field analyses to compute effective earthquake at the side boundaries are compared.

The displacements at the canyon surface computed by the two methods (Figure 6.2) are reasonably close for all types of incident waves and for a wide range of dimensionless frequencies η, thus suggesting that using 1D analysis to compute effective earthquake forces may be an acceptable approximation for this system. Later in this section, this approximation will be examined in the context of dam response. In part, the good agreement in Figure 6.2 is achieved because the foundation domain is sufficiently large: typical dimensions for a dam model (700 m × 700 m × 400 m) was used relative to a canyon radius of R = 100 m, thus ensuring sufficient distance from the center of the model to the side boundaries where the effective earthquake forces are applied. For a much smaller domain (200 m × 400 m × 400 m), the resulting errors are considerably larger, as shown in Figure 6.3.

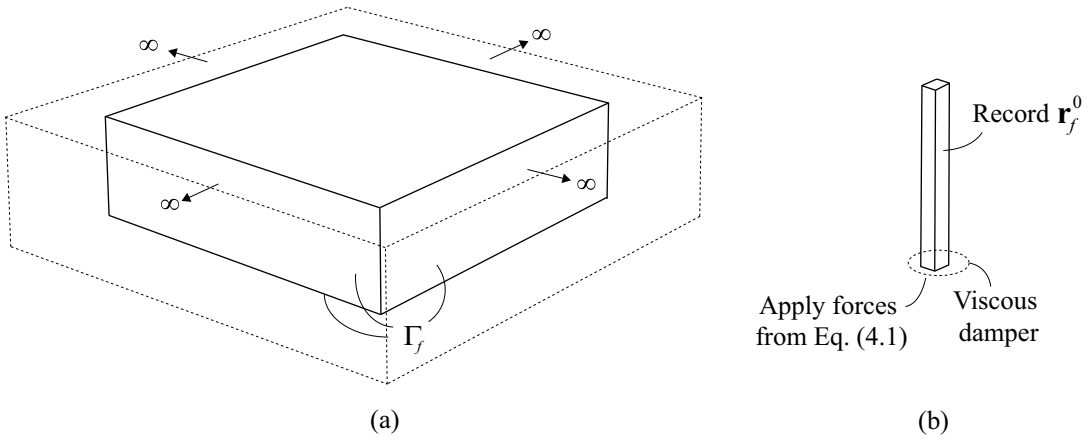

Figure 6.1 **(a) Free-field foundation-rock system without canyon; and (b) analysis of single column of foundation-rock elements to compute $\mathbf{r}_f^0$.**

The accuracy of using the simplified 1D free-field analysis when determining the dynamic response of concrete dams by the direct FE method is investigated by analyzing Morrow Point Dam (Figure 5.5). Frequency response functions for the amplitude of radial acceleration at the crest of the dam supported on flexible rock with empty reservoir are presented in Figure 6.4, where results obtained using 1D and 3D free-field analysis to compute effective earthquake forces are compared. The closeness of the two sets of results justifies the use of 1D free-field analysis to compute effective earthquake forces for this system.

Box 6.1 Computing effective earthquake forces $\mathbf{P}_f^0$ at side boundaries by 1D free-field analysis.

Determining $\mathbf{r}_f^0$ by analysis of single foundation-rock column

1. Develop a FE model of the simplified free-field foundation-rock system: a single column of foundation-rock elements with discretization to match the elevations of the boundary nodes in the main model [Figure 6.1(b)].
2. For each direction of ground motion, $k = x, y, z$ add a viscous damper at the base in the *k*-direction and constrain DOFs in the other directions to allow only shear ($k = x, y$) or axial ($k = z$) deformation of the column.
3. Apply effective earthquake forces from Equation (4.1) to the base in the *k*-direction, and compute the motion $\mathbf{r}_f^0$ at each node along the height.

As an alternative to Steps 1–3, the motion $\mathbf{r}_f^0$ may be extracted at every elevation directly from a 1D deconvolution analysis.

Compute effective earthquake forces $\mathbf{P}_f^0$

4. Compute $\dot{\mathbf{r}}_f^0$ as the time derivative of $\mathbf{r}_f^0$.
5. Compute boundary tractions from $\mathbf{r}_f^0$ using 1D stress-strain relations (Appendix E) and multiply them by the tributary area of each node to determine $\mathbf{R}_f^0$.
6. Calculate effective earthquake forces $\mathbf{P}_f^0$ at the side foundation boundaries from Equation (3.7a) using $\dot{\mathbf{r}}_f^0$ from Step 4 and $\mathbf{R}_f^0$ from Step 5.

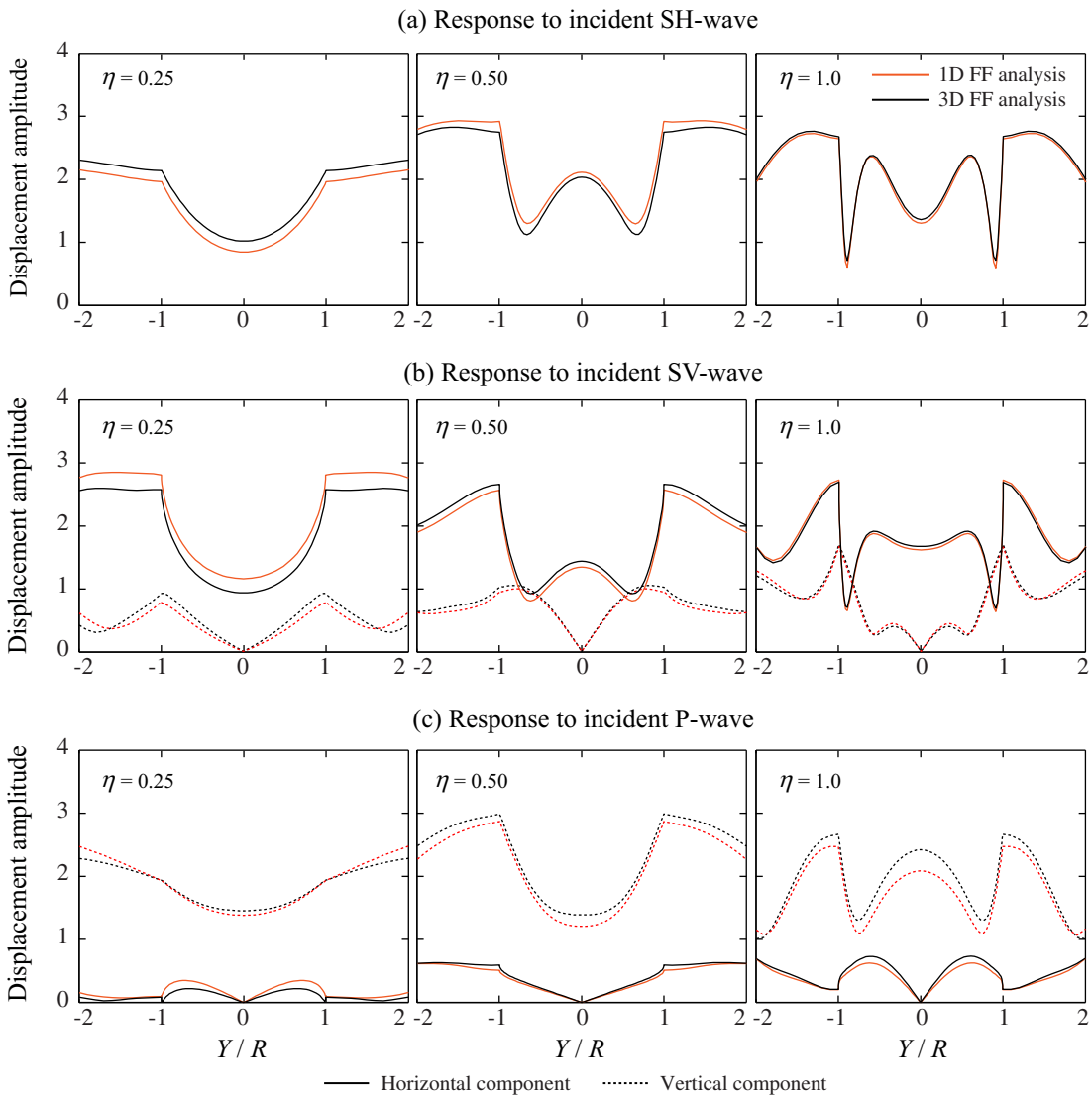

Figure 6.2 **Displacement amplitudes at semi-cylindrical canyon subjected to incident *SH*-, *SV*-, and *P*-waves. Results are computed by the direct FE method with effective earthquake forces $\mathbf{P}_f^0$ on the side boundaries determined from 1D and 3D free-field analyses.**

These results demonstrate that the loss of accuracy from using 1D free-field analysis is insignificant as long as the foundation domain is sufficiently large. As previously mentioned, this requirement is normally satisfied in the direct FE method when employing viscous-damper boundaries because these always require large domain sizes to ensure acceptable modeling of the semi-unbounded foundation domain. Thus, the use of 1D free-field analysis is appropriate for practical analyses in the direct FE method.

This conclusion puts the direct FE method at a significant advantage over previous analysis procedures [Basu 2004] where high-performing PML boundaries were used together with DRM to apply the seismic input. Because the attractiveness of such advanced methods lies in their ability to use very small domain sizes, they are not amenable for using such simplified 1D free-field analysis, and therefore require analysis of complicated 3D systems and extensive data transfer to determine the seismic input.

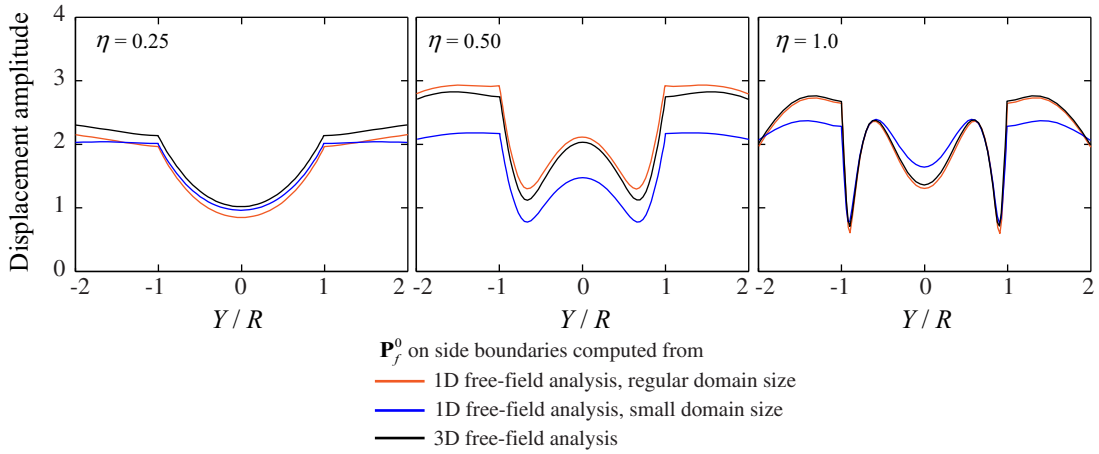

Figure 6.3 **Influence of domain size on the errors in displacement amplitudes at semi-cylindrical canyon subjected to incident *SH*-waves when using 1D free-field analysis to compute effective earthquake forces $\mathbf{P}_f^0$ on the side boundaries.**

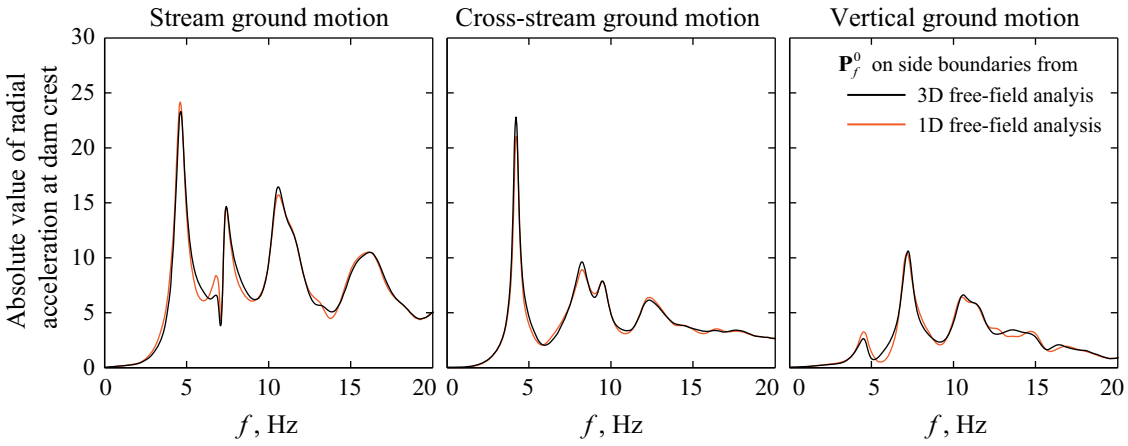

Figure 6.4 **Influence of using 1D free-field analysis to determine effective earthquake forces $\mathbf{P}_f^0$ on the side boundaries on the response of Morrow Point dam on flexible foundation rock with empty reservoir.**

6.2 IGNORING EFFECTIVE EARTHQUAKE FORCES AT SIDE FOUNDATION BOUNDARIES

The dam engineering profession has been using a variation of the direct FE method wherein effective earthquake forces $\mathbf{P}_f^0$ are applied only to the bottom boundary, and not to the side boundaries [Bureau of Reclamation 2013; Curtis et al. 2013; and Cvijanovic et al. 2014]. This approximation is attractive because it eliminates the need for analysis of the free-field foundation-rock system altogether; however, as will be demonstrated, the resulting errors in the dam response can be large.

First observed are the large errors in the free-field motion at the surface of the semi-cylindrical canyon of Figure 5.3 computed by the direct FE method with and without effective earthquake forces applied to the side boundaries. The results are unacceptable for all three types of excitation over a wide range of η-values (Figure 6.5) because, without effective earthquake forces applied to the side boundaries, the viscous dampers boundaries attenuate seismic waves as they propagate up through the model. Some researchers have referred to this effect as *leakage* [Nielsen 2014]. Because this leakage is frequency dependent, it affects the motion at some frequencies (η-values) more than others.

The errors can be reduced by increasing the domain size, i.e., by moving the absorbing boundaries further away from the center of the model. This is demonstrated in Figure 6.6, where results are presented for two domain sizes: the "regular" domain size (700 m × 700 m × 400 m) used in the preceding analyses, and a large domain size, 1400 m × 1400 m × 400 m. Increasing the horizontal dimensions of the foundation domain improves the results, but the errors remain significant even for this large domain.

Frequency response functions for the amplitude of radial acceleration at the crest of Morrow Point Dam supported on flexible foundation rock with empty reservoir are shown in Figure 6.7. Results are computed by the direct FE method with and without effective earthquake forces applied to the side boundaries. As anticipated by the poor agreement in the free-field response at the canyon surface, excluding $\mathbf{P}_f^0$ at the side boundaries cause significant error in the dam response to all components of ground motion.

In light of these results, there seems to be no justification in ignoring the effective earthquake forces on the side boundaries. Computing these forces using the simple 1D free-field

analysis (Box 6.1) requires very little effort, with minimal loss of accuracy compared to the more rigorous 3D free-field analysis summarized in Box 4.3.

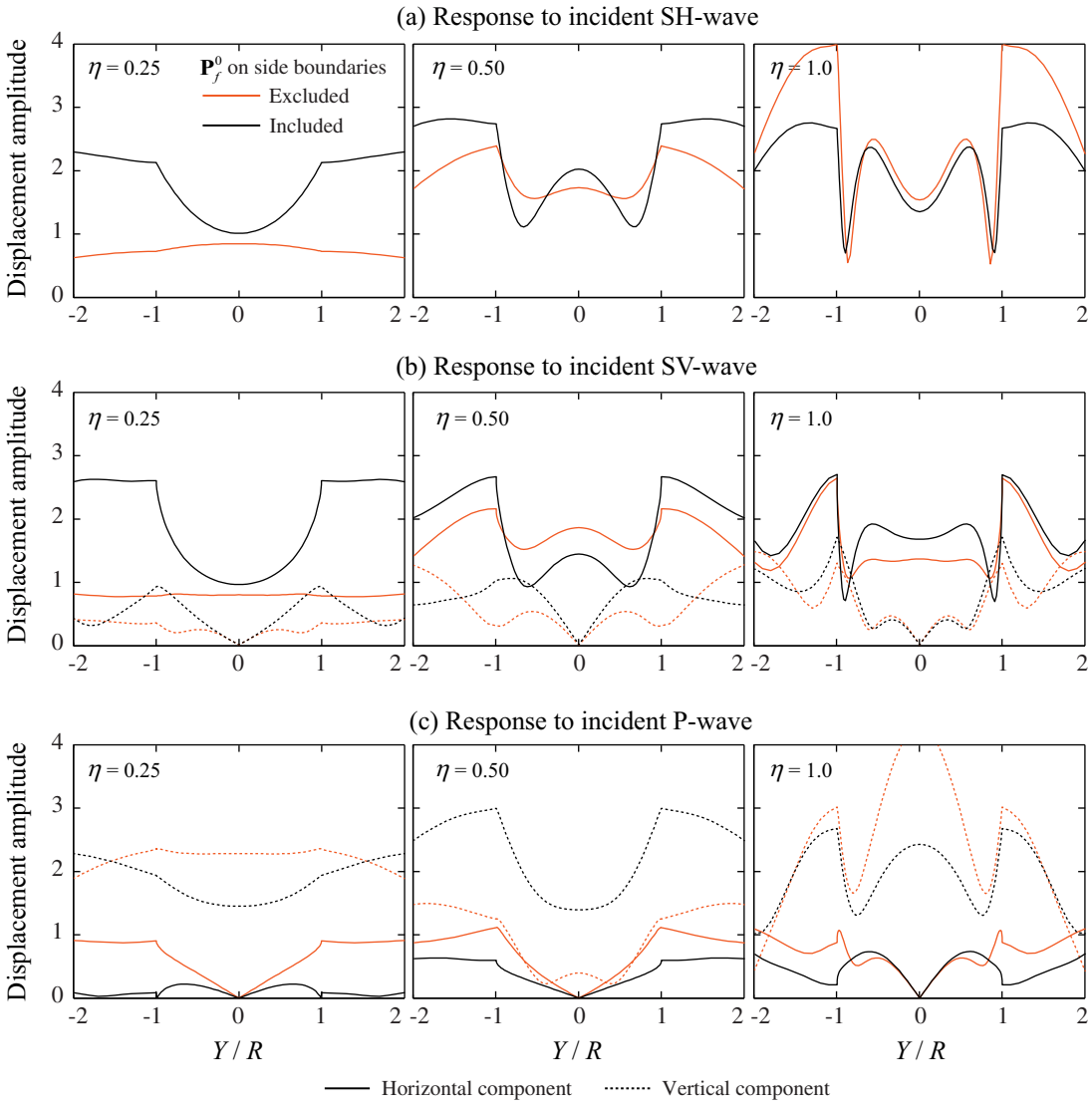

Figure 6.5 **Displacement amplitudes at semi-cylindrical canyon subjected to incident *SH*-, *SV*-, and *P*-waves. Results are computed from two analyses: excluding and including effective earthquake forces $\mathbf{P}_f^0$ on the side boundaries.**

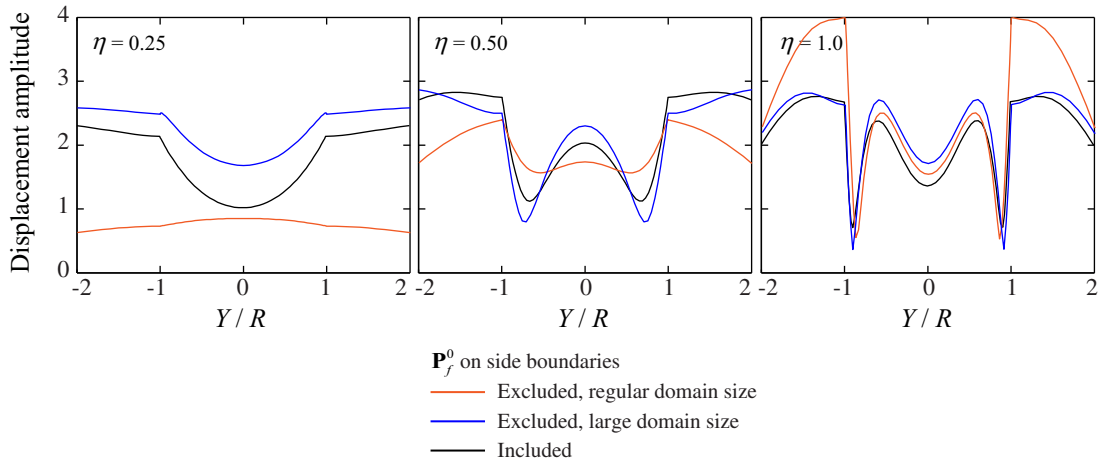

Figure 6.6 **Influence of domain size on the errors in displacement amplitudes at semi-cylindrical canyon subjected to incident *SH*-waves when excluding effective earthquake forces $\mathbf{P}_f^0$ on the side boundaries.**

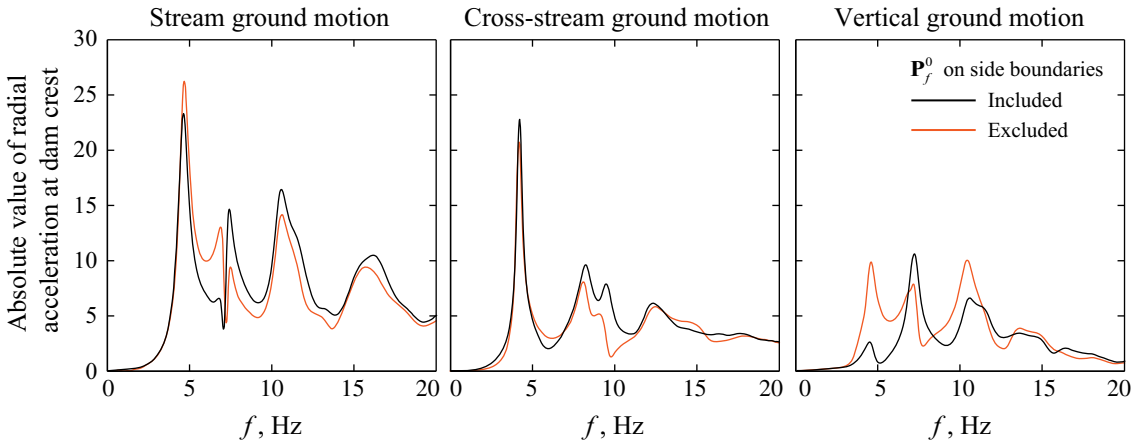

Figure 6.7 **Influence of excluding effective earthquake forces $\mathbf{P}_f^0$ on the side boundaries on the response of Morrow Point dam on flexible foundation rock with empty reservoir.**

6.3 AVOIDING DECONVOLUTION OF THE SURFACE CONTROL MOTION

Some researchers have avoided deconvolution of the specified surface control motion $a_g^k(t)$ by idealizing the foundation as a homogeneous, undamped, half-space [Zhang et al. 2009; Robbe et al. 2017]. In this special case, a vertically propagating plane wave does not attenuate, implying that the incident earthquake motion at the bottom boundary, $\mathbf{r}_I^0$, is equal to one-half the specified

surface motion, except for a time shift. The validity of this assumption for different foundation idealizations is investigated next.

A flat foundation box (Figure 5.1) is first analyzed by the direct FE method and the computed surface motions are compared against the specified control motion. Effective earthquake forces at the bottom and side boundaries are computed using two methods for obtaining the incident motion $\mathbf{r}_I^0$ at the bottom boundary: "rigorous" deconvolution of the surface control motion and one-half the surface control motion. Such comparison is presented in Figure 6.8 for three different foundation idealizations[†]: (a) homogeneous foundation with zero material damping; (b) homogeneous foundation with 4% material damping; and (c) horizontally layered foundation with zero material damping. For all three cases, the free-field control motion $a_g^k(t)$ is defined at the surface in the two horizontal and vertical directions by the S69E, S21W, and vertical component of the Taft ground motion, respectively.

Observe from the results in Figure 6.8 that when the incident motion $\mathbf{r}_I^0$ is determined by deconvolution of the surface control motion, the computed surface motion is essentially identical (to within FE discretization error) to the specified control motion for all three foundation idealizations. In contrast, specifying $\mathbf{r}_I^0$ as one-half the surface control motion gives essentially the exact results if the foundation is homogeneous and undamped [Figure 6.89a)], but leads to significant underestimation of the surface motion for a damped foundation [Figure 6.8(b)] and overestimation for a layered foundation [Figure 6.8(c)]. These results suggests that dam response would be accurately computed with $\mathbf{r}_I^0$ taken as one-half the surface control motion only if the foundation domain is homogeneous and undamped, but that errors will be introduced for other cases.

Frequency response functions for the amplitude of radial acceleration at the crest of Morrow Point Dam including dam–foundation interaction (empty reservoir) are presented in Figure 6.9 for two cases: (a) homogeneous foundation with zero material damping; and (b) homogeneous foundation with 4% material damping. For both cases, results obtained with $\mathbf{r}_I^0$ computed by deconvolution and as one-half the surface control motion are compared. As

[†] The material properties for the foundation are: density = 2723 kg/m^3 and Poisson's ratio = 0.20. The homogeneous foundation (Cases a and b) has shear wave velocity V_s = 2000 m/sec. The layered foundation (Case c) consists of three layers of equal thickness 133 m on top of homogenous bedrock, with shear-wave velocities that increase with depth: $V_{s,1}$ = 1500 m/sec, $V_{s,2}$ = 2000 m/s, $V_{s,3}$ = 2500 m/sed, and $V_{s,bedrock}$ = 3000 m/sec.

expected by the results shown in Figure 6.8, specifying $\mathbf{r}_I^0$ as one-half the surface control motion does not introduce error in dam response when the foundation is undamped [Figure 6.9(a)], but causes significant underestimation of the response for foundations with damping [Figure 6.9(b)].

To eliminate such errors, the incident motion $\mathbf{r}_I^0$ at the bottom foundation boundary should be computed by 1D deconvolution analysis. There is little justification in bypassing such analysis, especially because it is straightforward and requires very little computational effort compared to 3D analysis of the dam–water–foundation system.

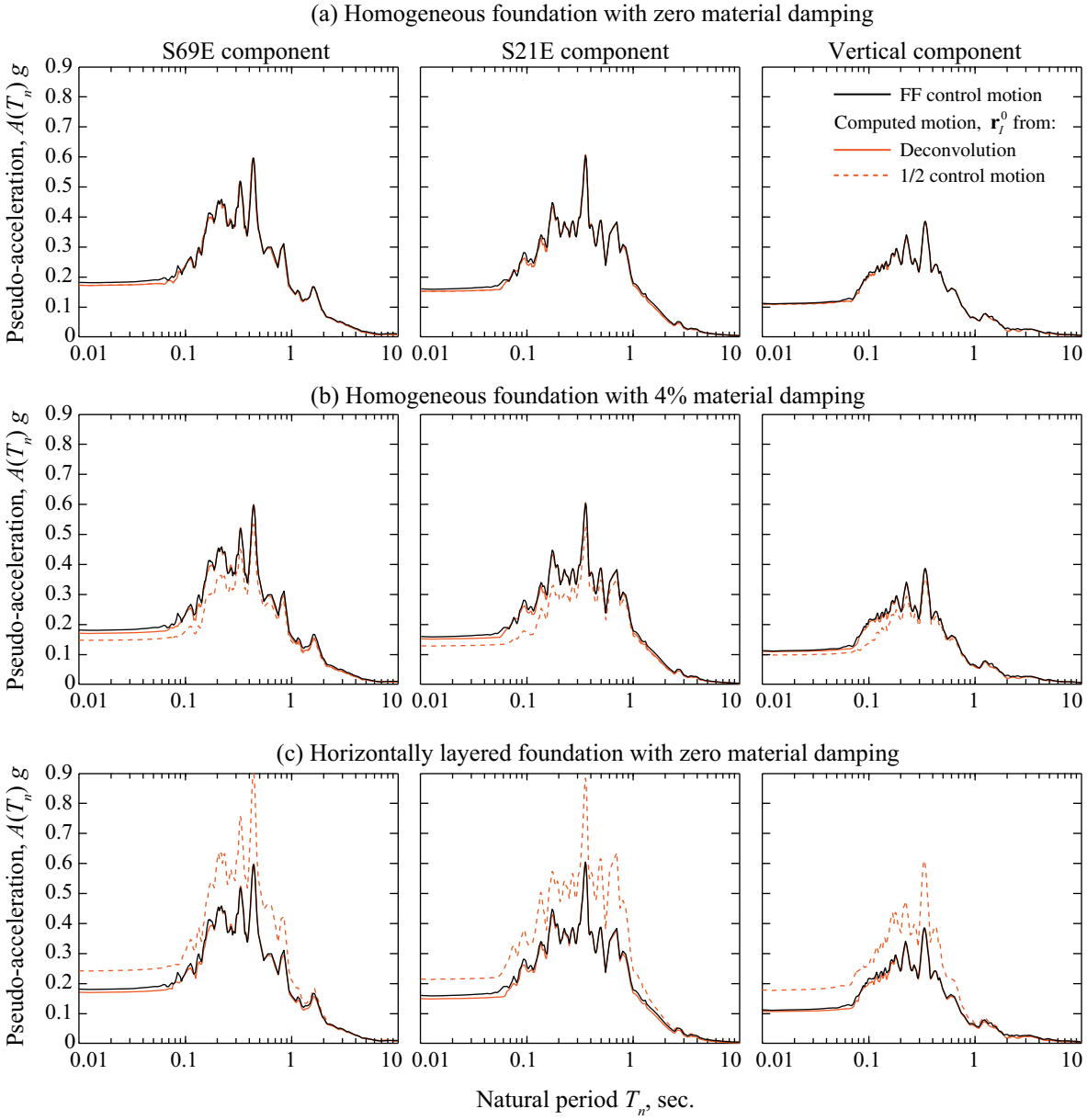

Figure 6.8 **Comparison of 5% damped pseudo-acceleration response spectra for specified free-field control motion and motion computed at the surface of flat foundation box for three foundation idealizations. Results obtained with $\mathbf{r}_I^0$ computed from deconvolution and as one-half the surface control motion are compared.**

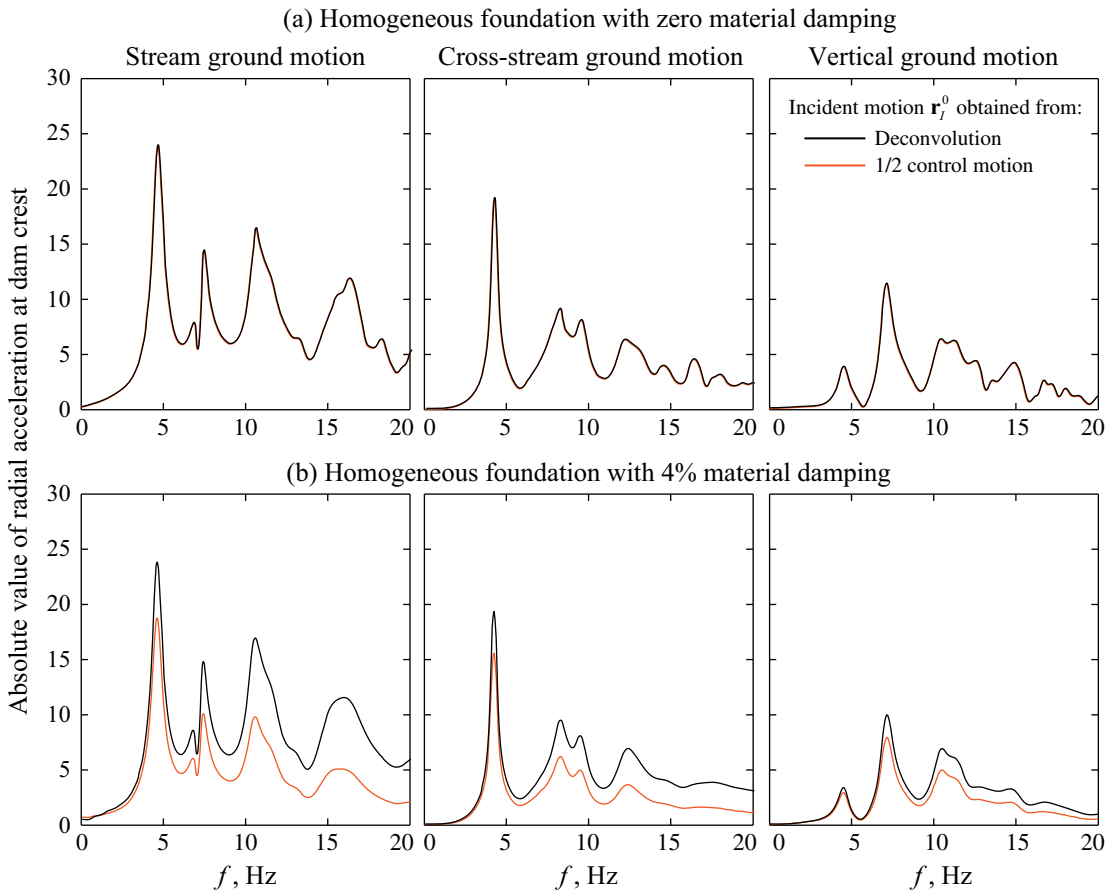

Figure 6.9 **Discrepancies introduced by approximating $\mathbf{r}_I^0$ as one-half the surface control motion on the response of Morrow Point Dam including dam–foundation interaction (reservoir is empty) for two foundation idealizations.**

6.4 IGNORING EFFECTIVE EARTHQUAKE FORCES ON UPSTREAM FLUID DOMAIN BOUNDARY

Implementation of the direct FE method may be simplified by excluding effective earthquake forces $\mathbf{P}_r^0$ at the upstream fluid boundary Γ_r, which are the forces associated with earthquake-induced hydrodynamic pressures in the semi-unbounded fluid channel upstream of Γ_r. This is attractive because it eliminates the need for the 2D auxiliary analysis of the fluid cross section (Section 4.3) for vertical and cross-stream components of ground motion

Presented in Figure 6.10 are frequency response functions for the radial acceleration at the crest of Morrow Point Dam on rigid foundation with full reservoir subjected to ground motions that are uniform at the dam–foundation and water–foundation interfaces for two values

of the wave reflection coefficient characterizing sediment absorption[†]: α = 0.50 and α = 0.80. Results from three analyses are presented for each α-value: (1) fluid domain length of $L = 2.5H$ including $\mathbf{P}_r^0$ on the upstream fluid boundary; (2) $L = 2.5H$ excluding $\mathbf{P}_r^0$; and (3) $L = 5H$ excluding $\mathbf{P}_r^0$. Excluding $\mathbf{P}_r^0$ for cross-stream and vertical ground motions has little influence on the response for α = 0.50, but leads to errors for higher α–values (α = 0.80) and short fluid domains ($L = 2.5H$). For the stream component of ground motion, $\mathbf{P}_r^0 = \mathbf{0}$ (Section 4.3), so all three cases give essentially identical results.

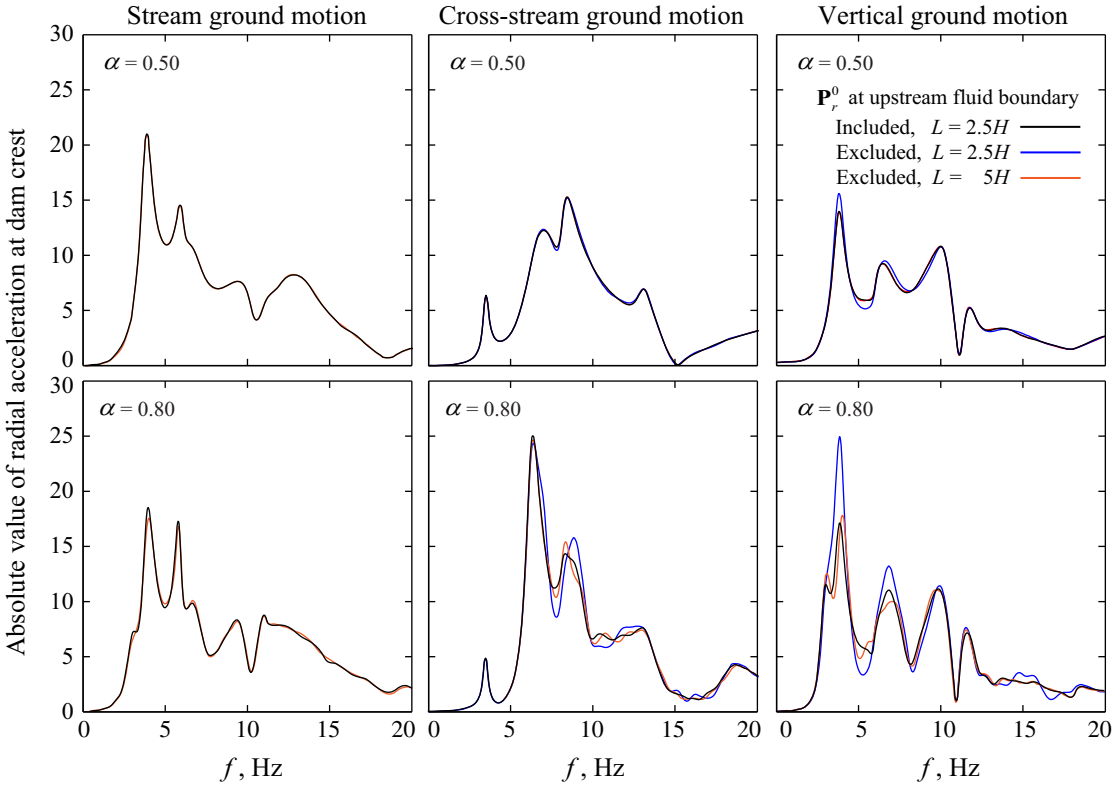

Figure 6.10 **Influence of excluding effective earthquake forces $\mathbf{P}_r^0$ on the upstream fluid boundary on the response of Morrow Point dam on rigid foundation with full reservoir. Results are presented for two values of the wave-reflection coefficient: α = 0.50 and α = 0.80. ζ_s = 3% damping is specified for the dam alone.**

[†] Sediments are included herein only for the purpose of introducing some energy absorption at the reservoir boundaries in the absence of dam–foundation and water–foundation interaction mechanisms in this system with rigid foundation.

These discrepancies occur because of the idealization of the system analyzed (Figure 2.1): the uniform fluid channel is unbounded in the upstream direction and the excitation is implicitly assumed to extend along the entire length of this channel. In reality, neither the uniform fluid channel nor the ground motion could extend to infinity in the upstream direction, so excluding $\mathbf{P}_r^0$ from the analysis, which implies that the excitation stops at the boundary Γ_r, seems to be a more appropriate idealization. Thus, it can be concluded that the errors observed in Figure 6.10 are inconsequential for analysis of actual dams, and that $\mathbf{P}_r^0$ can be left out of the analysis without loss of accuracy as long as the fluid domain is large enough to accurately model dam–water interaction and radiation damping using the viscous-damper boundaries; see Section 5.3.3.

7 Summary of Procedure

The earthquake input for the three-dimensional dam–water–foundation rock system is defined by the free-field ground acceleration $a_g^k(t)$, $k = x, y, z$, specified at a control point on the foundation surface at the level of the dam abutments; see Figure 2.4(c). This motion may for example be from an ensemble of recorded ground motions selected and scaled to "match" a target spectrum, or synthetic motions developed for an earthquake scenario.

By using the recommended simplifications presented in Sections 6.1 and 6.4, analysis of 3D dam–water–foundation rock systems by the direct FE method is organized in three parts: static analysis, linear analyses of the free-field foundation-rock system, and nonlinear dynamic analysis of the dam–water–foundation rock system.

Static analysis:

1. Develop a FE model for static analysis of the dam–foundation rock system with an appropriate material model for the dam concrete and an appropriate (static) model for the semi-unbounded foundation rock.
2. Compute the response of this system to self-weight and hydrostatic forces; for arch dams this may include effects of a staged construction sequence.
3. Record the static state of the dam and foundation rock, including reactions from the foundation rock at the boundary Γ_f.

Linear analysis of the free-field foundation-rock system (using 1D free-field analysis):

4. Obtain the outcrop motion at the base of the foundation-rock model by deconvolution of the surface control motion $a_g^k(t)$.
5. Calculate the effective earthquake forces $\mathbf{P}_f^0$ at the bottom boundary of the foundation domain from the procedure in Box 4.1.

6. Compute the effective earthquake forces $\mathbf{P}_f^0$ at the side boundaries of the foundation domain from the procedure in Box 6.1.

Step 6 may be avoided if free-field boundary elements [Nielsen 2014] are employed at the side boundaries of the truncated foundation domain.

Nonlinear dynamic analysis of dam–water–foundation rock system:

7. Develop a FE model of the dam–water–foundation rock system with viscous-damper boundaries to truncate the semi-unbounded foundation and fluid domains at Γ_f and Γ_r, respectively. Use solid elements for the dam and foundation rock, fluid elements for the water, and interface elements (or tie constraints) at the dam–water and water–foundation rock interfaces. Sediments at the reservoir bottom can be modelled approximately by surface elements based on the 1D absorption model, or by using more sophisticated viscoelastic or poroelastic material models.

8. Calculate the response of this FE model subjected to effective earthquake forces $\mathbf{P}_f^0$ computed in Step 5 at the bottom foundation boundary and in Step 6 at the side boundaries, as well as self-weight, hydrostatic forces and static foundation reactions at Γ_f. The static state of the dam (Step 3) is taken as the initial state in the nonlinear dynamic analysis.

8 Conclusions

The direct FE method developed in Part I of this report for nonlinear earthquake analysis of 2D dam–water–foundation rock systems has been generalized for 3D systems. Formulated by interpreting dam–water–foundation rock interaction as a scattering problem where the dam perturbs a free-field state of the system, the direct FE method considers all the factors important in the earthquake response of arch dams: dam–water interaction including water compressibility and wave absorption at the reservoir boundaries; dam–foundation rock interaction including mass, stiffness and damping in the rock; radiation damping due to the semi-unbounded sizes of the foundation rock and reservoir domains; spatial variation of the ground motions around the dam–canyon interface; and nonlinear behavior in the dam and adjacent parts of the foundation and fluid domains.

The seismic input to the procedure is specified by a ground motion at a control point on the foundation surface. The free-field motion at depth in the foundation rock is determined by deconvolution of this control motion. Then, effective earthquake forces are computed from a set of 1D and 2D analysis and applied to the boundaries of the FE model. Each of these analyses requires very little computational effort and can be implemented without modifying the FE source code, the main challenge is management and transfer of large amounts of data.

Several examples are presented to validate the accuracy of the direct FE method applied to 3D problems. One of these examples compares the dynamic response of Morrow Point Dam computed by the direct FE method with independent benchmark solutions obtained by the substructure method. The excellent agreement achieved for a wide range of analysis cases demonstrates that: (1) the effects of dam–water–foundation rock interaction are accurately modeled; (2) the bounded foundation and fluid models with viscous-damper boundaries are able to simulate the semi-unbounded extent of these domains; and (3) the earthquake excitation is

properly defined by specifying—at the boundaries of the FE model—effective earthquake forces determined from a surface control motion.

To facilitate implementation of the direct FE method, several simplifications of the analysis procedure are proposed and their efficacy evaluated. The presented results led to the following conclusions:

1. Using 1D free-field analysis to compute effective earthquake forces $\mathbf{P}_f^0$ at the side boundaries of the foundation rock, which drastically reduces the amount of data transfer and data management, is an appropriate approximation provided that the foundation domain is sufficiently large. This is normally the case when using viscous-damper boundaries because these already require large domain sizes to model the semi-unbounded foundation domain.

2. In contrast, ignoring the effective earthquake forces $\mathbf{P}_f^0$ at the side boundaries—a popular simplification in the dam engineering profession—can lead to large errors in the dam response. There seems to be no justification in ignoring these forces when they can be included with minimal effort using the simplified 1D free-field analysis.

3. Specifying the incident motion $\mathbf{r}_I^0$ at the bottom foundation boundary as one-half the surface motion—thereby avoiding 1D deconvolution analysis—can cause significant error in dam response for foundations with damping and for layered foundations. To eliminate such errors, the incident motion at the bottom foundation boundary should be computed by 1D deconvolution of the surface control motion.

4. Ignoring the effective earthquake forces $\mathbf{P}_r^0$ at the upstream fluid boundary—implying that the earthquake excitation stops at the fluid boundary—is appropriate for practical analysis as long as the fluid domain is long enough. This is normally the case in the direct FE method because large domains are already required to accurately model dam–water interaction.

The direct FE method is applicable to nonlinear systems, thus allowing for modeling of concrete cracking, as well as sliding and separation at construction joints, lift joints, and at

concrete-rock interfaces. The procedure can be implemented with any commercial FE program that permits modeling of viscous-damper boundaries and specification of effective earthquake forces at these boundaries.

PART III

Modeling and Practical Implementation of the Direct Finite-Element Method for Performance-Based Earthquake Engineering of Concrete Dams

1 Introduction

Performance-based earthquake engineering (PBEE), a framework for seismic design and safety assessments of structures, has been the subject of much research and development since 2000 [Cornell and Krawinkler 2000], and PBEE has been applied to evaluate structures such as buildings, nuclear power plants, and bridges [Porter 2003; Moehle and Deierlein 2004; Goulet et al. 2007; and Zhang et al. 2008]. Much less work has been done on PBEE in the context of concrete dams (with a few notable exceptions, e.g., Hariri-Ardebili [2015]), and most of the conducted research have been focused investigations on developing seismic fragility curves for 2D gravity dam systems [Tekie and Ellingwood 2003; Ghanaat et al. 2012; and Hariri-Ardebili and Saouma 2016a].

One obstacle for the adaption of PBEE by the dam engineering community is the lack of accurate and efficient analysis procedures for conducting the large number of nonlinear response history analyses (RHA) required to quantify the uncertainties in earthquake ground motions and material properties of the system. For years, nonlinear RHA of concrete dams were limited by major deficiencies: overly simplistic models for dam–water–foundation rock interaction, not accounting for radiation damping in the semi-unbounded foundation and fluid domains, and ignoring spatial variation of ground motions along the dam–canyon interface. These limitations were overcome in the direct FE method developed in Parts I and II of this report. Because this direct FE method was developed in a form that can be implemented with any commercial FE program, it is readily available for researchers and engineers who may be committed to using a particular program.

Presented in this part of the report is an introduction to modeling and practical implementation of the direct FE method within the framework of PBEE of concrete dams. In Chapter 2, an introduction to PBEE of concrete dams is presented. The basic principles of PBEE are described, key equations are explained, and the current state of knowledge for PBEE of

concrete dams is contrasted to that for buildings. Chapter 3 presents a discussion on nonlinear modeling of concrete dams by the direct FE method. First, the most significant nonlinear mechanisms that can develop in concrete dams are reviewed, and suitable modeling alternatives presented. In the second part of Chapter 3, the discussion focuses on the various types of linear energy dissipation (damping) that takes place within a dam–water–foundation rock system. Practical suggestions on how to model energy dissipation at the reservoir boundaries are presented, and recommendations are given for how to ensure consistency between damping in the numerical model and the damping measured at actual dams. Finally, in Chapter 4, the capabilities of the direct FE method when implemented with a commercial FE code is demonstrated by performing a nonlinear earthquake analysis of an actual arch dam using the commercial FE program ABAQUS [Dassault Systems 2013].

2 Performance-Based Earthquake Engineering of Dams

Performance-based earthquake engineering (PBEE) is a probabilistic framework for seismic design and safety assessments of structures that considers all the inherent uncertainties in earthquake performance assessments. In contrast to traditional load-and-resistance-factor design procedures, which typically result in a "binary" fail or safe conclusion, PBEE offers a complete framework for performance evaluations that considers and quantifies the various sources of uncertainty along the way. Performance-based earthquake engineering is well developed and has been used for performance evaluations of buildings, bridges, and nuclear power plants; but it has yet to be adapted to a comprehensive degree by the dam engineering community.

2.1 THE PACIFIC EARTHQUAKE ENGINEERING RESEARCH CENTER PBEE FRAMEWORK

Several variations of PBEE have been proposed after the introduction of the first generation of PBEE and design procedures for buildings in the United States [ATC 1996; FEMA 1997]. Today, the most commonly used "version" of PBEE is the framework developed by the Pacific Earthquake Engineering Research Center (PEER). First proposed by Cornell and Krawinkler [2003], The PEER PBEE framework provides a general tool to determine the probability distribution and rate of exceedance for various system-level performance measures for a given structure at a given site. From this information, and the information obtained in intermediate steps, a wide range of useful performance metrics (e.g., risk of collapse, annualized repair costs, expected number of casualties, etc.) can be extracted and used to make risk-informed decisions regarding the design of new dams or safety evaluations of an existing dam.

The PEER framework can be summarized in the following equation [Cornell and Krawinkler 2000]:

$$\lambda(DV) = \int_{IM} \int_{EDP} \int_{DM} G(DV \mid DM) \left| dG(DM \mid EDP) \right| \left| dG(EDP \mid IM) \right| \left| d\lambda(IM) \right| \tag{2.1}$$

where $G(X \mid Y)$ is the probability that X exceeds a specified value (also known as the complimentary cumulative distribution function) for a given Y; $\lambda(X)$ is the mean annual rate of exceedance of X; and DV = decision variable, DM = damage measure, EDP = engineering demand parameter, and IM = intensity measure.

Recognizing the complexity and multi-disciplinary nature of problem, the PEER framework can be separated into four phases, each of which can be solved using appropriate techniques and tools (Figure 2.1): (1) seismic hazard analysis, (2) structural analysis, (3) damage analysis, and (4) loss analysis. The output from each phase is quantified using the four variables *IM*, *EDP*, *DM*, and *DV*. This convenient decomposition is based on the assumption that, conditioned on *EDP*, *DM* is independent of *IM*, and, conditioned on *DM*, *DV* is independent of *EDP* and *IM* [Der Kiureghian 2005]. Each of the four phases provides valuable information about the seismic hazard, structural response, and uncertainties in the analysis.

From Equation (2.1), several analogous formulas can be written out for intermediate measures. For example, the annual rate of exceedance of a given DM is

$$\lambda(DM) = \int_{IM} \int_{EDP} G(DM \mid EDP) \left| dG(EDP \mid IM) \right| \left| d\lambda(IM) \right| \tag{2.2}$$

and the annual rate of exceedance of a given EDP is given by

$$\lambda(EDP) = \int_{IM} G(EDP \mid IM) \left| d\lambda(IM) \right| \tag{2.3}$$

Equation (2.3) is often referred to as the *seismic demand hazard curve* (SDHC) [Kwong et al. 2015]. Evaluation of the SDHCs directly provides the rate of the *EDP* exceeding a given structural capacity, or the seismic demand associated with a specified return period.

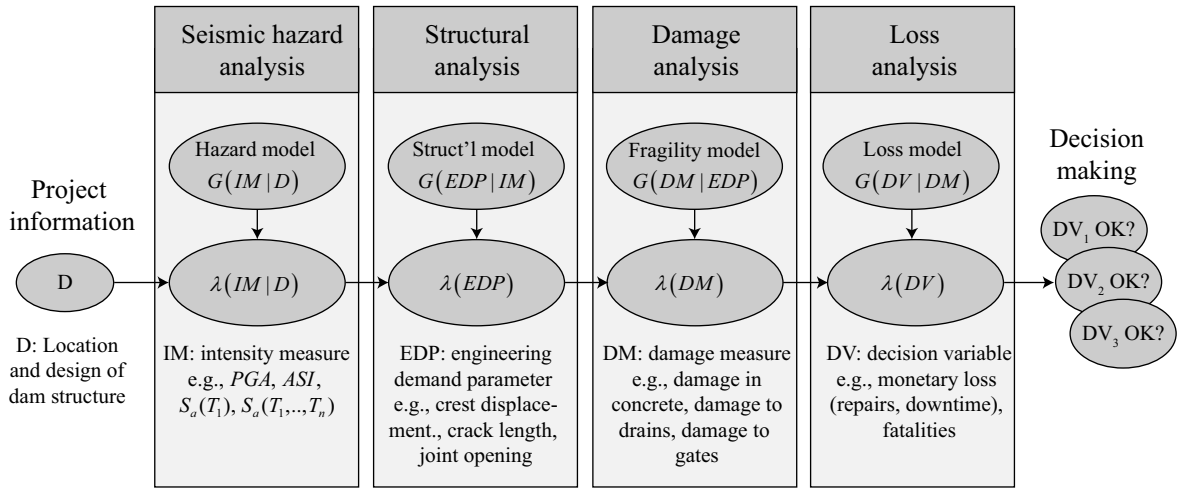

Figure 2.1 Pacific Earthquake Engineering Research Center PBEE framework applied to concrete dams. Figure adapted from Porter [2003].

Another metric, the so-called *fragility function* or *fragility curve*[†] is obtained by isolating the integrand in Equation (2.2):

$$G(DM \mid IM) = \int_{EDP} G(DM \mid EDP) \left| dG(EDP \mid IM) \right| \tag{2.4}$$

The fragility function describes the probability of exceeding a certain damage state (or limit state) in the structure as a function of the *IM*, for example, the probability of exceeding a certain crest displacement at different levels of peak ground acceleration (PGA). In the following sections, each phase of the PBEE framework is described in more detail and put into context of concrete dam analysis.

2.2 SEISMIC HAZARD ANALYSIS

Probabilistic seismic hazard analysis (PSHA) [McGuire 2004; Baker 2011] of the dam site results in the intensity measure hazard curve (IMHC), $\lambda(IM \mid D)$, which quantifies the annual rate of exceedance for an *IM* given the site characteristics *D*. Probabilistic seismic hazard analysis is based on ground-motion prediction models (GMPMs) that consider the seismic

[†] The "fragility function" is here defined as the probability of exceeding a DM given an *IM*, $G(DM \mid IM)$. The same terminology is sometimes used to describe other metrics such as the probability of exceeding an *EDP* given an IM, $G(EDP \mid IM)$, or the probability of exceeding a *DM* given an *EDP*, $G(DM \mid EDP)$.

environment such as nearby faults, recurrence rates, site conditions, etc. Several online tools and open-source computer programs are available for this purpose [Field et al. 2003; USGS 2018].

The *IM* in the PSHA may be defined as a scalar or a vector. Most often, the spectral acceleration $S_a(T_1)$ at the fundamental period T_1 of the structural system is chosen. Several other *IMs* are also possible, for example, peak ground acceleration (PGA), acceleration spectrum intensity (ASI), or multiple-period intensity $S_a(T_1,T_2,...,T_N)$.

From the IMHC, the next step is to develop a target spectrum for a given hazard level (or return period). This can for example be the uniform hazard spectrum (UHS) or some variation of the conditional mean spectrum (CMS) [Baker 2011]. Finally, an ensemble of ground motions whose *IM* matches the target spectrum at T_1 (or closely matches the target spectrum over a period range of interest) is selected for the structural analysis. Because it is unlikely to find a sufficient number of unscaled records that matches the target spectrum, this process requires scaling and modification of existing ground motions [Haselton 2009] or, alternatively, development of synthetic motions [Douglas and Aochi 2008].

Methods for selecting a target spectrum and one component of horizontal ground motion conditioned on a single vibration period are well developed. These methods must be extended to consider three simultaneous components of ground motion (two horizontal and one vertical) over multiple vibration periods for application to concrete dam analysis; such work is in progress [Kwong and Chopra 2017; 2018].

2.3 STRUCTURAL ANALYSIS

In the structural analysis phase, a large number of nonlinear response history analyses (RHA) of the dam are conducted to determine $G\left(EDP \mid IM\right)$, the response of an *EDP* given an *IM*. Relevant *EDPs* for concrete dams can be maximum displacements or accelerations at the dam crest (for operability of appurtenant structures); maximum opening at contraction joints or sliding at lift joints; extent of tensile cracking in the dam concrete; or relative movement of rock wedges and dam abutments. These *EDPs* are highly sensitive to the choice of modeling assumptions and selection of material parameters in the analysis. Thus, the sensitivity of the results to the choice of modeling assumptions should be checked as part of the analysis.

The results of the nonlinear RHA can be integrated with the IMHC $\lambda(IM)$ from the seismic hazard analysis to form the SDHC [Equation (2.3)]. Construction of the seismic demand hazard curve is illustrated in Figure 2.2. First, the IMHC is discretized at different intensity levels [Figure 2.2(a)] and ground motions are selected and scaled to match the *IM* [Figure 2.2(b)] at a given intensity level im_0. Nonlinear RHA of the system to the selected ensemble of ground motions provide the data to determine the probability distribution $G(EDP \mid IM)$, often by fitting a lognormal distribution to the individual data points [Figure 2.2(c)]. Numerical evaluation of Equation (2.3) at discrete levels gives annual rate of exceeding edp_0 [Figure 2.2(d)]. Repeating the process at multiple intensity levels im_0 provides the complete SDHC. This curve can be used to determine the annual rate of exceedance for a specific structural capacity (e.g., the exceedance rate of a certain crest displacement value), or to determine the structural demand for a given return period (e.g., the maximum joint opening expected for a 10,000 year return period).

Implementation of these nonlinear RHA requires accurate and efficient analysis procedures. Accuracy is obviously needed to ensure meaningful results. Efficiency is also essential for two reasons: (1) nonlinear RHA of the large FE models required to model dam–water–foundation rock systems is computationally demanding, even by modern standards; and (2) a large number of nonlinear RHAs are required to quantify the uncertainties in earthquake ground motions and material properties of the system. The direct FE method developed in Parts I and II of this report meets both of these requirements.

Significant resources have been spent developing and validating (through experimental programs) nonlinear models for the behavior of the various structural components that make up multi-story buildings. The state of research for concrete dams is much less mature because it is difficult to perform meaningful experimental tests on dams, and there is little field data since very few concrete dams have been subjected to damaging earthquakes. Much research is necessary to reduce the substantial uncertainties involved in estimating nonlinear dam response.

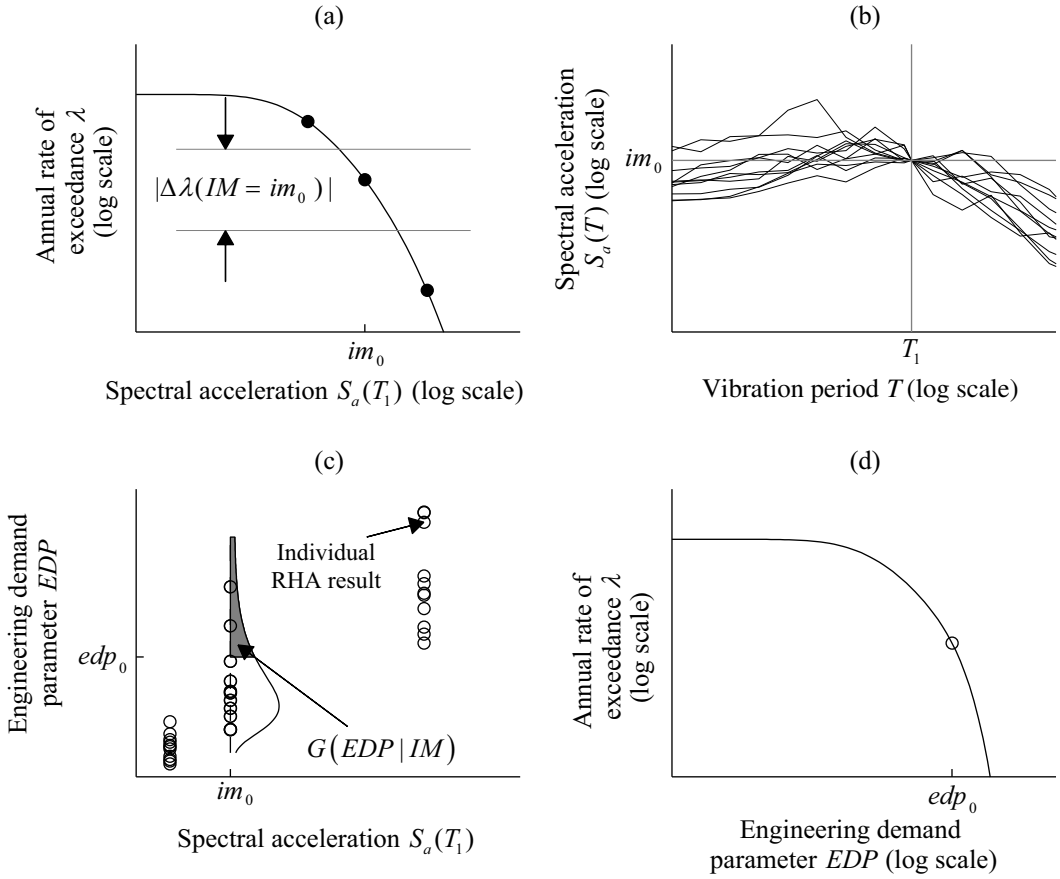

Figure 2.2 **Construction of the SDHC when $IM = S_a(T_1)$: (a) discretization of the IMHC, $\lambda(IM)$; (b) selection and scaling of ground motions so that $IM = IM_0$; (c) nonlinear RHA of the dam to estimate $G(EDP|IM)$; and (d) resulting SDHC, $\lambda(EDP)$. Figure adapted from Kwong et al. [2015].**

2.4 DAMAGE ANALYSIS

The damage analysis seeks to determine the level of physical damage *DM* given an *EDP*, $G(DM|EDP)$. For buildings, this damage analysis is usually performed on a component level using available data on the expected damage given various deformations, force levels, etc., compiled from laboratory experiments and field experience. Unfortunately, such data is not available for concrete dams because laboratory data is lacking, and very few dams have been subjected to damaging earthquakes. Thus, it is often more useful to define damage states (or limit states) for the dam directly on the structural level, and use damage measures to quantify the

damage in each of these states. Defining such meaningful damage states requires identification of the potential failure modes of the dam [Hariri-Ardebili et al. 2016].

The resulting output can be visualized in the form of fragility curves for the dam, $G(DM \mid IM)$, defined by Equation (2.4). Construction of the fragility curve is illustrated in Figure 2.3(a): first, outputs from a large number of nonlinear RHA at several intensity levels are used to determine the fraction of analyses exceeding a certain damage threshold. A fragility function is then fitted to the data set, usually in the form of a lognormal cumulative distribution Baker 2015]. Examples of fragility curves for relevant damage states in concrete dams are shown in Figure 2.3(b). If an important objective for the dam is to ensure operability of flood gates at the crest, a useful damage measure can for example be the maximum crest displacement. Such curves should be computed not only for extreme damage states (e.g., uncontrolled release of the reservoir), but rather at multiple intermediate stages to give a complete description of the gate performance at different hazard levels.

Researchers have successfully applied the concepts of seismic fragility analysis to study the influence of modeling assumptions on the seismic performance of gravity dams at different intensity levels [Tekie and Ellingwood 2003; Ghanaat et al. 2012; and Hariri-Ardebili and Saouma 2016a].

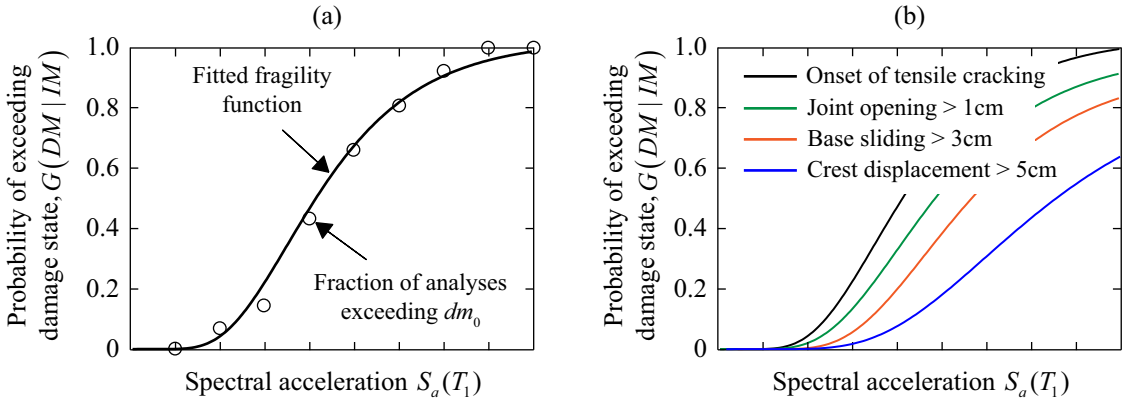

Figure 2.3 **Illustration of fragility curve: (a) fitting of fragility curve to output from nonlinear RHA; and (b) examples of fragility curves relevant for concrete dams.**

2.5 LOSS ANALYSIS

The last phase in the PBEE framework is loss analysis, which seeks to determine $\lambda(DV)$, the rate of exceedance of a certain decision variable. For concrete dams, these can be system-level measures such as repair costs, loss of power generation or loss of life downstream of the dam, or local measures such as gate operability.

Information about the rate of exceedance of these DVs—as well as other performance metrics derivable from $\lambda(DV)$ [Moehle and Deierlein 2004] —is useful for making risk-informed decisions for a broad range of problems. For example, we may wish to determine whether the expected future earthquake repair cost of a dam is acceptable, or to assess the effectiveness of a planned retrofit of a dam to reduce the expected loss of power generation due to earthquakes. Detailed loss models have been developed and made available to researchers and engineers to systematically estimate repair costs, downtime, number of casualties, etc. in buildings at different damage levels [Porter 2003]. Such models are currently not available for concrete dams. As for the damage analysis phase, more research on this topic is needed before PBEE can become a routine part of dam safety assessments.

2.6 MODELING OF UNCERTAINTY

Uncertainty is present at every step of the analysis process. The integration of conditional probabilities in Equation (2.1) ensures that this uncertainty is allowed to propagate from one step of the analysis to the next in the PBEE framework, thus achieving in the end a probabilistic overall prediction of the dam performance.

The resulting total uncertainty can be separated into two categories: aleatory and epistemic. The aleatory uncertainty is associated with the inherent randomness of processes, such as future earthquake events, and cannot (at least as of now) be completely eliminated. This form of uncertainty is accounted for in the PSHA, which considers a range of earthquake events and aggregates their contribution to the overall seismic risk, and in the structural analysis by considering an ensemble of different ground motions. In contrast, epistemic uncertainty is that caused by lack of knowledge about modeling assumptions, material parameters, etc., which can be reduced by gathering more information.

The epistemic uncertainty in the analysis can be quantified by treating each input parameter as a random variable and applying statistical sampling techniques (e.g., Monte Carlo simulations or Latin Hypercube Sampling) to estimate the variance of the analysis outputs (*EDP*, *DM*, *DV*, etc.) to changes in the input; however, these methods require very large number (tens of thousands) of nonlinear RHAs of 3D dam–water–foundation rock systems.

A more practical alternative is to quantify the influence of epistemic uncertainty using a so-called tornado-diagram-analysis [Porter et al. 2002; Hariri-Ardebili and Saouma 2016b], wherein the change in output is measured for each uncertain input by varying it from a lower limit to an upper limit while keeping all other parameters constant. As shown in Figure 2.4, a tornado diagram is developed from these results: the parameters that produce the greatest uncertainties in the overall response can be identified, and those that have insignificant influence on the results can be identified and treated as deterministic in subsequent analyses.

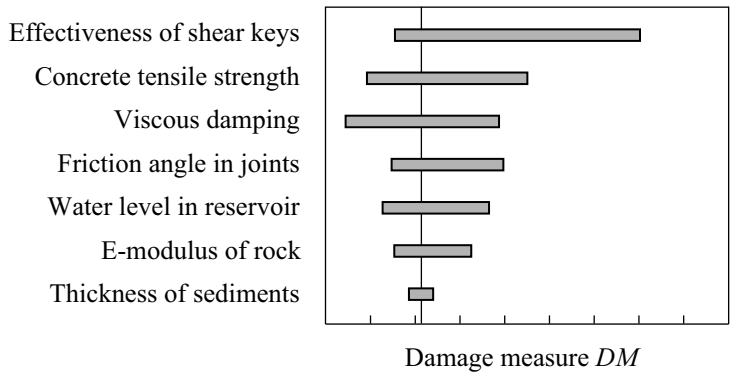

Figure 2.4 Illustration of tornado diagram. Figure adapted from Porter [2003].

3 Modeling of Concrete Dams by the Direct Finite-Element Method

Having accurate and reliable analysis procedures for predicting the nonlinear earthquake response of concrete dams is essential for successful application of the PBEE framework. To avoid introducing unnecessary error in the results, the nonlinear FE model must consider all the significant factors in the earthquake response of concrete dams (see Part II). Implementation of the large number of RHA required for PBEE also requires that the analysis procedure is efficient, robust, and capable of being implemented into various commercial FE programs preferred by dam engineers. The direct FE method developed in Parts I and II of this report meets all these requirements. In this chapter, recommendations for practical modeling of concrete dams by the direct FE method are presented, with emphasis on modeling of nonlinear mechanisms and energy dissipation (damping).

3.1 MODELING OF NONLINEAR MECHANISMS

Linear analyses cannot predict the performance of dams during ground motions intense enough to cause extensive cracking in concrete or initiate other mechanisms of nonlinear behavior. Examples of such nonlinear mechanisms are: cracking in the dam concrete [Bhattacharjee and Léger 1993; Lee and Fenves 1998; and Pan et al. 2011]; opening, closing and sliding of vertical contraction joints [Niwa and Clough 1982; Lau et al. 1998; and He et al. 2016]; sliding and separation at lift joints and at concrete–rock interfaces [Léger and Katsouli 1989; Fronteddu et al. 1998; Chávez and Fenves 1995b]; relative movement of discontinuous rock wedges in the foundation [Lemos 1999; 2008]; and possibly, separation of water from the upstream face of the dam causing cavitation [Zienkiewicz et al. 1983].

The study of these mechanisms and their influence on dam response is a vast field with extensive literature. In this section, the discussion is limited to a brief introduction to how the

most influential mechanisms can be practically modeled in the direct FE method using commercial FE programs. These findings will then be utilized in the example nonlinear analysis of an actual arch dam presented in Chapter 4.

3.1.1 Cracking of Concrete

Concrete dams are designed to resist static loads primarily through compressive stress fields that are much below the compressive strength of concrete. Intense ground motions are likely to induce tensile stresses in the dam that exceed the low tensile resistance of the unreinforced mass concrete used in dam construction, typically around 10% of the compressive strength. Thus, cracking of concrete is an important mechanism to consider when evaluating the seismic safety of concrete dams.

The two most common methods for modeling crack propagation in concrete dams are the *discrete crack model* and the *smeared crack model*; see Figure 3.1. Both of these models are briefly presented below; the reader is referred to the review by Bhattacharjee and Léger [1992] for a more comprehensive discussion.

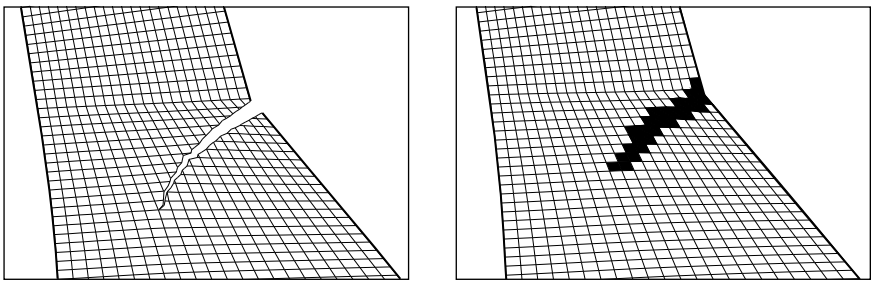

(a) (b)

Figure 3.1 **Two approaches to modeling crack propagation in FE models of concrete dams: (a) discrete crack model based on the Extended Finite Element Method (XFEM); and (b) smeared crack model.**

3.1.1.1 The discrete crack model

Since the late 1960s, numerous models have been proposed for modeling crack propagation in concrete. Early studies for concrete dams employed linear fracture mechanics theory and the *discrete crack model* to study concrete cracking in 2D gravity dam models [Ayari and Saouma 1990; Pekau et al. 1991]. Modeling of discrete cracks would appear to be a physically realistic

approach that can explicitly consider penetration of water in the crack, uplift pressure on crack-open surfaces, aggregate interlock at rough-crack surfaces, opening and closing of cracks, and impact and sliding of sections of the dam after extensive cracking. However, the approach is computationally challenging because the FE mesh is redefined at each time step, and the crack propagation is strongly dependent on the size, shape, orientation, and order of FEs in the mesh; thus the results are not unique.

The preferred way to model discrete crack propagation today is to use the extended FE method (XFEM) [Belytschlo and Black 1999], which allows cracks to propagate through the FEs and hence does not require modification of the FE mesh. This is achieved by adding enrichment functions to the FE approximation to account for the presence of a crack that can propagate arbitrarily through the elements. The XFEM has been employed to study the nonlinear earthquake response of both gravity dams and arch dams [Pan et al. 2011; Zhang et al. 2013; and Goldgruber 2015]; however, most current implementations of XFEM do not allow for multiple cracks to form within any single region, which is a significant limitation for practical analysis of concrete dams.

3.1.1.2 The smeared crack model

To overcome the aforementioned difficulties encountered in the discrete crack model, the fracture can instead be idealized as "smeared" over the FEs or over a certain bandwidth of the element. The *smeared crack model* employs a suitable constitutive model to describe the crack initiation and the softening response of concrete during crack propagation. This way, the constitutive relation is updated as the dynamic analysis progresses in time, but the FE mesh remains unchanged.

The smeared crack model has its share of disadvantages. First, the numerical results are not necessarily objective with respect to the FE mesh; as the element size decreases, the fracture zone becomes smaller, and the force required to propagate the crack can decrease to a very small value. Second, this approach is not amenable to model impact and sliding of sections after extensive cracking because the discontinuous displacements across the interacting surfaces are not well approximated. Third, the diffuse crack pattern computed by this model does not provide any information about the physical dimensions of cracks or their locations within elements.

The plastic damage model for cyclic loading of concrete proposed by Lee and Fenves [1998] is a variation of the smeared crack model. Several features of this model have made it attractive for earthquake analysis of concrete dams. By keeping track of tensile damage and compressive damage through two damage variables, d_t and d_c, stiffness change in concrete during cycling loading [Figure 3.2(a)]—where the stiffness in compression is recovered when a crack closes, but the stiffness in tension is not—can be simulated. The model also allows for the conceptual separation of the behavior in tension into two parts: linear stress–strain relation before the tensile strength, f_t, is exceeded [Figure 3.2(b)]; and softening behavior after crack initiation described by fracture mechanics theory relating stresses to crack opening displacements [Figure 3.2(c)]. This approach to defining the behavior after crack initiation offers two important advantages. First, the dissipated fracture energy per unit length of crack remains independent of the FE mesh, thus ensuring that the results are less sensitive to mesh size. Second, this approach introduces the concept of *specific fracture energy* for concrete, G_F, defined as the area under the tensile stress–crack width curve [Figure 3.2(c)]. The two significant material parameters for this model, the tensile strength f_t and the specific fracture energy G_F, can both be determined experimentally: f_t from a splitting-tensile or direct-tensile test [Raphael 1984], and G_F from a wedge-splitting test [Brühwiler and Wittmann 1990a].

Various implementations of the smeared crack model have been used to study crack propagation in 2D analysis of gravity dam monoliths [Bhattacharjee and Léger 1993; El-Aidi and Hall 1989; and Lee and Fenves 1998] and in 3D analysis of arch dams [Pan et al. 2011; Wang et al. 2013]. Most commercial FE programs (e.g., ABAQUS, LS-DYNA, DIANA, and ANSYS) used for concrete dam analyses have one or more variations of the smeared crack model available.

Experimental tests have shown that the strength of mass concrete increases at higher strain rates, which can be modeled by increasing the static fracture parameters [Raphael 1984; Bhattacharjee and Leger 1992]; however, there is no clear consensus in the literature on what is an appropriate value. Because of the high uncertainty in specifying material parameters for cracking models, the sensitivity of the results to the selected values should always be checked.

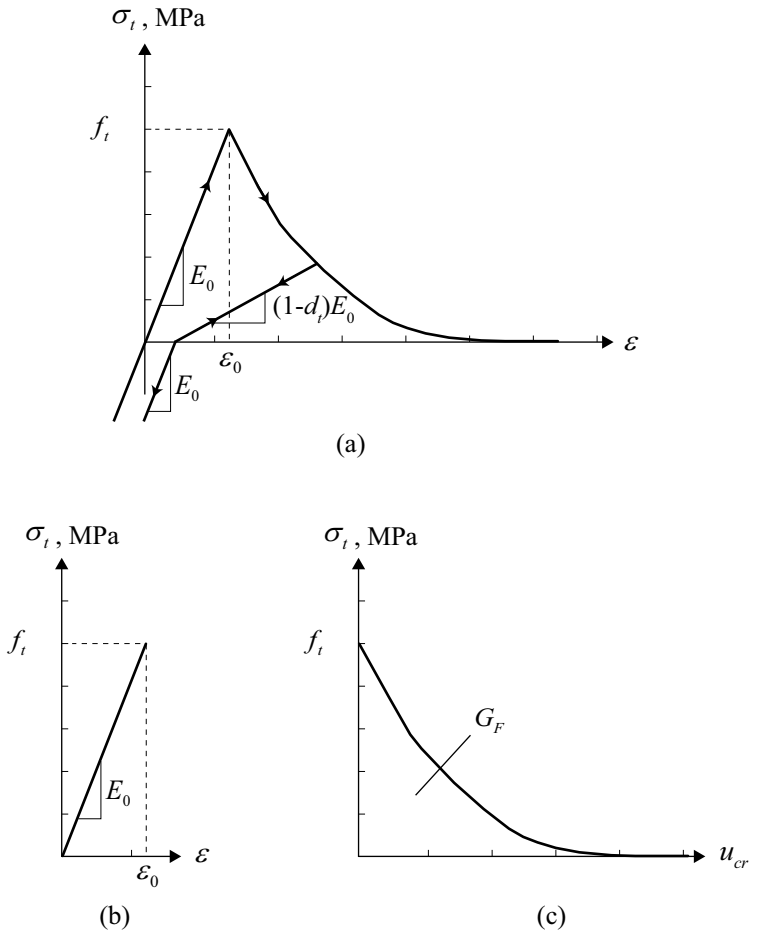

Figure 3.2 **(a) Softening response of concrete under uniaxial cyclic loading; (b) linear stress–strain curve for pre-failure response; and (c) post-failure stress–crack opening displacement curve, where the area under the curve is the fracture energy G_F. Figure adapted from Brühwiler [1990].**

3.1.2 Opening and Closing of Vertical Contraction Joints

Vertical contraction joints between cantilevers, which are grouted possibly with shear keys, are unable to resist any significant net tension in the arch direction and are therefore likely to open and close during intense ground motions. This nonlinear response mechanism affects the dam response in two ways: (1) opening of a joint temporarily reduces the resistance in the arch direction, causing an increase in flexural stress and possibly horizontal cracking of cantilevers; and (2) repeated opening-closing may cause compression failure of the joint. Model tests have

demonstrated that these effects can have significant influence on the dynamic response of arch dams [Niwa and Clough 1982].

Several numerical formulations are available to model contraction joints; frequently used are discrete joint elements [Dowling and Hall 1989; Fenves et al. 1992; and Lau et al. 1998] or a contact formulation at the surfaces between cantilevers [Zhang et al. 2009; Goldgruber 2015; and Wang et al. 2012]. Opening and closing of the joint in the normal direction may be specified by a zero-tensile strength master-slave contact relation with a pressure-overclosure relationship [Figure 3.39a)] to prevent node penetration to prevent node penetration [Dassault System 2013]. Alternatively, the joint failure under combined normal and shear forces can be modeled by a traction separation law based on nonlinear fracture mechanics theory. In the tangential directions, shear keys can be modeled by very stiff linear springs (excluding the possibility of shear key failure) or more accurately by a traction separation law; if shear keys are not present, frictional sliding can be modeled by the Mohr–Coulomb friction criterion [Figure 3.3(b)]: $\tau = \sigma \tan\phi + c$, where τ is the shear stress, σ the normal stress, and the material parameters ϕ and c represents the fiction angle and cohesion of the joint, respectively. At least one of these models is available in most commercial FE programs.

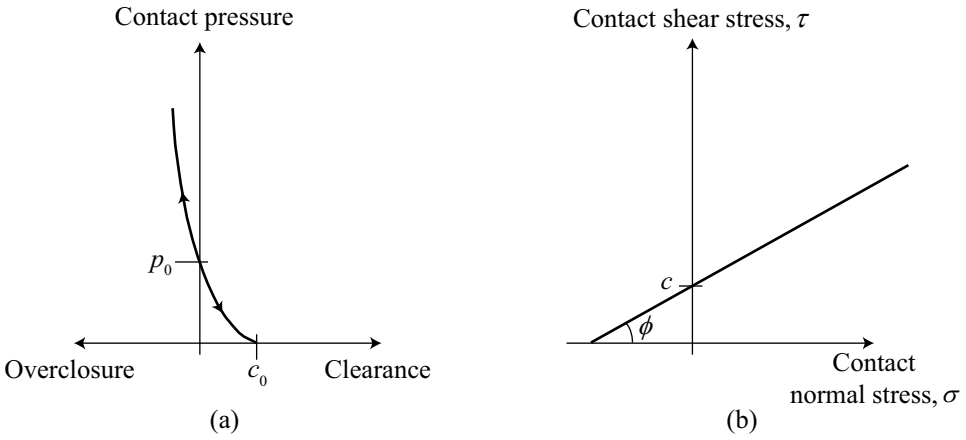

Figure 3.3 **(a) Exponential pressure-overclosure relation for normal contact in contraction joint, where c_0 is the clearance at zero pressure and p_0 the pressure at zero opening; and (b) Mohr–Coulomb friction criterion. Figure adapted from Dassault Systems [2013].**

3.1.3 Sliding and Separation at Lift Joints and Concrete–Rock Interfaces

The properties of lift joints and concrete–rock interfaces are greatly influenced by how the surface was prepared before pouring the next concrete lift. Even with good preparation, the strength and fracture properties at these joints are usually much lower than values for mass concrete [Saouma et al. 1991; Fronteddu et al. 1998; and Tinawi et al. 1998]. Thus, cracks are likely to form along these joints rather than through the mass concrete.

Lift joints and concrete–rock interfaces can be modeled by joint interface elements [Goodman et al. 1968; Léger and Katsouli 1989] or by a contact formulation. The failure of the joint can be defined by a traction-separation law, with the residual strength described by the Mohr–Coulomb friction criterion. That said, the high degree of uncertainty regarding the properties of lift joints and concrete–rock interfaces—such as tensile strength, fracture energy and roughness—makes it difficult to specify material parameters for these models with confidence. Thus, sensitivity analyses should always be conducted.

3.1.4 Discontinuities in the Foundation Rock

The foundation near a dam behaves nonlinearly because it is often fractured and discontinuous, with weak planes permitting sliding and separation of rock masses at these surfaces. During an earthquake, the increase in forces transmitted to the foundation from the dam may initiate shear failure along these weak planes. Planes of weakness in the foundation can be modeled using nonlinear joint elements [Goodman et al. 1968; Léger and Katsouli 1989] or assemblages of rock wedges can be modeled using the discrete element method (DEM) [Lemos 2008]. Such modeling is a very challenging problem, particularly because detailed information about the subsurface rock conditions is usually limited. Consequently, such detailed modeling is often excluded from the dynamic analysis of the dam–water–foundation system; however, the potential for instabilities in the foundation should always be evaluated by supplemental analyses.

3.2 MODELING OF ENERGY DISSIPATING MECHANISMS

The FE model of the dam–water–foundation rock system includes three main sources of energy dissipation that combine to form the total (linear) damping in the system: (1) material damping in

the concrete and rock; (2) radiation damping in the semi-unbounded foundation and fluid domains; and (3) dissipation of hydrodynamic wave energy at the reservoir boundaries.

3.2.1 Material Damping

Modeling of material damping in dam concrete and foundation rock is highly uncertain, even when restricted to the linear range of behavior. Phenomenological modeling of these mechanisms is not practical due to the lack of experimental data on the energy-dissipating behavior of mass concrete and rock under seismic loading conditions [Bhattacharjee and Léger 1993]. As a substitute, highly idealized linear viscous damping models, such as modal damping or Rayleigh damping, are used for their mathematical convenience.

3.2.1.1 Modification of Rayleigh damping for nonlinear modeling

For linear systems, the standard damping matrix, $\mathbf{c}$, is constructed by assembling damping submatrices $\mathbf{c}_c$ and $\mathbf{c}_r$ for the dam and foundation rock, respectively [Chopra 2012b]. Although Rayleigh damping and modal damping are commonly used for several classes of structures, including buildings and bridges, they do not seem to be appropriate for continua of mass concrete and rock.

Mass-proportional damping is inappropriate in the presence of sliding of the dam along the dam–foundation interface or cracks that extends through the dam thickness because it causes spurious damping forces that prohibit sliding and overturning of sections above an open crack [El-Aidi and Hall 1989; Hall 2006]. Stiffness proportional damping is intuitively more appealing because the element damping forces are proportional to deformation rates in the element. Stiffness proportional damping matrices for the dam and foundation subsystems are defined as: $\mathbf{c}_c = a_{1c}\mathbf{k}_c$ and $\mathbf{c}_r = a_{1r}\mathbf{k}_r$, where $\mathbf{k}_c$ and $\mathbf{k}_r$ are the elastic stiffness matrices and the coefficients a_{1c} and a_{1r} are determined from viscous damping ratios specified for the dam alone and foundation domain, separately, at a selected frequency. Usually, this frequency is selected as the fundamental natural frequency of the dam–foundation or dam–water–foundation system. The damping ratios for these two substructures should be selected to be small enough to ensure that the overall damping in the dam–water–foundation system does not exceed the range of measured values; see Section 3.2.4.

The damping matrix, so constructed, should be modified to recognize that damping forces cannot exist in a FE across an open crack [Bhattacharjee and Léger 1993; El-Aidi and Hall 1989; and Hall 2006]. To achieve this goal, several solutions have been proposed: (1) setting the element damping to zero upon initial cracking of an element [El-Aidi and Hall 1989]; (2) using the tangent stiffness matrix instead of the initial stiffness matrix [Bhattacharjee and Léger 1993]; (3) capping the damping forces at a maximum value for each element [Hall 2006]; or (4) using the degraded elastic stiffness matrix $\mathbf{k}^{el}(t)$ [Lee and Fenves 1998], which is a function of the damage variables d_t and d_c; see Section 3.1.1.2. The latter of these approaches has the advantage that it eliminates transfer of tensile damping forces when a crack is open ($d = 1$) but allows for recovery of compressive damping forces upon closing of the crack ($d < 1$). Most commercial FE software has one or several of these options available; however, they are not always activated in the default settings.

3.2.2 Radiation Damping

Seismic waves reflected off the dam will generally not return unless there is a sharp impedance difference in the foundation. This mechanism for energy dissipation, called radiation damping, can be significant for seismic waves in the foundation domain, but less so for hydrodynamic waves in the fluid domain, except at high frequencies [Fenves and Chopra 1985].

Figure 3.4 shows the added damping due to dam–foundation rock interaction—which is primarily attributable to radiation damping—for 2D gravity dams and 3D arch dams supported on homogeneous foundations. Observe that radiation damping is a major source of energy dissipation for 2D gravity dam models unless the rock is much stiffer than concrete; however, for 3D arch dam models the effect is less significant. The large added damping in the 2D system is caused by the assumption of homogeneous rock, which implies no wave reflections in the foundation domain. For other foundation idealizations (e.g., a layered half-space) the radiation damping effects will be smaller due to multiple reflections and refractions of waves in the layered system.

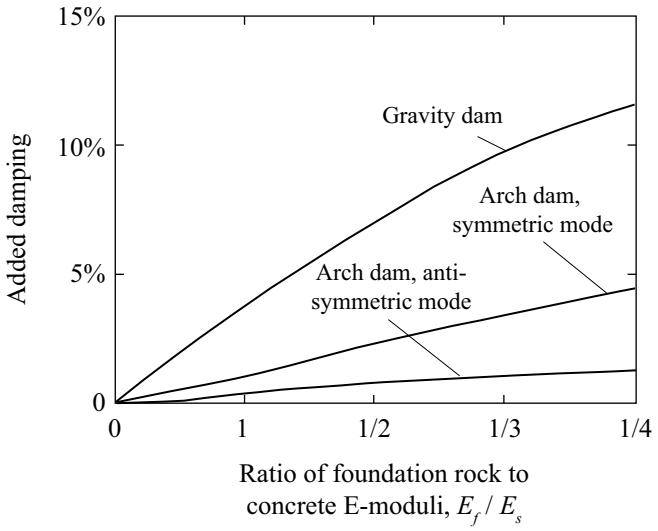

Figure 3.4 **Additional damping in the fundamental mode of vibration due to dam–foundation interaction for 2D gravity dams and 3D arch dams supported on foundation modeled as a homogeneous half-space. Data for gravity dams are from Fenves and Chopra [1984a] and for arch dams from Tan and Chopra [1995].**

3.2.3 Energy Dissipation at the Reservoir Boundaries

The bottom of a reservoir upstream of the dam may consist of highly variable layers of exposed bedrock, alluvium, silt, and other sedimentary materials. Hydrodynamic wave energy is dissipated at these boundaries by two mechanisms (Figure 3.5): (1) water–foundation rock interaction causing radiation of wave energy to the underlying semi-unbounded foundation domain; and (2) energy absorption in the sediments deposited at the reservoir boundaries. Most of the past investigations of the effects of sediments deposited at reservoir boundaries have been based on results from the substructure method, wherein water–foundation interaction is ignored and sediments modeled implicitly by a 1D wave reflection coefficient α [Fenves and Chopra 1985; Tan and Chopra 1995b]. The effects of sediments on dam response are re-investigated here by the direct FE method, where water–foundation interaction is included automatically, and the sediments (thickness and extent) can be explicitly modeled by FEs.

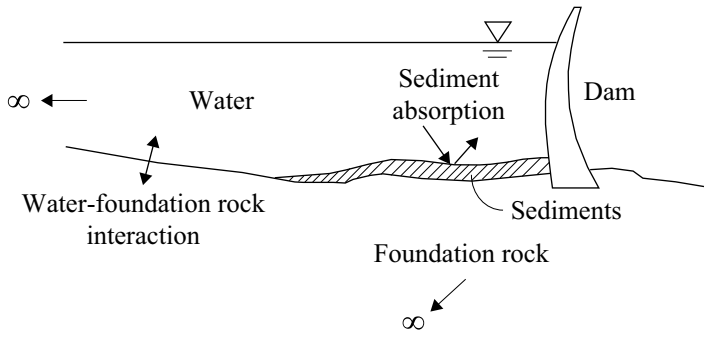

Figure 3.5 **Conceptual overview of two mechanisms for energy dissipation at reservoir boundaries: (1) water–foundation rock interaction, and (2) absorption in sediments deposited at the reservoir bottom.**

Researchers have primarily investigated two types of material models for sediments: (1) a two-phase fluid saturated poroelastic model, and (2) a viscoelastic model. The most sophisticated of these is the two-phase fluid-saturated poroelastic material [Domínguez et al. 1997]. As demonstrated, sediments modeled in this manner have little influence on the response of concrete dams if the sediments are fully saturated, but show great influence if they are partially saturated, even for very small variations in the degree of saturation [Domínguez et al. 1997; Maeso et al. 2004]. This two-phase poroelastic model is presently not ready for practical application for two reasons: (1) the dam response is extremely sensitive to the degree to which sediments are saturated, a quantity that cannot be determined precisely; and (2) the model requires detailed information on sediment properties, such as grain size, porosity and hydraulic conductivity, for which data is not available for reservoirs impounded behind dams.

A simpler model for sediments is a viscoelastic material [Lofti et al. 1987; Medina et al. 1990], characterized by familiar parameters: modulus of elasticity E_{sed}, Poisson's ratio ν_{sed}, material density ρ_{sed}, and material damping ratio. These properties have rarely been measured at dam sites, but data exists in the literature for river delta deposits and marine underwater sediments (e.g., see Hamilton [1971]). Thus, the viscoelastic material model appears to be a pragmatic choice for modeling sediments in the direct FE method. As demonstrated next, sediments modeled in this manner may have very little influence on dam response.

3.2.3.1 Gravity dams

The effect of sediments on the dynamic response of a gravity dam is investigated first. Determined by the direct FE method, frequency response functions for the idealized 2D gravity dam on flexible foundation with full reservoir defined in Section 5.4 of Part I are presented in Figure 3.6 for three values of the moduli ratio E_f / E_s. For each moduli ratio, two cases are compared: (1) no sediments at the reservoir bottom; and (2) sediment layer modeled as a viscoelastic material. The viscoelastic sediments have uniform thickness $H_{\text{sed}} = 0.1H$, where H = 120 m is the height of the dam, ρ_{sed} = 1600 kg/m^3, ν_{sed} = 0.46, viscous damping = 10%, and pressure-wave velocity = 1700 m/sec (E_{sed} = 1.0 GPa). These properties are based on typical values for saturated underwater sediments [Hamilton 1971].

The results shown in Figure 3.6 demonstrate that sediments have little influence on gravity dam response to horizontal ground motion; the first resonant peak—which is the most significant in earthquake response of dams—is unaffected, but the response at higher frequencies is more noticeably affected. However, the influence of sediments on the earthquake response of the gravity dam is not significant, as confirmed by the two sets of response histories presented in Figure 3.7(a), which are essentially identical. Similar results have been reported by other researchers [Medina et al. 1990; Hatami 1997; and Zhang et al. 2001].

Relatively speaking, sediments have more influence on the frequency response functions for vertical ground motion. The discrepancy in response at the first two resonant frequencies (Figure 3.6) is noticeable, although it is small, and the response at higher resonant frequencies is greatly influenced by sediments with the resonance peaks almost completely eliminated. Note that the earthquake response of the dam is again essentially unaffected, as demonstrated by the closeness of the results in Figure 3.7(b).

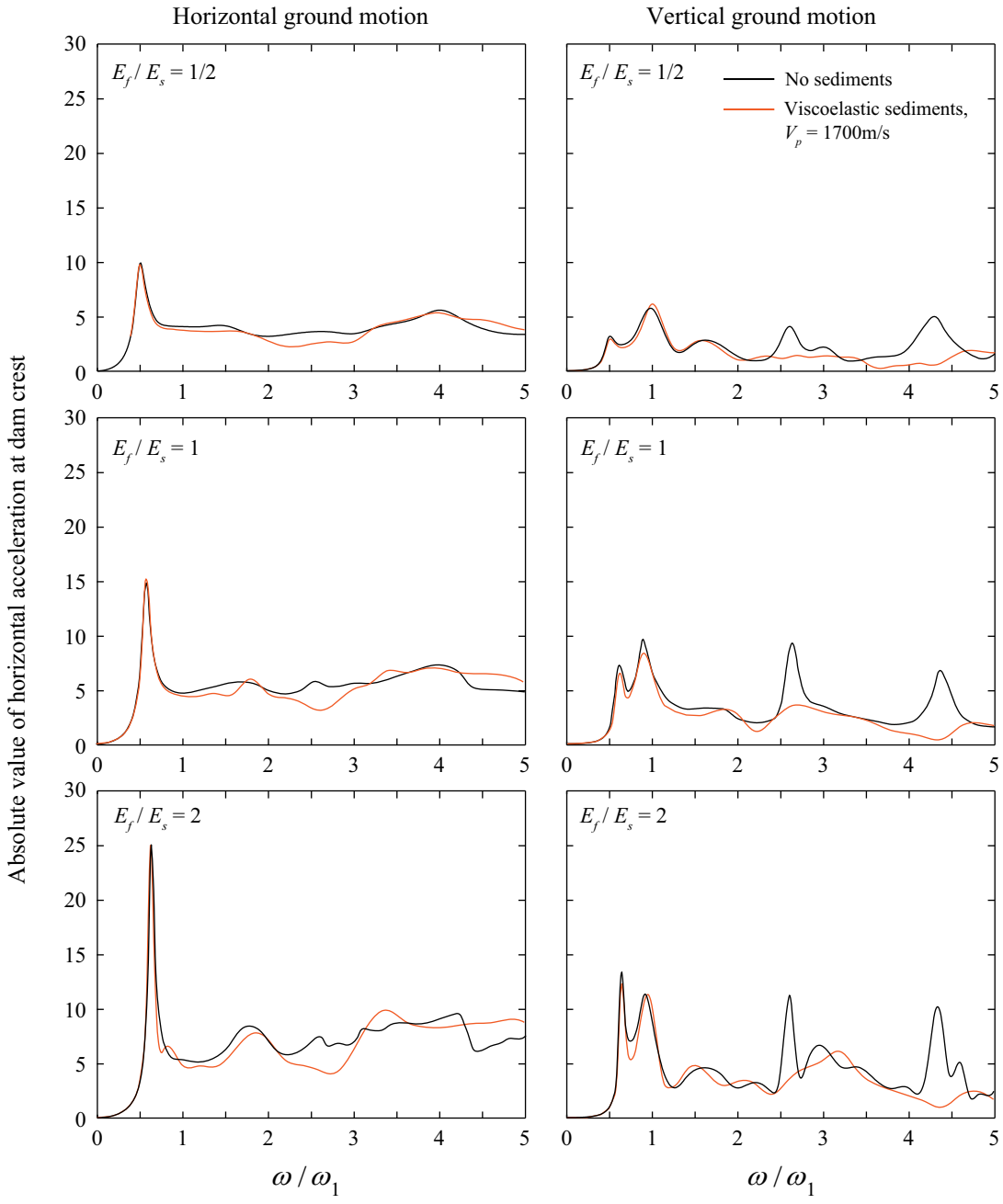

Figure 3.6 **Influence of sediments on the response of idealized gravity dam on flexible foundation rock with full reservoir due to horizontal and vertical ground motion. Results are plotted against normalized frequency ω / ω_1 where ω_1 is the fundamental frequency of the dam on rigid foundation.**

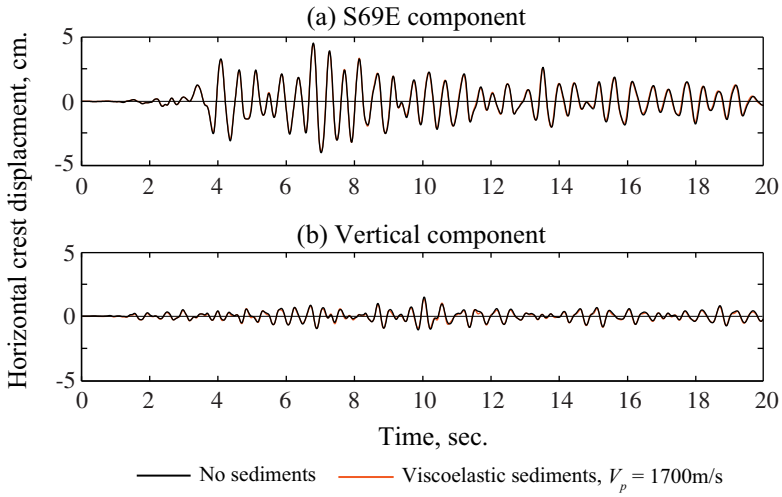

Figure 3.7 **Influence of sediments on the displacement response of idealized gravity dam on flexible foundation rock with full reservoir due to the S69E and vertical components, separately, of the Taft ground motion; E_f / E_s = 1.0.**

3.2.3.2 Arch dams

Determined by the direct FE method, frequency response functions for Morrow Point Dam (properties defined in Section 5.2.1 of Part II) are presented in Figure 3.8 for two cases: (1) no sediments at the reservoir boundaries; and (2) sediment layer modeled as a viscoelastic material. The sediments have uniform thickness $H_{sed} = 0.1H$, where H = 142 m is the dam height, ρ_{sed} = 1600 kg/m^3, ν_{sed} = 0.46, and viscous damping = 10%; two values for the pressure-wave velocity are considered, 1400 m/sec (E_{sed} = 0.68 GPa) and 1800 m/sec (E_{sed} = 1.12 GPa).

The results demonstrate that, just as in the case of gravity dams, sediments have small influence on the dam response: the first two resonant peaks due to ground motions in the stream and cross-stream directions, and the first resonant peak due to vertical ground motion are essentially unaffected. Although the responses at higher resonant frequencies are more noticeably affected, the overall influence of sediments on earthquake response is not significant, as demonstrated by the two sets of displacement and acceleration response histories presented in Figure 3.9, which are nearly identical.

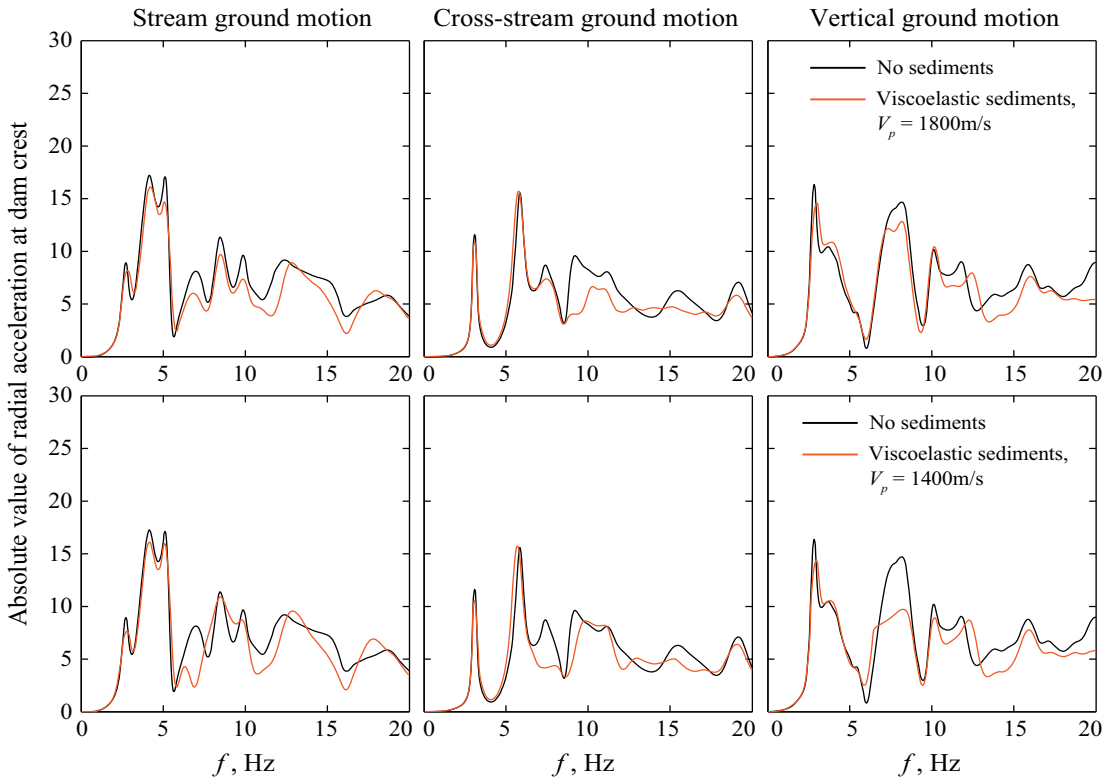

Figure 3.8 **Influence of sediments on the response of Morrow Point Dam on flexible foundation rock with full reservoir subjected to stream, cross-stream, and vertical ground motions.**

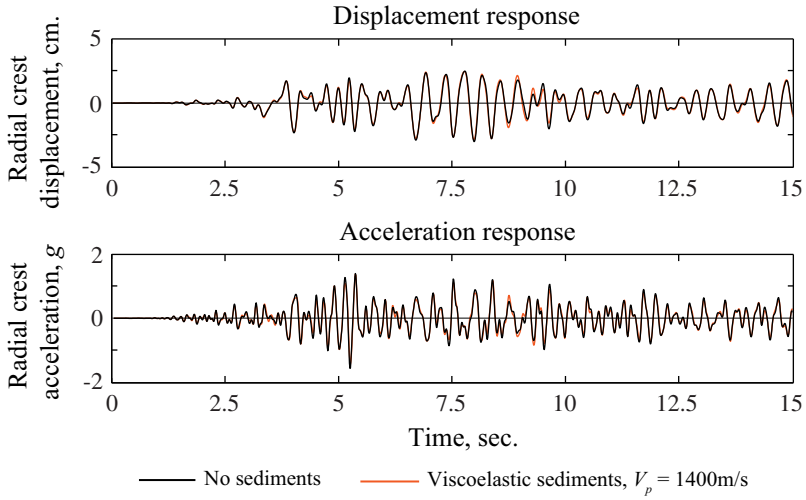

Figure 3.9 **Influence of sediments on the earthquake response of Morrow Point Dam on flexible foundation rock with full reservoir subjected to the S69E, S21W, and vertical components, applied simultaneously, of the Taft ground motion.**

3.2.3.3 Can sediments be ignored?

The preceding results indicate that the influence of sediments at the reservoir boundaries—modeled as a viscoelastic material—has negligible influence on the response of gravity dams as well as arch dams. Because water–foundation rock interaction and the associated radiation damping are included in the analysis, the additional loss of vibration energy due to sediments is apparently of little consequence. Thus, at the present time, it seems reasonable to ignore sediments in analysis of dam–water–foundation rock systems by the direct FE method.

This conclusion may seem to contradict earlier results obtained by the substructure method, which found that sediments may influence dam response significantly [Fenves and Chopra 1985; Tan and Chopra 1995b]; however, water–foundation rock interaction (and the associated radiation damping) are ignored in the substructure method, the loss of vibration energy associated with wave absorption in the α-model apparently becomes significant. These findings also have implications for analysis of dam–water–foundation rock systems modeled by the substructure method. Water–foundation rock interaction, which is neglected in this method, can be approximately modeled by the 1D α-model with the value of α based on rock properties alone. With water–foundation rock interaction modeled in this manner, reservoir bottom sediments can be ignored in the substructure method just as in the direct FE method; see Appendix F for detailed discussion of this topic and numerical results.

3.2.4 Calibration of Damping Values

Damping in the numerical model for the dam–water–foundation rock system should be consistent with measured values at the dam determined from low-amplitude motions (i.e., within the linear range of response) recorded during forced vibration tests, ambient vibrations, or small earthquakes. Obviously, these measured values represent the *overall* damping in the system, including material damping, radiation damping, and energy loss at the reservoir boundaries; experimental data on the contributions of individual sources is generally not available.

Summarized in Figure 3.10 are data for damping "measured" at 32 concrete dams during forced vibration tests and estimated based on ambient vibration measurements [Hall 1988; Proulx and Paultre 1997; and Proulx et al. 2004]. Both gravity dams and arch dams covering a wide range of system parameters are included. The overall damping values measured at these

dams are all in the range of approximately 1–5%. These comprehensive data lead to an important conclusion: overall damping in the numerical model should not exceed 5% unless a larger value was "measured" at the particular dam. In contrast, the current practice of specifying a viscous damping ratio of 5% for the concrete dam alone and a similar value for the foundation domain is likely to lead to damping in the range of 10–15% in the overall dam–water–foundation system for "common" system parameters [Fenves and Chopra 1984a; Tan and Chopra 1995a]; a wider range of 6–30% overall damping was identified by Bybordiani et. al. [2017] for 2D and 3D idealizations of a gravity dam–water–foundation system covering several values for the foundation stiffness and different ratios of the canyon width to the height of the dam. Thus, the current practice of choosing damping values should be abandoned because it will likely underestimate the earthquake response of dams.

Material damping in the numerical model is usually specified separately for the two substructures: dam and foundation. Because the contributions from energy loss at the reservoir boundaries and radiation damping are not known prior to the earthquake analysis of the dam, it is therefore not possible to know in advance the damping values that should be specified for the two substructures to achieve a target value of, say, 5% overall damping. Thus, material damping in the two substructures must be determined by trial and error to achieve an overall damping consistent with the target value. The overall damping in the numerical model can be determined from frequency response functions or system identification techniques applied to the response histories.

Researchers have demonstrated that damping in the range of 1–2% for the dam concrete and 1–4% for the foundation is likely to lead to overall damping in 3D numerical models that is consistent with the range of measured values [Chopra and Wang 2009; Løkke and Chopra 2017]. For example, viscous damping ratios of 1% and 3% for the dam and foundation, respectively, in the case of Mauvoisin Dam; 2% and 4%, respectively, for Pacoima Dam; and 1% and 2%, respectively, for Morrow Point Dam, combined to provide damping in the overall dam–water–foundation rock system that was consistent with measured damping for these dams: 2–3% for Mauvoisin Dam, 6–7% for Pacoima Dam and 1.5–4% for Morrow Point Dam. Responses computed from the numerical models for Mauvoisin Dam and Pacoima Dam were in good agreement with motions recorded during small earthquakes at these two dams [Chopra and Wang

2009]. More recent examples include analyses of Tagokura gravity dam (1% in dam, 0% in foundation) and Kurobe arch dam (1% in dam, 0% in foundation) [Robbe et al. 2017].

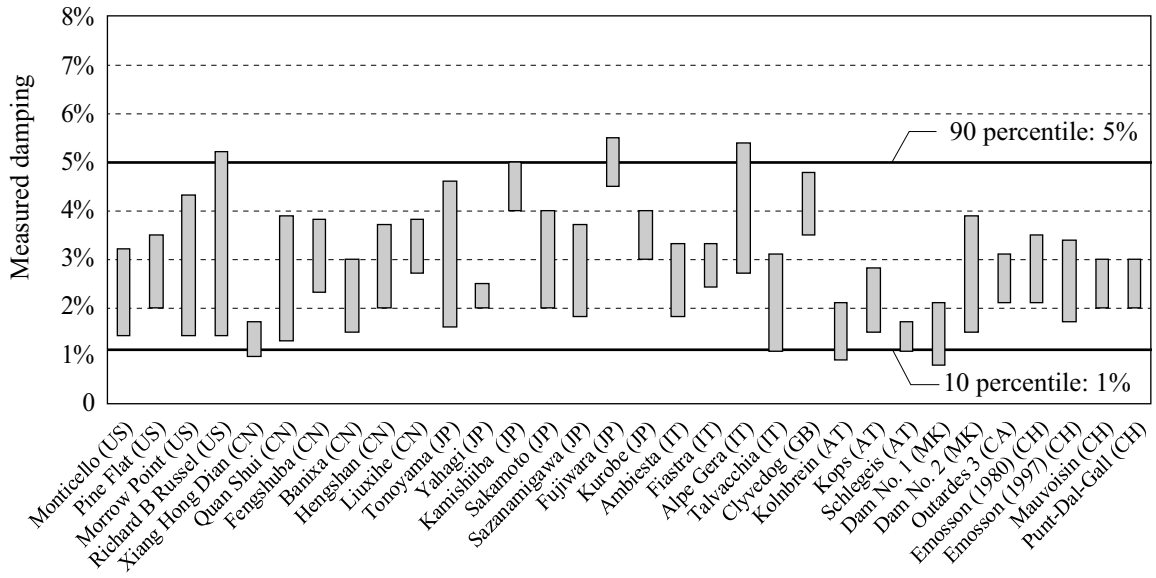

Figure 3.10 **Damping at 32 concrete dams measured during forced vibration field tests and estimated from ambient vibration measurements, compiled from Hall [1988]; Proulx and Paultre [1997]; and Proulx et al. [2004]. The range for each dam shows the minimum and maximum damping values measured in the first few (1 to 5) resonant frequencies. Four data points that were deemed inaccurate in Hall [1988] due to excessive modal interference in the dam response are excluded from the dataset.**

Limiting the overall damping to less than 5% in 2D numerical models is very difficult because of the large amount of radiation damping associated with 2D homogeneous, semi-unbounded foundation models; see Figure 3.4. The additional damping erroneously introduced to the system by using a 2D idealization to represent a 3D gravity dam system can be significant unless the canyon is very wide [Bybordiani and Arici 2017]. Presented in Table 3.1 are examples of total damping in a 2D model of Pine Flat Dam computed by the substructure method [Fenves and Chopra 1984b] for several values of the parameters that characterize energy loss in the system: material damping in the dam, ζ_s; material damping in the foundation, ζ_f; the moduli ratio of the foundation to the dam concrete, E_f / E_s; and the reservoir bottom reflection

coefficient α, which is computed based on rock properties alone to approximately account for water–foundation interaction in the substructure method; see Appendix F. For example, specifying 2% damping in the dam and 2% for the foundation domain (Case 2 in Table 3.1) leads to overall damping of approximately 10% in the 2D numerical model, which is much higher than the 2–4% damping "measured" at Pine Flat Dam during forced vibration tests [Rea et al. 1974].

Observe that it is not possible to achieve consistency with the measured damping values for this dam unless the foundation is much stiffer than concrete, and essentially zero material damping is specified in the dam as well as the foundation. Thus, caution should be exercised when using 2D analysis models to ensure that the overall damping is not excessive. For 2D response spectrum analyses (RSA) [Løkke and Chopra 2015], implemented in the computer program CADAM [Leclerc et al. 2003], which is frequently used in the preliminary phase of design and for safety evaluation of concrete gravity dams, the damping ratio for the first-mode spectral ordinate can be directly specified at a desired level consistent with the measured data in Figure 3.10 (e.g., 5%). Limiting the overall damping in RHA of 2D models in a similar manner is generally not feasible; however, site specific conditions, such as inhomogeneities in the rock, may limit radiation damping. The last recourse is to use 3D numerical models, which also permit realistic modeling of the 3D geometries of gravity dams.

Table 3.1 **Overall damping resulting in a 2D numerical model of Pine Flat Dam computed by the substructure method for several values of the parameters that characterize energy loss in the system.**

	Dam	Foundation rock		Reservoir bottom	Overall damping
Case	ζ_s	E_f / E_s	ζ_f	α	
1	5%	1	5%	0.68	13%
2	2%	1	2%	0.68	10%
3	0%	1	0.5%	0.68	8.5%
4	0%	2	0.5%	0.77	5.0%
5	0%	3	0.5%	0.80	3.7%

4 Nonlinear Earthquake Analysis of Morrow Point Dam

To demonstrate the capabilities and effectiveness of the direct FE method developed in Parts I and II of this report, including the simplifications recommended in Chapter 3, the method is implemented with the commercial FE program ABAQUS; example results of nonlinear RHA are presented herein.

4.1 SYSTEM AND GROUND MOTION

4.1.1 Finite-Element Model of Dam–Water–Foundation Rock System

Chosen for the example analysis is Morrow Point Dam, with properties of the dam–water–foundation rock system as described in Section 5.4 of Part I, but for two exceptions: (1) sediments at the reservoir bottom and sides are not included because their effects on the dynamic response of arch dams are negligible (Section 3.2.3); and (2) material damping in the dam and foundation is modeled by stiffness proportional damping using the degraded elastic stiffness matrix instead of the initial stiffness (Section 3.2.1.1). The damping coefficients $a_{1c} = 1.1 \times 10^{-3}$ and $a_{1r} = 2.2 \times 10^{-3}$ were chosen to give 1% damping in the dam and 2% in the foundation at the first dominant resonance frequency of the dam–water–foundation rock system in the ABAQUS model. These values were determined by trial and error to provide overall damping in the system, determined from the resulting frequency response function, to be consistent with the 1.5–4% damping measured at the first few resonant frequencies during forced vibration tests [Duron and Hall 1988].

The FE model shown in Figure 4.1 consists of 27,600 elements and approximately 64,000 degrees-of-freedom. This includes 4196 solid elements for the dam (with four elements through the thickness of the dam), 14,175 solid elements for the foundation domain, and 9200 acoustic

elements for the fluid domain. A tie constraint couples accelerations with hydrodynamic pressures at the dam–water and water–foundation interfaces, and standard viscous dampers are included at all outer boundaries to model the semi-unbounded extent of the foundation and fluid domains. The overall dimensions of the FE model are 700 m × 700 m × 400 m, corresponding to approx. $5H \times 5H \times 3H$, where H is the height of the dam.

4.1.2 Nonlinear Modeling Parameters

Included in the numerical model are several nonlinear mechanisms based on the review in Section 3.1. Opening and closing of contraction joints [Figure 4.1(a)] is modeled using the "general contact" model in ABAQU, with behavior in the normal direction specified by a zero-tensile-strength contact constraint with an exponential pressure-overclosure relationship given the following properties: initial clearance c_0 = 0.1 mm and contact pressure at zero opening p_0 = 5 MPa. Morrow Point Dam was constructed with large and frequent shear keys that limit relative tangential movements between cantilevers unless the joint opens more than approximately 150 mm (6 in.) [Noble and Nuss 2004b]. The effect of these are modeled by linear springs given very high stiffness to effectively prevent tangential slip at the joint; note that this simple model does not consider the possibility of shear-key failure at the joints.

The dam–foundation rock interface is approximately modeled using a zero-tensile-strength contact constraint to allow opening and closing of this joint, but relative tangential sliding is prevented using linear springs with high stiffness. For simplicity, the effects of weaker planes along lift lines in the dam are not modeled.

Cracking of the dam concrete is modeled by the Lee–Fenves concrete damage model [1998] implemented in ABAQUS, but excluding the possibility of compression failure after an initial analysis confirmed that the maximum compressive stresses are much lower than the compressive strength of concrete. The tensile fracture properties for this model (Figure 4.2) are based on typical values for dam concrete [Brühwiler and Wittmann 1990b; Bhattacharjee and Léger 1992]: tensile strength, f_t = 2.5 MPa and specific fracture energy G_F = 250 N/m (the area under the tensile stress-crack width curve). These static values are increased by a dynamic magnification factor of 1.20 to represent the effects of higher strain rates in the dynamic analysis; thus $f_{t,\mathrm{dyn}}$ = 3.0 MPa and $G_{F,\mathrm{dyn}}$ = 300 N/m.

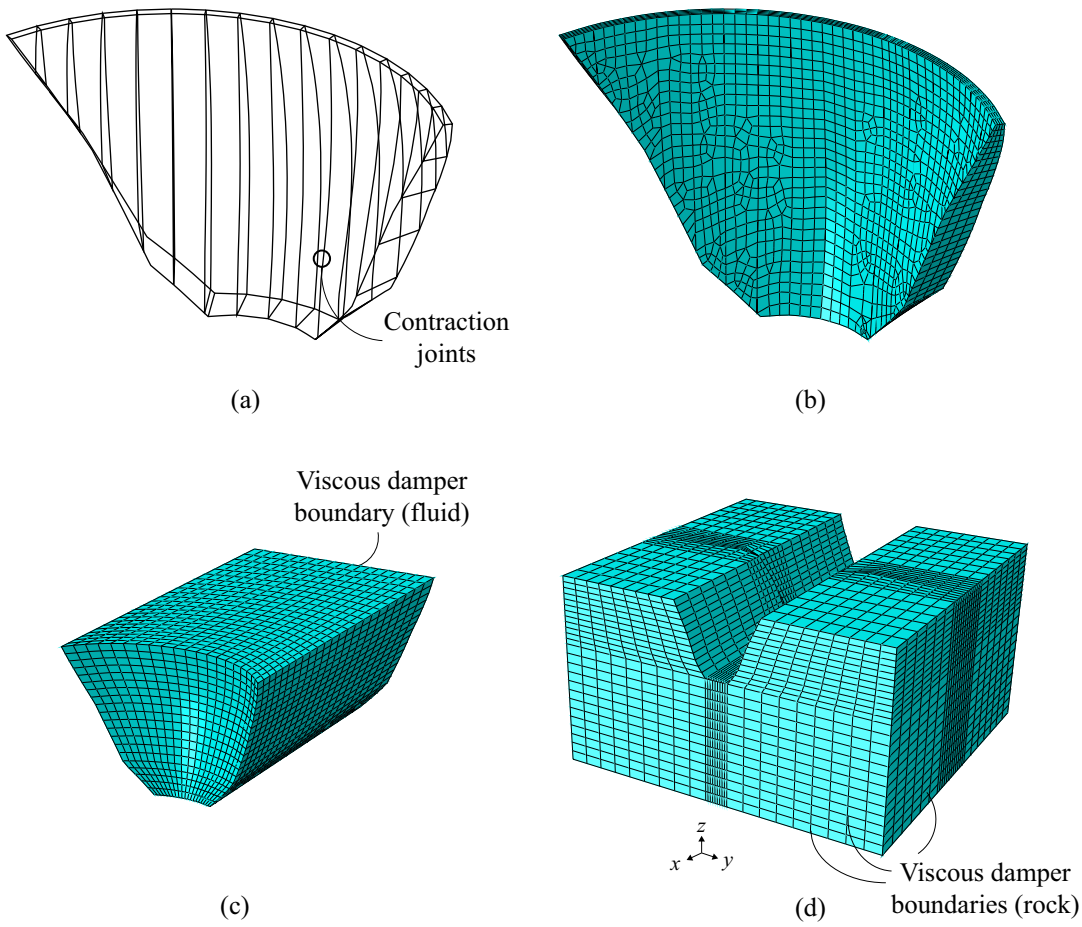

Figure 4.1 **Morrow Point Dam showing (a) location of contraction joints; (b) FE model of dam; (c) FE model of water in reservoir; and (d) FE model of foundation rock.**

The nonlinear dynamic analysis is conducted in ABAQUS/Standard using the implicit HHT-alpha [Hilber et al. 1977] time integration scheme and an automatic time step control that changes the time increment depending on the convergence rate of the solution. Convergence is checked at the end of each time step as the analysis progresses, and in addition, the energy balance error [Bhattacharjee and Léger 1993] is controlled at the end of the analysis to ensure that the overall solution has remained stable.

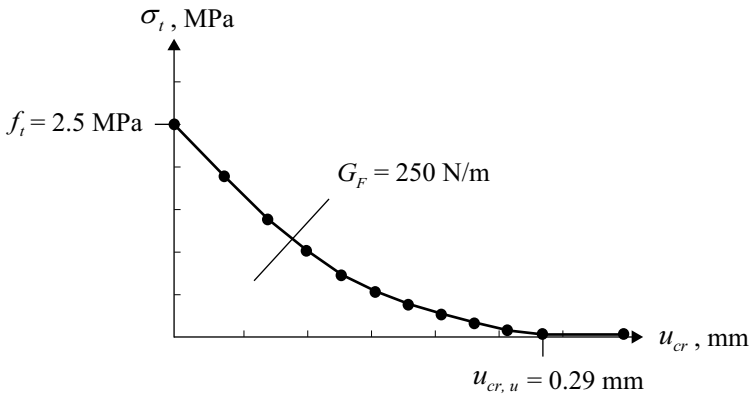

Figure 4.2 Stress-displacement curve for concrete in tension (static values).

4.1.3 Static and Dynamic Loads

An initial static analysis is conducted using a model with outer boundaries of the foundation domain fixed. Gravity loads are applied to the dam cantilevers first, and then the reservoir is filled and hydrostatic pressures applied. Uplift pressures at the dam–foundation rock interface are not modeled. The state of the dam and foundation domain at the end of this static analysis is recorded to define the initial state for the nonlinear dynamic analysis.

The free-field control motion, $a_g^k(t)$, specified at the surface of the foundation domain (at the level of the dam abutments) is defined in the stream, cross-stream, and vertical directions by the S69E, S21W, and vertical components, respectively, of the Taft ground motion. Each component of ground motion is amplitude-scaled by a factor of 2.0; this corresponds to a PGA of approximately 0.35g for the S69E component[†]. From these control motions, the effective earthquake forces to be applied at the absorbing boundaries of the foundation domain are determined by the method described in Section 6.1 of Part II.

4.2 IMPLEMENTATION OF THE DIRECT FE METHOD WITH ABAQUS

The direct FE method has been developed in a form that can be implemented with any commercial FE code. Here we have chosen ABAQUS with a simple pre-processing script in MATLAB developed to interact with the input file to compute and store the effective earthquake

[†] No attempt has been made to select ground motions consistent with the seismic hazard at the site of Morrow Point Dam; thus, the results presented in Section 4.3 are merely illustrative

forces. This procedure is organized in three phases (Figure 4.3): (1) an initial static analysis simulates the sequence of construction of the dam and filling of the reservoir; (2) deconvolution of the control motion followed by analysis of a 1D foundation column determines the free-field motions that are in turn used to compute effective earthquake forces at the bottom and side foundation boundaries; and (3) nonlinear dynamic analysis of the FE model subjected to effective earthquake forces from Step 2, where the results from Step 1 provide the initial state of the system. Thus, the only addition to a "standard" dynamic analysis in ABAQUS is the use of the MATLAB script in Step 2.

This process for setting up the model for nonlinear dynamic analysis is general and can be implemented with any commercial FE code. The process is entirely automated, requiring less than a few minutes to produce an updated input file that, together with the static state of the system, contains all information required for dynamic analysis. Thus, the analysis can easily be set up to run repeatedly for a large number of ground motions or for the same ground motion for a range of input parameters, both of which are required to quantify uncertainty within the PBEE framework; see Chapter 2.

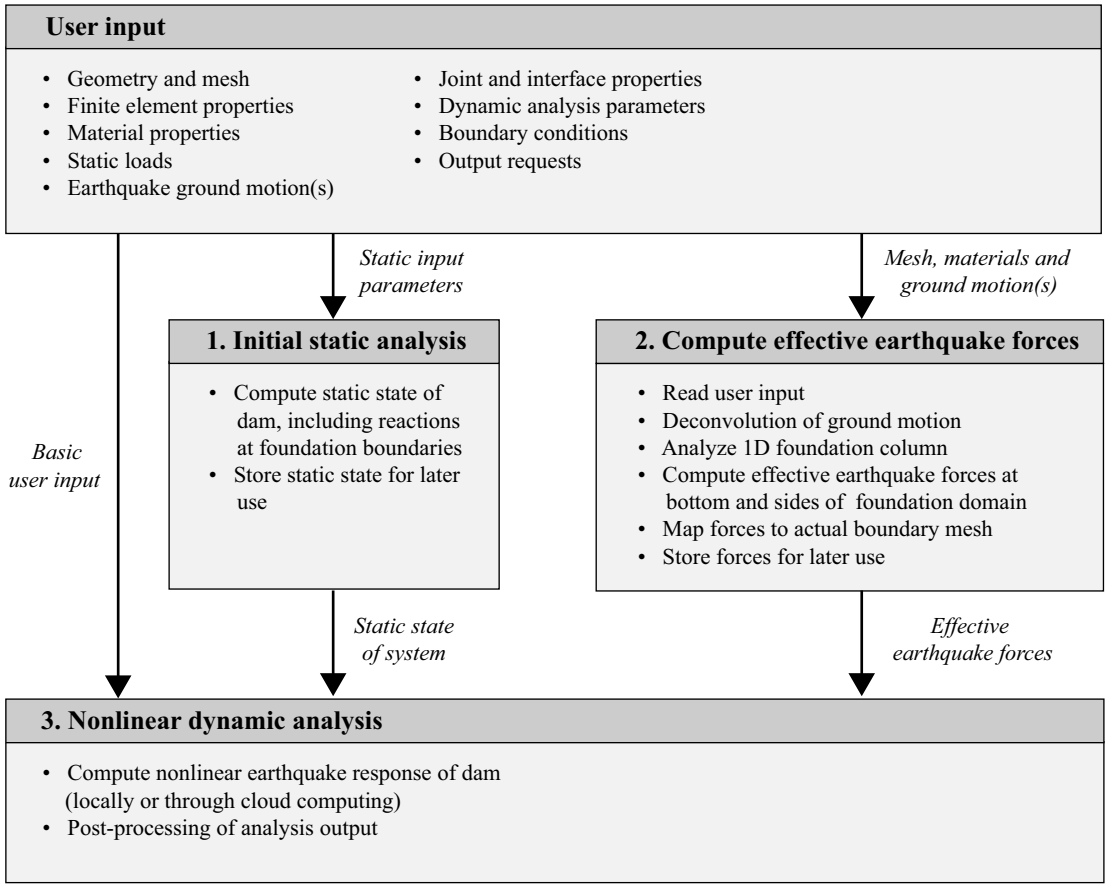

Figure 4.3 Implementation of the direct FE method with a commercial FE program.

4.3 RESULTS FROM NONLINEAR DYNAMIC ANALYSIS

Commercial FE codes can provide results for any response quantity of engineering interest; examples of such output are presented in Figures 4.4–4.8. Displacement response histories in the stream, cross-stream, and vertical directions at the mid-point on the dam crest are shown in Figure 4.4, and envelope values of the stream displacements over the length of the crest in Figure 4.5. Such results are of interest in evaluating the operability of appurtenant structures, such as mechanical equipment, gates, and roadway bridges, over any spillway.

To illustrate the nonlinear contraction joint response, two types of output are presented: response histories for the opening of two contraction joints at the crest level are plotted as a function of time in Figure 4.6, and envelope values of the maximum (over time) opening of all joints at the crest level is presented in Figure 4.7. The maximum opening of any contraction joint

is approximately 25 mm (near the right abutment), which is much less than the 150 mm "depth" of the shear keys, implying that the shear keys remain interlocked during the selected ground motion. Observe also that the maximum joint opening occurs near the right abutment, and not at the center of the dam (Figure 4.7), which illustrates the significance of the cross-stream component of ground motion for this particular system. Had the dam been excited only in the stream and vertical directions, it would have responded much more symmetrically due to its (almost) symmetric design.

The distribution of tensile damage over the two faces of the dam is presented in Figure 4.8. While this is not a direct measurement of cracking in the concrete, it gives an indication of areas to expect cracks in the dam. The tensile damage is greater on the downstream face of the dam and along one side of the dam–foundation rock interface [Figures 4.8(a) and (b)]. The dam is beginning to show signs of a semi-circular crack pattern in the upper, central part of the dam, which has been observed as a potential failure mode during model studies of arch dams [Bureau of Reclamation 2002]; however, no single crack has yet formed through thickness of the dam [Figure 4.8(c)] to fully develop such a failure model.

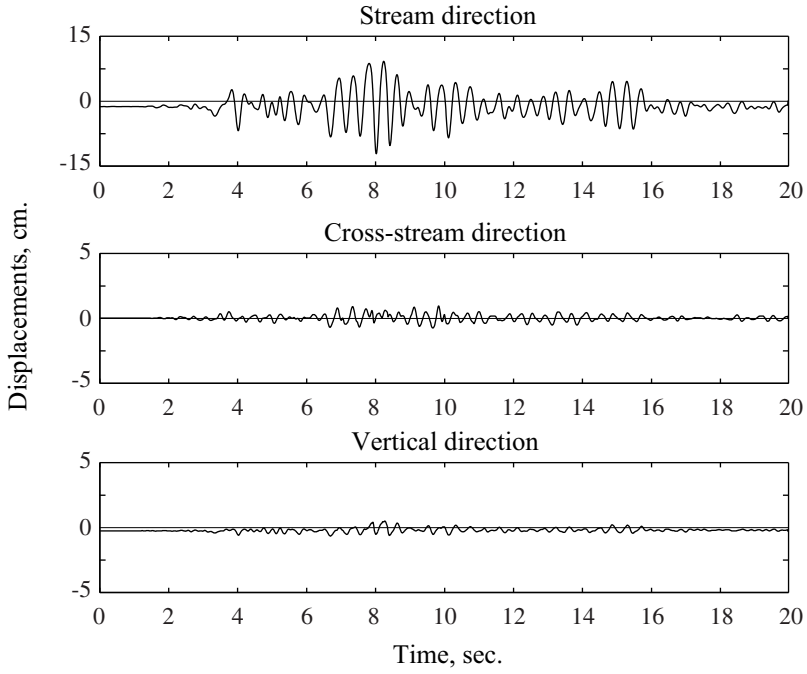

Figure 4.4 **Displacements histories at center of dam crest in the stream, cross-stream and vertical directions, caused by simultaneous application of the S69E, S21W and vertical components of the Taft ground motion.**

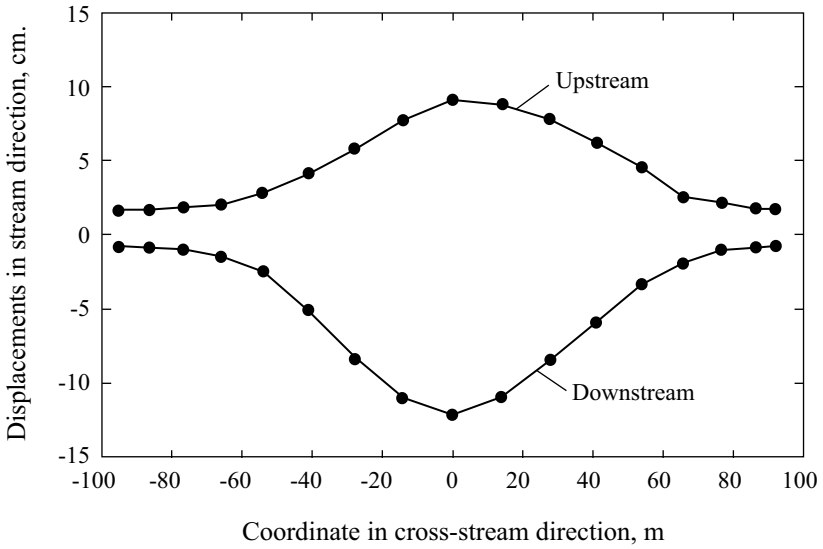

Figure 4.5 **Envelope values of maximum and minimum displacements along dam crest.**

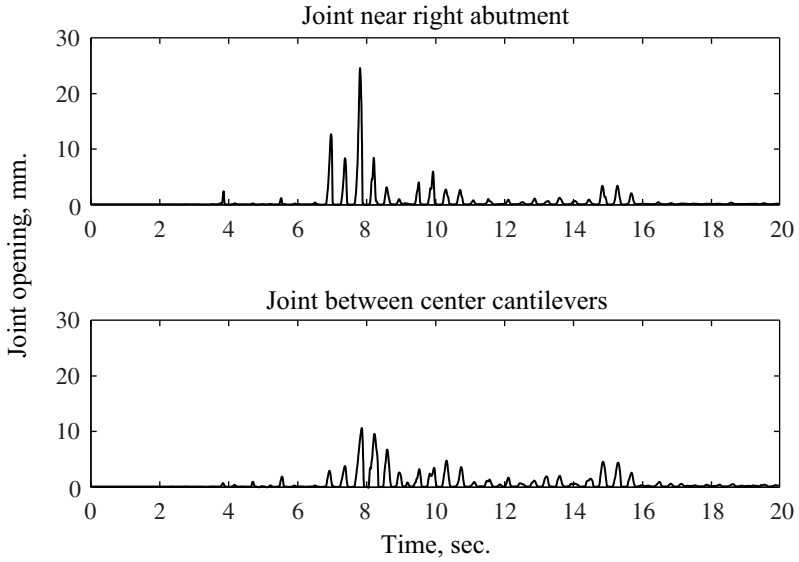

Figure 4.6 **Opening of contraction joints at two locations: at the joint near the right abutment where maximum joint opening occurs, and at the joint between the center cantilevers.**

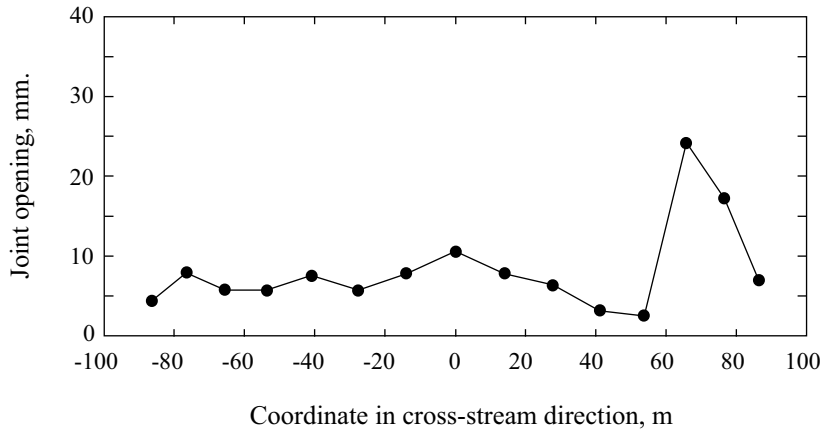

Figure 4.7 **Envelope values of maximum contraction joint opening along the dam crest.**

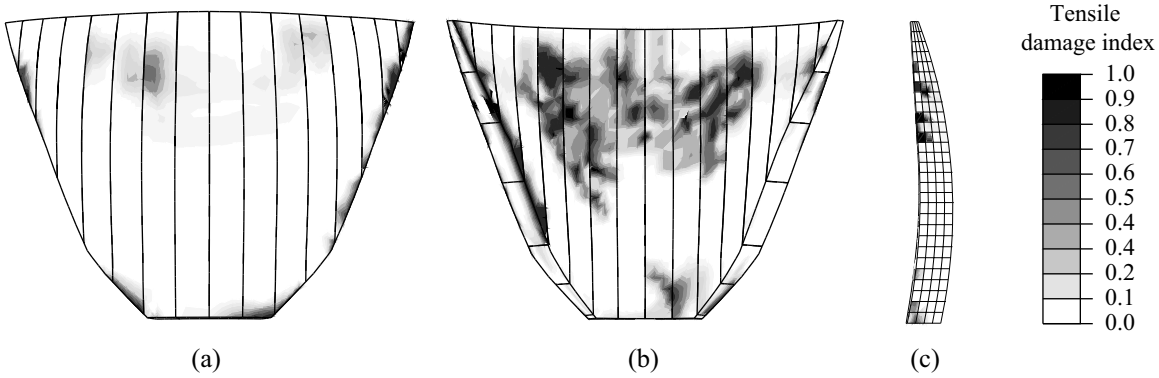

Figure 4.8 **Distribution of tensile damage on (a) upstream face, (b) downstream face; and (c) section through center (crown) cantilever.**

Engineering demand parameters obtained from nonlinear RHA (such as the ones presented in Figures 4.4–4.8) can be systemized to quantify the performance of concrete dams over a wide range of possible scenarios. For example, by doing repeated nonlinear RHA for an ensemble of ground motions scaled to different intensity levels, the SDHC and fragility curves (Sections 2.3–2.4) for the structure can be computed for any *EDP* or *DM* of interest. The effects of uncertainty in input parameters can be estimated by repeated analysis of the system in a tornado-diagram analysis.

The total runtime for the analysis was approximately 15 hours on a local workstation, of which only a few minutes were required for setting up the effective earthquake forces. This runtime can be reduced significantly by deploying the analysis to a high-performance cloud

computing service or a local computing cluster. Such services are especially attractive when a large number of nonlinear analyses are required to consider the inherent uncertainties in ground motions and the material properties of the system.

5 Conclusions

Using the direct FE method for conducting the large number of nonlinear RHAs required for PBEE of concrete dams has been proposed. The discussion and results presented Part III of this report can be summarized as follows:

- The state-of-research for PBEE of concrete dams is behind that for other classes of structures such as buildings and nuclear power plants. Two factors that have contributed to this situation are: (1) the deficiencies in commonly used procedures for RHA of concrete dams; and (2) the lack of knowledge about the nonlinear behavior and failure mechanisms of concrete dams during earthquakes. Development of the direct FE method addresses the first of these issues.
- Sediments at the reservoir boundaries—modeled as a viscoelastic material—have negligible influence on the response of gravity dams as well as arch dams when water–foundation rock interaction and the associated radiation damping is included in the analysis. Thus, at the present time, it appears reasonable to ignore sediments in analysis of dam–water–foundation systems using the direct FE method.
- Based on "measured" data at 32 concrete dams, the overall damping in the numerical model of the dam–water–foundation rock system should not exceed 5% unless a larger value was measured at the dam to be analyzed. Specifying viscous damping ratios in the range of 1–2% for the dam alone and 1–4% for the foundation domain is likely to lead to overall damping that is consistent with these measure values. Consequently, the common practice of specifying 5% viscous damping for the dam and a similar value for the foundation should

be abandoned because it would significantly underestimate the earthquake response of dams.

- The direct FE method has been developed in a form that can be implemented in any commercial FE code; an example analysis implemented in ABAQUS has been presented. The procedure is entirely automated, and requires less than a few minutes of computation to produce an updated input file that—together with the static state of the system—contains all information required for dynamic analysis. The effectiveness of the procedure makes it attractive for conducting the large number of nonlinear RHAs required to recognize the uncertainties in ground motions and the material properties of the system.

Evaluating the seismic performance of concrete dams subjected to ground motions intense enough to cause damage is a very challenging problem. Although commercial FE programs contain models and material libraries capable of modeling a wide range of nonlinear mechanisms, experience in their application is limited. Quantitative measures for the extent of damage—cracking in concrete, sliding at lift joints or at cracked interfaces, and opening of contraction joints—that dams can sustain while still retaining the impounded water are lacking. A great deal of innovative experimental, modeling, and analytical research must yet be done to accurately model the nonlinear behavior of mass concrete, rock, and joints; and extensive numerical parameter studies must be performed to better understand the factors that control the seismic safety of concrete dams.

REFERENCES

Alves S.W., Hall J.F. (2006). Generation of spatially nonuniform ground motion for nonlinear analysis of a concrete arch dam, *Earthq. Eng. Struct. Dyn.,* 35(11): 1339–1357. DOI: 10.1002/eqe.576.

ATC (1996). Seismic evaluation and retrofit of concrete buildings, *Report No. ATC-40*, Applied Technology Council, Redwood City, CA.

Ayari M.L., Saouma V. (1990). A fracture mechanics based seismic analysis of concrete gravity dams using discrete cracks, *Eng. Fract. Mech.*, 35(1–3): 587–598. DOI: 10.1016/0013-7944(90)90233-7.

Aydinoglu M.N. (1993). Consistent formulation of direct and substructure methods in nonlinear soil-structure interaction, *Soil Dyn. Earthq. Eng.*, 12(7): 403–410. DOI: 10.1016/0267-7261(93)90003-A.

Baker J.W. (2011). Conditional mean spectrum: Tool for ground motion selection, ASCE, *J. Struct. Eng.,* 137(3): 322–331. DOI: 10.1061/(ASCE)ST.1943-541X.0000215.

Baker J.W. (2015). Efficient analytical fragility function fitting using dynamic structural analysis, *Earthq. Spectra*, 31(1): 579–599. DOI: 10.1193/021113EQS025M.

Bao H., Bielak J., Ghattas O., Kallivokas L.F., O'Hallaron D.R., Shewchuk J.R.,Xu, J. (1998). Large-scale simulation of elastic wave propagation in heterogeneous media on parallel computers. *Comp. Meth. Appl. Mech. Eng*., 152(1–2): 85–102. DOI: 10.1016/S0045-7825(97)00183-7.

Basu U. (2004). *Perfectly Matched Layers for Acoustic and Elastic Waves: Theory, Finite-Element Implementation and Application to Earthquake Analysis of Dam-Water-Foundation Rock Systems*, Ph.D thesis, Department of Civil and Environmental Engineering, University of California, Berkeley, CA.

Basu U. (2009). Explicit finite element perfectly matched layer for transient three-dimensional elastic waves, *Int. J. Numer. Meth. Eng.,* 77(2): 151–176. DOI: 10.1002/nme.2397.

Basu U., Chopra A.K. (2003). Perfectly matched layers for time-harmonic elastodynamics of unbounded domains: Theory and finite-element implementation, *Comp. Meth. Appl. Mech. Eng.,* 192(11–12): 1337–1375. DOI: 10.1016/S0045-7825(02)00642-4.

Basu U., Chopra A.K. (2004). Perfectly matched layers for transient elastodynamics of unbounded domains, *Int. J. Numer. Meth. Eng.,* 59(8): 1039–1074. DOI: 10.1002/nme.896.

Belytschko T., Black T. (1999). Elastic crack growth in finite elements with minimal remeshing, *Int. J. Numer. Meth. Eng.,* 45(5): 601–620. DOI: 10.1002/(SICI)1097-0207(19990620)45:5<601:AID-NME598>3.0.CO;2-S.

Bhattacharjee S.S., Léger P. (1992). Concrete constitutive models for nonlinear seismic analysis of gravity dams - state-of-the-art, *Can. J. Civil Eng.*., 19(3): 492–509. DOI: 10.1139/l92-059.

Bhattacharjee S.S., Léger P. (1993). Seismic cracking and energy dissipation in concrete gravity dams, *Earthq. Eng. Struct. Dyn.,* 22(11): 991–1007. DOI: 10.1002/eqe.4290221106.

Bielak J., Christiano P. (1984). On the effective seismic input for non-linear soil-structure interaction systems, *Earthq. Eng. Struct. Dyn.,* 12(3): 107–119. DOI: 10.1002/eqe.4290120108.

Bielak J., Loukakis K., Hisada Y., Yoshimura C. (2003). Domain reduction method for three-dimensional earthquake modeling in localized regions, Part I: Theory, *Bull. Seismol. Soc. Am.*, 93(2): 817–824. DOI: 10.1785/0120010251.

Bougacha S., Tassoulas J.L. (1991). Seismic analysis of gravity dams. I: Modeling of sediments, *J. Eng Mech.*, 117(8): 1826–1837. DOI: 10.1061/(ASCE)0733-9399(1991)117:8(1826).

Brinkgreve R., Engin E., Swolfs W.M. (2016). Plaxis Reference Manual, Plaxis BV, The Netherlands.

Brühwiler E. (1990). Fracture of mass concrete under simulated seismic action, *Dam Eng.,* 1990; 1(3): 153–176.

Brühwiler E, Wittmann F.H. (1990a). The wedge splitting test, a new method of performing stable fracture mechanics tests, *Eng. Fract. Mech*., 35(1–3): 117–125. DOI: 10.1016/0013-7944(90)90189-N.

Brühwiler E., Wittmann F H. (1990b). Failure of dam concrete subjected to seismic loading conditions, *Eng. Fract. Mech*., 35(1–3): 565–571. DOI: 10.1016/0013-7944(90)90231-5.

Bureau of Reclamation (2002). Investigation of the failure modes of concrete dams - physical model tests, U.S. Department of the Interior, *Report No. DSO-02-02*, Denver, CO.

Bureau of Reclamation (2013). *State-of-Practice for the Nonlinear Analysis of Concrete Dams,* U.S. Department of the Interior, Denver, CO.

Bybordiani M., Arıcı Y. (2017). The use of 3D modeling for the prediction of the seismic demands on the gravity dams, *Earthq. Eng. Struct. Dyn.,* 46(11): 1769–1789. DOI: 10.1002/eqe.2880.

Cervera M, Oliver J, Faria R. (1995) Seismic evaluation of concrete dams via continuum damage models, *Earthq. Eng. Struct. Dyn.,* 24(9): 1225–1245. DOI: 10.1002/eqe.4290240905.
Chávez J.W., Fenves G. (1995a). Earthquake response of concrete gravity dams including base sliding, ASCE, *J. Struct. Eng.,* 121(5): 865–875. DOI: 10.1061/(ASCE)0733-9445(1995)121:5(865).
Chávez J.W., Fenves G. (1995b). Earthquake analysis of concrete gravity dams including base sliding, *Earthq. Eng. Struct. Dyn.,* 24(5): 673–686. DOI: 10.1002/eqe.4290240505.
Chopra A.K. (1967). Hydrodynamic pressures on dams during earthquakes, ASCE, *J. Eng Mech. Div.*, 93(6): 205–224.
Chopra A.K. (2012). Earthquake analysis of arch dams: Factors to be considered, ASCE, *J. Struct. Eng.*, 138(2): 205–214. DOI: 10.1061/(ASCE)ST.1943-541X.0000431.
Chopra A.K. (2012). *Dynamics of Structures: Theory and Applications to Earthquake Engineering*, 4th ed., Prentice Hall, Upper Saddle River, NJ.
Chopra A.K., Wang J.T. (2009). Earthquake response of arch dams to spatially varying ground motion, *Earthq. Eng. Struct Dyn*., 39(8): 887–906. DOI: 10.1002/eqe.974.
Chopra A.K., Zhang L. (1991). Earthquake-induced base sliding of concrete gravity dams, ASCE, *J. Struct. Eng.,* 117(12): 3698–3719.
Clayton R., Engquist B. (1977). Absorbing boundary conditions for acoustic and elastic wave equations, *Bull. Seismol. Soc. Am.*, 67(6): 1529–1540.
Clough R.W. (1980). Nonlinear mechanisms in the seismic response of arch dams, *Proceedings, International Reserach Conference on Earthquake Engineering*, Skopje, Yugoslavia.
Cook R.D., Malkus D.S., Plesha M.E., Witt R.J. (2007). *Concepts and Applications of Finite Element Analysis*, 4th ed., John Wiley & Sons, New York.
Cvijanovic V., Schultz M., Armstrong R. (2014). Application of nonlinear analysis methods to hydraulic structures subject to extreme loading conditions, *Proceedings, 34th Annual USSD Conference*, San Francisco, CA.
Cornell C.A., Krawinkler H. (2000). Progress and challenges in seismic performance assessment. *PEER Center News*, 3(2): 1–3.
Curtis D.D., Sooch G., Brewer T., Schildmeyer A. (2013). Explicit seismic analysis of Mossyrock Dam, *Proceedings, 33rd Annual USSD Conference*, Phoenix, AZ.
Dasgupta G., Chopra A.K. (1979). Dynamic stiffness matrices for viscoelastic half planes, *J. Eng. Mech. Div*., 105(5): 729–745.
Dassault Systems (2013). *Abaqus/Standard User's Manual*, version 6.13.
Der Kiureghian A. (2005). Non-ergodicity and PEER's framework formula, *Earthq. Eng. Struct. Dyn.,* 34(13): 1643–1652.
Domínguez J., Gallego R., Japón B.R. (1997). Effects of porous sediments on seismic response of concrete gravity dams, ASCE, *J. Eng. Mech.*, 123(4): 302–311. DOI: 10.1061/(ASCE)0733-9399(1997)123:4(302).
Douglas J., Aochi H. (2008). A survey of techniques for predicting earthquake ground motions for engineering purposes, *Surv. Geophys.*, 29(3): 187–220. DOI: 10.1007/s10712-008-9046-y.
Dowling M.J., Hall J.F. (1989). Nonlinear seismic analysis of arch dams, ASCE, *J. Eng. Mech.* 115(4): 768–789.
Duron Z.H., Hall J.F. (1988). Experimental and finite element studies of the forced vibration response of Morrow Point Dam, *Earthq. Eng. Struct. Dyn.,* 16(7): 1021–1039.
El-Aidi B., Hall J.F. (1989). Non-linear earthquake response of concrete gravity dams part 1: modelling, *Earthq. Eng. Struct. Dyn.,* 18(6): 837–851. DOI: 10.1002/eqe.4290180607.
Engquist B., Majda A. (1977). Absorbing boundary conditions for numerical simulation of waves, *Proceedings, National Academy of Sciences*, 74(5): 1765–1766.
FEMA (1997). NEHRP guidelines for the seismic rehabilitation of buildings. *Report No. FEMA-273*, Federal Emergency Management Agency, Washington, D.C.
Fenves G, Chopra A.K. (1983). Effects of reservoir bottom absorption on earthquake response of concrete gravity dams, *Earthq. Eng. Struct. Dyn.,* 11(6): 809–829. DOI: 10.1002/eqe.4290110607.
Fenves G., Chopra A.K. (1984a). Earthquake analysis and response of concrete gravity dams, *Report No. UCB/EERC-84/10*, Earthquake Engineering Research Center, University of California, Berkeley, CA.
Fenves G., Chopra A.K. (1984b). EAGD-84: A computer program for earthquake analysis of concrete gravity dams, *Report No. UCB/EERC-84/11*, Earthquake Engineering Research Center, University of California, Berkeley, CA.

Fenves G., Chopra A.K. (1984c). Earthquake analysis of concrete gravity dams including reservoir bottom absorption and dam-water-foundation rock interaction, *Earthq. Eng. Struct. Dyn.,* 12(5): 663–680. DOI: 10.1002/eqe.4290120507.

Fenves G, Chopra A.K. (1985) Effects of reservoir bottom absorption and dam-water-foundation rock interaction on frequency response functions for concrete gravity dams, *Earthq. Eng. Struct. Dyn.,* 1985; 13(1): 13–31. DOI: 10.1002/eqe.4290130104.

Fenves G., Mojtahedi S., Reimer R.B. (1992). Effect of contraction joints on earthquake response of an arch dam, ASCE, *J. Struct. Eng.,* 118(4): 1039–1055. DOI: 10.1061/(ASCE)0733-9445(1992)118:4(1039).

Field E.H., Jordan T.H., Cornell C.A. (2003). OpenSHA: a developing community-modeling environment for seismic hazard analysis. *Seismol. Res. Lett.,* 74(4): 406–419. DOI: 10.1785/gssrl.74.4.406.

Fok K.L., Chopra A.K. (1986). Hydrodynamic and foundation flexibility effects in earthquake response of arch dams, ASCE, *J. Struct. Eng.,* 112(8): 1810–1828. DOI: 10.1061/(ASCE)0733-9445(1986)112:8(1810).

Fronteddu L., Léger P., Tinawi R. (1998). Static and dynamic behavior of concrete lift joint interfaces, ASCE, *J. Struct. Eng.,* 1998; 124(12): 1418–1430. DOI: 10.1061/(ASCE)0733-9445(1998)124:12(1418).

García F., Aznárez J.J., Padrón L.A., Maeso O. (2016). Relevance of the incidence angle of the seismic waves on the dynamic response of arch dams, *Soil Dyn. Earthq. Eng.*, 90: 442–453. DOI: 10.1002/eqe.4290201104.

Gazetas G. Dynamic compliance matrix of rigid strip footing bonded to a viscoelastic cross anisotropic halfspace. *Int. J. Mech. Sci.,* 1981; 23(9): 547–559. DOI: 10.1016/0020-7403(81)90060-6.

Ghanaat Y., Patev R., Chudgar A. (2012). Seismic fragility analysis of concrete gravity dams, *Proceedings, 15th World Conference on Earthquake Engineering*, Lisbon, Portugal.

Goodman R.E., Taylor R.L., Brekke T.L. (1968). A model for the mechanics of jointed rock, ASCE, *J. Soil Mech. Found. Div*., 94(3): 637–660.

Goldgruber M. (2015). *Nonlinear Seismic Modelling of Concrete Dams*, Ph.D. thesis, Graz University of Technology, Graz, Switzerland. DOI: 10.13140/RG.2.1.3001.6485.

Goulet C.A., Haselton C.B., Mitrani-Reiser J., Beck J.L., Deierlein G.G., Porter K.A., Stewart, J.P. (2007). Evaluation of the seismic performance of a code-conforming reinforced-concrete frame building—from seismic hazard to collapse safety and economic losses, *Earthq. Eng. Struct. Dyn.,* 36(13): 1973–1997. DOI: 10.1002/eqe.694.

Graves R.W. (1996). Simulating seismic wave propagation in 3D elastic media using staggered-grid finite differences, *Bull. Seismol. Soc. Am.*, 86(4): 1091–1106.

Hall J.F. (1988). The dynamic and earthquake behaviour of concrete dams: review of experimental behaviour and observational evidence, *Soil Dyn. Earthq. Eng.*, 7(2): 58–121. DOI: 10.1016/S0267-7261(88)80001-0.

Hall J.F. (2006). Problems encountered from the use (or misuse) of Rayleigh damping, *Earthq. Eng. Struct. Dyn.,* 35(5): 525–545. DOI: 10.1002/eqe.541.

Hall J.F., Chopra A.K. (1982). Hydrodynamic effects in the dynamic response of concrete gravity dams, *Earthq. Eng. Struct. Dyn.,* 10(2): 333–345. DOI: 10.1002/eqe.4290100212.

Hall J.F., Chopra A.K. (1983). Dynamic analysis of arch dams including hydrodynamic effects, ASCE, *J. Eng. Mech.,*109(1): 149–167.

Hallquist J.O. (2016). *LS-DYNA Keyword User's Manual*, Livermore Software Technology Corporation, Livermore, CA.

Hamilton E.L. (1971). Elastic properties of marine sediments. *J. Geophy. Res.,* 76(2): 579–604. DOI: 10.1029/JB076i002p00579.

Hariri-Ardebili M.A. (2015). *Performance Based Earthquake Engineering of Concrete dams*, Ph.D. thesis, University of Colorado, Boulder, CO.

Hariri-Ardebili M.A., Saouma V.E. (2016a). Collapse fragility curves for concrete dams: comprehensive study, ASCE, *J. Struct. Eng.,* 142(10): 04016075. DOI: 10.1061/(ASCE)ST.1943-541X.0001541.

Hariri-Ardebili M.A., Saouma V.E. (2016b). Sensitivity and uncertainty quantification of the cohesive crack model, *Eng. Fract. Mech.,* 155: 18–35. DOI: 10.1016/j.engfracmech.2016.01.008.

Hariri-Ardebili M.A., Saouma V.E., Porter K.A. (2016). Quantification of seismic potential failure modes in concrete dams, *Earthq. Eng. Struct. Dyn.,* 45(6): 979–997. DOI: 10.1002/eqe.2697.

Haselton C.B. (2009). Evaluation of ground motion selection and modification methods: predicting median interstory drift response of buildings. *Report No. PEER 2009/01*, Pacific Earthquake Engineering Research Center, University of California, Berkeley, CA.

Hashash Y.M.A., Groholski D.R., Phillips C.A., Park D., Musgrove M. (2011). *DEEPSOIL User Manual and Tutorial*, Version 5.0, University of Illinois, Urbana, IL.
Hatami K. (1997). Effect of reservoir bottom on earthquake response of concrete dams, *Soil Dyn. Earthq. Eng.*, 16(7–8): 407–415. DOI: 10.1016/S0267-7261(97)00023-7.
He C., Wang J.T., Zhang C.H. (2016). Nonlinear spectral-element method for 3D seismic-wave propagation, *Bull. Seismol. Soc. Am.*, 106(3): 1074–1087. DOI: 10.1785/0120150341.
Herrera I., Bielak J. (1977). Soil-structure interaction as a diffraction problem, *Proceedings, 6th World Conference on Earthquake Engineering*, Vol. 2, New Delhi, India.
Higdon R.L. (1986). Absorbing boundary conditions for difference approximations to the multi-dimensional wave equation, *Math. Comput.*, 47(176): 437–459. DOI: 10.1090/S0025-5718-1986-0856696-4.
Higdon R.L. (1987). Numerical absorbing boundary conditions for the wave equation, *Math. Comput.,* 49(179): 65–90. DOI: 10.1090/S0025-5718-1987-0890254-1.
Hilber H.M., Hughes T.J.R., Taylor R.L. (1977). Improved numerical dissipation for time integration algorithms in structural dynamics, *Earthq. Eng. Struct. Dyn.,* 5(3): 283–292. DOI: 10.1002/eqe.4290050306.
Itasca Consulting Group Inc. (2012). *FLAC3D - Fast Lagrangian Analysis of Continua in Three-Dimensions*, Ver. 5.0., Minneapolis, MN.
Joyner W.B., Chen A.T.F. (1975). Calculation of nonlinear ground response in earthquakes, *Bull. Seismol. Soc. Am.*, 65(5): 1315–1336.
Katsanos E.I., Sextos A.G., Manolis G.D. (2010). Selection of earthquake ground motion records: A state-of-the-art review from a structural engineering perspective, *Soil Dyn. Earthq. Eng.*, 30(4): 157–169. DOI: 10.1016/j.soildyn.2009.10.005.
Kausel E., Tassoulas J.L. (1981). Transmitting boundaries: A closed-form comparison, *Bull. Seismol. Soc. Am.*, 71(1): 143–159.
Kellezi L. (2000). Local transmitting boundaries for transient elastic analysis, *Soil Dyn. Earthq. Eng.*, 19(7): 533–547. DOI: 10.1016/S0267-7261(00)00029-4.
Kontoe S., Zdravkovic L., Potts D.M. (2009). An assessment of the domain reduction method as an advanced boundary condition and some pitfalls in the use of conventional absorbing boundaries, *Int. J. Numer. Analy. Meth. Geomech.,* 33(3): 309–330.
Kwong N.S., Chopra A.K. (2017). A generalized conditional mean spectrum and its application for intensity-based assessments of seismic demands, *Earthq. Spectra*, 33(1): 123–143. DOI: 10.1193/040416EQS050M.
Kwong N.S., Chopra A.K. (2018). Determining bi-directional ground motions for nonlinear response history analysis of buildings at far-field sites, *Earthq. Spectra*, 34(4). DOI: 10.1193/052217EQS093M.
Kwong N.S., Chopra A.K., McGuire R.K. (2015). A framework for the evaluation of ground motion selection and modification procedures, *Earthq. Eng. Struct. Dyn.,* 44(5): 795–815. DOI: 10.1002/eqe.2502.
Kramer S.L. (1996). *Geotechnical Earthquake Engineering*. Vol. 6. 1st ed., Prentice Hall, Upper Saddle River, NJ, DOI: 10.1007/978-3-540-35783-4.
Kuhlemeyer R.L., Lysmer J. (1973). Finite element method accuracy for wave propagation problems, ASCE, *J. Soil Mech. Found. Div*., 99(5): 421–427.
Lau D.T., Noruziaan B., Razaqpur A.G. (1998). Modelling of contraction joint and shear sliding effects on earthquake response of arch dams, *Earthq. Eng. Struct. Dyn.,* 27(10): 1013–1029. DOI: 10.1002/(SICI)1096-9845(199810)27:10<1013::AID-EQE765>3.0.CO;2-0.
Leclerc M., Léger P., Tinawi R. (2003). Computer aided stability analysis of gravity dams-CADAM, *Adv. Eng. Softw.*, 34(7): 403–420. DOI: 10.1016/S0965-9978(03)00040-1.
Lee J., Fenves G. (1998). A plastic-damage concrete model for earthquake analysis of dams, *Earthq. Eng. Struct. Dyn.,* 27(9): 937–956. DOI: 10.1002/(SICI)1096-9845(199809)27:9<937::AID-EQE764>3.0.CO;2-5.
Léger P., Katsouli M. (1989). Seismic stability of concrete gravity dams, *Earthq. Eng. Struct. Dyn.,* 1989; 18(6): 889–902. DOI: 10.1002/eqe.4290180611.
Lemos J.V. (1999). Discrete element analysis of dam foundations. in *Distinct Element Modelling in Geomechanics*, Rotterdam: Balkema.
Lemos J.V. (2008). Block modelling of rock masses: concepts and application to dam foundations, Eur. J. Environ. Civil. Eng., 12(7–8): 915–949. DOI: 10.1080/19648189.2008.9693054.
Liao Z.P., Wong H.L. (1984). A transmitting boundary for the numerical simulation of elastic wave propagation, *Soil Dyn. Earthq. Eng.*, 3(4): 174–183. DOI: 10.1016/0261-7277(84)90033-0.

Løkke A. (2013). *User Manual: Pre- and Post-Processing Modules to Facilitate Analysis with EAGD*, NISEE, Earthquake Engineering Research Center, University of California, Berkeley, CA.
Løkke A., Chopra A.K. (2015). Response spectrum analysis of concrete gravity dams including dam-water-foundation interaction, ASCE, *J. Struct. Eng.,* 2015; 141(8): 04014202. DOI: 10.1061/(ASCE)ST.1943-541X.0001172.
Løkke A., Chopra A.K. (2018). Direct finite element method for nonlinear earthquake analysis of 3-dimensional semi-unbounded dam-water-foundation rock systems, *Earthq. Eng. Struct. Dyn.,* 47(5): 1309–1328. DOI: 10.1002/eqe.3019.
Lotfi V., Roesset J.M., Tassoulas J.L. (1987). A technique for the analysis of the response of dams to earthquakes, *Earthq. Eng. Struct. Dyn.,* 15(4): 463–489. DOI: 10.1002/eqe.4290150405.
Luco J.E , Westmann R A. (1972). Dynamic response of a rigid footing bonded to an elastic half space. *J. Appl. Mech*., 39(2): 527–534.
Lysmer J., Kuhlemeyer R.L. (1969). Finite dynamic model for infinite media, ASCE, *J. Eng. Mech. Div.,* 95(4): 859–878.
Lysmer J., Waas G. (1972). Shear waves in plane infinite structures, ASCE, *J. Eng. Mech. Div*. 98(1): 85–105.
Maeso O., Aznárez J.J, Domínguez J. (2002). Effects of space distribution of excitation on seismic response of arch dams, ASCE, *J. Eng. Mech*., 128(7): 759–768. DOI: 10.1061/(ASCE)0733-9399(2002)128:7(759).
Maeso O., Aznárez J.J, Domínguez J. (2004). Three-dimensional models of reservoir sediment and effects on the seismic response of arch dams, *Earthq. Eng. Struct. Dyn.,* 33(10): 1103–1123. DOI: 10.1002/eqe.392.
McGuire R.K. (2004). *Seismic Hazard and Risk Analysis*. Earthquake Engineering Research Institute, Oakland, CA.
McKenna F. (2011). OpenSees: A framework for earthquake engineering simulation, *Comput. Sci. Eng.,* 13(4): 58–66. DOI: 10.1109/MCSE.2011.66.
Medina F., Dominguez J., Tassoulas J.L. (1990). Response of dams to earthquakes including effects of sediments, ASCE, *J. Struct. Eng.,* 116(11): 3108–3121. DOI: 10.1061/(ASCE)0733-9445(1990)116:11(3108).
Meek J.W., Wolf J.P. (1993). Why cone models can represent the elastic half-space, *Earthq. Eng. Struct. Dyn.,* 122(9): 759–771. DOI: 10.1002/eqe.4290220903.
Mejia L.H., Dawson E.M. (2006). Earthquake deconvolution for FLAC, *Proceedings, the 4th International FLAC Symposium on Numerical Modeling in Geomechanics*, Lima, Peru.
Mills-Bria B., Nuss L., Chopra A.K. (2008). Current methodology at the Bureau of Reclamation for the nonlinear analyses of arch dams using explicit finite element techniques, *Proceedings, 14th World Conference on Earthquake Engineering*, Beijing, China.
Mlakar P.F. (1987). Nonlinear response of concrete gravity dams to strong earthquake-induced ground motion, *Comp. Struct.*, 26(1–2): 165–173.
Moczo P., Kristek J., Galis M., Pazak P., Balazovjech M. (2007). The finite-difference and finite-element modeling of seismic wave propagation and earthquake motion, *Acta Physica Slovaca*, 57(2): 177–406.
Moehle J.P. Deierlein G.G. (2004). A framework methodology for performance-based earthquake engineering, *Proceedings, 13th World Conference on Earthquake Engineering*, Vol. 679, Vancouver, Canada.
Nielsen A.H. (2006). Absorbing boundary conditions for seismic analysis in ABAQUS, *Proceedings, 2006 ABAQUS Users' Conference*, Boston, MA.
Nielsen A.H. (2014). Towards a complete framework for seismic analysis in ABAQUS, *Proceedings, Institution of Civil Engineers–Engineering and Computational Mechanics*, 167(1): 3–12. DOI: 10.1680/eacm.12.00004.
Niwa A., Clough R.W. (1982). Non-linear seismic response of arch dams, *Earthq. Eng. Struct. Dyn.,* 10(2): 267–281. DOI: 10.1002/eqe.4290100208.
Noble C.R., Nuss L. (2004). Implicit and explicit nonlinear dynamic analysis of a large thin-arch dam using massively parallel computing, *Proceedings, 13th World Conference on Earthquake Engineering*, Vancouver, Canada.
Noble C.R., Nuss L. (2004). Nonlinear seismic analysis of Morrow Point Dam, *Proceedings, 13th World Conference on Earthquake Engineering*, Vancouver, Canada.
Nuss L. (20010. Comparison of EACD3D96 computed response to shaker tests on Morrow Point Dam, Bureau of Reclamation, *Technical Memorandum No. MP-D8110-IE-2001-2*, Denver, CO.
Ordóñez G.A. (2000). SHAKE2000: A computer program for the 1D analysis of geotechnical earthquake engineering problems, Geomotions, L.L.C., Lacey WA.

Pan J.W., Zhang C.H., Xu Y., Jin F. (2011). A comparative study of the different procedures for seismic cracking analysis of concrete dams, *Soil Dyn. Earthq. Eng.*, 31(11): 1594–1606. DOI: 10.1016/j.soildyn.2011.06.011.

Pekau O.A., Chuhan Z., Lingmin F. (1991). Seismic fracture analysis of concrete gravity dams, *Earthq. Eng. Struct. Dyn.,* 20(4): 335–354. DOI: 10.1002/eqe.4290200404.

Porter K.A. (2003). An overview of PEER's performance-based earthquake engineering methodology, *Proceedings, 9th International Conference on Applications of Statistics and Probability in Civil Engineering*, San Francisco, CA.

Porter K.A., Beck J.L., Shaikhutdinov R.V. (2002). Sensitivity of building loss estimates to major uncertain variables, *Earthq. Spectra*, 18(4): 719–743. DOI: 10.1193/1.1516201.

Priscu R., Popovici A., Stematiu D., Stere C. (1985). *Earthquake Engineering for Large Dams*, 2nd ed**.** John Wiley and Sons, Inc.; New York, NY.

Proulx J., Darbre G.R., Kamileris N. (2004). Analytical and experimental investigation of damping in arch dams based on recorded earthquakes, *Proceedings, 13th World Conference on Earthquake Engineering*, Vancouver, Canada.

Proulx J., Paultre P. (1997). Experimental and numerical investigation of dam-reservoir-foundation interaction for a large gravity dam, *Can. J. Civil Eng.,* 24(1): 90–105. DOI: 10.1139/l96-086.

Raphael J.M. (1984). Tensile strength of concrete, *J. Am. Concrete I.*, 81(2): 158–165.

Rea D., Liaw C.Y, Chopra A.K. (1974). Mathematical models for the dynamic analysis of concrete gravity dams, *Earthq. Eng. Struct. Dyn.,* 3(3): 249–258. DOI: 10.1002/eqe.4290030304.

Robbe E., Kashiwayanagi M., Yamane Y. (2017). Seismic analyses of concrete dam, comparison between finite-element analyses and seismic records, *Proceedings, 16th World Conference on Earthquake Engineering*, Santiago, Chile.

Saouma V.E., Broz J.J., Brühwiler E., Boggs H.L. (1991). Effect of aggregate and specimen size on fracture properties of dam concrete, *J. Mat. Civil Eng.,* 3(3): 204–218. DOI: 10.1061/(ASCE)0899-1561(1991)3:3(204).

Saouma V.E., Cervenka J., Reich R. (2013). *Merlin Finite Element User's Manual*, University of Colorado, Boulder, CO. 37. Saouma V., Miura F., Lebon G., Yagome Y. (2011). A simplified 3D model for soil-structure interaction with radiation damping and free field input. *Bull. Earthq. Eng.,* 9(5): 1387–1402. DOI: 10.1007/s10518-011-9261-7.

Schnabel P.B, Lysmer J., Seed H.B. (1972). SHAKE: A computer program for earthquake response analysis of horizontally layered sites, *Report No. UCB/EERC-72/12*, Earthquake Engineering Research Center, University of California, Berkeley, CA.

Smith W.D. (1974). A nonreflecting plane boundary for wave propagation problems, ASCE, *J. Comput. Phys.*, 15(4): 492–503. DOI: 10.1016/0021-9991(74)90075-8.

Tan H., Chopra A.K. (1995a). Earthquake analysis and response of concrete arch dams. *Report No. UCB/EERC-95/07*, Earthquake Engineering Research Center, University of California, Berkeley, CA.

Tan H., Chopra A K. (1995b). Dam-foundation rock interaction effects in frequency-response functions of arch dams, *Earthq. Eng. Struct. Dyn.,* 24(11): 1475–1489. DOI: 10.1002/eqe.4290241105.

Tan H., Chopra A.K. (1996). Dam-foundation rock interaction effects in earthquake response of arch dams, ASCE, *J. Struct. Eng.,* 122(5): 528–538. DOI: 10.1061/(ASCE)0733-9445(1996)122:5(528).

Tekie P.B., Ellingwood B.R. (2003). Seismic fragility assessment of concrete gravity dams, *Earthq. Eng. Struct. Dyn.,* 32(14): 2221–2240. DOI: 10.1002/eqe.325.

The MathWorks Inc. (2012). *MATLAB User's Guide (R2012a)*, Natick, MA.

Tinawi R., Léger P., Ghrib F., Bhattacharjee S.S., Leclerc M. (1998). *Structural Safety of Existing Concrete Dams: Influence of Construction Joints*, Report to the Canadian Electrical Association, Montreal, Canada.

Trifunac M.D. (1972). Scattering of plane SH waves by a semi-cylindrical canyon, *Earthq. Eng. Struct. Dyn.,* 1(3): 267–281. DOI: 10.1002/eqe.4290010307.

Underwood P., Geers T.L. (1981). Doubly asymptotic, boundary-element analysis of dynamic soil-structure interaction. *Int. J. Solids Struct.*, 17(7): 687–697. DOI: 10.1016/0020-7683(81)90005-6.

U.S. Geological Survey. Unified Hazard Tool. https://earthquake.usgs.gov/hazards/interactive/, 2018.

Vargas-Loli L.M., Fenves G. (1989). Effects of concrete cracking on the earthquake response of gravity dams, *Earthq. Eng. Struct. Dyn.,* 18(4): 575–592.

Wang J.T., Chopra A.K. (2004). EACD-3D-2008: A computer program for three-dimensional earthquake analysis of concrete dams considering spatially-varying ground motion. *Report No. UCB/EERC-2008/04*, Earthquake Engineering Research Center, University of California, Berkeley, CA.

Wang J.T., Chopra A.K. (2010). Linear analysis of concrete arch dams including dam-water-foundation rock interaction considering spatially varying ground motions, *Earthq. Eng. Struct. Dyn.,* 39(7): 731–750. DOI: 10.1002/eqe.968.

Wang J.T, Lv D.D, Jin F., Zhang C.H. (2013). Earthquake damage analysis of arch dams considering dam–water–foundation interaction, *Soil Dyn. Earthq. Eng.*, 49: 64–74. DOI: 10.1016/j.soildyn.2013.02.006.

Wang J.T., Zhang C.H., Jin F. (2012). Nonlinear earthquake analysis of high arch dam-water-foundation rock systems, *Earthq. Eng. Struct. Dyn.*, 41(7): 1157–1176. DOI: 10.1002/eqe.1178.

White W., Lee I.K., Valliappan S. (1977). Unified boundary for finite dynamic models, ASCE, *J. Eng. Mech. Div.,* 103(5): 949–964.

Wilson E L. (2002). *Three-Dimensional Static and Dynamic Analysis of Structures: A Physical Approach With Emphasis on Earthquake Engineering*. 3rd ed., Computers and Structures Inc.

Wolf J.P. (1985). *Dynamic Soil-Structure Interaction*. Prentice Hall, Englewood Cliffs, NJ.

Wolf J.P. (1988). *Soil-Structure Interaction in Time Domain*, Prentice Hall, Englewood Cliffs, NJ.

Wolf J.P, Song C. (1995). Doubly asymptotic multi-directional transmitting boundary for dynamic unbounded medium-structure-interaction analysis, *Earthq. Eng. Struct. Dyn.,* 24(2): 175–188.

Wolf J.P, Song C. (1996). *Finite-Element Modelling of Unbounded Media*, John Wiley and Sons, Chichester, U.K..

Wong H.L. (1982). Effect of surface topography on the diffraction of P, SV, and Rayleigh waves, *Bull. Seismol. Soc. Am.*, 72(4): 1167–1183.

Zhang C., Yan C., Wang G. (2001). Numerical simulation of reservoir sediment and effects on hydro-dynamic response of arch dams, *Earthq. Eng. Struct. Dyn.,* 30(12): 1817–1837. DOI: 10.1002/eqe.96.

Zhang C.H., Pan J.W., Wang J.T. (2009). Influence of seismic input mechanisms and radiation damping on arch dam response, *Soil Dyn. Earthq. Eng.*, 29(9): 1282–1293. DOI: 10.1016/j.soildyn.2009.03.003.

Zhang L., Chopra A.K. (1991). Impedance functions for three-dimensional foundations supported on an infinitely-long canyon of uniform cross-section in a homogeneous half-space, *Earthq. Eng. Struct. Dyn.,* 20(11): 1011–1027. DOI: 10.1002/eqe.4290201104.

Zhang S., Wang G., Yu X. (2013). Seismic cracking analysis of concrete gravity dams with initial cracks using the extended finite element method, *Eng. Struct.,* 56: 528–543. DOI: 10.1016/j.engstruct.2013.05.037.

Zhang Y., Conte J.P., Yang Z., Elgamal A., Bielak J., Acero G. (2008). Two-dimensional nonlinear earthquake response analysis of a bridge-foundation-ground system, *Earthq. Spectra*, 24(2): 343–386. DOI: 10.1193/1.2923925.

Zienkiewicz O.C., Bettess P. (1978). Fluid-structure dynamic interaction and wave forces. An introduction to numerical treatment, *Inter. J. Numer. Meth. Eng.*., 13(1): 1–16. DOI: 10.1002/nme.1620130102.

Zienkiewicz O.C., Bicanic N., Shen F.Q. (1989). Earthquake input definition and the transmitting boundary conditions, Chapter 3, in *Advances in Computational Nonlinear Mechanics*, Springer-Verlag.

Zienkiewicz O.C., Paul D.K., Hinton E. (1983). Cavitation in fluid-structure response (with particular reference to dams under earthquake loading), *Earthq. Eng. Struct. Dyn.,* 11(4): 463–481. DOI: 10.1002/eqe.4290110403.

NOTATION

Roman symbols

A	tributary area of node on absorbing boundary
a_g^k	k -component of free-field ground acceleration at the foundation surface
$\mathbf{b}$	"damping" matrix of FE model of fluid
$\mathbf{c}$	damping matrix of FE model of dam and foundation rock
c_p, c_s	$= A\rho_f V_p$ or $A\rho_f V_s$, coefficient for viscous damper at foundation boundary in the normal or tangential direction, respectively
c_r	$= A / C$, coefficient for viscous damper at fluid boundary
$\mathbf{c}_f$, $\mathbf{c}_r$	matrix of damper coefficients for nodes on absorbing boundaries Γ_f and Γ_r, respectively
C	speed of pressure waves in water
d_c, d_t	damage index for concrete in compression and tension, respectively
E_f, E_s	Young's modulus of elasticity for foundation rock and dam concrete, respectively
f	excitation frequency, in Hz
f_t	tensile strength of concrete
$\mathbf{f}(\mathbf{r}^t)$	vector of (nonlinear) internal forces in dam and foundation rock
$G(X \mid Y)$	probability that X exceeds a specified value given Y
G_F	specific fracture energy for concrete
g	acceleration due to gravity
$\mathbf{h}$	"stiffness" matrix of FE model of fluid
$\mathbf{H}_r$	vector of dynamic forces associated with absorbing boundary Γ_r
H	height of arch dam
$\mathbf{k}$	stiffness matrix of linear part of FE model of dam and foundation rock
$\mathbf{k}^0$	initial (linear) stiffness matrix
$\mathbf{k}^{el}(t)$	$= [1 - d(t)]\mathbf{k}^0$, the degraded elastic stiffness matrix
L	length of bounded fluid domain
$\mathbf{m}$	mass matrix of FE model of dam and foundation rock
$\mathbf{n}$	outward normal vector to fluid domain
$\mathbf{p}^t$	vector of (total) hydrodynamic pressures at FE nodes in fluid
$\mathbf{P}_f^0$	effective earthquake forces on foundation boundary Γ_f

$\mathbf{P}_r^0$	effective earthquake forces on fluid boundary Γ_r
$\mathbf{Q}$	fluid-solid coupling matrix
$\mathbf{r}^t$	vector of total displacements at FE nodes in dam and foundation rock
$\mathbf{r}_I^0$	vector of displacements for incident seismic wave
$\mathbf{R}_f$	vector of dynamic forces associated with absorbing boundary Γ_f
R	radius of semi-cylindrical canyon
$\mathbf{s}$	"mass" matrix of FE model of fluid
$S_a(T_1)$	spectral acceleration at the fundamental vibration period T_1
u_{cr}	crack opening displacement in concrete cracking model
V_p, V_s	velocity of pressure waves and shear waves, respectively, in foundation rock

Nodal subscripts on matrices and vectors

b	nodes on water–foundation rock interface, i.e., the reservoir bottom and sides
f	nodes on absorbing boundary in foundation domain, Γ_f
h	nodes on dam–water interface, i.e., the upstream face of the dam
r	nodes on absorbing boundary in fluid domain, Γ_r

Superscripts on matrices and vectors

0	quantities in free-field foundation rock or free-field fluid systems
a	quantities in auxiliary water–foundation rock system
st	static forces
t	total displacements, pressures or forces

Greek symbols

α	wave reflection coefficient for reservoir bottom materials
Γ_b	water–foundation rock interface
Γ_f, Γ_r	absorbing boundaries in foundation and fluid domains, respectively
Γ_h	dam–water interface
ζ_f, ζ_s	viscous damping ratio of foundation rock and dam concrete, respectively
η_f, η_s	hysteretic (rate-independent) damping factors of foundation rock and dam concrete, respectively
η	$= 2fR/V_s$, dimensionless frequency (in Chapters 5 and 6)
λ	wavelength of scattered waves
$\lambda(X)$	mean annual rate of exceedance of X
ν_f, ν_s	Poisson's ratio of foundation rock and dam concrete, respectively

ρ_f, ρ_s, ρ	density of foundation rock, dam concrete and water, respectively
σ	normal tractions on foundation boundary
τ	tangential tractions on foundation boundary
ω_1	natural angular frequency of dam with empty reservoir on rigid foundation rock
Ω	region interior of absorbing boundaries, i.e., the truncated FE model
Ω^0	region interior of Γ_f for free-field foundation-rock system
Ω^a	region interior of Γ_f and Γ_r for auxiliary water–foundation rock system
Ω^+	regions exterior of absorbing boundaries Γ_f and Γ_r

Abbreviations

BEM	Boundary Element Method
CMS	Conditional Mean Spectrum
DRM	Domain Reduction Method
DM	Damage measure
DV	Decision Variable
EDP	Engineering Demand Parameter
ESI	Effective Seismic Input Method
FEM	Finite Element Method
IM	Intensity Measure
IMHC	Intensity Measure Hazard Curve
UHS	Uniform Hazard Spectrum
PBEE	Performance-Based Earthquake Engineering
PEER	Pacific Earthquake Engineering Research Center
PSHA	Probabilistic Seismic Hazard Analysis
PML	Perfectly Matched Layer
RHA	Response History Analysis
SDHC	Seismic Demand Hazard Curve

APPENDIX A Selection of Domain Size for Two-Dimensional Dam–Water–Foundation Rock Systems

A.1 INTRODUCTION

An important requirement to ensure accurate results when using the direct FE method for earthquake analysis of concrete dams is that the viscous-damper boundaries at the truncations of the foundation domain absorb the outgoing (scattered) waves caused by dam–foundation rock interaction. The primary factor determining the effectiveness of these boundaries is the size of foundation domain included in the FE model. In this appendix, guidelines for selecting appropriate domain sizes for 2D gravity dam systems are presented. First, the dynamic response of a rigid footing on a viscoelastic half-space is analyzed, and then the response of a concrete gravity dam is investigated.

A.2 DYNAMIC RESPONSE OF RIGID FOOTING ON A VISCOELASTIC HALF-SPACE

Much research has been devoted to the developing generalized dynamic force-displacement relationships for rigid footings of various shapes bonded to a viscoelastic half-space, as these play an important role in the study of vibrating machinery and soil–structure interaction [Luco and Westmann 1972; Dasgupta and Chopra 1979; and Gazetas 1981]. For long and relatively uniform structures, the footing can best be idealized as an infinitely long strip. If the dynamic loading is uniform in the longitudinal direction, a plain-strain condition is appropriate, and the steady-state harmonic response is fully described by a set of dynamic flexibility (or compliance) coefficients.

In this section, these dynamic flexibility coefficients are used to evaluate the performance of the viscous-damper absorbing boundary for different sized foundation domains. These results will subsequently be used to recommend an appropriate size of the foundation domain to be used for dam–water–foundation interaction analyses.

A.2.1 Formulation of the Problem

The infinitely long rigid strip footing of width 2b perfectly bonded to a semi-unbounded homogeneous viscoelastic half-space (Figure A.1a) is analyzed. The rigid footing has three degrees-of-freedom: horizontal translation (*H*), vertical translation (*V*) and rocking (*M*). The properties of the half-space is defined by its shear modulus μ, Poisson's ratio ν, density ρ, and damping ratio ζ. If $\overline{P}_i$ and $\overline{\Delta}_i$, $i = V, H, M$ denotes the amplitudes of a unit harmonic force and harmonic displacement, respectively, along the *i*th DOF, the dynamic force-displacement relationship can be written as:

$$\begin{Bmatrix} \overline{\Delta}_V \\ \overline{\Delta}_H \\ b\overline{\Delta}_R \end{Bmatrix} = \frac{1}{\pi\mu} \begin{bmatrix} F_{VV}(a_0) & 0 & 0 \\ 0 & F_{HH}(a_0) & F_{HM}(a_0) \\ 0 & F_{MH}(a_0) & F_{MM}(a_0) \end{bmatrix} \begin{Bmatrix} \overline{P}_V \\ \overline{P}_H \\ \overline{P}_M / b \end{Bmatrix} \tag{A.1}$$

The coefficients of the dynamic flexibility matrix are complex-valued quantities with real and imaginary components $F_{ij}(a_0) = f_{ij}(a_0) + ig_{ij}(a_0)$ that are a function of the dimensionless frequency parameter

$$a_0 = \omega b / v_s \tag{A.2}$$

The real and imaginary parts of these dynamic flexibility coefficients can be interpreted as measures of flexibility (i.e., inverse of the stiffness) and damping of the underlying half-space, respectively. The system is implemented in the FE program OpenSees using a mesh with 15 elements under the rigid strip footing, and gradually increasing element size towards the outer boundaries of the model; see Figure A.1(b). This mesh provides sufficient density to adequately model the range of frequencies considered in the analysis. Material damping is modeled by specifying ζ = 2% Raleigh damping at every given excitation frequency; this unconventional choice was implemented to match the constant hysteretic damping model in the benchmark solution. Viscous dampers are applied on the bottom and side boundaries of the foundation

domain, with the distance from the center of the footing to the boundaries ($n_x b$ and $n_y b$) varied in the analyses.

The steady-state displacement response of the footing due to unit harmonic excitation is determined for vertical, horizontal and rocking vibration modes, and the procedure is repeated at every excitation frequency considered. From the displacement response, components that are in-phase (real) and 90° out-of-phase (imaginary) with the input harmonic force are determined, and the results are compared with available semi-analytical benchmark solutions [Dasgupta and Chopra 1979]. These benchmark results are denoted "exact" in Figures A.2–A.4.

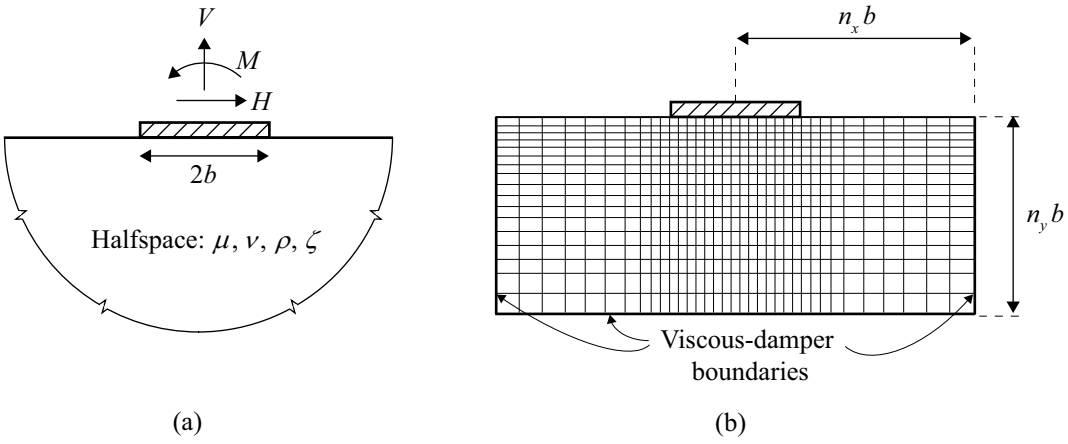

Figure A.1 **(a) Cross section of rigid footing on viscoelastic half-space; and (b) FE model with characteristic width and height.**

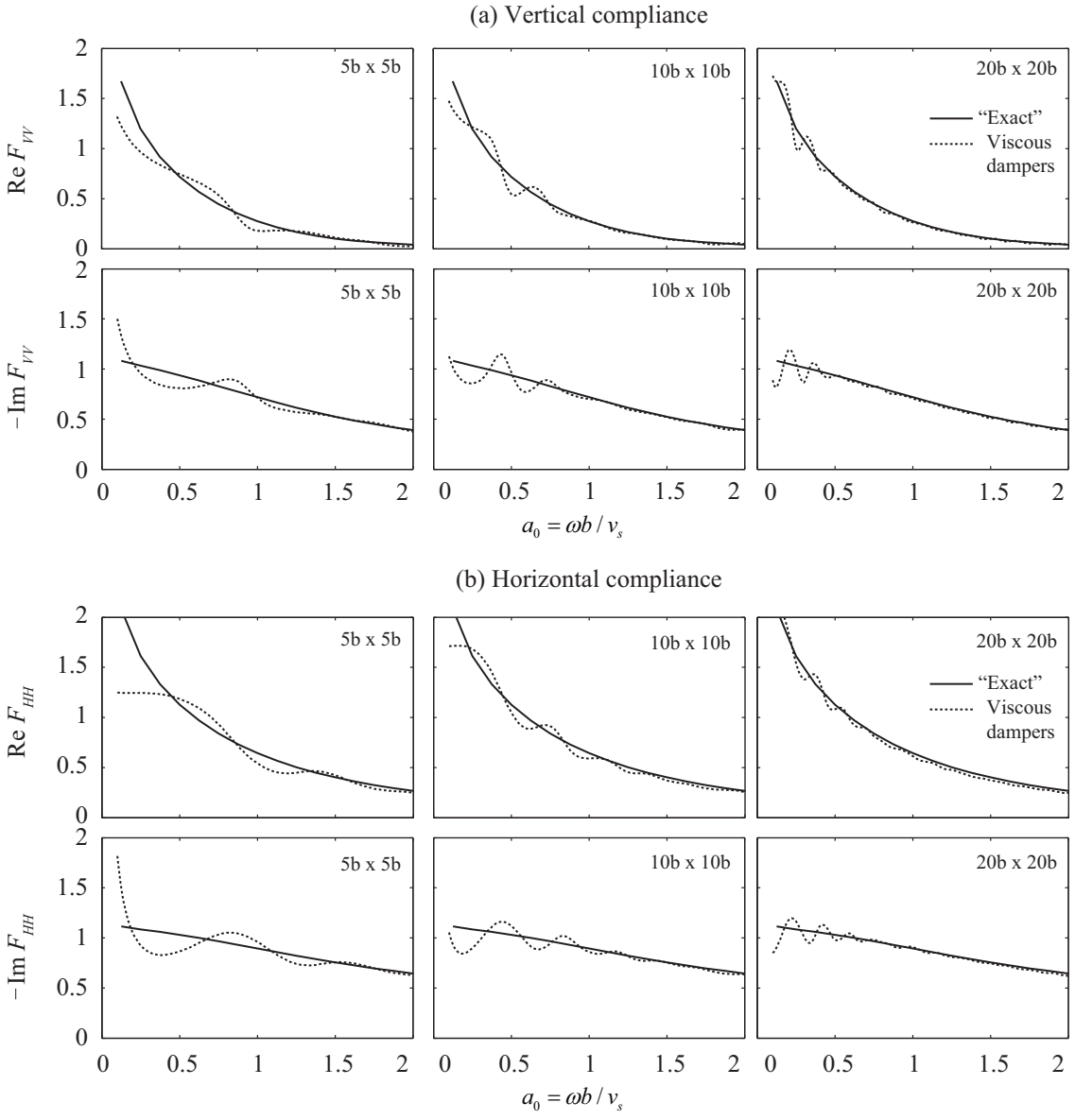

Figure A.2 **Dynamic flexibility coefficients for rigid strip footing on viscoelastic homogeneous half space due to (a) vertical excitation; and (b) horizontal excitation. ν = 1/3; ζ = 2%.**

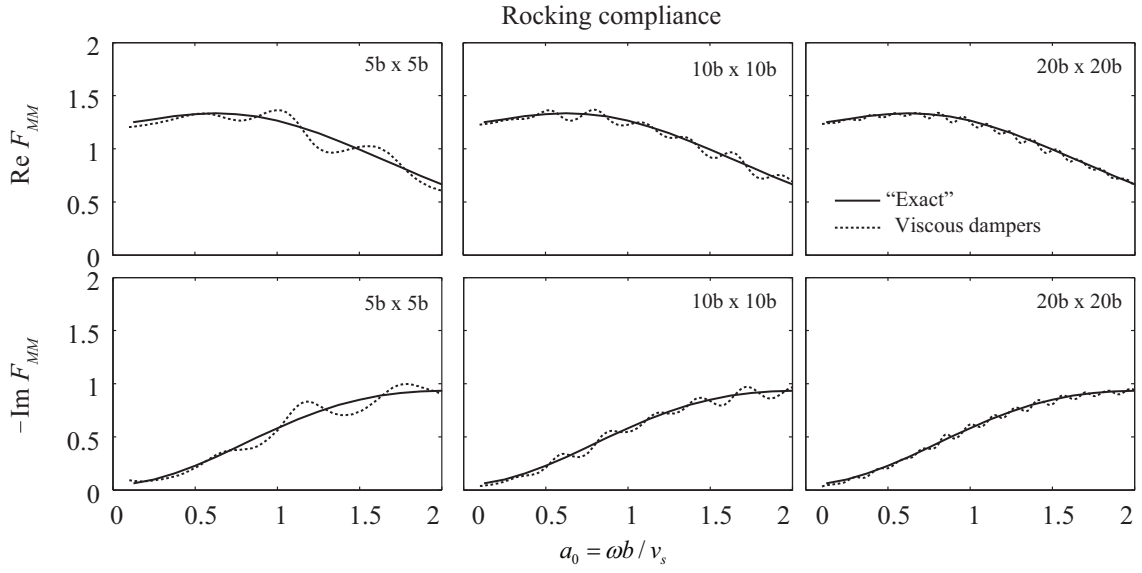

Figure A.3 **Dynamic flexibility coefficients for rigid strip footing on viscoelastic homogeneous half space due to harmonic rocking motion. ν = 1/3; ζ = 2%.**

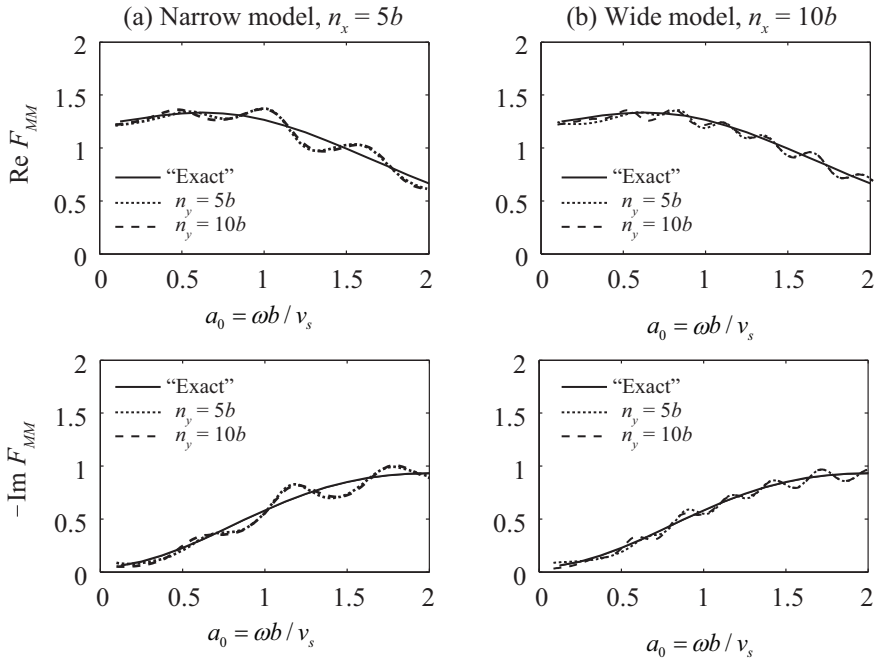

Figure A.4 **Dynamic flexibility coefficients for rigid strip footing on viscoelastic homogeneous half-space due to harmonic rocking motion: (a) $n_x = 5b$; and (b) $n_x = 10b$. For both sizes, ν = 1/3, ζ = 2%.**

A.2.2 Influence of Domain Size

Results for the horizontal, vertical and rocking compliance are presented in Figures A.2 and A.3, for three domain sizes: $5b \times 5b$, $10b \times 10b$ and $20b \times 20b$. The viscous-damper boundary generally performs well, with increasing accuracy at higher excitation frequencies and for larger domain sizes. This is consistent with results reported elsewhere [Wolf 1988]. The convergence towards the exact solution at higher frequencies is prominent for vertical and horizontal excitation of the footing (Figure A.2), but less so for rocking (Figure A.3). For rocking motion, the wave field is shallower, and more of the energy is radiated through surface waves, even at high frequencies [Meek and Wolf 1993]. Because the viscous dampers are less effective in absorbing these waves, noticeable oscillations are seen in the results for all domain sizes and at all frequencies. These oscillations are caused by "standing waves" in the model, i.e., small resonance patterns that occur when the ratio of the horizontal distance to the excitation wave length approaches certain values. Such oscillations will be less of a concern for a transient-type excitation.

Table A.1 shows the mean relative error between the computed results and the benchmark solution for several domain sizes, computed as $\sum_{j=1}^{N} e_j = |(y_j - \hat{y}_j)/\hat{y}_j|$ where y_j is the computed value, $\hat{y}_j$ is the benchmark value at frequency ω_j, and N is the total number of sampling points, The accuracy of the viscous-damper boundary improves for all modes of vibration when the domain size is increased. "Acceptable" accuracy is obtained at most frequencies with a foundation size of approx. $10b \times 10b$ or higher, with mean relative error around 5–8% for all modes.

Table A.1 **Mean relative error compared to exact analytical solution, in %, for different domain sizes; error computed between a_0 = 0.25 and 2.0. ν = 1/3, ζ = 2%.**

Distance to boundary	Re(F_{VV})	-Im(F_{VV})	Re(F_{HH})	-Im(F_{HH})	Re(F_{MM})	-Im(F_{MM})
2.5b	23.6	7	16.3	10.8	6.8	19.2
5.0b	16.2	6.1	9.4	7.5	5.1	9.2
7.5b	9.6	5.2	7.4	5.4	3.2	7.3
10b	8.3	4.1	6.5	4	3.1	6.8
15b	5.5	3.2	5.9	2.9	2.2	4.4
20b	5.2	2.1	5.7	2.3	1.7	3.8

A.2.3 Influence of Aspect Ratio on Rocking Compliance

Rocking motion is a significant part of the overall dynamic response of stiff and heavy structures such as concrete gravity dams. Because rocking generally causes shallower wave fields than horizontal or vertical excitation, it is interesting to investigate whether acceptable accuracy can be obtained for a shallow domain.

Figure A.4 compares the results for rocking compliance for two horizontal domain sizes: narrow ($n_x = 5b$) and wide ($n_x = 10b$), and two vertical domain sizes: shallow ($n_y = 5b$) and deep ($n_y = 10b$). The accuracy is generally much better for the wide model than for the narrow model; however, there seems to be no benefit of increasing the vertical dimension beyond the shallow domain size. This indicates that a shallow and wide model will be the ideal aspect ratio for concrete gravity dam analyses where rocking is important.

A.3 DYNAMIC RESPONSE OF PINE FLAT DAM

The required size of the foundation domain to be used with the direct FE method developed in Part II of this report is investigated by analyzing the dam–foundation rock system shown in Figure A.5. The dam cross section chosen is that of Pine Flat Dam [Figure A.5(a)], which has a geometry representative of many concrete gravity dams. The concrete in the dam was assumed to be homogeneous, isotropic and linear elastic, in a state of plain strain, with modulus of elasticity $E_s = 22.4$ GPa, density $\rho_s = 2483$ kg/m^3, and Poisson's ratio $\nu_s = 0.20$. The foundation rock was assumed to be homogeneous, isotropic, and linear elastic, in a state of plain strain, with modulus of elasticity $E_f = E_s$, $\rho_f = 2643$ kg/m^3, and $\nu_f = 0.33$. The dam was assumed to be supported on the surface of the half-space. Material damping in the dam and foundation was modeled in the direct FE method analyses by Rayleigh damping with ζ_s and ζ_f = 2% damping specified in the two first periods of vibration for the dam–foundation rock system. Using the substructure method analyses as benchmark, material damping was modeled by constant hysteretic damping with equivalent hysteretic damping factor $\eta = 2\zeta$.

$n_x H$
$n_y H$

The FE model for the dam cross section consisted of four-node solid elements and had 15 elements along the base and 30 elements along the height. The FE model for the foundation rock also consisted of four-node solid elements and had a maximum element size chosen to be less than one-tenth of the shortest wavelength considered in the analysis [Kuhlemeyer and Lysmer

[168]. Viscous-damper boundaries were applied at the bottom and sides of the model. The overall size of the foundation domain in the horizontal and vertical directions was defined by $n_x H$ and $n_y H$, where H is the dam height; see Figure A.5(b).

Frequency response functions are computed by defining a unit-amplitude harmonic surface ground motion, computing effective earthquake forces following the procedure summarized in Boxes 3.1 and 3.2 of Part I, and analyzing the system for long enough time to determine the steady-state response. Results obtained using the substructure method—wherein the foundation rock is modeled rigorously as a semi-infinite half-space—provided the benchmark for comparison.

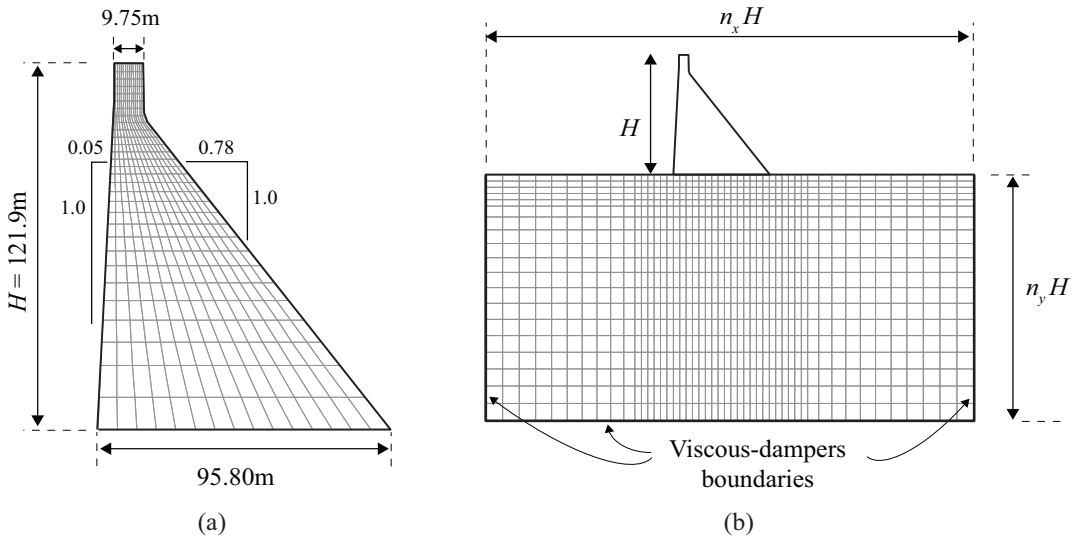

Figure A.5 **(a) Finite-element model of dam cross section (Pine Flat Dam); and (b) dam–foundation rock system with viscous-damper boundaries to simulate the semi-unbounded foundation domain.**

A.3.1 Influence of Foundation Domain Size

Frequency response functions for the dam–foundation rock system subjected to horizontal and vertical ground motion are shown in Figure A.6. Results are computed for three different of foundation domain sizes: $4H \times 2H$, $8H \times 4H$, and $16H \times 8H$. For all three foundation sizes, the direct FE method is able to closely represent the effects of dam–foundation rock interaction. The shape and amplitude of the response function is close to the benchmark solution for both

horizontal and vertical excitation. The peak at the first resonance frequencies is overestimated for the smallest sized foundation domain, but the agreement increases for larger domain sizes. This is consistent with the results observed in Section A.2, where "standing waves" caused oscillations in the compliance coefficients when the ratio of the distance to the boundary to the excitation wave length approached certain values. Choosing a domain size of $8H \times 4$H seems sufficient to ensure that these oscillations have minimal influence on the dam response, and there is little additional benefit of further increasing the domain size to $16H \times 8H$.

A.3.2 Influence of Foundation Domain Aspect Ratio

Figure A.7 compares the accuracy of the direct FE method with viscous-damper boundaries for different aspect ratios of the foundation domain. The aspect ratio of the foundation domain clearly influences the results: there is little improvement by increasing the domain size from $4H \times 2H$ to $4H \times 4H$, and correspondingly, the results for $8H \times 4H$ are almost identical to those for $8H \times 8H$. This lack of improvement in accuracy when increasing the vertical dimension occurs because the scattered wave field from the dam is largely caused by rocking motion, which generates a shallow wave field primarily propagating in the horizontal directions. Additional increase of the vertical dimension will therefore not provide much additional absorption from the viscous dampers. These results indicate that a vertical dimension between $2H$ and $4H$ will likely provide sufficient accuracy for practical analyses.

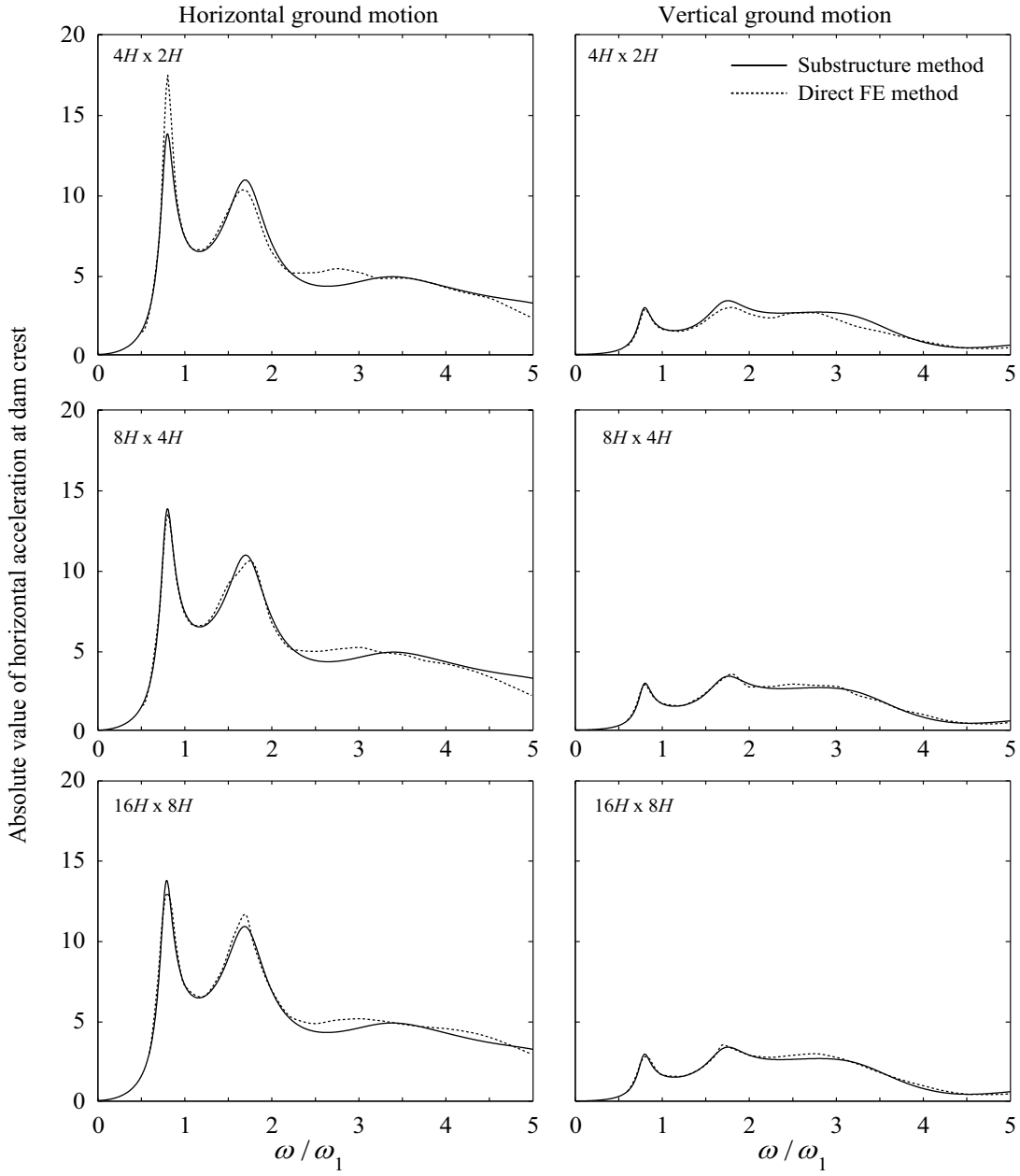

Figure A.6 **Influence of foundation domain size on the accuracy of direct FE method in computing the response of dam on flexible foundation due to harmonic horizontal and vertical ground motion.** $\zeta_s = \zeta_f$ **= 2%;** E_f / E_s **= 1.0.**

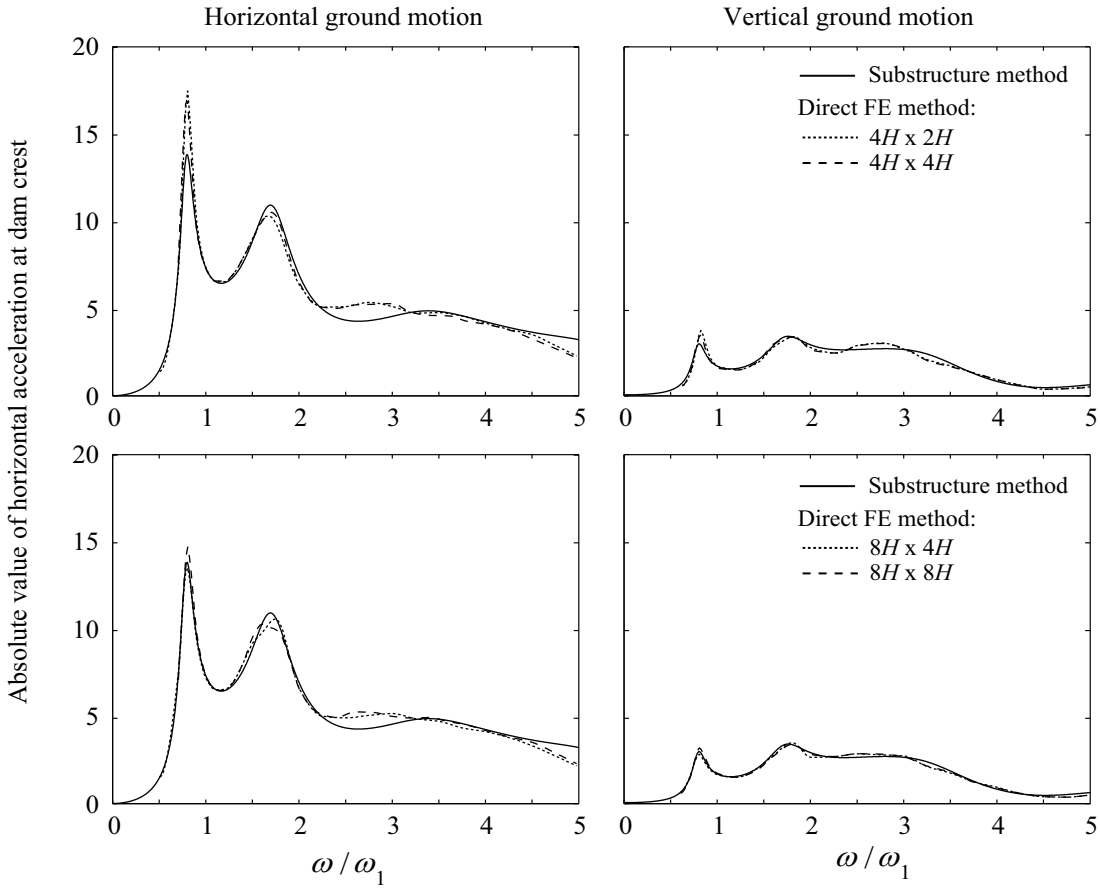

Figure A.7 **Influence of foundation domain aspect ratio on the accuracy of direct FE method in computing the response of dam on flexible foundation due to harmonic horizontal and vertical ground motion.** $\zeta_s = \zeta_f$ **= 2%;** E_f / E_s **= 1.0.**

A.3.3 Influence of Foundation Stiffness

To investigate how the accuracy of the direct FE method is influenced by changes in the stiffness of the foundation rock, results are presented in Figure A.8 for E_f/E_s = 2, 1, and 1/4. The accuracy generally increases as the moduli ratio E_f/E_s decreases, which for a fixed value of E_s implies increasingly flexible foundation rock. Although somewhat counter-intuitive result, as one might have expected the accuracy to worsen for a more flexible foundation because the effects of dam–foundation interaction are more prominent, the opposite occurs because the ability of the viscous dampers to absorb body waves improves when the ratio of distance to excitation wave length increases [Wolf 1988], and this ratio will decrease with increasing foundation stiffness

E_f. The same trend was observed in Figures A.2 and A.3, where the accuracy was seen to increase for higher values of a_0, which for a fixed frequency implies a more flexible foundation.

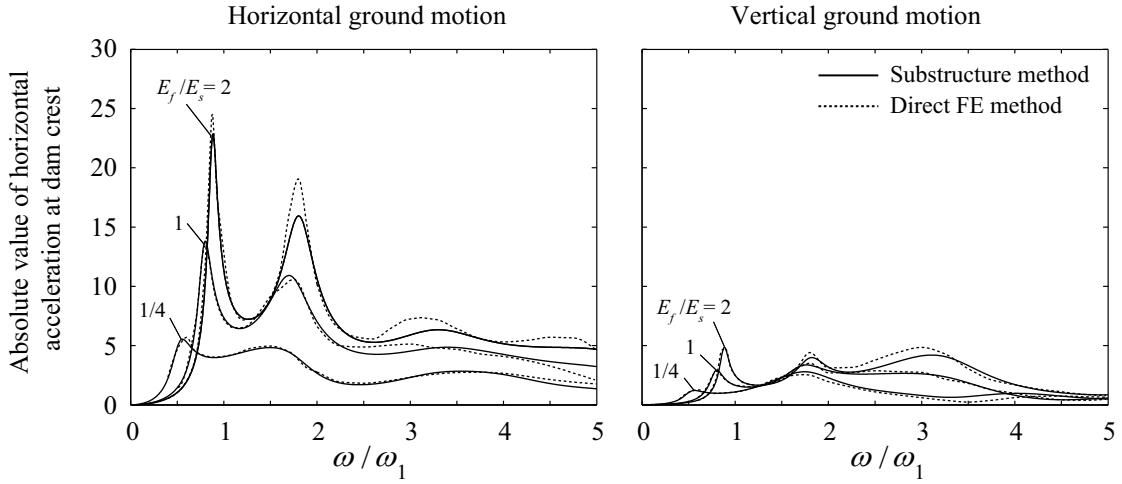

Figure A.8 **Influence of foundation stiffness on the accuracy of direct FE method in computing the response of dam on flexible foundation due to harmonic horizontal and vertical ground motion. Size of foundation domain = 8*H* x 4*H*; $\zeta_s = \zeta_f$ = 2%.**

A.3.4 Influence of Material Damping

Figure A.9 presents the response of the system for two values of material damping in the dam and foundation rock: $\zeta_s = \zeta_f = 2\%$ and $\zeta_s = \zeta_f = 5\%$. Increasing the amount of material damping slightly improves the accuracy of the results from the truncated model because: (1) the amplitude of the outward propagating wave is reduced before it hits the boundary leading to less energy for the viscous dampers to absorb; and (2) the wave reflected from the boundary is further damped before it reaches the structure. Note of caution: increasing the amount of material damping is not a substitute for accurate modeling of the semi-unbounded foundation domain.

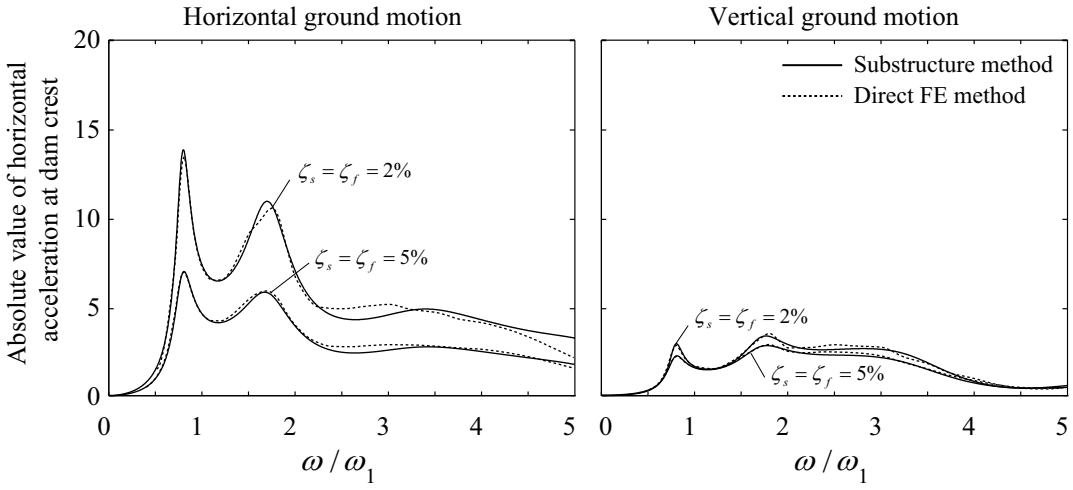

Figure A.9 **Influence of material damping on the accuracy of direct FE method in computing the response of dam on flexible foundation due to harmonic horizontal and vertical ground motion. Size of foundation domain = 8*H* x 4*H*; E_f / E_s = 1.0.**

A.3.5 Recommendations for Domain Size

Based on the preceding results, the following conclusions can be stated:

- An overall foundation-domain size of $8H \times 4H$ is sufficient to ensure accurate results in the direct FE method when using viscous-damper boundaries to model the semi-unbounded foundation domain. Further increase in the domain size does not improve the accuracy.
- Increasing the vertical size of the foundation domain beyond a certain minimum value does not improve the results. These presented results indicate that a vertical dimension between $2H$ and $4H$ will likely suffice for practical analyses.
- The accuracy is generally better for more flexible foundations (lower value of E_f) because the performance of the viscous-damper boundary is inversely proportional to the foundation stiffness. For stiff foundations, the dimensions recommended above may have to be increased.

- Increasing the amount of material damping in the foundation slightly improves the accuracy of the results, but the trend is only modest.

APPENDIX B The Domain Reduction Method for Seismic Input in Soil–Structure Interaction Analyses

B.1 INTRODUCTION

The domain reduction method (DRM) [Bielak et al. 2003] is a modular, two-step FE methodology developed for modeling response to earthquake ground motion in situations where large contrasts exist between the physical scale of the background model and a smaller localized feature. The method overcomes the problem of multiple physical scales by subdividing the original problem into two simpler ones. The first is an auxiliary problem that simulates the earthquake source and propagation path effects by using a model that encompasses the source and a simpler background structure where the localized feature has been removed. The second problem models the local site effects by using a set of equivalent localized forces derived from the first step as the effective seismic input.

Although primarily developed for large scale geological simulations, the DRM is also directly applicable for soil–structure interaction (SSI) problems. Under external excitation such as earthquake motion, SSI problems may be viewed as a scattering problem, where a local feature perturbs the free-field motion in a larger soil domain. This concept was utilized to formulate the direct FE method in Parts I and II of this report. The local feature could in this context be any type of structure or local geological feature, either supported on or embedded in the soil domain. The DRM then only requires that the free-field motion is known in a single continuous layer of elements interior of an absorbing boundary.

For SSI analysis, the large-scale simulation approach has the advantage that because the 3D wave field is directly available from the motions recorded in the first step, it is not necessary to make simplifying assumptions restricting the shape of the wave field, such as the assumption

of vertically propagating waves. The DRM can also be used for seismic input under more restrictive assumption where the free-field motion is obtained from a simpler auxiliary problem.

B.2 FORMULATION OF METHOD

Consider the large, but finite, seismic region Ω^+ that contains a seismic source P_e [Figure B.1(a)]. Within the larger region Ω^+ is a smaller region Ω that contains a local feature such as a structure or a geological feature for which the seismic response is to be computed. The material in the following derivation is for simplicity assumed to be linear elastic in both Ω^+ and Ω, however, this assumption can be partly removed later.

Presented herein in its original notation [Bielak et al. 2003], the equations of motion for this system are governed by Navier's equations of elastodynamics, which when discretized spatially by FEs can be expressed in partitioned form as

$$\begin{bmatrix} M_{ii}^{\Omega} & M_{ib}^{\Omega} \\ M_{bi}^{\Omega} & M_{bb}^{\Omega} \end{bmatrix} \begin{Bmatrix} \ddot{u}_i \\ \ddot{u}_b \end{Bmatrix} + \begin{bmatrix} C_{ii}^{\Omega} & C_{ib}^{\Omega} \\ C_{bi}^{\Omega} & C_{bb}^{\Omega} \end{bmatrix} \begin{Bmatrix} \dot{u}_i \\ \dot{u}_b \end{Bmatrix} + \begin{bmatrix} K_{ii}^{\Omega} & K_{ib}^{\Omega} \\ K_{bi}^{\Omega} & K_{bb}^{\Omega} \end{bmatrix} \begin{Bmatrix} u_i \\ u_b \end{Bmatrix} = \begin{Bmatrix} 0 \\ P_b \end{Bmatrix}, \ in \ \Omega \tag{B.1a}$$

$$\begin{bmatrix} M_{bb}^{\Omega^+} & M_{be}^{\Omega^+} \\ M_{eb}^{\Omega^+} & M_{ee}^{\Omega^+} \end{bmatrix} \begin{Bmatrix} \ddot{u}_b \\ \ddot{u}_e \end{Bmatrix} + \begin{bmatrix} C_{bb}^{\Omega^+} & C_{be}^{\Omega^+} \\ C_{eb}^{\Omega^+} & C_{ee}^{\Omega^+} \end{bmatrix} \begin{Bmatrix} \dot{u}_i \\ \dot{u}_e \end{Bmatrix} + \begin{bmatrix} K_{bb}^{\Omega^+} & K_{be}^{\Omega^+} \\ K_{eb}^{\Omega^+} & K_{ee}^{\Omega^+} \end{bmatrix} \begin{Bmatrix} u_i \\ u_e \end{Bmatrix} = \begin{Bmatrix} -P_b \\ P_e \end{Bmatrix}, \ in \ \Omega^+ \tag{B.1b}$$

where the matrices M, C, and K are the mass, damping, and stiffness matrices, respectively, and the subscripts i, e, b refer to nodes in the interior, exterior and on the boundary between them [Figure B.1(a)], respectively. To obtain the traditional form of the equations of motion, these equations are added to obtain

$$\begin{bmatrix} M_{ii}^{\Omega} & M_{ib}^{\Omega} & 0 \\ & M_{bb}^{\Omega} + M_{bb}^{\Omega^+} & M_{be}^{\Omega^+} \\ sym & & M_{ee}^{\Omega^+} \end{bmatrix} \begin{Bmatrix} \ddot{u}_i \\ \ddot{u}_b \\ \ddot{u}_e \end{Bmatrix} + \begin{bmatrix} C_{ii}^{\Omega} & C_{ib}^{\Omega} & 0 \\ & C_{bb}^{\Omega} + C_{bb}^{\Omega^+} & C_{be}^{\Omega^+} \\ sym & & C_{ee}^{\Omega^+} \end{bmatrix} \begin{Bmatrix} \dot{u}_i \\ \dot{u}_b \\ \dot{u}_e \end{Bmatrix}$$
$$\begin{bmatrix} K_{ii}^{\Omega} & K_{ib}^{\Omega} & 0 \\ & K_{bb}^{\Omega} + K_{bb}^{\Omega^+} & K_{be}^{\Omega^+} \\ sym & & K_{ee}^{\Omega^+} \end{bmatrix} \begin{Bmatrix} u_i \\ u_b \\ u_e \end{Bmatrix} = \begin{Bmatrix} 0 \\ 0 \\ P_e \end{Bmatrix} \tag{B.2}$$

To transfer the seismic excitation to the interior region Ω, an auxiliary free-field problem is considered, in which the region Ω is replaced by the simpler background region Ω_0 that does

not include the local feature; see Figure B.1(b). The outer region Ω^+ remains identical. All variables in the auxiliary free-field problem will be denoted using the superscript 0.

With the replacement of the interior region, the equations of motion for the auxiliary "free-field" problem in the outer region Ω^+ can now be written as

$$\begin{bmatrix} M_{bb}^{\Omega^+} & M_{be}^{\Omega^+} \\ M_{eb}^{\Omega^+} & M_{ee}^{\Omega^+} \end{bmatrix} \begin{Bmatrix} \ddot{u}_b^0 \\ \ddot{u}_e^0 \end{Bmatrix} + \begin{bmatrix} C_{bb}^{\Omega^+} & C_{be}^{\Omega^+} \\ C_{eb}^{\Omega^+} & C_{ee}^{\Omega^+} \end{bmatrix} \begin{Bmatrix} \dot{u}_b^0 \\ \dot{u}_e^0 \end{Bmatrix} + \begin{bmatrix} K_{bb}^{\Omega^+} & K_{be}^{\Omega^+} \\ K_{eb}^{\Omega^+} & K_{ee}^{\Omega^+} \end{bmatrix} \begin{Bmatrix} u_b^0 \\ u_e^0 \end{Bmatrix} = \begin{Bmatrix} -P_b^0 \\ P_e \end{Bmatrix} \tag{B.3}$$

where P_b^0 are the interface forces at the boundary Γ. Since there is no change in the exterior region Ω^+, the mass, stiffness and damping matrices M, C, and K, M , C , and force vector P_e, remain the same.

From the second of these equations, the force vector P_e can be expressed as

$$P_e = M_{eb}^{\Omega^+} \ddot{u}_b^0 + M_{ee}^{\Omega^+} \ddot{u}_e^0 + C_{eb}^{\Omega^+} \dot{u}_b^0 + C_{ee}^{\Omega^+} \dot{u}_e^0 + K_{eb}^{\Omega^+} u_b^0 + K_{ee}^{\Omega^+} u_e^0 \tag{B.4}$$

One can solve for the displacement field for the complete domain by substituting Equation (B.4) into Equation (B.2). This is not a very practical approach as it requires that the free-field motion u_e^0 to be computed and stored in the entire domain Ω^+. To simplify, a substitution of variables is introduced to expresses the total variables u_e as the sum of the free-field u_e^0 and the scattered field w_e due to the local feature:

$$u_e = u_e^0 + w_e \tag{B.5}$$

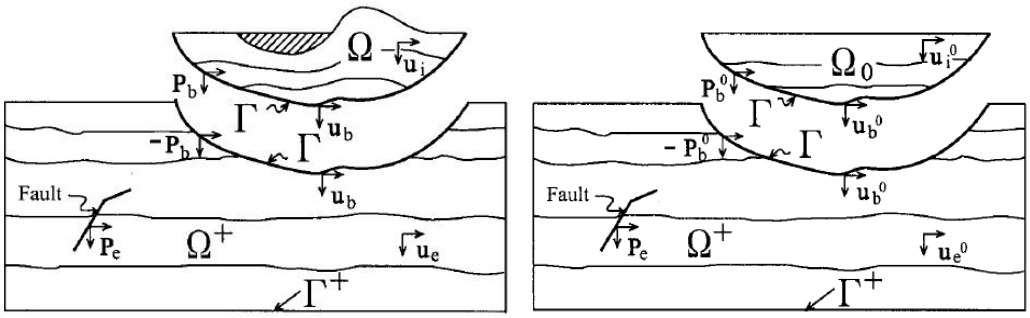

Figure B.1 **(a) Original seismic regions partitioned into two substructures Ω and Ω^+ by a fictitious divide Γ; and (b) auxiliary free-field problem where localized features of the actual problem in Ω have been replaced by a simpler background model over domain Ω_0. Figure from Bielak et al. [2003].**

Substituting Equation (B.5) into Equation (B.2), and then substituting for P_e from Equation (B.4), the desired equation is obtained as

$$\begin{bmatrix} M_{ii}^{\Omega} & M_{ib}^{\Omega} & 0 \\ & M_{bb}^{\Omega}+M_{bb}^{\Omega^+} & M_{be}^{\Omega^+} \\ sym & & M_{ee}^{\Omega^+} \end{bmatrix} \begin{Bmatrix} \ddot{u}_i \\ \ddot{u}_b \\ \ddot{w}_e \end{Bmatrix} + \begin{bmatrix} C_{ii}^{\Omega} & C_{ib}^{\Omega} & 0 \\ & C_{bb}^{\Omega}+C_{bb}^{\Omega^+} & C_{be}^{\Omega^+} \\ sym & & C_{ee}^{\Omega^+} \end{bmatrix} \begin{Bmatrix} \dot{u}_i \\ \dot{u}_b \\ \dot{w}_e \end{Bmatrix}$$

$$\begin{bmatrix} K_{ii}^{\Omega} & K_{ib}^{\Omega} & 0 \\ & K_{bb}^{\Omega}+K_{bb}^{\Omega^+} & K_{be}^{\Omega^+} \\ sym & & K_{ee}^{\Omega^+} \end{bmatrix} \begin{Bmatrix} u_i \\ u_b \\ w_e \end{Bmatrix} = \begin{Bmatrix} 0 \\ -M_{be}^{\Omega^+}\ddot{u}_e^0 - C_{be}^{\Omega^+}\dot{u}_e^0 - K_{be}^{\Omega^+}u_e^0 \\ M_{eb}^{\Omega^+}\ddot{u}_b^0 + C_{eb}^{\Omega^+}\dot{u}_b^0 + K_{eb}^{\Omega^+}u_b^0 \end{Bmatrix} \tag{B.6}$$

It can be seen that all the system matrices *M*, *C*, and *K* are identical as before; however, seismic forces P_e have now been replaced by the effective earthquake forces P^{eff}, given by the right hand side of Equation (B.6)

$$P^{\text{eff}} = \begin{Bmatrix} P_i^{\text{eff}} \\ P_b^{\text{eff}} \\ P_e^{\text{eff}} \end{Bmatrix} \begin{Bmatrix} 0 \\ -M_{be}^{\Omega^+}\ddot{u}_e^0 - C_{be}^{\Omega^+}\dot{u}_e^0 - K_{be}^{\Omega^+}u_e^0 \\ M_{eb}^{\Omega^+}\ddot{u}_b^0 + C_{eb}^{\Omega^+}\dot{u}_b^0 + K_{eb}^{\Omega^+}u_b^0 \end{Bmatrix} \tag{B.7}$$

This formulation has the advantage that $P^{\text{eff}} \equiv 0$ everywhere except in a single layer of elements adjacent to the boundary Γ [Figure B.2(b)], and that only the solution of the auxiliary free-field wave field is needed to determine the forces. Since the effective forces P^{eff} depend only on the material properties of the exterior region Ω^+, the procedure is also fully applicable for cases where the material in the interior region Ω behaves nonlinearly.

The results from the above derivations are summarized in the two-step procedure shown in Figure B.2. In Step II, the original exterior region Ω^+ is replaced by a truncated portion $\hat{\Omega}^+$. The wave field in this region consists only of outgoing waves corresponding to the scattered motion w_e due to the presence of the local feature. Appropriate absorbing boundary conditions must therefore be applied at the boundary $\hat{\Gamma}^+$ to avoid spurious reflections back into the interior region. Hence, the dimensions of the truncated exterior region $\hat{\Omega}^+$ are only determined by the performance of the chosen boundary conditions to eliminate these reflections.

Note that in the DRM, the location of the absorbing boundary needed to truncate the exterior region $\hat{\Gamma}^+$ is decoupled from the location of the seismic input. This is an advantage for SSI type analyses since any type of absorbing boundary formulation can then be applied without

having to allow for the incoming seismic motion to pass through the boundary; therefore, the DRM represents a convenient way to apply seismic input in SSI analyses when the wave field is known beforehand at a predefined layer of elements encompassing a local region of interest. This is the case if the seismic input motion is obtained directly using large-scale earthquake simulations, or if certain restrictions are imposed to simplify the shape of the wave field.

When the exterior region is truncated by $\hat{\Gamma}^+$ in Step II, the accuracy is determined by the adequacy of the absorbing boundaries applied at $\hat{\Gamma}^+$ to absorb the scattered wave field w_e. Since the wave field in the exterior region $\hat{\Omega}^+$ in Step II consists only of outgoing waves, the wave field can be monitored to provide information about the dynamic characteristics of the local feature and the performance of the absorbing boundaries.

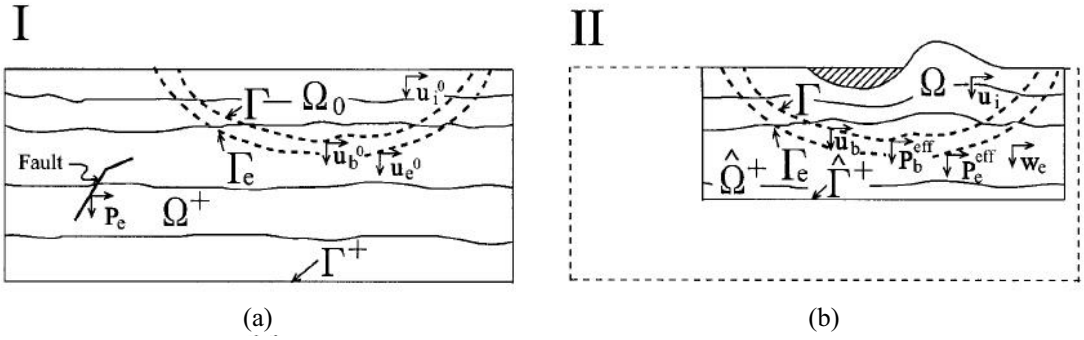

Figure B.2 **Summary of the DRM: (a) Step I defines the auxiliary free-field problem for the background model. Resulting motion at the boundaries Γ, Γ_e, and the region between them are recorded and used to evaluate effective seismic forces P^{eff}; and (b) Step II, defined over the reduced region made up of Ω and $\hat{\Omega}^+$ (a truncated portion of Ω^+).The effective seismic forces P^{eff} are applied within Γ and Γ_e. Figure from Bielak et al. [2003].**

B.3 DRM FOR SEISMIC INPUT IN SSI MODELS

Assume that the DRM is used to model the same dam–foundation rock problem from Appendix A (Figure A.5), where viscous dampers are used to model the unbounded extend of the foundation domain. The equations of motion for this system are given by Equation (B.6). The effective seismic input forces are given in terms of the free-field motion by Equation (B.7) and applied to a single layer of elements somewhere interior of the absorbing boundary between Γ and Γ_e; see Figure B.3.

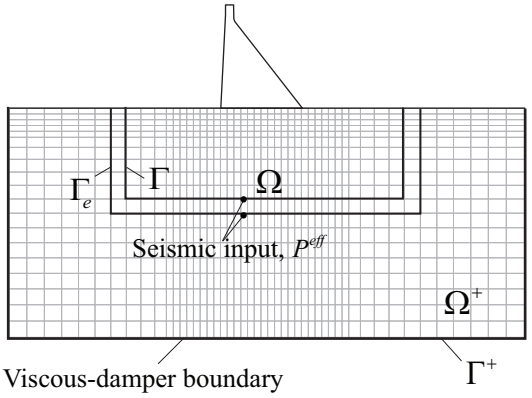

Figure B.3 DRM for seismic input to dam–foundation rock system.

Viscous dampers are applied at the outer boundary of the exterior region Ω^+. At this boundary, the viscous dampers must absorb the motion relative to the free-field motion, which by definition in the DRM formulation [Equation (B.5)] is equal to $w_e = u_e - u_e^0$. This means viscous dampers with coefficients $\rho A V_k$ can be applied at the truncation boundary without further modification.

Even though the formulation for the DRM seems very different from the direct FE method formulated in Part I, they are in fact quite similar when used for soil–structure interaction models: both formulations provide a method to apply effective earthquake forces to the model, and both allow for the outgoing (scattered) motion to be absorbed at the absorbing boundary. The advantage of the DRM is that it decouples the location of the absorbing boundary from application of earthquake forces, thus allowing advanced boundary conditions to be used and the domain sizes to be reduced accordingly. Two significant disadvantages are: (1) implementation of DRM requires modification of the FE source code, effectively limiting its application to users of LS-DYNA, the only FE code routinely used in dam engineering where DRM is available; and (2) specifying the seismic input for a combined dam–water–foundation rock system with small domain sizes is impractical because it requires auxiliary analysis of a complex water–foundation rock system and extensive book-keeping. For these reasons, the DRM was not chosen as the method for applying seismic input in the direct FE method developed in Part I and II of this report.

B.4 COMPARISON OF DIRECT FE METHOD TO DRM

To compare the DRM and the direct FE method, the dynamic response of Pine Flat Dam is computed by both methods. The FE mesh and material properties of this system are described in Section A.3 of Appendix A. The seismic input for the DRM is computed from Equation (B.7) with the free-field motions obtained from the same auxiliary analysis that is used for the direct FE method (described in Box 3.2 of Part I). This way, both methods are based on the same set of assumptions regarding the seismic wave field (vertically propagating waves).

Frequency response functions for the dam computed by the two methods are compared in Figure B.4. The response computed by the direct FE method is essentially identical to that when using the DRM, only some insignificant differences exist because of the numerical discretization. This demonstrates the equivalency of the two methods when used to specify seismic inputs: the DRM will give identical results as the direct FE method when used to analyze the same dam–foundation rock system with the same boundary condition and free-field motions based on the same assumptions.

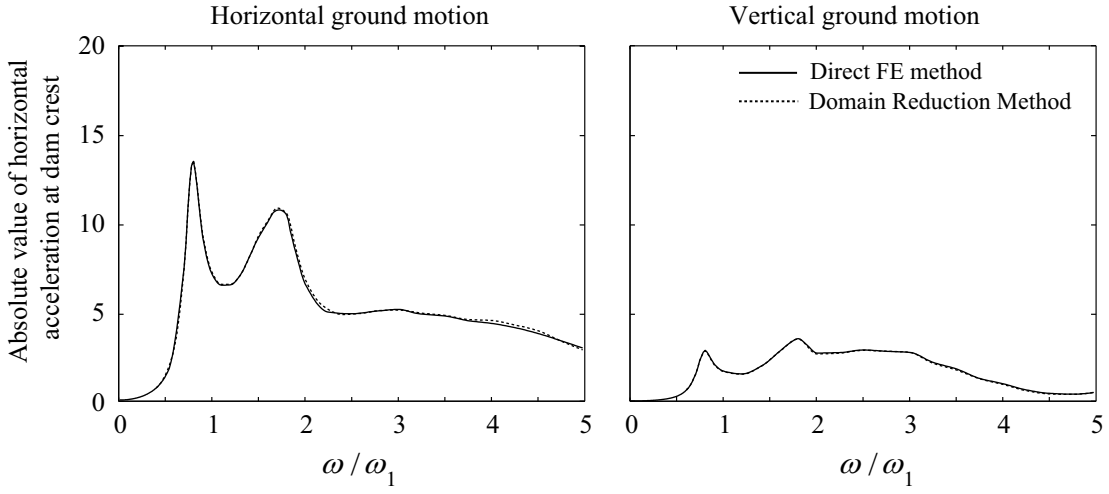

Figure B.4 **Comparison of frequency response functions computed by the direct FE method and DRM for dam on flexible foundation rock due to horizontal and vertical ground motion.** $\zeta_s = \zeta_f = 2\%$ **.**

APPENDIX C Computing Frequency Response Functions in the Time Domain

The frequency response functions for the dam response that are computed and compared to results from the substructure method in Parts I and II are dimensionless response factors that represent the radial acceleration at the crest of the dam to unit harmonic, free-field acceleration. The details of two procedures for computing these frequency response functions in the direct FE method are presented in this appendix, and both procedures are verified individually by comparing against independent solutions obtained using the substructure method.

C.1 FREQUENCY RESPONSE FUNCTIONS BY REPEATED STEADY-STATE ANALYSIS

The first method to determine the frequency response function $H(\omega)$ for the system is to perform repeated steady-state analysis (Figure C.1): (1) first, the steady-state response u_n of the system to a single excitation frequency f_n is computed by solving the by equations of motion for long enough for steady-state to occur; and (2) this analysis is repeated at a sufficient number of frequencies to generate a smooth frequency response function. This approach is straightforward, but because it requires repeated steady-state analyses of the system at a high number of frequencies, it becomes excessively time consuming for 3D dam–water–foundation rock systems that may easily have several hundreds of thousands of FEs. An alternative procedure that is much more computationally effective is presented next.

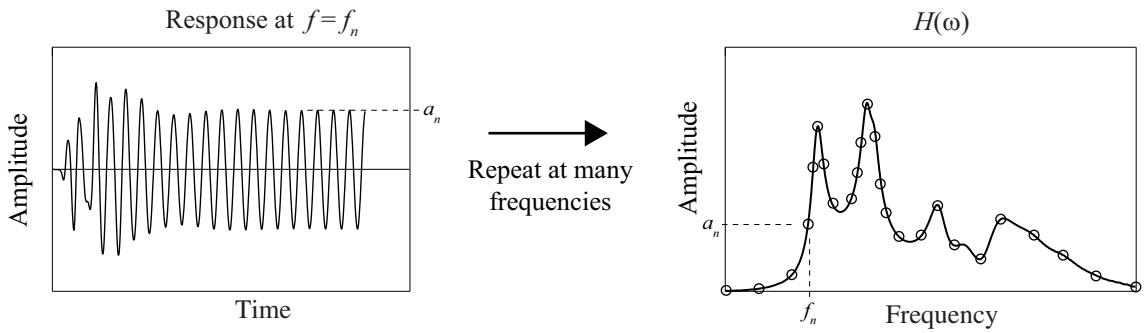

Figure C.1 Schematic overview of procedure for computing frequency response functions by repeated steady-state analysis.

C.2 FREQUENCY RESPONSE FUNCTIONS BY FOURIER ANALYSIS

The dynamic response $u(t)$ of a system can be expressed in the frequency domain as the product of the frequency response function for the system and the Fourier transfer of the applied excitation [Chopra 2012b]:

$$U(\omega) = H(\omega)\, A(\omega) \tag{C.1}$$

where $U(\omega)$ $U(\omega)$ is the Fourier transform of the dynamic response $u(t)$, $H(\omega)$ is the frequency response function (FRF), and $A(\omega)$ is the Fourier transform of the applied excitation $a_g(t)$. Rearranging Equation (C.1), an expression for the FRF for the system is obtained as

$$H(\omega) = U(\omega) / A(\omega) \tag{C.2}$$

If the input and outputs signals were described by analytical expressions valid for all frequencies, it would be possible to obtain the exact FRF from Equation (C.2). Such analytical expressions are rarely available except for very simple systems; thus, the above equation will normally provide a numerical estimate of the FRF, which is valid only within a given range of frequencies. Such an estimate is obtained for the arch dam–water–foundation rock system using the following procedure (Figure C.2):

1. The free-field control motion $a_g(t)$ is defined as a long series of continuous unit harmonic sine waves that has gradually increasing frequency. A sufficient number of frequencies are included in $a_g(t)$ to ensure that the system is excited adequately over the frequency range of interest between approx. 2–20 Hz.

2. The dynamic response $u(t)$, here selected as the radial acceleration at the crest of the dam, is computed by time-domain analysis of the FE model by the direct FE method.

3. The Fourier transforms $A(\omega)$ and $U(\omega)$ of the input and output signals, respectively, are computed using the fast Fourier transform (FFT). The FRF for the dam response is computed from Equation (C.2).

The advantage of this approach is that it requires only a single dynamic analysis, thus significantly reducing the computational effort compared to doing a repeated number of steady-state analyses. For example, it takes just under three hours to accurately compute the FRF for the arch dam–water–foundation rock system analyzed in Part II of this report between 2–20 Hz using the Fourier analysis approach. In contrast, obtaining the same FRF using repeated steady-state analysis takes in excess of 12 hours.

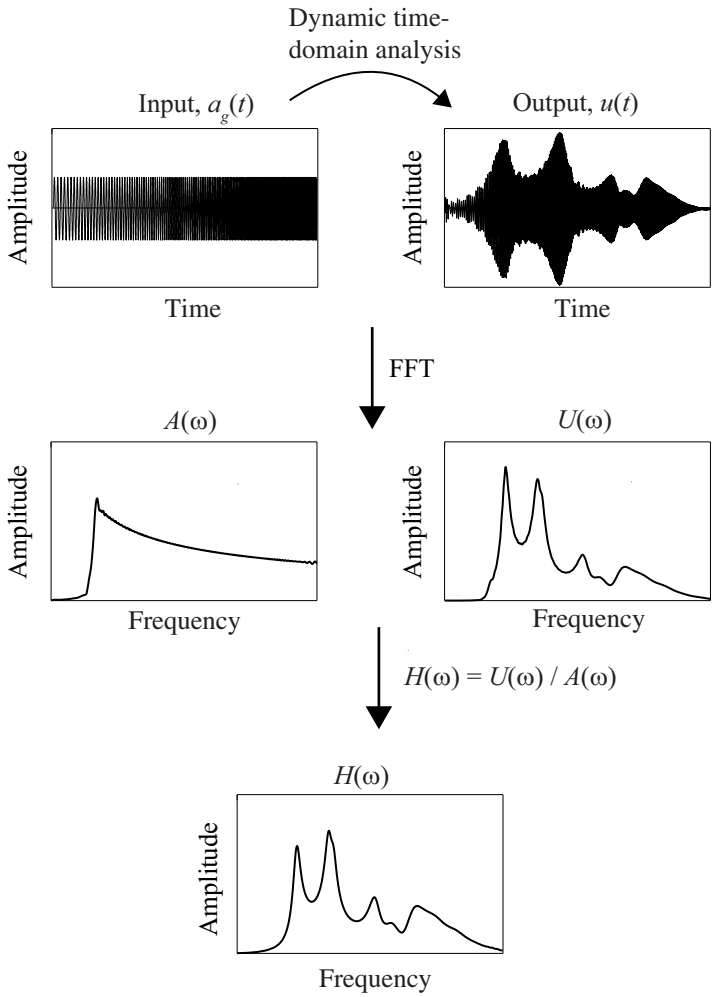

Figure C.2 **Schematic overview of procedure for computing frequency response functions using Fourier analysis.**

C.3 VERIFICATION OF IMPLEMENTATION

Implementation of the two procedures for obtaining FRFs in the time domain is verified by computing the response of Morrow Point Dam alone on rigid foundation with empty reservoir and comparing against results obtained using the substructure method. The mesh and material properties for the dam are the same as those described in Section 5.2.1 of Part II. The results presented in Figure C.3 demonstrates that the two procedures for obtaining FRFs give near identical results, and that these results are very close to those obtained using the substructure method.

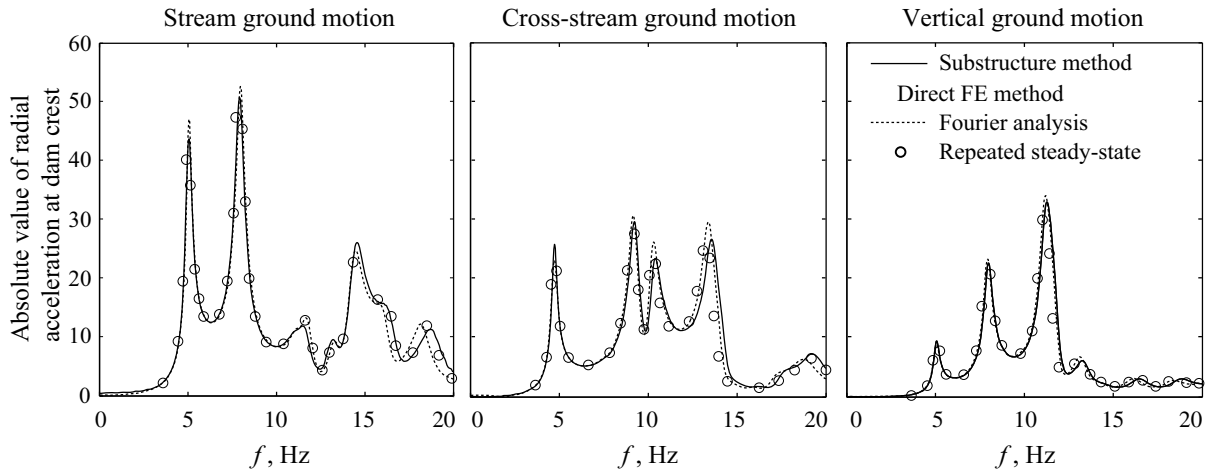

Figure C.3 **Comparison of frequency response functions for the amplitude of relative radial acceleration at the crest of dam on rigid foundation with empty reservoir due to uniform stream, cross-stream and vertical ground motions. ζ_s = 3%.**

APPENDIX D Applying Uniform Ground Motion in the Direct FE Method

The response results presented in Section 5.3 of Part II for several dam–water–foundation rock systems were computed under the assumption that the ground motion $a_g(t)$ was uniform at the dam–foundation interface and water–foundation interface. For these analyses, the seismic input method proposed by Wilson [2002] was extended and implemented to apply the earthquake excitation to the FE model. This method is derived below for the dam–water–foundation rock system

D.1 EQUATIONS OF MOTION

Consider the dam–water–foundation rock system (Figure 3.1 of Part II) whose equations of motion were given by Equation (3.1) in Part II. For convenience of notation in the subsequent derivation, it is assumed that the system is linear elastic with no material damping, thus reducing the governing equation for the dam–water–foundation rock system to:

$$\begin{bmatrix} \mathbf{m} & \mathbf{0} \\ \rho(\mathbf{Q}_h^{\mathrm{T}} + \mathbf{Q}_b^{\mathrm{T}}) & \mathbf{s} \end{bmatrix} \begin{Bmatrix} \ddot{\mathbf{r}}^t \\ \ddot{\mathbf{p}}^t \end{Bmatrix} + \begin{bmatrix} \mathbf{k} & -(\mathbf{Q}_h + \mathbf{Q}_b) \\ \mathbf{0} & \mathbf{h} \end{bmatrix} \begin{Bmatrix} \mathbf{r}^t \\ \mathbf{p}^t \end{Bmatrix} = \begin{Bmatrix} \mathbf{R}_f^t \\ \mathbf{H}_r^t \end{Bmatrix} \tag{D.1}$$

If water–foundation rock is ignored upstream of the absorbing boundary Γ_r and the free-field foundation-rock motion $\mathbf{r}^0$ is known, we can express the total motion $\mathbf{r}^t$ in terms of the displacements $\mathbf{r}$ relative to the free-field motion $\mathbf{r}^0$, i.e., $\mathbf{r}^t = \mathbf{r} + \mathbf{r}^0$. Rewriting Equation (D.1) and collecting terms that involve $\mathbf{r}^0$ on the right hand side, the following equation is obtained:

$$\begin{bmatrix} \mathbf{m} & \mathbf{0} \\ \rho(\mathbf{Q}_h^{\mathrm{T}} + \mathbf{Q}_b^{\mathrm{T}}) & \mathbf{s} \end{bmatrix} \begin{Bmatrix} \ddot{\mathbf{r}} \\ \ddot{\mathbf{p}}^t \end{Bmatrix} + \begin{bmatrix} \mathbf{k} & -(\mathbf{Q}_h + \mathbf{Q}_b) \\ \mathbf{0} & \mathbf{h} \end{bmatrix} \begin{Bmatrix} \mathbf{r} \\ \mathbf{p}^t \end{Bmatrix} = \begin{Bmatrix} \mathbf{R}_f \\ \mathbf{H}_r^t \end{Bmatrix} - \begin{Bmatrix} \mathbf{m}\ddot{\mathbf{r}}^0 + \mathbf{k}\mathbf{r}^0 - \mathbf{R}_f^0 \\ \rho(\mathbf{Q}_h^{\mathrm{T}} + \mathbf{Q}_b^{\mathrm{T}})\ddot{\mathbf{r}}^0 \end{Bmatrix} \tag{D.2}$$

This equation can be simplified when the free-field displacements $\mathbf{r}_b^0$ at the dam–foundation interface are uniform. Under this assumption, the static rigid body motion of the dam is:

$$\mathbf{k}_d \mathbf{r}_b^0 = \mathbf{0} \tag{D.3}$$

where $\mathbf{k}_d$ is the stiffness matrix for the dam alone. Furthermore, the equation governing displacements in the free-field foundation-rock system are

$$\mathbf{m}_0 \ddot{\mathbf{r}}^0 + \mathbf{k}_0 \mathbf{r}^0 = \mathbf{R}_f^0 \tag{D.4}$$

where $\mathbf{m}_0$ and $\mathbf{k}_0$ are the mass and stiffness matrices, respectively, for the foundation rock alone. Using Equations (D.3) and (D.4) and cancelling terms, Equation (D.2) becomes

$$\begin{bmatrix} \mathbf{m} & \mathbf{0} \\ \rho(\mathbf{Q}_h^{\mathrm{T}} + \mathbf{Q}_b^{\mathrm{T}}) & \mathbf{s} \end{bmatrix} \begin{Bmatrix} \ddot{\mathbf{r}} \\ \ddot{\mathbf{p}}^t \end{Bmatrix} + \begin{bmatrix} \mathbf{k} & -(\mathbf{Q}_h + \mathbf{Q}_b) \\ \mathbf{0} & \mathbf{h} \end{bmatrix} \begin{Bmatrix} \mathbf{r} \\ \mathbf{p}^t \end{Bmatrix} = \begin{Bmatrix} \mathbf{R}_f \\ \mathbf{H}_r^t \end{Bmatrix} + \begin{Bmatrix} \mathbf{P}_d^0 \\ -\rho(\mathbf{Q}_h^{\mathrm{T}} + \mathbf{Q}_b^{\mathrm{T}}) \ddot{\mathbf{r}}_b^0 \end{Bmatrix} \tag{D.5}$$

where the effective earthquake forces $\mathbf{P}_d^0$ applied to the dam nodes are

$$\mathbf{P}_d^0 = -\mathbf{m}_d \ddot{\mathbf{r}}_b^0 = -\mathbf{m}_d \boldsymbol{\iota} a_g(t) \tag{D.6}$$

where $\boldsymbol{\iota}$ is the influence vector [Chopra 2012b], and $a_g(t)$ is the free-field ground motion assumed at the dam–foundation interface.

Substituting Equations (3.2a) and (3.4b) of Part II for $\mathbf{R}_f$ and $\mathbf{H}_r^t$, respectively, in Equation (D.6), and adding material damping and static forces to the formulation, gives the final equations of motion for the dam–water–foundation rock system with uniform excitation:

$$\begin{aligned} &\begin{bmatrix} \mathbf{m} & \mathbf{0} \\ \rho(\mathbf{Q}_h^{\mathrm{T}} + \mathbf{Q}_b^{\mathrm{T}}) & \mathbf{s} \end{bmatrix} \begin{Bmatrix} \ddot{\mathbf{r}} \\ \ddot{\mathbf{p}}^t \end{Bmatrix} + \begin{bmatrix} \mathbf{c} + \mathbf{c}_f & \mathbf{0} \\ \mathbf{0} & \mathbf{b} + \mathbf{c}_r \end{bmatrix} \begin{Bmatrix} \dot{\mathbf{r}} \\ \dot{\mathbf{p}}^t \end{Bmatrix} \\ &\qquad + \begin{bmatrix} \mathbf{k} & -(\mathbf{Q}_h + \mathbf{Q}_b) \\ \mathbf{0} & \mathbf{h} \end{bmatrix} \begin{Bmatrix} \mathbf{r} \\ \mathbf{p}^t \end{Bmatrix} = \begin{Bmatrix} \mathbf{R}^{\mathrm{st}} \\ \mathbf{0} \end{Bmatrix} + \begin{Bmatrix} \mathbf{P}_d^0 \\ \mathbf{P}_r^0 - \rho(\mathbf{Q}_h^{\mathrm{T}} + \mathbf{Q}_b^{\mathrm{T}}) \ddot{\mathbf{r}}_b^0 \end{Bmatrix} \end{aligned} \tag{D.7}$$

Comparing Equation (D.7) to Equation (3.6) demonstrates that changing variable $\mathbf{r}^t = \mathbf{r} + \mathbf{r}^0$ in the dam and foundation rock has led to two changes: (1) the effective earthquake forces $\mathbf{P}_f^0$ at the foundation boundaries have been replaced by the effective earthquake forces $\mathbf{P}_d^0$ applied to the dam only; and (2) the effective earthquake forces $\mathbf{P}_r^0$ at the fluid boundary have been supplemented by forces $-\rho(\mathbf{Q}_h^{\mathrm{T}} + \mathbf{Q}_b^{\mathrm{T}})\ddot{\mathbf{r}}_b^0$ applied to the dam–water and water–foundation interfaces. These modifications allow for application of effective earthquake forces that is consistent with the assumption of uniform ground motion at the dam–foundation and water–foundation interfaces.

D.2 VERIFICATION OF IMPLEMENTATION

Implementation of the method is verified by computing the response of Morrow Point Dam on rigid foundation with full reservoir, with mesh and material properties chosen as the same as those described in Section 5.2.1 of Part II. The results obtained using the method derived in Section D.1 are compared with independent results obtained by directly prescribing the free-field displacements at the dam–foundation and water–foundation interfaces.

The frequency response functions for the amplitude of relative radial acceleration at the crest of the dam obtained by the two methods are presented in Figure D.1. The results obtained using Equation (D.7) leads to results that are essentially identical to those obtained by directly prescribing the free-field displacements for the system. The small differences in the results are due to the slight numerical differences associated with applying forces based on accelerations vs. directly prescribing base displacements.

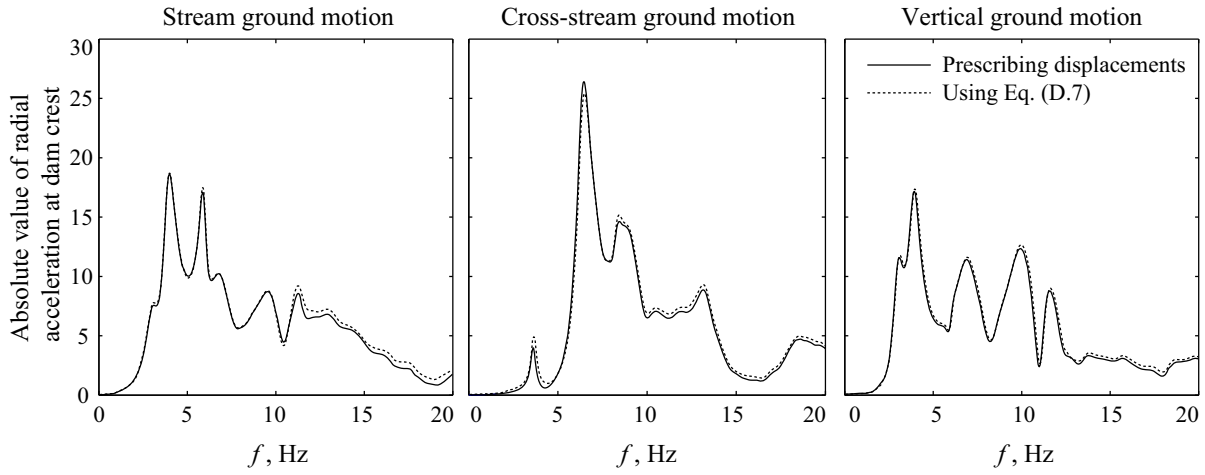

Figure D.1 **Comparison of frequency response functions for the amplitude of relative radial acceleration at the crest of dam on rigid foundation with full reservoir due to uniform-stream, cross-stream, and vertical ground motions. ζ_s = 3%; α = 0.80.**

APPENDIX E Computing Boundary Tractions from 1D Stress–Strain Relations

E.1 ONE-DIMENSIONAL STRESS–STRAIN RELATIONS

The simplified 1D free-field analysis presented in Section 6.1 of Part II replaced the actual free-field foundation-rock system by a much simpler system [Figure 6.1(b)]: a homogeneous or horizontally layered half-space without the canyon topography. Under the assumption of vertically propagating seismic waves, this system reduces to a single column of foundation-rock elements that only allows for shear and axial deformation [Figure E.1(a)]. The boundary tractions for this system can be computed using standard 1D stress-strain relationships:

$$\tau_{xz} = \mu \frac{du}{dz} n_x \qquad \text{for } x\text{-component of ground motion} \tag{E.1a}$$

$$\tau_{yz} = \mu \frac{dv}{dz} n_y \qquad \text{for } y\text{-component of ground motion} \tag{E.1b}$$

$$\sigma_x = \lambda \frac{dw}{dz} n_x,\ \sigma_y = \lambda \frac{dw}{dz} n_y \qquad \text{for } z\text{-component of ground motion} \tag{E.1c}$$

where σ_k and τ_{kz}, $k = x, y$ are the normal and tangential boundary tractions [Figure E.1(b)]; u, v, w are the displacements in the x-, y-, and z-direction, respectively; λ and μ are the first and second Lamé parameters for the foundation rock; and $n_k = +1$ or -1 if an outward normal points in the positive or negative k-direction, respectively.

Horizontal excitation will only produce tangential tractions because $dw/dz = 0$, and vertical motion will only produce normal tractions because $du/dz = 0$ and $dv/dz = 0$ (Figure E.1a). From the boundary tractions σ_k and τ_{kz}, nodal forces are computed by multiplying by the tributary area of each node.

E.2 VERIFICATION OF IMPLEMENTATION

Implementation of the method is verified by computing the surface response of the flat foundation domain of Figure 5.1 of Part II with the free-field control motion $a_g^k(t)$ defined at the surface by the S69E, S21W, and vertical components of the Taft ground motion. Effective earthquake forces $\mathbf{P}_f^0$ are computed from the procedures summarized in Box 4.1 of Part II at the bottom boundary and from a 1D free-field analysis (Box 6.1) with boundary tractions computed from Equation (E.1) at the side boundaries, and the motion at the surface of the flat foundation domain is determined.

The results presented in Figure E.2 shows a near-perfect match between the assumed free-field control motion and the computed motion at the surface of the flat foundation domain, thus verifying the implementation of the procedure.

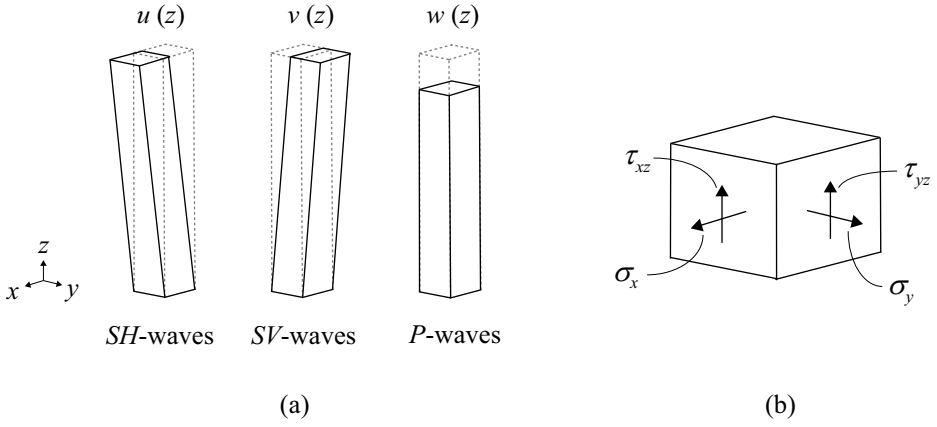

Figure E.1 **(a) Deformation of foundation rock column due to vertically propagating *SH*-, *SV*-, and *P*-waves; and (b) normal and tangential boundary tractions for foundation-rock element.**

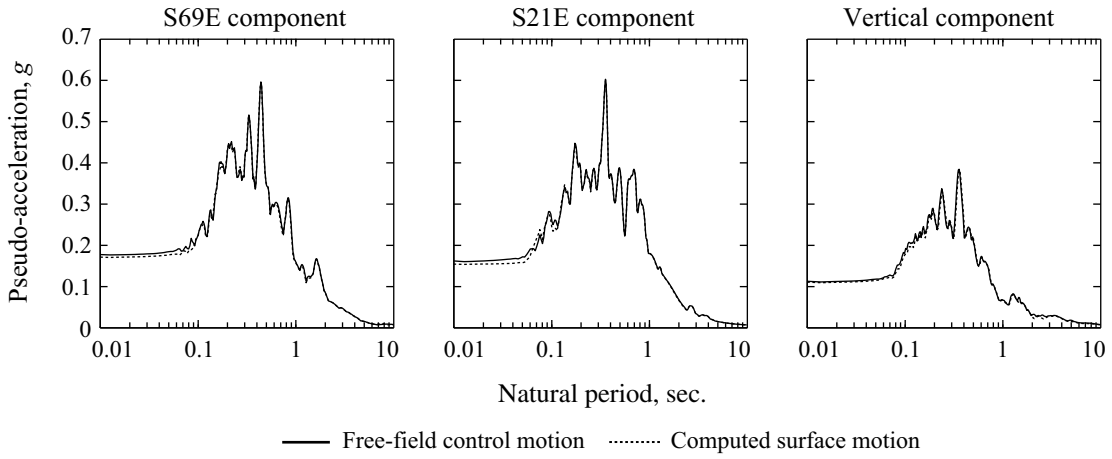

Figure E.2 **Results from Flat Box Test: comparison of 5% damped pseudo-acceleration response spectra of free-field control motion and motion computed at nodes on the flax box surface.**

APPENDIX F Influence of Water–Foundation Rock Interaction and Implications for the Substructure Method

The conclusion that sediments can be ignored in analysis of dam–water–foundation rock systems (Section 3.2.3 of Part III) is based on results from the direct FE method, which rigorously includes water–foundation rock interaction. In contrast, earlier results computed by the substructure method, which ignores water–foundation rock interaction, concluded that the influence of sediments can be significant [Fenves and Chopra 1985; Tan and Chopra 1995b]. The influence of neglecting water–foundation rock interaction on dam response, and its implications for use of the substructure method for earthquake analysis of concrete dams, is investigated next.

F.1 EFFECTS OF WATER–FOUNDATION ROCK INTERACTION

Investigated first are the errors arising from neglecting water–foundation rock interaction. Determined by the direct FE method, the frequency response functions for the idealized gravity dam system described in Section 3.2.3.1 of Part III with full reservoir but no sediment at the reservoir bottom are presented in Figure F.1 for two cases: water–foundation rock interaction is included in one case but excluded in the other. Results are presented for both components of ground motion and for three values of E_f / E_s.

The results demonstrate that water–foundation rock interaction has negligible influence on the response of gravity dams to horizontal ground motion at all excitation frequencies, except for those frequencies very close to the resonant frequencies of the system where the influence is noticeable. Note, this influence is not significant for earthquake response, as confirmed by the two sets of response histories presented in Figure F.2(a), which are essentially identical.

The preceding observation based on frequency response functions is generally valid also for response to vertical ground motion, but for one important exception. At the resonant frequencies of the reservoir, the dam response is greatly overestimated if water–foundation rock interaction is ignored. Because this discrepancy occurs within a narrow range of frequencies around the reservoir natural frequencies, the overestimation is much less in the earthquake response of the dam [Figure F.2(b)]; this observation is expected to be valid for most ground motions. These results support the approximation of neglecting water–foundation rock interaction in the substructure method.

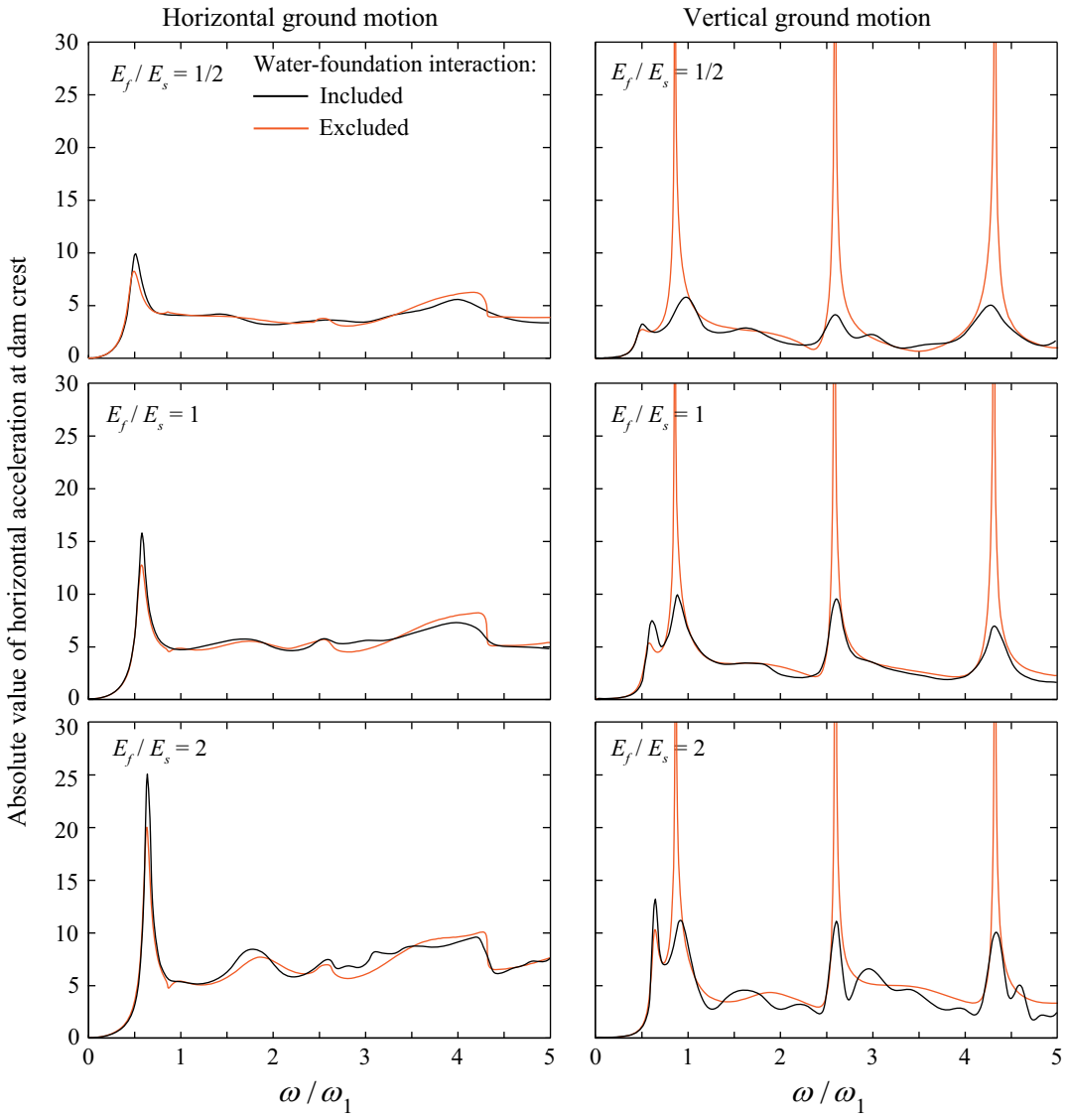

Figure F.1 **Effects of water–foundation rock interaction on frequency response function for gravity dams with full reservoir but no sediments due to horizontal and vertical ground motions. Results are presented for three values of E_f / E_s = ½, 1, and 2.**

F.2 APPROXIMATE MODELING OF WATER–FOUNDATION ROCK INTERACTION

Although the errors introduced by neglecting water–foundation rock interaction are not large, they can be essentially eliminated by a simple model that can conveniently be included in the substructure method. For this purpose, water–foundation rock interaction is modeled approximately by the wave-reflection coefficient α, introduced in the substructure method to model wave absorption in sedimentary deposits at the reservoir bottom [Fenves and Chopra 1985; Tan and Chopra 1995b]:

$$\alpha = \frac{1-\xi C}{1+\xi C}, \tag{F1}$$

where $\xi = \rho / \rho_r C_r$, C is the speed of pressure waves in the water, ρ is the density of water, C_r is the compression wave velocity in the rock, and ρ_r is the density of the rock. Observe that α is now determined based on the properties of the rock, not the sediments.

Determined by the direct FE method, the frequency response functions for a gravity dam with full reservoir but no sediments at the reservoir bottom are presented in Figure F.3 for two models for water–foundation rock interaction: (1) rigorous, and (2) approximate α-model with α values computed from Equation (F1) based on rock properties. The results demonstrate that near the resonant frequencies, the response is underestimated by the α-model; but at all other excitation frequencies, the α-model is highly accurate. Note: the α-model—with the value of α based on rock properties—is able to predict the response to earthquake ground motion quite accurately, which is apparent from the close agreement of the results in Figure F.4.

These results demonstrate that modeling water–foundation rock interaction by the α-model with α based on rock properties is a reasonable approximation for earthquake analysis of concrete dams by the substructure method, where water–foundation rock interaction is ignored in the formulation of the method. A corollary of the results and conclusions presented in Section 3.2.3 is that with water–foundation rock interaction modeled in this manner, reservoir bottom sediments can be ignored in the substructure method just as in the direct FE method.

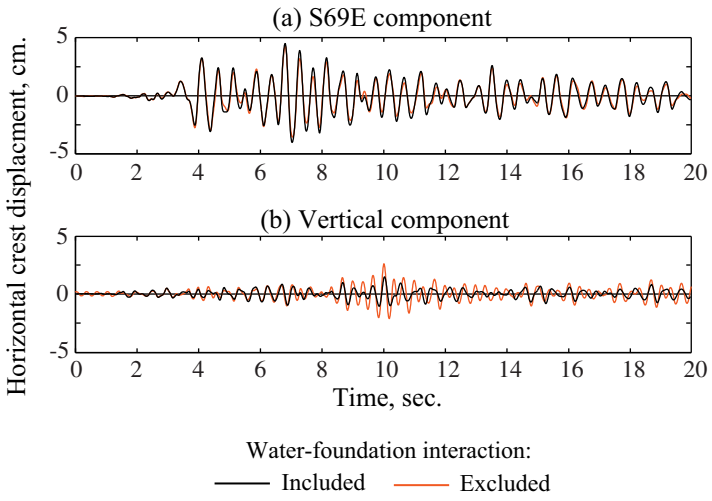

Figure F.2 **Effects of water–foundation rock interaction on earthquake response of a gravity dam with full reservoir but no sediments, E_f / E_s = 1. Responses presented are for the (a) S69E component and (b) vertical component of the Taft ground motion.**

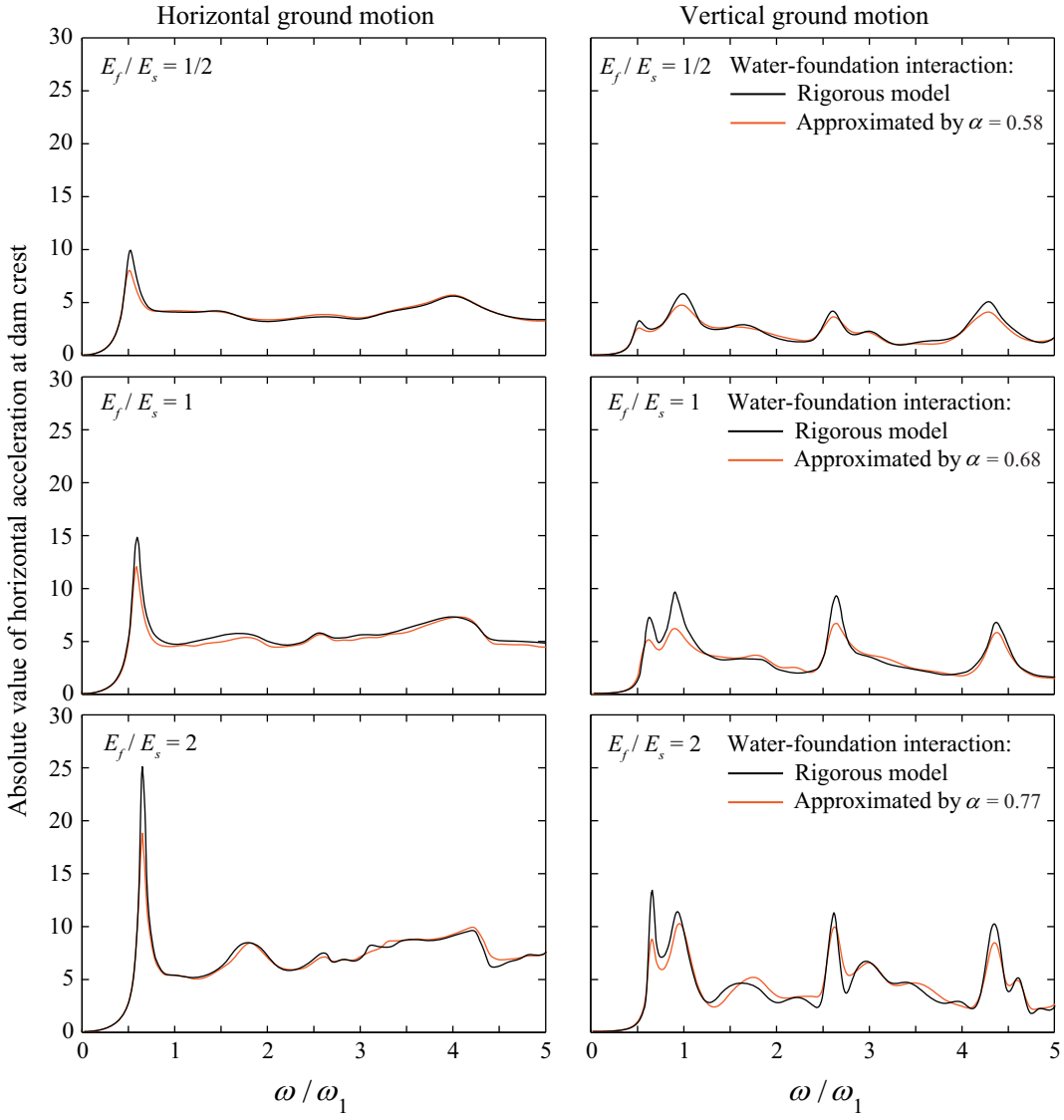

Figure F.3 **Effects of water–foundation rock interaction on frequency response function for gravity dams with full reservoir but no sediments due to horizontal and vertical ground motions. Results are presented for two models for water–foundation rock interaction: (1) rigorous and (2) approximate α-model.**

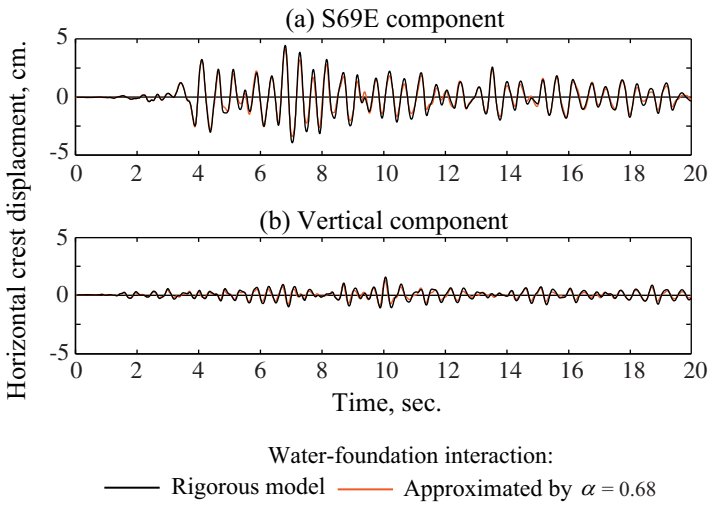

Figure F.4 **Earthquake response of gravity dam with full reservoir but no sediments, E_f / E_s = 1. Responses presented are for the (a) S69E component and (b) vertical component of the Taft ground motion.**

PEER REPORTS

PEER reports are available as a free PDF download from https://peer.berkeley.edu/peer-reports. In addition, printed hard copies of PEER reports can be ordered directly from our printer by following the instructions at https://peer.berkeley.edu/peer-reports. For other related questions about the PEER Report Series, contact the Pacific Earthquake Engineering Research Center, 325 Davis Hall, Mail Code 1792, Berkeley, CA 94720. Tel.: (510) 642-3437; and Email: peer_center@berkeley.edu.

PEER 2019/01 *Flow-Failure Case History of the Las Palmas, Chile, Tailings Dam.* R. E. S. Moss, T. R. Gebhart, D. J. Frost, and C. Ledezma, January 2019.

PEER 2018/08 *Central and Eastern North America Ground-Motion Characterization: NGA-East Final Report*. Christine Goulet, Yousef Bozorgnia, Norman Abrahamson, Nicolas Kuehn, Linda Al Atik, Robert Youngs, Robert Graves, and Gail Atkinson. December 2018.

PEER 2018/07 *An Empirical Model for Fourier Amplitude Spectra using the NGA-West2 Database*. Jeff Bayless, and Norman A. Abrahamson. December 2018.

PEER 2018/06 *Estimation of Shear Demands on Rock-Socketed Drilled Shafts subjected to Lateral Loading*. Pedro Arduino, Long Chen, and Christopher R. McGann. December 2018.

PEER 2018/05 *Selection of Random Vibration Procedures for the NGA-East Project*. Albert Kottke, Norman A. Abrahamson, David M. Boore, Yousef Bozorgnia, Christine Goulet, Justin Hollenback, Tadahiro Kishida, Armen Der Kiureghian, Olga-Joan Ktenidou, Nicolas Kuehn, Ellen M. Rathje, Walter J. Silva, Eric Thompson, and Xiaoyue Wang. December 2018.

PEER 2018/04 *Capturing Directivity Effects in the Mean and Aleatory Variability of the NGA-West 2 Ground Motion Prediction Equations.* Jennie A. Watson-Lamprey. November 2018.

PEER 2018/03 *Probabilistic Seismic Hazard Analysis Code Verification*. Christie Hale, Norman Abrahamson, and Yousef Bozorgnia. July 2018.

PEER 2018/02 *Update of the BCHydro Subduction Ground-Motion Model using the NGA-Subduction Dataset.* Norman Abrahamson, Nicolas Kuehn, Zeynep Gulerce, Nicholas Gregor, Yousef Bozorgnia, Grace Parker, Jonathan Stewart, Brian Chiou, I. M. Idriss, Kenneth Campbell, and Robert Youngs. June 2018.

PEER 2018/01 *PEER Annual Report 2017–2018*. Khalid Mosalam, Amarnath Kasalanati, and Selim Günay. June 2018.

PEER 2017/12 *Experimental Investigation of the Behavior of Vintage and Retrofit Concentrically Braced Steel Frames under Cyclic Loading*. Barbara G. Simpson, Stephen A. Mahin, and Jiun-Wei Lai, December 2017.

PEER 2017/11 *Preliminary Studies on the Dynamic Response of a Seismically Isolated Prototype Gen-IV Sodium-Cooled Fast Reactor* (*PGSFR*). Benshun Shao, Andreas H. Schellenberg, Matthew J. Schoettler, and Stephen A. Mahin. December 2017.

PEER 2017/10 *Development of Time Histories for IEEE693 Testing and Analysis (including Seismically Isolated Equipment).* Shakhzod M. Takhirov, Eric Fujisaki, Leon Kempner, Michael Riley, and Brian Low. December 2017.

PEER 2017/09 *""R" Package for Computation of Earthquake Ground-Motion Response Spectra.* Pengfei Wang, Jonathan P. Stewart, Yousef Bozorgnia, David M. Boore, and Tadahiro Kishida. December 2017.

PEER 2017/08 *Influence of Kinematic SSI on Foundation Input Motions for Bridges on Deep Foundations*. Benjamin J. Turner, Scott J. Brandenberg, and Jonathan P. Stewart. November 2017.

PEER 2017/07 *A Nonlinear Kinetic Model for Multi-Stage Friction Pendulum Systems*. Paul L. Drazin and Sanjay Govindjee. September 2017.

PEER 2017/06 *Guidelines for Performance-Based Seismic Design of Tall Buildings, Version 2.02*. TBI Working Group led by co-chairs Ron Hamburger and Jack Moehle: Jack Baker, Jonathan Bray, C.B. Crouse, Greg Deierlein, John Hooper, Marshall Lew, Joe Maffei, Stephen Mahin, James Malley, Farzad Naeim, Jonathan Stewart, and John Wallace. May 2017.

PEER 2017/05 *Recommendations for Ergodic Nonlinear Site Amplification in Central and Eastern North America*. Youssef M.A. Hashash, Joseph A. Harmon, Okan Ilhan, Grace A. Parker, and Jonathan P. Stewart. March 2017.

PEER 2017/04 *Expert Panel Recommendations for Ergodic Site Amplification in Central and Eastern North America*. Jonathan P. Stewart, Grace A. Parker, Joseph P. Harmon, Gail M. Atkinson, David M. Boore, Robert B. Darragh, Walter J. Silva, and Youssef M.A. Hashash. March 2017.

PEER 2017/03 *NGA-East Ground-Motion Models for the U.S. Geological Survey National Seismic Hazard Maps*. Christine A. Goulet, Yousef Bozorgnia, Nicolas Kuehn, Linda Al Atik, Robert R. Youngs, Robert W. Graves, and Gail M. Atkinson. March 2017.

PEER 2017/02 *U.S.–New Zealand–Japan Workshop: Liquefaction-Induced Ground Movements Effects, University of California, Berkeley, California, 2–4 November 2016.* Jonathan D. Bray, Ross W. Boulanger, Misko Cubrinovski, Kohji Tokimatsu, Steven L. Kramer, Thomas O'Rourke, Ellen Rathje, Russell A. Green, Peter K. Robinson, and Christine Z. Beyzaei. March 2017.

PEER 2017/01 *2016 PEER Annual Report*. Khalid M. Mosalam, Amarnath Kasalanati, and Grace Kang. March 2017.

PEER 2016/10 *Performance-Based Robust Nonlinear Seismic Analysis with Application to Reinforced Concrete Bridge Systems*. Xiao Ling and Khalid M. Mosalam. December 2016.

PEER 2017/09 *Detailing Requirements for Column Plastic Hinges subjected to Combined Flexural, Axial, and Torsional Seismic Loading.* Gabriel Hurtado and Jack P. Moehle. December 2016.

PEER 2016/08 *Resilience of Critical Structures, Infrastructure, and Communities*. Gian Paolo Cimellaro, Ali Zamani-Noori, Omar Kamouh, Vesna Terzic, and Stephen A. Mahin. December 2016.

PEER 2016/07 *Hybrid Simulation Theory for a Classical Nonlinear Dynamical System*. Paul L. Drazin and Sanjay Govindjee. September 2016.

PEER 2016/06 *California Earthquake Early Warning System Benefit Study*. Laurie A. Johnson, Sharyl Rabinovici, Grace S. Kang, and Stephen A. Mahin. July 2006.

PEER 2016/05 *Ground-Motion Prediction Equations for Arias Intensity Consistent with the NGA-West2 Ground-Motion Models.* Charlotte Abrahamson, Hao-Jun Michael Shi, and Brian Yang. July 2016.

PEER 2016/04 *The M_W 6.0 South Napa Earthquake of August 24, 2014: A Wake-Up Call for Renewed Investment in Seismic Resilience Across California.* Prepared for the California Seismic Safety Commission, Laurie A. Johnson and Stephen A. Mahin. May 2016.

PEER 2016/03 *Simulation Confidence in Tsunami-Driven Overland Flow.* Patrick Lynett. May 2016.

PEER 2016/02 *Semi-Automated Procedure for Windowing time Series and Computing Fourier Amplitude Spectra for the NGA-West2 Database.* Tadahiro Kishida, Olga-Joan Ktenidou, Robert B. Darragh, and Walter J. Silva. May 2016.

PEER 2016/01 *A Methodology for the Estimation of Kappa (κ) from Large Datasets: Example Application to Rock Sites in the NGA-East Database and Implications on Design Motions.* Olga-Joan Ktenidou, Norman A. Abrahamson, Robert B. Darragh, and Walter J. Silva. April 2016.

PEER 2015/13 *Self-Centering Precast Concrete Dual-Steel-Shell Columns for Accelerated Bridge Construction: Seismic Performance, Analysis, and Design*. Gabriele Guerrini, José I. Restrepo, Athanassios Vervelidis, and Milena Massari. December 2015.

PEER 2015/12 *Shear-Flexure Interaction Modeling for Reinforced Concrete Structural Walls and Columns under Reversed Cyclic Loading*. Kristijan Kolozvari, Kutay Orakcal, and John Wallace. December 2015.

PEER 2015/11 *Selection and Scaling of Ground Motions for Nonlinear Response History Analysis of Buildings in Performance-Based Earthquake Engineering*. N. Simon Kwong and Anil K. Chopra. December 2015.

PEER 2015/10 *Structural Behavior of Column-Bent Cap Beam-Box Girder Systems in Reinforced Concrete Bridges Subjected to Gravity and Seismic Loads. Part II: Hybrid Simulation and Post-Test Analysis*. Mohamed A. Moustafa and Khalid M. Mosalam. November 2015.

PEER 2015/09 *Structural Behavior of Column-Bent Cap Beam-Box Girder Systems in Reinforced Concrete Bridges Subjected to Gravity and Seismic Loads. Part I: Pre-Test Analysis and Quasi-Static Experiments*. Mohamed A. Moustafa and Khalid M. Mosalam. September 2015.

PEER 2015/08 *NGA-East: Adjustments to Median Ground-Motion Models for Center and Eastern North America*. August 2015.

PEER 2015/07 *NGA-East: Ground-Motion Standard-Deviation Models for Central and Eastern North America*. Linda Al Atik. June 2015.

PEER 2015/06 *Adjusting Ground-Motion Intensity Measures to a Reference Site for which V_{S30} = 3000 m/sec*. David M. Boore. May 2015.

PEER 2015/05 *Hybrid Simulation of Seismic Isolation Systems Applied to an APR-1400 Nuclear Power Plant.* Andreas H. Schellenberg, Alireza Sarebanha, Matthew J. Schoettler, Gilberto Mosqueda, Gianmario Benzoni, and Stephen A. Mahin. April 2015.

PEER 2015/04 *NGA-East: Median Ground-Motion Models for the Central and Eastern North America Region*. April 2015.

PEER 2015/03 *Single Series Solution for the Rectangular Fiber-Reinforced Elastomeric Isolator Compression Modulus*. James M. Kelly and Niel C. Van Engelen. March 2015.

PEER 2015/02 *A Full-Scale, Single-Column Bridge Bent Tested by Shake-Table Excitation.* Matthew J. Schoettler, José I. Restrepo, Gabriele Guerrini, David E. Duck, and Francesco Carrea. March 2015.

PEER 2015/01 *Concrete Column Blind Prediction Contest 2010: Outcomes and Observations.* Vesna Terzic, Matthew J. Schoettler, José I. Restrepo, and Stephen A Mahin. March 2015.

PEER 2014/20 *Stochastic Modeling and Simulation of Near-Fault Ground Motions for Performance-Based Earthquake Engineering*. Mayssa Dabaghi and Armen Der Kiureghian. December 2014.

PEER 2014/19 *Seismic Response of a Hybrid Fiber-Reinforced Concrete Bridge Column Detailed for Accelerated Bridge Construction*. Wilson Nguyen, William Trono, Marios Panagiotou, and Claudia P. Ostertag. December 2014.

PEER 2014/18 *Three-Dimensional Beam-Truss Model for Reinforced Concrete Walls and Slabs Subjected to Cyclic Static or Dynamic Loading*. Yuan Lu, Marios Panagiotou, and Ioannis Koutromanos. December 2014.

PEER 2014/17 *PEER NGA-East Database*. Christine A. Goulet, Tadahiro Kishida, Timothy D. Ancheta, Chris H. Cramer, Robert B. Darragh, Walter J. Silva, Youssef M.A. Hashash, Joseph Harmon, Jonathan P. Stewart, Katie E. Wooddell, and Robert R. Youngs. October 2014.

PEER 2014/16 *Guidelines for Performing Hazard-Consistent One-Dimensional Ground Response Analysis for Ground Motion Prediction*. Jonathan P. Stewart, Kioumars Afshari, and Youssef M.A. Hashash. October 2014.

PEER 2014/15 *NGA-East Regionalization Report: Comparison of Four Crustal Regions within Central and Eastern North America using Waveform Modeling and 5%-Damped Pseudo-Spectral Acceleration Response*. Jennifer Dreiling, Marius P. Isken, Walter D. Mooney, Martin C. Chapman, and Richard W. Godbee. October 2014.

PEER 2014/14 *Scaling Relations between Seismic Moment and Rupture Area of Earthquakes in Stable Continental Regions*. Paul Somerville. August 2014.

PEER 2014/13 *PEER Preliminary Notes and Observations on the August 24, 2014, South Napa Earthquake*. Grace S. Kang and Stephen A. Mahin, Editors. September 2014.

PEER 2014/12 *Reference-Rock Site Conditions for Central and Eastern North America: Part II – Attenuation (Kappa) Definition*. Kenneth W. Campbell, Youssef M.A. Hashash, Byungmin Kim, Albert R. Kottke, Ellen M. Rathje, Walter J. Silva, and Jonathan P. Stewart. August 2014.

PEER 2014/11 *Reference-Rock Site Conditions for Central and Eastern North America: Part I - Velocity Definition*. Youssef M.A. Hashash, Albert R. Kottke, Jonathan P. Stewart, Kenneth W. Campbell, Byungmin Kim, Ellen M. Rathje, Walter J. Silva, Sissy Nikolaou, and Cheryl Moss. August 2014.

PEER 2014/10 *Evaluation of Collapse and Non-Collapse of Parallel Bridges Affected by Liquefaction and Lateral Spreading*. Benjamin Turner, Scott J. Brandenberg, and Jonathan P. Stewart. August 2014.

PEER 2014/09 *PEER Arizona Strong-Motion Database and GMPEs Evaluation*. Tadahiro Kishida, Robert E. Kayen, Olga-Joan Ktenidou, Walter J. Silva, Robert B. Darragh, and Jennie Watson-Lamprey. June 2014.

PEER 2014/08 *Unbonded Pretensioned Bridge Columns with Rocking Detail*. Jeffrey A. Schaefer, Bryan Kennedy, Marc O. Eberhard, and John F. Stanton. June 2014.

PEER 2014/07 *Northridge 20 Symposium Summary Report: Impacts, Outcomes, and Next Steps*. May 2014.

PEER 2014/06 *Report of the Tenth Planning Meeting of NEES/E-Defense Collaborative Research on Earthquake Engineering*. December 2013.

PEER 2014/05 *Seismic Velocity Site Characterization of Thirty-One Chilean Seismometer Stations by Spectral Analysis of Surface Wave Dispersion*. Robert Kayen, Brad D. Carkin, Skye Corbet, Camilo Pinilla, Allan Ng, Edward Gorbis, and Christine Truong. April 2014.

PEER 2014/04 Effect of Vertical Acceleration on Shear Strength of Reinforced Concrete Columns. Hyerin Lee and Khalid M. Mosalam. April 2014.

PEER 2014/03 *Retest of Thirty-Year-Old Neoprene Isolation Bearings.* James M. Kelly and Niel C. Van Engelen. March 2014.

PEER 2014/02 *Theoretical Development of Hybrid Simulation Applied to Plate Structures.* Ahmed A. Bakhaty, Khalid M. Mosalam, and Sanjay Govindjee. January 2014.

PEER 2014/01 *Performance-Based Seismic Assessment of Skewed Bridges.* Peyman Kaviani, Farzin Zareian, and Ertugrul Taciroglu. January 2014.

PEER 2013/26 *Urban Earthquake Engineerin*g. Proceedings of the U.S.-Iran Seismic Workshop. December 2013.

PEER 2013/25 *Earthquake Engineering for Resilient Communities: 2013 PEER Internship Program Research Report Collection.* Heidi Tremayne (Editor), Stephen A. Mahin (Editor), Jorge Archbold Monterossa, Matt Brosman, Shelly Dean, Katherine deLaveaga, Curtis Fong, Donovan Holder, Rakeeb Khan, Elizabeth Jachens, David Lam, Daniela Martinez Lopez, Mara Minner, Geffen Oren, Julia Pavicic, Melissa Quinonez, Lorena Rodriguez, Sean Salazar, Kelli Slaven, Vivian Steyert, Jenny Taing, and Salvador Tena. December 2013.

PEER 2013/24 *NGA-West2 Ground Motion Prediction Equations for Vertical Ground Motions*. September 2013.

PEER 2013/23 *Coordinated Planning and Preparedness for Fire Following Major Earthquakes*. Charles Scawthorn. November 2013.

PEER 2013/22 *GEM-PEER Task 3 Project: Selection of a Global Set of Ground Motion Prediction Equations.* Jonathan P. Stewart, John Douglas, Mohammad B. Javanbarg, Carola Di Alessandro, Yousef Bozorgnia, Norman A. Abrahamson, David M. Boore, Kenneth W. Campbell, Elise Delavaud, Mustafa Erdik, and Peter J. Stafford. December 2013.

PEER 2013/21 *Seismic Design and Performance of Bridges with Columns on Rocking Foundations*. Grigorios Antonellis and Marios Panagiotou. September 2013.

PEER 2013/20 *Experimental and Analytical Studies on the Seismic Behavior of Conventional and Hybrid Braced Frames*. Jiun-Wei Lai and Stephen A. Mahin. September 2013.

PEER 2013/19 *Toward Resilient Communities: A Performance-Based Engineering Framework for Design and Evaluation of the Built Environment.* Michael William Mieler, Bozidar Stojadinovic, Robert J. Budnitz, Stephen A. Mahin, and Mary C. Comerio. September 2013.

PEER 2013/18 *Identification of Site Parameters that Improve Predictions of Site Amplification*. Ellen M. Rathje and Sara Navidi. July 2013.

PEER 2013/17 *Response Spectrum Analysis of Concrete Gravity Dams Including Dam-Water-Foundation Interaction*. Arnkjell Løkke and Anil K. Chopra. July 2013.

PEER 2013/16 *Effect of Hoop Reinforcement Spacing on the Cyclic Response of Large Reinforced Concrete Special Moment Frame Beams.* Marios Panagiotou, Tea Visnjic, Grigorios Antonellis, Panagiotis Galanis, and Jack P. Moehle. June 2013.

PEER 2013/15 *A Probabilistic Framework to Include the Effects of Near-Fault Directivity in Seismic Hazard Assessment*. Shrey Kumar Shahi, Jack W. Baker. October 2013.

PEER 2013/14 *Hanging-Wall Scaling using Finite-Fault Simulations.* Jennifer L. Donahue and Norman A. Abrahamson. September 2013.

PEER 2013/13 *Semi-Empirical Nonlinear Site Amplification and its Application in NEHRP Site Factors*. Jonathan P. Stewart and Emel Seyhan. November 2013.

PEER 2013/12 *Nonlinear Horizontal Site Response for the NGA-West2 Project.* Ronnie Kamai, Norman A. Abramson, Walter J. Silva. May 2013.

PEER 2013/11 *Epistemic Uncertainty for NGA-West2 Models.* Linda Al Atik and Robert R. Youngs. May 2013.

PEER 2013/10 *NGA-West 2 Models for Ground-Motion Directionality.* Shrey K. Shahi and Jack W. Baker. May 2013.

PEER 2013/09 *Final Report of the NGA-West2 Directivity Working Group.* Paul Spudich, Jeffrey R. Bayless, Jack W. Baker, Brian S.J. Chiou, Badie Rowshandel, Shrey Shahi, and Paul Somerville. May 2013.

PEER 2013/08 *NGA-West2 Model for Estimating Average Horizontal Values of Pseudo-Absolute Spectral Accelerations Generated by Crustal Earthquakes*. I. M. Idriss. May 2013.

PEER 2013/07 *Update of the Chiou and Youngs NGA Ground Motion Model for Average Horizontal Component of Peak Ground Motion and Response Spectra*. Brian Chiou and Robert Youngs. May 2013.

PEER 2013/06 *NGA-West2 Campbell-Bozorgnia Ground Motion Model for the Horizontal Components of PGA, PGV, and 5%-Damped Elastic Pseudo-Acceleration Response Spectra for Periods Ranging from 0.01 to 10 sec.* Kenneth W. Campbell and Yousef Bozorgnia. May 2013.

PEER 2013/05 *NGA-West 2 Equations for Predicting Response Spectral Accelerations for Shallow Crustal Earthquakes*. David M. Boore, Jonathan P. Stewart, Emel Seyhan, and Gail M. Atkinson. May 2013.

PEER 2013/04 *Update of the AS08 Ground-Motion Prediction Equations Based on the NGA-West2 Data Set*. Norman Abrahamson, Walter Silva, and Ronnie Kamai. May 2013.

PEER 2013/03 *PEER NGA-West2 Database.* Timothy D. Ancheta, Robert B. Darragh, Jonathan P. Stewart, Emel Seyhan, Walter J. Silva, Brian S.J. Chiou, Katie E. Wooddell, Robert W. Graves, Albert R. Kottke, David M. Boore, Tadahiro Kishida, and Jennifer L. Donahue. May 2013.

PEER 2013/02 *Hybrid Simulation of the Seismic Response of Squat Reinforced Concrete Shear Walls*. Catherine A. Whyte and Bozidar Stojadinovic. May 2013.

PEER 2013/01 *Housing Recovery in Chile: A Qualitative Mid-program Review*. Mary C. Comerio. February 2013.

PEER 2012/08 *Guidelines for Estimation of Shear Wave Velocity.* Bernard R. Wair, Jason T. DeJong, and Thomas Shantz. December 2012.

PEER 2012/07 *Earthquake Engineering for Resilient Communities: 2012 PEER Internship Program Research Report Collection.* Heidi Tremayne (Editor), Stephen A. Mahin (Editor), Collin Anderson, Dustin Cook, Michael Erceg, Carlos Esparza, Jose Jimenez, Dorian Krausz, Andrew Lo, Stephanie Lopez, Nicole McCurdy, Paul Shipman, Alexander Strum, Eduardo Vega. December 2012.

PEER 2012/06 *Fragilities for Precarious Rocks at Yucca Mountain.* Matthew D. Purvance, Rasool Anooshehpoor, and James N. Brune. December 2012.

PEER 2012/05 *Development of Simplified Analysis Procedure for Piles in Laterally Spreading Layered Soils.* Christopher R. McGann, Pedro Arduino, and Peter Mackenzie–Helnwein. December 2012.

PEER 2012/04 *Unbonded Pre-Tensioned Columns for Bridges in Seismic Regions.* Phillip M. Davis, Todd M. Janes, Marc O. Eberhard, and John F. Stanton. December 2012.

PEER 2012/03 *Experimental and Analytical Studies on Reinforced Concrete Buildings with Seismically Vulnerable Beam-Column Joints*. Sangjoon Park and Khalid M. Mosalam. October 2012.

PEER 2012/02 *Seismic Performance of Reinforced Concrete Bridges Allowed to Uplift during Multi-Directional Excitation*. Andres Oscar Espinoza and Stephen A. Mahin. July 2012.

PEER 2012/01 *Spectral Damping Scaling Factors for Shallow Crustal Earthquakes in Active Tectonic Regions.* Sanaz Rezaeian, Yousef Bozorgnia, I. M. Idriss, Kenneth Campbell, Norman Abrahamson, and Walter Silva. July 2012.

PEER 2011/10 *Earthquake Engineering for Resilient Communities: 2011 PEER Internship Program Research Report Collection*. Heidi Faison and Stephen A. Mahin, Editors. December 2011.

PEER 2011/09 *Calibration of Semi-Stochastic Procedure for Simulating High-Frequency Ground Motions*. Jonathan P. Stewart, Emel Seyhan, and Robert W. Graves. December 2011.

PEER 2011/08 *Water Supply in regard to Fire Following Earthquake*. Charles Scawthorn. November 2011.

PEER 2011/07 *Seismic Risk Management in Urban Areas*. Proceedings of a U.S.-Iran-Turkey Seismic Workshop. September 2011.

PEER 2011/06 *The Use of Base Isolation Systems to Achieve Complex Seismic Performance Objectives*. Troy A. Morgan and Stephen A. Mahin. July 2011.

PEER 2011/05 *Case Studies of the Seismic Performance of Tall Buildings Designed by Alternative Means.* Task 12 Report for the Tall Buildings Initiative. Jack Moehle, Yousef Bozorgnia, Nirmal Jayaram, Pierson Jones, Mohsen Rahnama, Nilesh Shome, Zeynep Tuna, John Wallace, Tony Yang, and Farzin Zareian. July 2011.

PEER 2011/04 *Recommended Design Practice for Pile Foundations in Laterally Spreading Ground.* Scott A. Ashford, Ross W. Boulanger, and Scott J. Brandenberg. June 2011.

PEER 2011/03 *New Ground Motion Selection Procedures and Selected Motions for the PEER Transportation Research Program*. Jack W. Baker, Ting Lin, Shrey K. Shahi, and Nirmal Jayaram. March 2011.

PEER 2011/02 *A Bayesian Network Methodology for Infrastructure Seismic Risk Assessment and Decision Support*. Michelle T. Bensi, Armen Der Kiureghian, and Daniel Straub. March 2011.

PEER 2011/01 *Demand Fragility Surfaces for Bridges in Liquefied and Laterally Spreading Ground*. Scott J. Brandenberg, Jian Zhang, Pirooz Kashighandi, Yili Huo, and Minxing Zhao. March 2011.

PEER 2010/05 *Guidelines for Performance-Based Seismic Design of Tall Buildings.* Developed by the Tall Buildings Initiative. November 2010.

PEER 2010/04 *Application Guide for the Design of Flexible and Rigid Bus Connections between Substation Equipment Subjected to Earthquakes.* Jean-Bernard Dastous and Armen Der Kiureghian. September 2010.

PEER 2010/03 *Shear Wave Velocity as a Statistical Function of Standard Penetration Test Resistance and Vertical Effective Stress at Caltrans Bridge Sites.* Scott J. Brandenberg, Naresh Bellana, and Thomas Shantz. June 2010.

PEER 2010/02 *Stochastic Modeling and Simulation of Ground Motions for Performance-Based Earthquake Engineering.* Sanaz Rezaeian and Armen Der Kiureghian. June 2010.

PEER 2010/01 *Structural Response and Cost Characterization of Bridge Construction Using Seismic Performance Enhancement Strategies.* Ady Aviram, Božidar Stojadinović, Gustavo J. Parra-Montesinos, and Kevin R. Mackie. March 2010.

PEER 2009/03 *The Integration of Experimental and Simulation Data in the Study of Reinforced Concrete Bridge Systems Including Soil-Foundation-Structure Interaction.* Matthew Dryden and Gregory L. Fenves. November 2009.

PEER 2009/02 *Improving Earthquake Mitigation through Innovations and Applications in Seismic Science, Engineering, Communication, and Response*. Proceedings of a U.S.-Iran Seismic Workshop. October 2009.

PEER 2009/01 *Evaluation of Ground Motion Selection and Modification Methods: Predicting Median Interstory Drift Response of Buildings*. Curt B. Haselton, Editor. June 2009.

PEER 2008/10 *Technical Manual for Strata.* Albert R. Kottke and Ellen M. Rathje. February 2009.

PEER 2008/09 *NGA Model for Average Horizontal Component of Peak Ground Motion and Response Spectra.* Brian S.-J. Chiou and Robert R. Youngs. November 2008.

PEER 2008/08 *Toward Earthquake-Resistant Design of Concentrically Braced Steel Structures*. Patxi Uriz and Stephen A. Mahin. November 2008.

PEER 2008/07 *Using OpenSees for Performance-Based Evaluation of Bridges on Liquefiable Soils*. Stephen L. Kramer, Pedro Arduino, and HyungSuk Shin. November 2008.

PEER 2008/06 *Shaking Table Tests and Numerical Investigation of Self-Centering Reinforced Concrete Bridge Columns*. Hyung IL Jeong, Junichi Sakai, and Stephen A. Mahin. September 2008.

PEER 2008/05 *Performance-Based Earthquake Engineering Design Evaluation Procedure for Bridge Foundations Undergoing Liquefaction-Induced Lateral Ground Displacement*. Christian A. Ledezma and Jonathan D. Bray. August 2008.

PEER 2008/04 *Benchmarking of Nonlinear Geotechnical Ground Response Analysis Procedures.* Jonathan P. Stewart, Annie On-Lei Kwok, Youssef M. A. Hashash, Neven Matasovic, Robert Pyke, Zhiliang Wang, and Zhaohui Yang. August 2008.

PEER 2008/03 *Guidelines for Nonlinear Analysis of Bridge Structures in California.* Ady Aviram, Kevin R. Mackie, and Božidar Stojadinović. August 2008.

PEER 2008/02 *Treatment of Uncertainties in Seismic-Risk Analysis of Transportation Systems*. Evangelos Stergiou and Anne S. Kiremidjian. July 2008.

PEER 2008/01 *Seismic Performance Objectives for Tall Buildings.* William T. Holmes, Charles Kircher, William Petak, and Nabih Youssef. August 2008.

PEER 2007/12 *An Assessment to Benchmark the Seismic Performance of a Code-Conforming Reinforced Concrete Moment-Frame Building.* Curt Haselton, Christine A. Goulet, Judith Mitrani-Reiser, James L. Beck, Gregory G. Deierlein, Keith A. Porter, Jonathan P. Stewart, and Ertugrul Taciroglu. August 2008.

PEER 2007/11 *Bar Buckling in Reinforced Concrete Bridge Columns.* Wayne A. Brown, Dawn E. Lehman, and John F. Stanton. February 2008.

PEER 2007/10 *Computational Modeling of Progressive Collapse in Reinforced Concrete Frame Structures*. Mohamed M. Talaat and Khalid M. Mosalam. May 2008.

PEER 2007/09 *Integrated Probabilistic Performance-Based Evaluation of Benchmark Reinforced Concrete Bridges*. Kevin R. Mackie, John-Michael Wong, and Božidar Stojadinović. January 2008.

PEER 2007/08 *Assessing Seismic Collapse Safety of Modern Reinforced Concrete Moment-Frame Buildings*. Curt B. Haselton and Gregory G. Deierlein. February 2008.

PEER 2007/07 *Performance Modeling Strategies for Modern Reinforced Concrete Bridge Columns*. Michael P. Berry and Marc O. Eberhard. April 2008.

PEER 2007/06 *Development of Improved Procedures for Seismic Design of Buried and Partially Buried Structures*. Linda Al Atik and Nicholas Sitar. June 2007.

PEER 2007/05 *Uncertainty and Correlation in Seismic Risk Assessment of Transportation Systems*. Renee G. Lee and Anne S. Kiremidjian. July 2007.

PEER 2007/04 *Numerical Models for Analysis and Performance-Based Design of Shallow Foundations Subjected to Seismic Loading.* Sivapalan Gajan, Tara C. Hutchinson, Bruce L. Kutter, Prishati Raychowdhury, José A. Ugalde, and Jonathan P. Stewart. May 2008.

PEER 2007/03 *Beam-Column Element Model Calibrated for Predicting Flexural Response Leading to Global Collapse of RC Frame Buildings*. Curt B. Haselton, Abbie B. Liel, Sarah Taylor Lange, and Gregory G. Deierlein. May 2008.

PEER 2007/02 *Campbell-Bozorgnia NGA Ground Motion Relations for the Geometric Mean Horizontal Component of Peak and Spectral Ground Motion Parameters*. Kenneth W. Campbell and Yousef Bozorgnia. May 2007.

PEER 2007/01 *Boore-Atkinson NGA Ground Motion Relations for the Geometric Mean Horizontal Component of Peak and Spectral Ground Motion Parameters*. David M. Boore and Gail M. Atkinson. May 2007.

PEER 2006/12 Societal Implications of Performance-Based Earthquake Engineering. Peter J. May. May 2007.

PEER 2006/11 *Probabilistic Seismic Demand Analysis Using Advanced Ground Motion Intensity Measures, Attenuation Relationships, and Near-Fault Effects*. Polsak Tothong and C. Allin Cornell. March 2007.

PEER 2006/10 *Application of the PEER PBEE Methodology to the I-880 Viaduct*. Sashi Kunnath. February 2007.

PEER 2006/09 *Quantifying Economic Losses from Travel Forgone Following a Large Metropolitan Earthquake*. James Moore, Sungbin Cho, Yue Yue Fan, and Stuart Werner. November 2006.

PEER 2006/08 *Vector-Valued Ground Motion Intensity Measures for Probabilistic Seismic Demand Analysis*. Jack W. Baker and C. Allin Cornell. October 2006.

PEER 2006/07 *Analytical Modeling of Reinforced Concrete Walls for Predicting Flexural and Coupled–Shear-Flexural Responses*. Kutay Orakcal, Leonardo M. Massone, and John W. Wallace. October 2006.

PEER 2006/06 *Nonlinear Analysis of a Soil-Drilled Pier System under Static and Dynamic Axial Loading*. Gang Wang and Nicholas Sitar. November 2006.

PEER 2006/05 *Advanced Seismic Assessment Guidelines.* Paolo Bazzurro, C. Allin Cornell, Charles Menun, Maziar Motahari, and Nicolas Luco. September 2006.

PEER 2006/04 *Probabilistic Seismic Evaluation of Reinforced Concrete Structural Components and Systems*. Tae Hyung Lee and Khalid M. Mosalam. August 2006.

PEER 2006/03 *Performance of Lifelines Subjected to Lateral Spreading*. Scott A. Ashford and Teerawut Juirnarongrit. July 2006.

PEER 2006/02 *Pacific Earthquake Engineering Research Center Highway Demonstration Project.* Anne Kiremidjian, James Moore, Yue Yue Fan, Nesrin Basoz, Ozgur Yazali, and Meredith Williams. April 2006.

PEER 2006/01 *Bracing Berkeley. A Guide to Seismic Safety on the UC Berkeley Campus.* Mary C. Comerio, Stephen Tobriner, and Ariane Fehrenkamp. January 2006.

PEER 2005/17 *Earthquake Simulation Tests on Reducing Residual Displacements of Reinforced Concrete Bridges.* Junichi Sakai, Stephen A Mahin, and Andres Espinoza. December 2005.

PEER 2005/16 *Seismic Response and Reliability of Electrical Substation Equipment and Systems.* Junho Song, Armen Der Kiureghian, and Jerome L. Sackman. April 2006.

PEER 2005/15 *CPT-Based Probabilistic Assessment of Seismic Soil Liquefaction Initiation.* R. E. S. Moss, R. B. Seed, R. E. Kayen, J. P. Stewart, and A. Der Kiureghian. April 2006.

PEER 2005/14 *Workshop on Modeling of Nonlinear Cyclic Load-Deformation Behavior of Shallow Foundations*. Bruce L. Kutter, Geoffrey Martin, Tara Hutchinson, Chad Harden, Sivapalan Gajan, and Justin Phalen. March 2006.

PEER 2005/13 *Stochastic Characterization and Decision Bases under Time-Dependent Aftershock Risk in Performance-Based Earthquake Engineering*. Gee Liek Yeo and C. Allin Cornell. July 2005.

PEER 2005/12 *PEER Testbed Study on a Laboratory Building: Exercising Seismic Performance Assessment.* Mary C. Comerio, Editor. November 2005.

PEER 2005/11 *Van Nuys Hotel Building Testbed Report: Exercising Seismic Performance Assessment.* Helmut Krawinkler, Editor. October 2005.

PEER 2005/10 *First NEES/E-Defense Workshop on Collapse Simulation of Reinforced Concrete Building Structures.* September 2005.

PEER 2005/09 *Test Applications of Advanced Seismic Assessment Guidelines.* Joe Maffei, Karl Telleen, Danya Mohr, William Holmes, and Yuki Nakayama. August 2006.

PEER 2005/08 *Damage Accumulation in Lightly Confined Reinforced Concrete Bridge Columns.* R. Tyler Ranf, Jared M. Nelson, Zach Price, Marc O. Eberhard, and John F. Stanton. April 2006.

PEER 2005/07 *Experimental and Analytical Studies on the Seismic Response of Freestanding and Anchored Laboratory Equipment.* Dimitrios Konstantinidis and Nicos Makris. January 2005.

PEER 2005/06 *Global Collapse of Frame Structures under Seismic Excitations*. Luis F. Ibarra and Helmut Krawinkler. September 2005.

PEER 2005//05 *Performance Characterization of Bench- and Shelf-Mounted Equipment.* Samit Ray Chaudhuri and Tara C. Hutchinson. May 2006.

PEER 2005/04 *Numerical Modeling of the Nonlinear Cyclic Response of Shallow Foundations.* Chad Harden, Tara Hutchinson, Geoffrey R. Martin, and Bruce L. Kutter. August 2005.

PEER 2005/03 *A Taxonomy of Building Components for Performance-Based Earthquake Engineering.* Keith A. Porter. September 2005.

PEER 2005/02 *Fragility Basis for California Highway Overpass Bridge Seismic Decision Making*. Kevin R. Mackie and Božidar Stojadinović. June 2005.

PEER 2005/01 *Empirical Characterization of Site Conditions on Strong Ground Motion.* Jonathan P. Stewart, Yoojoong Choi, and Robert W. Graves. June 2005.

PEER 2004/09 *Electrical Substation Equipment Interaction: Experimental Rigid Conductor Studies.* Christopher Stearns and André Filiatrault. February 2005.

PEER 2004/08 *Seismic Qualification and Fragility Testing of Line Break 550-kV Disconnect Switches.* Shakhzod M. Takhirov, Gregory L. Fenves, and Eric Fujisaki. January 2005.

PEER 2004/07 *Ground Motions for Earthquake Simulator Qualification of Electrical Substation Equipment.* Shakhzod M. Takhirov, Gregory L. Fenves, Eric Fujisaki, and Don Clyde. January 2005.

PEER 2004/06 *Performance-Based Regulation and Regulatory Regimes.* Peter J. May and Chris Koski. September 2004.

PEER 2004/05 *Performance-Based Seismic Design Concepts and Implementation: Proceedings of an International Workshop.* Peter Fajfar and Helmut Krawinkler, Editors. September 2004.

PEER 2004/04 *Seismic Performance of an Instrumented Tilt-up Wall Building.* James C. Anderson and Vitelmo V. Bertero. July 2004.

PEER 2004/03 *Evaluation and Application of Concrete Tilt-up Assessment Methodologies.* Timothy Graf and James O. Malley. October 2004.

PEER 2004/02 *Analytical Investigations of New Methods for Reducing Residual Displacements of Reinforced Concrete Bridge Columns.* Junichi Sakai and Stephen A. Mahin. August 2004.

PEER 2004/01 *Seismic Performance of Masonry Buildings and Design Implications.* Kerri Anne Taeko Tokoro, James C. Anderson, and Vitelmo V. Bertero. February 2004.

PEER 2003/18 *Performance Models for Flexural Damage in Reinforced Concrete Columns.* Michael Berry and Marc Eberhard. August 2003.

PEER 2003/17 *Predicting Earthquake Damage in Older Reinforced Concrete Beam-Column Joints.* Catherine Pagni and Laura Lowes. October 2004.

PEER 2003/16 *Seismic Demands for Performance-Based Design of Bridges.* Kevin Mackie and Božidar Stojadinović. August 2003.

PEER 2003/15 *Seismic Demands for Nondeteriorating Frame Structures and Their Dependence on Ground Motions.* Ricardo Antonio Medina and Helmut Krawinkler. May 2004.

PEER 2003/14 *Finite Element Reliability and Sensitivity Methods for Performance-Based Earthquake Engineering*. Terje Haukaas and Armen Der Kiureghian. April 2004.

PEER 2003/13 *Effects of Connection Hysteretic Degradation on the Seismic Behavior of Steel Moment-Resisting Frames.* Janise E. Rodgers and Stephen A. Mahin. March 2004.

PEER 2003/12 *Implementation Manual for the Seismic Protection of Laboratory Contents: Format and Case Studies*. William T. Holmes and Mary C. Comerio. October 2003.

PEER 2003/11 *Fifth U.S.-Japan Workshop on Performance-Based Earthquake Engineering Methodology for Reinforced Concrete Building Structures*. February 2004.

PEER 2003/10 *A Beam-Column Joint Model for Simulating the Earthquake Response of Reinforced Concrete Frames.* Laura N. Lowes, Nilanjan Mitra, and Arash Altoontash. February 2004.

PEER 2003/09 *Sequencing Repairs after an Earthquake: An Economic Approach.* Marco Casari and Simon J. Wilkie. April 2004.

PEER 2003/08 *A Technical Framework for Probability-Based Demand and Capacity Factor Design (DCFD) Seismic Formats*. Fatemeh Jalayer and C. Allin Cornell. November 2003.

PEER 2003/07 *Uncertainty Specification and Propagation for Loss Estimation Using FOSM Methods.* Jack W. Baker and C. Allin Cornell. September 2003.

PEER 2003/06 *Performance of Circular Reinforced Concrete Bridge Columns under Bidirectional Earthquake Loading*. Mahmoud M. Hachem, Stephen A. Mahin, and Jack P. Moehle. February 2003.

PEER 2003/05 *Response Assessment for Building-Specific Loss Estimation.* Eduardo Miranda and Shahram Taghavi. September 2003.

PEER 2003/04 *Experimental Assessment of Columns with Short Lap Splices Subjected to Cyclic Loads*. Murat Melek, John W. Wallace, and Joel Conte. April 2003.

PEER 2003/03 *Probabilistic Response Assessment for Building-Specific Loss Estimation*. Eduardo Miranda and Hesameddin Aslani. September 2003.

PEER 2003/02 *Software Framework for Collaborative Development of Nonlinear Dynamic Analysis Program*. Jun Peng and Kincho H. Law. September 2003.

PEER 2003/01 *Shake Table Tests and Analytical Studies on the Gravity Load Collapse of Reinforced Concrete Frames.* Kenneth John Elwood and Jack P. Moehle. November 2003.

PEER 2002/24 *Performance of Beam to Column Bridge Joints Subjected to a Large Velocity Pulse.* Natalie Gibson, André Filiatrault, and Scott A. Ashford. April 2002.

PEER 2002/23 *Effects of Large Velocity Pulses on Reinforced Concrete Bridge Columns.* Greg L. Orozco and Scott A. Ashford. April 2002.

PEER 2002/22 *Characterization of Large Velocity Pulses for Laboratory Testing.* Kenneth E. Cox and Scott A. Ashford. April 2002.

PEER 2002/21 *Fourth U.S.-Japan Workshop on Performance-Based Earthquake Engineering Methodology for Reinforced Concrete Building Structures*. December 2002.

PEER 2002/20 *Barriers to Adoption and Implementation of PBEE Innovations.* Peter J. May. August 2002.

PEER 2002/19 *Economic-Engineered Integrated Models for Earthquakes: Socioeconomic Impacts.* Peter Gordon, James E. Moore II, and Harry W. Richardson. July 2002.

PEER 2002/18 *Assessment of Reinforced Concrete Building Exterior Joints with Substandard Details.* Chris P. Pantelides, Jon Hansen, Justin Nadauld, and Lawrence D. Reaveley. May 2002.

PEER 2002/17 *Structural Characterization and Seismic Response Analysis of a Highway Overcrossing Equipped with Elastomeric Bearings and Fluid Dampers: A Case Study*. Nicos Makris and Jian Zhang. November 2002.

PEER 2002/16 *Estimation of Uncertainty in Geotechnical Properties for Performance-Based Earthquake Engineering*. Allen L. Jones, Steven L. Kramer, and Pedro Arduino. December 2002.

PEER 2002/15 *Seismic Behavior of Bridge Columns Subjected to Various Loading Patterns*. Asadollah Esmaeily-Gh. and Yan Xiao. December 2002.

PEER 2002/14 *Inelastic Seismic Response of Extended Pile Shaft Supported Bridge Structures.* T.C. Hutchinson, R.W. Boulanger, Y.H. Chai, and I.M. Idriss. December 2002.

PEER 2002/13 *Probabilistic Models and Fragility Estimates for Bridge Components and Systems.* Paolo Gardoni, Armen Der Kiureghian, and Khalid M. Mosalam. June 2002.

PEER 2002/12 *Effects of Fault Dip and Slip Rake on Near-Source Ground Motions: Why Chi-Chi Was a Relatively Mild M7.6 Earthquake*. Brad T. Aagaard, John F. Hall, and Thomas H. Heaton. December 2002.

PEER 2002/11 *Analytical and Experimental Study of Fiber-Reinforced Strip Isolators*. James M. Kelly and Shakhzod M. Takhirov. September 2002.

PEER 2002/10 *Centrifuge Modeling of Settlement and Lateral Spreading with Comparisons to Numerical Analyses***.** Sivapalan Gajan and Bruce L. Kutter. January 2003.

PEER 2002/09 *Documentation and Analysis of Field Case Histories of Seismic Compression during the 1994 Northridge, California, Earthquake*. Jonathan P. Stewart, Patrick M. Smith, Daniel H. Whang, and Jonathan D. Bray. October 2002.

PEER 2002/08 *Component Testing, Stability Analysis and Characterization of Buckling-Restrained Unbonded Braces™*. Cameron Black, Nicos Makris, and Ian Aiken. September 2002.

PEER 2002/07 *Seismic Performance of Pile-Wharf Connections.* Charles W. Roeder, Robert Graff, Jennifer Soderstrom, and Jun Han Yoo. December 2001.

PEER 2002/06 *The Use of Benefit-Cost Analysis for Evaluation of Performance-Based Earthquake Engineering Decisions*. Richard O. Zerbe and Anthony Falit-Baiamonte. September 2001.

PEER 2002/05 *Guidelines, Specifications, and Seismic Performance Characterization of Nonstructural Building Components and Equipment*. André Filiatrault, Constantin Christopoulos, and Christopher Stearns. September 2001.

PEER 2002/04 *Consortium of Organizations for Strong-Motion Observation Systems and the Pacific Earthquake Engineering Research Center Lifelines Program: Invited Workshop on Archiving and Web Dissemination of Geotechnical Data, 4–5 October 2001*. September 2002.

PEER 2002/03 *Investigation of Sensitivity of Building Loss Estimates to Major Uncertain Variables for the Van Nuys Testbed*. Keith A. Porter, James L. Beck, and Rustem V. Shaikhutdinov. August 2002.

PEER 2002/02 *The Third U.S.-Japan Workshop on Performance-Based Earthquake Engineering Methodology for Reinforced Concrete Building Structures*. July 2002.

PEER 2002/01 *Nonstructural Loss Estimation: The UC Berkeley Case Study.* Mary C. Comerio and John C. Stallmeyer. December 2001.

PEER 2001/16 *Statistics of SDF-System Estimate of Roof Displacement for Pushover Analysis of Buildings.* Anil K. Chopra, Rakesh K. Goel, and Chatpan Chintanapakdee. December 2001.

PEER 2001/15 *Damage to Bridges during the 2001 Nisqually Earthquake.* R. Tyler Ranf, Marc O. Eberhard, and Michael P. Berry. November 2001.

PEER 2001/14 *Rocking Response of Equipment Anchored to a Base Foundation.* Nicos Makris and Cameron J. Black. September 2001.

PEER 2001/13 *Modeling Soil Liquefaction Hazards for Performance-Based Earthquake Engineering*. Steven L. Kramer and Ahmed-W. Elgamal. February 2001.

PEER 2001/12 *Development of Geotechnical Capabilities in OpenSees*. Boris Jeremić. September 2001.

PEER 2001/11 *Analytical and Experimental Study of Fiber-Reinforced Elastomeric Isolators*. James M. Kelly and Shakhzod M. Takhirov. September 2001.

PEER 2001/10 *Amplification Factors for Spectral Acceleration in Active Regions.* Jonathan P. Stewart, Andrew H. Liu, Yoojoong Choi, and Mehmet B. Baturay. December 2001.

PEER 2001/09 *Ground Motion Evaluation Procedures for Performance-Based Design.* Jonathan P. Stewart, Shyh-Jeng Chiou, Jonathan D. Bray, Robert W. Graves, Paul G. Somerville, and Norman A. Abrahamson. September 2001.

PEER 2001/08 *Experimental and Computational Evaluation of Reinforced Concrete Bridge Beam-Column Connections for Seismic Performance*. Clay J. Naito, Jack P. Moehle, and Khalid M. Mosalam. November 2001.

PEER 2001/07 *The Rocking Spectrum and the Shortcomings of Design Guidelines.* Nicos Makris and Dimitrios Konstantinidis. August 2001.

PEER 2001/06 *Development of an Electrical Substation Equipment Performance Database for Evaluation of Equipment Fragilities*. Thalia Agnanos. April 1999.

PEER 2001/05 *Stiffness Analysis of Fiber-Reinforced Elastomeric Isolators.* Hsiang-Chuan Tsai and James M. Kelly. May 2001.

PEER 2001/04 *Organizational and Societal Considerations for Performance-Based Earthquake Engineering*. Peter J. May. April 2001.

PEER 2001/03 *A Modal Pushover Analysis Procedure to Estimate Seismic Demands for Buildings: Theory and Preliminary Evaluation*. Anil K. Chopra and Rakesh K. Goel. January 2001.

PEER 2001/02 *Seismic Response Analysis of Highway Overcrossings Including Soil-Structure Interaction*. Jian Zhang and Nicos Makris. March 2001.

PEER 2001/01 *Experimental Study of Large Seismic Steel Beam-to-Column Connections.* Egor P. Popov and Shakhzod M. Takhirov. November 2000.

PEER 2000/10 *The Second U.S.-Japan Workshop on Performance-Based Earthquake Engineering Methodology for Reinforced Concrete Building Structures*. March 2000.

PEER 2000/09 *Structural Engineering Reconnaissance of the August 17, 1999 Earthquake: Kocaeli (Izmit), Turkey.* Halil Sezen, Kenneth J. Elwood, Andrew S. Whittaker, Khalid Mosalam, John J. Wallace, and John F. Stanton. December 2000.

PEER 2000/08 *Behavior of Reinforced Concrete Bridge Columns Having Varying Aspect Ratios and Varying Lengths of Confinement*. Anthony J. Calderone, Dawn E. Lehman, and Jack P. Moehle. January 2001.

PEER 2000/07 *Cover-Plate and Flange-Plate Reinforced Steel Moment-Resisting Connections*. Taejin Kim, Andrew S. Whittaker, Amir S. Gilani, Vitelmo V. Bertero, and Shakhzod M. Takhirov. September 2000.

PEER 2000/06 *Seismic Evaluation and Analysis of 230-kV Disconnect Switches*. Amir S. J. Gilani, Andrew S. Whittaker, Gregory L. Fenves, Chun-Hao Chen, Henry Ho, and Eric Fujisaki. July 2000.

PEER 2000/05 *Performance-Based Evaluation of Exterior Reinforced Concrete Building Joints for Seismic Excitation*. Chandra Clyde, Chris P. Pantelides, and Lawrence D. Reaveley. July 2000.

PEER 2000/04 *An Evaluation of Seismic Energy Demand: An Attenuation Approach*. Chung-Che Chou and Chia-Ming Uang. July 1999.

PEER 2000/03 *Framing Earthquake Retrofitting Decisions: The Case of Hillside Homes in Los Angeles*. Detlof von Winterfeldt, Nels Roselund, and Alicia Kitsuse. March 2000.

PEER 2000/02 *U.S.-Japan Workshop on the Effects of Near-Field Earthquake Shaking*. Andrew Whittaker, Editor. July 2000.

PEER 2000/01 *Further Studies on Seismic Interaction in Interconnected Electrical Substation Equipment*. Armen Der Kiureghian, Kee-Jeung Hong, and Jerome L. Sackman. November 1999.

PEER 1999/14 *Seismic Evaluation and Retrofit of 230-kV Porcelain Transformer Bushings*. Amir S. Gilani, Andrew S. Whittaker, Gregory L. Fenves, and Eric Fujisaki. December 1999.

PEER 1999/13 *Building Vulnerability Studies: Modeling and Evaluation of Tilt-up and Steel Reinforced Concrete Buildings*. John W. Wallace, Jonathan P. Stewart, and Andrew S. Whittaker, Editors. December 1999.

PEER 1999/12 *Rehabilitation of Nonductile RC Frame Building Using Encasement Plates and Energy-Dissipating Devices*. Mehrdad Sasani, Vitelmo V. Bertero, James C. Anderson. December 1999.

PEER 1999/11 *Performance Evaluation Database for Concrete Bridge Components and Systems under Simulated Seismic Loads*. Yael D. Hose and Frieder Seible. November 1999.

PEER 1999/10 *U.S.-Japan Workshop on Performance-Based Earthquake Engineering Methodology for Reinforced Concrete Building Structures*. December 1999.

PEER 1999/09 *Performance Improvement of Long Period Building Structures Subjected to Severe Pulse-Type Ground Motions*. James C. Anderson, Vitelmo V. Bertero, and Raul Bertero. October 1999.

PEER 1999/08 *Envelopes for Seismic Response Vectors*. Charles Menun and Armen Der Kiureghian. July 1999.

PEER 1999/07 *Documentation of Strengths and Weaknesses of Current Computer Analysis Methods for Seismic Performance of Reinforced Concrete Members*. William F. Cofer. November 1999.

PEER 1999/06 *Rocking Response and Overturning of Anchored Equipment under Seismic Excitations*. Nicos Makris and Jian Zhang. November 1999.

PEER 1999/05 *Seismic Evaluation of 550 kV Porcelain Transformer Bushings*. Amir S. Gilani, Andrew S. Whittaker, Gregory L. Fenves, and Eric Fujisaki. October 1999.

PEER 1999/04 *Adoption and Enforcement of Earthquake Risk-Reduction Measures*. Peter J. May, Raymond J. Burby, T. Jens Feeley, and Robert Wood. August 1999.

PEER 1999/03 *Task 3 Characterization of Site Response General Site Categories*. Adrian Rodriguez-Marek, Jonathan D. Bray and Norman Abrahamson. February 1999.

PEER 1999/02 *Capacity-Demand-Diagram Methods for Estimating Seismic Deformation of Inelastic Structures: SDF Systems*. Anil K. Chopra and Rakesh Goel. April 1999.

PEER 1999/01 *Interaction in Interconnected Electrical Substation Equipment Subjected to Earthquake Ground Motions*. Armen Der Kiureghian, Jerome L. Sackman, and Kee-Jeung Hong. February 1999.

PEER 1998/08 *Behavior and Failure Analysis of a Multiple-Frame Highway Bridge in the 1994 Northridge Earthquake*. Gregory L. Fenves and Michael Ellery. December 1998.

PEER 1998/07 *Empirical Evaluation of Inertial Soil-Structure Interaction Effects*. Jonathan P. Stewart, Raymond B. Seed, and Gregory L. Fenves. November 1998.

PEER 1998/06 *Effect of Damping Mechanisms on the Response of Seismic Isolated Structures*. Nicos Makris and Shih-Po Chang. November 1998.

PEER 1998/05 *Rocking Response and Overturning of Equipment under Horizontal Pulse-Type Motions*. Nicos Makris and Yiannis Roussos. October 1998.

PEER 1998/04 *Pacific Earthquake Engineering Research Invitational Workshop Proceedings, May 14–15, 1998: Defining the Links between Planning, Policy Analysis, Economics and Earthquake Engineering*. Mary Comerio and Peter Gordon. September 1998.

PEER 1998/03 *Repair/Upgrade Procedures for Welded Beam to Column Connections*. James C. Anderson and Xiaojing Duan. May 1998.

PEER 1998/02 *Seismic Evaluation of 196 kV Porcelain Transformer Bushings.* Amir S. Gilani, Juan W. Chavez, Gregory L. Fenves, and Andrew S. Whittaker. May 1998.

PEER 1998/01 *Seismic Performance of Well-Confined Concrete Bridge Columns.* Dawn E. Lehman and Jack P. Moehle. December 2000.

PEER REPORTS: ONE HUNDRED SERIES

The following PEER reports are available by Internet only at http://peer.berkeley.edu/publications/peer_reports_complete.html.

PEER 2012/103 *Performance-Based Seismic Demand Assessment of Concentrically Braced Steel Frame Buildings.* Chui-Hsin Chen and Stephen A. Mahin. December 2012.

PEER 2012/102 *Procedure to Restart an Interrupted Hybrid Simulation: Addendum to PEER Report 2010/103.* Vesna Terzic and Bozidar Stojadinovic. October 2012.

PEER 2012/101 *Mechanics of Fiber Reinforced Bearings.* James M. Kelly and Andrea Calabrese. February 2012.

PEER 2011/107 *Nonlinear Site Response and Seismic Compression at Vertical Array Strongly Shaken by 2007 Niigata-ken Chuetsu-oki Earthquake.* Eric Yee, Jonathan P. Stewart, and Kohji Tokimatsu. December 2011.

PEER 2011/106 *Self Compacting Hybrid Fiber Reinforced Concrete Composites for Bridge Columns.* Pardeep Kumar, Gabriel Jen, William Trono, Marios Panagiotou, and Claudia Ostertag. September 2011.

PEER 2011/105 *Stochastic Dynamic Analysis of Bridges Subjected to Spacially Varying Ground Motions.* Katerina Konakli and Armen Der Kiureghian. August 2011.

PEER 2011/104 *Design and Instrumentation of the 2010 E-Defense Four-Story Reinforced Concrete and Post-Tensioned Concrete Buildings.* Takuya Nagae, Kenichi Tahara, Taizo Matsumori, Hitoshi Shiohara, Toshimi Kabeyasawa, Susumu Kono, Minehiro Nishiyama (Japanese Research Team) and John Wallace, Wassim Ghannoum, Jack Moehle, Richard Sause, Wesley Keller, Zeynep Tuna (U.S. Research Team). June 2011.

PEER 2011/103 *In-Situ Monitoring of the Force Output of Fluid Dampers: Experimental Investigation.* Dimitrios Konstantinidis, James M. Kelly, and Nicos Makris. April 2011.

PEER 2011/102 *Ground-Motion Prediction Equations 1964–2010.* John Douglas. April 2011.

PEER 2011/101 *Report of the Eighth Planning Meeting of NEES/E-Defense Collaborative Research on Earthquake Engineering.* Convened by the Hyogo Earthquake Engineering Research Center (NIED), NEES Consortium, Inc. February 2011.

PEER 2010/111 *Modeling and Acceptance Criteria for Seismic Design and Analysis of Tall Buildings.* Task 7 Report for the Tall Buildings Initiative - Published jointly by the Applied Technology Council. October 2010.

PEER 2010/110 *Seismic Performance Assessment and Probabilistic Repair Cost Analysis of Precast Concrete Cladding Systems for Multistory Buildlings.* Jeffrey P. Hunt and Božidar Stojadinovic. November 2010.

PEER 2010/109 *Report of the Seventh Joint Planning Meeting of NEES/E-Defense Collaboration on Earthquake Engineering. Held at the E-Defense, Miki, and Shin-Kobe, Japan, September 18–19, 2009.* August 2010.

PEER 2010/108 *Probabilistic Tsunami Hazard in California.* Hong Kie Thio, Paul Somerville, and Jascha Polet, preparers. October 2010.

PEER 2010/107 *Performance and Reliability of Exposed Column Base Plate Connections for Steel Moment-Resisting Frames.* Ady Aviram, Božidar Stojadinovic, and Armen Der Kiureghian. August 2010.

PEER 2010/106 *Verification of Probabilistic Seismic Hazard Analysis Computer Programs.* Patricia Thomas, Ivan Wong, and Norman Abrahamson. May 2010.

PEER 2010/105 *Structural Engineering Reconnaissance of the April 6, 2009, Abruzzo, Italy, Earthquake, and Lessons Learned.* M. Selim Günay and Khalid M. Mosalam. April 2010.

PEER 2010/104 *Simulating the Inelastic Seismic Behavior of Steel Braced Frames, Including the Effects of Low-Cycle Fatigue.* Yuli Huang and Stephen A. Mahin. April 2010.

PEER 2010/103 *Post-Earthquake Traffic Capacity of Modern Bridges in California.* Vesna Terzic and Božidar Stojadinović. March 2010.

PEER 2010/102 *Analysis of Cumulative Absolute Velocity (CAV) and JMA Instrumental Seismic Intensity (I_{JMA}) Using the PEER–NGA Strong Motion Database.* Kenneth W. Campbell and Yousef Bozorgnia. February 2010.

PEER 2010/101 *Rocking Response of Bridges on Shallow Foundations.* Jose A. Ugalde, Bruce L. Kutter, and Boris Jeremic. April 2010.

PEER 2009/109 *Simulation and Performance-Based Earthquake Engineering Assessment of Self-Centering Post-Tensioned Concrete Bridge Systems.* Won K. Lee and Sarah L. Billington. December 2009.

PEER 2009/108 *PEER Lifelines Geotechnical Virtual Data Center.* J. Carl Stepp, Daniel J. Ponti, Loren L. Turner, Jennifer N. Swift, Sean Devlin, Yang Zhu, Jean Benoit, and John Bobbitt. September 2009.

PEER 2009/107 *Experimental and Computational Evaluation of Current and Innovative In-Span Hinge Details in Reinforced Concrete Box-Girder Bridges: Part 2: Post-Test Analysis and Design Recommendations.* Matias A. Hube and Khalid M. Mosalam. December 2009.

PEER 2009/106 *Shear Strength Models of Exterior Beam-Column Joints without Transverse Reinforcement.* Sangjoon Park and Khalid M. Mosalam. November 2009.

PEER 2009/105 *Reduced Uncertainty of Ground Motion Prediction Equations through Bayesian Variance Analysis.* Robb Eric S. Moss. November 2009.

PEER 2009/104 *Advanced Implementation of Hybrid Simulation.* Andreas H. Schellenberg, Stephen A. Mahin, Gregory L. Fenves. November 2009.

PEER 2009/103 *Performance Evaluation of Innovative Steel Braced Frames.* T. Y. Yang, Jack P. Moehle, and Božidar Stojadinovic. August 2009.

PEER 2009/102 *Reinvestigation of Liquefaction and Nonliquefaction Case Histories from the 1976 Tangshan Earthquake.* Robb Eric Moss, Robert E. Kayen, Liyuan Tong, Songyu Liu, Guojun Cai, and Jiaer Wu. August 2009.

PEER 2009/101 *Report of the First Joint Planning Meeting for the Second Phase of NEES/E-Defense Collaborative Research on Earthquake Engineering.* Stephen A. Mahin et al. July 2009.

PEER 2008/104 *Experimental and Analytical Study of the Seismic Performance of Retaining Structures.* Linda Al Atik and Nicholas Sitar. January 2009.

PEER 2008/103 *Experimental and Computational Evaluation of Current and Innovative In-Span Hinge Details in Reinforced Concrete Box-Girder Bridges. Part 1: Experimental Findings and Pre-Test Analysis.* Matias A. Hube and Khalid M. Mosalam. January 2009.

PEER 2008/102 *Modeling of Unreinforced Masonry Infill Walls Considering In-Plane and Out-of-Plane Interaction.* Stephen Kadysiewski and Khalid M. Mosalam. January 2009.

PEER 2008/101 *Seismic Performance Objectives for Tall Buildings.* William T. Holmes, Charles Kircher, William Petak, and Nabih Youssef. August 2008.

PEER 2007/101 *Generalized Hybrid Simulation Framework for Structural Systems Subjected to Seismic Loading*. Tarek Elkhoraibi and Khalid M. Mosalam. July 2007.

PEER 2007/100 *Seismic Evaluation of Reinforced Concrete Buildings Including Effects of Masonry Infill Walls*. Alidad Hashemi and Khalid M. Mosalam. July 2007.

The Pacifi c Earthquake Engineering Research Center (PEER) is a multi-institutional research and education center with headquarters at the University of California, Berkeley. Investigators from over 20 universities, several consulting companies, and researchers at various state and federal government agencies contribute to research programs focused on performance-based earthquake engineering.

These research programs aim to identify and reduce the risks from major earthquakes to life safety and to the economy by including research in a wide variety of disciplines including structural and geotechnical engineering, geology/seismology, lifelines, transportation, architecture, economics, risk management, and public policy.

PEER is supported by federal, state, local, and regional agencies, together with industry partners.

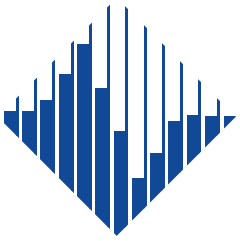

PEER Core Institutions

University of California, Berkeley (Lead Institution)
California Institute of Technology
Oregon State University
Stanford University
University of California, Davis
University of California, Irvine
University of California, Los Angeles
University of California, San Diego
University of Nevada, Reno
University of Southern California
University of Washington

PEER reports can be ordered at https://peer.berkeley.edu/peer-reports or by contacting

Pacific Earthquake Engineering Research Center
University of California, Berkeley
325 Davis Hall, Mail Code 1792
Berkeley, CA 94720-1792
Tel: 510-642-3437
Email: peer_center@berkeley.edu

ISSN 2770-8314
https://doi.org/10.55461/CRJY2161